Surface–atmosphere interactions of heterogeneous surfaces on multiple scales by means of large-eddy simulations and analytical approaches

Zur Erlangung des akademischen Grades eines
DOKTORS DER NATURWISSENSCHAFTEN
von der Fakultät für
Bauingenieur-, Geo- und Umweltwissenschaften

des Karlsruher Instituts für Technologie (KIT)
genehmigte
DISSERTATION
von
M.Sc. Konstantin Kröniger
aus Unterammergau

Tag der mündlichen
Prüfung: 26.11.2018

Referent: Matthias Mauder

Korreferent: Olivier Eiff
Korreferent: Björn Maronga

Karlsruhe (2018)

Abstract

The effect of surface heterogeneities on surface–atmosphere exchange is of significant importance not only for atmospheric measurements but also for numerical weather or climate simulations, as these heterogeneities interact with the atmospheric turbulence on many different scales. While the number of numerical investigations on atmospheric flow above heterogeneous surfaces is continuously increasing, only a small amount of analytical theories exist, which is due to the nonlinearity of the governing equations. In the current thesis, surface–atmosphere interactions of heterogeneous surfaces were studied on several scales by means of analytical and numerical approaches, where large-eddy simulations (LES) were employed for the latter. At first, the micro-γ-scale heterogeneity of leading canopy edges was investigated by constructing an analytical solution to the governing equations of two-dimensional edge flow in neutral atmospheric stratification. To determine the missing model parameters (integration constants) and to test the model against LES, several simulations of varying canopy length scales were performed. The canopy-edge-flow model was further compared to the analytical model of Belcher et al. [*J. Fluid. Mech.*, 44:479-504, 2003]. This comparison showed that the Belcher et al. (2003) model is mainly applicable to shallow canopies, while the newly developed model featured the best results for canopies that were dense enough to ensure a full adjustment of the atmospheric flow. Besides investigating the interactions of micro-γ-scale heterogeneities, a distinct meso-γ-scale heterogeneity, namely the isolated semi-arid forest Yatir, was analyzed by detailed LES. These simulations were used to determine occurrence, location and strength of secondary circulations, as these flow features could be of major importance for the surface–atmosphere exchange of the semi-arid ecosystem. The numerical exploration revealed the formation of secondary circulations in all three cases of varying atmospheric stability (weakly-convective, mildly-convective, and strongly-convective scenarios). While the occurring circulations featured a horizontal extent that was too small to couple the full forest to the surrounding shrubland, investigations on the aerodynamic resistance to heat transfer showed that the secondary circulations affect the surface–atmosphere exchange by enhancing exchange in regions of updraft and reducing exchange in regions of downdraft. As the aforementioned mechanisms are directly related to surface heterogeneities, homogeneous parametrizations of surface–atmosphere exchange are insufficient to capture those. However, parametrizing surface heterogeneities is important for the application of meso-scale models to simulate atmospheric flow, as the grid resolution of these models is too coarse to resolve many important heterogeneity scales. To account for those scales, an aerodynamic resistance parametrization for heterogeneous surfaces was constructed from analytical investigations, which is the third part of this thesis. The analytical derivation is

based on linking the covariance function of the actual heterogeneous scenario to a corresponding homogeneous covariance function in spectral space. From assuming the shape of the turbulent spectra for the homogeneous case and by neglecting advection and dispersive fluxes, correction factors to the bulk aerodynamic resistance were extracted. Comparison of this novel covariance-function approach with the conventional bulk and tile approaches for three scenarios of idealized surface heterogneities revealed that the covariance-function approach features the smallest deviation from the LES reference, which illustrates the advantage of using this novel parametrization within the framework of meso-scale models.

Zusammenfassung

Der Einfluss von Oberflächenheterogenität auf die Wechselwirkungen zwischen Oberfläche und Atmosphäre ist nicht nur für Messungen des turbulenten Austausches, sondern auch für Wetter- und Klimasimulationen von signifikanter Bedeutung, da Oberflächenheterogenitäten mit der atmosphärischen Turbulenz auf verschiedenen Skalen wechselwirken. Während die Anzahl an numerischen Studien zu atmosphärischen Flüssen über heterogenen Oberflächen stetig zunimmt, existiert nur eine geringe Zahl an analytischen Theorien, was durch die nichtlineare Natur der zugrundeliegenden Gleichungen begründet ist. In dieser Dissertation wurden Wechselwirkungen von heterogenen Oberflächen mit der Atmosphäre unter Zuhilfenahme von analytischen und numerischen Methoden auf verschiedenen Skalen untersucht, wobei „large-eddy" Simulationen (LES) für den numerischen Teil Verwendung fanden. Die erste Untersuchung bezog sich auf die mikro-γ skalige Heterogenität von windzugewandten Vegetationskanten, die in einer analytische Lösung für den mittleren atmosphärischen Fluss durch eine solche Kante in neutraler Schichtung resultierte. Um die fehlenden Modellparameter (Integrationskonstanten) zu bestimmen, und um das Modell gegen LES zu testen, wurden mehrere Simulationen mit variierten Vegetationslängenskalen durchgeführt. Des Weiteren wurde das neu entwickelte Modell mit dem analytischen Modell von Belcher et al. [*J. Fluid. Mech.*, 44:479-504, 2003] verglichen. Dieser Vergleich zeigte, dass das Modell von Belcher et al. (2003) hauptsächlich für Vegetation von geringer Dichte angewandt werden kann, während das neu entwickelte Modell die besten Ergebnisse für Vegetation erzielte, die dicht genug war um eine vollständige Anpassung des atmosphärischen Flusses zu bewirken. Neben atmosphärischen Wechselwirkungen von mikro-γ skaligen Heterogenitäten, wurde mit dem semiariden Yatirwald auch eine ausgeprägte meso-γ skalige Heterogenität unter Zuhilfenahme von detaillierten LES untersucht. Diese Simulationen fanden bei der Bestimmung von Auftreten, Position und Stärke von Sekundärzirkulationen Verwendung, welche eine entscheidende Rolle für den atmosphärischen Austausch des semiariden Ökosystems spielen könnten. Die numerische Studie resultierte in einem Auftreten von Sekundärzirkulationen in allen drei Fällen von unterschiedlicher atmosphärischer Stabilität (schwach konvektiver, leicht konvektiver und stark konvektiver Fall). Obwohl die horizontale Ausdehnung der Zirkulationen zu klein war um den ganzen Wald mit dem umgebenden Buschland zu koppeln, zeigten Untersuchungen des aerodynamischen Widerstandes für Wärmeaustausch, dass die Sekundärzirkulationen die atmosphärischen Wechselwirkungen in Regionen mit Aufwind verstärkten und in Regionen mit Abwind abschwächten. Da die zuvor genannten Mechanismen direkt mit der Heterogenität der Oberfläche verknüpft sind, können sie nicht durch homogenen Parametrisierungen

beschrieben werden. Dennoch ist die Parametrisierung von heterogenen Oberflächen für atmosphärische Simulationen unter Verwendung von mesoskaligen Modellen wichtig, da die Rasterung dieser Modelle zu grob ist um viele wichtige Skalen der Oberflächenheterogenität aufzulösen. Um auch diese Skalen zu berücksichtigen, wurde eine Parametrisierung des aerodynamischen Widerstandes für heterogene Oberflächen entwickelt, was den dritten Teil dieser Dissertation darstellt. Die analytische Herleitung der Parametrisierung basiert auf der Verknüpfung der Kovarianzfunktion des eigentlichen, heterogenen, Szenarios mit der Kovarianzfunktion eines zugehörigen, homogenen, Szenarios im Spektralraum. Unter Annahmen über die Form der Turbulenzspektren des homogenen Szenarios, und unter Vernachlässigung von Advektion und dispersiven Flüssen, wurden Korrekturfaktoren für den aerodynamischen Bulkwiderstand bestimmt. Des weiteren zeigte ein Vergleich des Kovarianzfunktionsansatzes mit den konventionellen „bulk" und „tile" Methoden für drei Szenarien von idealisierten Oberflächenheterogenitäten, dass der Kovarianzfunktionsansatz die kleinsten Abweichungen von der LES Referenz besitzt. Dieses Ergebnis demonstriert den Vorteil einer Verwendung der neuen Methode in mesoskaligen Modellen.

Contents

Acknowledements

First of all I want to thank everybody how supported me the last three years, whether during the working hours, during the lunch breaks, or in the spare time. I especially want to thank Matthias Mauder, who was by far the best supervisor in my former career, as he supported me when I needed help, but on the other side gave me enough freedom to follow my own ideas, which worked out perfectly. Besides, he gave me the opportunity to take part in two workshops in Isreal and in four conferences, where three took place in the states. It was always a pleasure traveling with you, not only because of your down-to-earth character, but also because of lots of interesting conversations. I also want to thank the PALM-team Frederik and Sadiq, who heavily supported me during countless hours of bug fixing and struggling with compiler issues. Besides helping with PALM, Frederik was never tired to answer the multiple questions I had, which really helped me a lot, especially in the beginning of the project. Of course, I also want to mention my office colleague Peter, who is really one of the most relaxed guys I met. I want to thank you not only for the scientific discussions, but also for the fun we had during the last years. The working atmosphere was always great, especially when the two of us started to "own" the office. I also want to thank Tirtha Banerjee. Even if you only spend one year in Garmisch, you heavily influenced my work through your endless flow of ideas. Your motivation was really impressive and also pushed me to develop further. Concerning science, I made the most important step through getting to know Gaby. The few month you spend in Garmisch were really the most enlightening for me. Without your input, I would not have been able to develop the aerodynamic resistance parametrization for heterogeneous surfaces. At this point I also want to thank Matthias again, as he gave me the freedom to extensively work together with Gaby, which was really fruitful for all of us. Besides, I also want to thank all the members of our cooking group, Tirtha, Peter, Daniel, Miriam, Tabea, Chritopher, and Simon for the nice meals and the good conversations I got to enjoy throughout the years. Sometimes it was quite hard to stop these conversations and to go back to work. Last but not least I want to thank all my friends, my family, and the best girlfriend on earth, for supporting and motivating me whenever it was needed.

List of manuscripts

This dissertation is presented in cumulative form and consists of three individual manuscripts. All manuscripts have been submitted to the peer-reviewed journals Agricultural and Forest Meteorology, Boundary-Layer Meteorology, and the Journal of the Atmospheric Sciences, were the first two papers are published and the third paper is currently under review.

Manuscripts included in this thesis

Kröniger, K., Banerjee, T., De Roo, F., and Mauder, M. (2018). Flow adjustment inside homogeneous canopies after a leading edge–An analytical approach backed by LES. *Agric. For. Meterorol.*, 255:17–30. Honoring W.J. Massman's Discoversies: Bringing Physics to Agriculture, doi: 10.1016/j.agrformet.2017.09.019

Kröniger, K., De Roo, F., Brugger, P., Huq, S., Banerjee, T., Zinsser, J., Rotenberg, E., Yakir, D., Rohatyn, S., and Mauder, M. (2018). Effect of secondary circulations on surface–atmosphere exchange of energy at an isolated semi-arid forest. *Boundary-Layer Meteorol.*, doi: 10.1007/s10546-018-0370-6

Kröniger, K., Katul, G. G., De Roo, F., Brugger, P., and Mauder, M. (2018). Aerodynamic resistance parametrization for heterogeneous surfaces using structural function approaches. *J. Atmos. Sci.*, (under review)

List of Symbols

A	area of a meso-scale-model grid cell [m^2]
a	plant-area dansity [m^2 m^{-3}]
c_d	drag coefficient
$\chi_{V_1V_2}$	scale-wise distortions of heterogeneity on the planar homogeneous covariance function
d	displacement height [m]
D_{nh}	Length scale of surface heterogeneities for aerodynamic resistance comparisons [m]
$\overline{E}_{V_1V_2}$	covariance function for flow variables V_1 and V_2
e	turbulent kinetic energy [m^2 s^{-2}]
ϵ	dissipation of turbulent kinetic energy [m^2 s^{-3}]
$\overline{F}_{V_1V_2}$	turbulent spectrum of $\overline{V_1'V_2'}$ flux
f_{di}	components of the drag force $\mathbf{f}_d$ [m s^{-2}]
f_i	Coriolis parameter [s^{-1}]
g	gravitational acceleration [m s^{-2}]
h_c	canopy height [m]
$I_{V_1V_2}$	heterogeneity correction factors
K	eddy diffusivity [m^2 s^{-1}]
k_i	components of the wave vector $\mathbf{k}$ [m^{-1}]
κ	von Kármán constant
L	Obukhov length [m]
l	canopy length [m]

l_c	adjustment length scale [m]
Λ	x dependency of $\overline{u}$ and $\overline{w}$ in canopy-edge-flow model
N_θ	thermal variance dissipation rate [K^2 s^{-1}]
ν	kinematic viscosity of air [m^2 s^{-1}]
p_s	pressure scale in canopy-edge-flow model [Pa]
ϕ	stability correction function
p	pressure fluctuations [Pa]
ψ	integrated stability correction functions
Q	source heat flux [K m s^{-1}]
$\mathbf{r}$	position vector in the horizontal plane $\mathbf{r} = (x, y)$ [m]
r	aerodynamic resistance for heat transfer [s m^{-1}]
r_h	aerodynamic resistance for homogeneous conditions [s m^{-1}]
r_cf	aerodynamic resistance from the covariance-function approach [s m^{-1}]
ρ_0	density of air [kg m^{-3}]
S	potential temperature source strength [K s^{-1}]
$\mathcal{T}$	transfer of turbulent kinetic energy between scales [m^4 s^{-3}]
τ	relaxation time scale of the Rotta model [s]
θ	potential temperature [K]
θ_*	scaling temperature [K]
t	time [s]
u_i	components of the velocity vector $\mathbf{u} = (u, v, w)$ [m s^{-1}]
u	velocity component along x ($u = u_1$) [m s^{-1}]
u_*	friction velocity [m s^{-1}]
$\mathbf{u}_g$	Geostrophic wind vector [m s^{-1}]
u_s	velocity scale in canopy-edge-flow model [m s^{-1}]
v	velocity component along y ($v = u_2$) [m s^{-1}]
$\langle V \rangle$	spatial average of flow variable V

V'' spatial fluctuations of flow variable V

$\overline{V}$ temporal mean of flow variable V

V' temporal fluctuation of flow variable V

$\|\mathbf{v}\|$ absolute value of vector $\mathbf{v}$

w velocity component along z ($w = u_3$) [m s^{-1}]

x longitudinal direction ($x = x_1$) [m]

x_I horizontal extension of the adjustment region [m]

x_i components of the position vector $\mathbf{x} = (x, y, z)$ [m]

Δx meso-scale-model grid resolution in x-direction [m]

Δx_{LES} LES grid resolution in x-direction [m]

y lateral direction ($y = x_2$) [m]

Δy meso-scale-model grid resolution in y-direction [m]

Δy_{LES} LES grid resolution in y-direction [m]

z vertical direction ($z = x_3$) [m]

z_0 roughness length [m]

Δz_{LES} LES grid resolution in z-direction [m]

ζ stability parameter

1 | Introduction

While the land's surface features heterogeneities on multiple scales, many investigations of surface–atmosphere interactions in the past were performed for homogeneous surfaces. This is mainly due to a lack of analytic theories for heterogeneous surfaces, while Monin–Obukhov similarity theory (MOST) is heavily used in homogeneous scenarios. However, a profound understanding of the relevant mechanisms of interactions between heterogeneous surfaces and the atmosphere above is crucial, not only for understanding measurements of the atmospheric flow, but also for performing numerical studies of realistic scenarios. Besides, enhanced exchange related to surface heterogeneities is not only able to increase the chance of survival of semi-arid eco-systems (Rotenberg and Yakir, 2010), but can, for example, also affect the micro-climate in urban areas (Wang, 2009). Due to the aforementioned lack of analytic theories, investigations of surface–atmosphere interactions in heterogeneous scenarios mainly rely on atmospheric measurements and numerical simulations. While measurements of atmospheric flow are often performed by using the eddy-covariance technique (Verma, 1990) or remote sensing, large-eddy simulations (LES) have been established as a suitable research approach to model surface–atmosphere exchange for heterogeneous surfaces (e.g., Hechtel et al., 1990; Avissar et al., 1998; Albertson and Parlange, 1999; Bou-Zeid et al., 2004; Prabha et al., 2007; Huang and Margulis, 2009, 2010; Maronga and Raasch, 2013; Miller and Stoll, 2013; Schlegel et al., 2015; Kenny et al., 2017), as these simulations have the advantage of resolving turbulent transport on multiple scales.

To further investigate surface–atmosphere interactions in heterogeneous scenarios, different scales of surface heterogeneity are studied in this thesis by means of analytical approaches and by means of LES. At first, surface–atmosphere interactions of micro-γ scale (Orlanski, 1975) heterogeneities are investigated, namely, the effect of leading canopy edges on the mean flow (Kröniger et al., 2018a, Appendix B). This investigation contains the derivation of an analytical model for canopy edge flow from combining a solution to the governing equations of two-dimensional flow in the adjustment region (Belcher et al., 2003) with the model of Massman (1997) for the canopy interior. To compare the derived model with the analytical model of Belcher et al. (2003), several LES were performed. At second, the surface–atmosphere interactions of a natural meso-γ scale (Orlanski, 1975) heterogeneity were investigated

by performing detailed LES simulations of the semi-arid forest Yatir (Kröniger et al., 2018b, Appendix C). This isolated forest, which represents a distinct heterogeneity in aerodynamic roughness and albedo (Rotenberg and Yakir, 2010, 2011; Eder et al., 2015; Brugger et al., 2018), was found to trigger secondary circulations coupling the forest and the surrounding shrubland. With the help of the detailed LES, initialized by data from two measurement campaigns, occurence, location and strength of these circulations were investigated for varying geostrophic wind speed.
While the aforementioned studies are beneficial for predicting the influence of heterogeneities on surface–atmosphere exchange on the corresponding scales (micro-γ and meso-γ scales), all scales of surface heterogeneity have to be taken into account when performing simulations of atmospheric flow using meso-scale models. As the resolution of those numerical models is usually of the order of several kilometers, many important features of surface heterogeneity cannot be resolved and, therefore, have to be parametrized. However, a large fraction of the existing parametrizations are not able to include all heterogeneity scales. Therefore, the third part of this thesis is the analytical derivation of a novel heterogeneity parametrization, which respects all surface heterogeneity scales by employing covariance functions in spectral space (Kröniger et al., 2018c, Appendix D). In addition, three LES of distinct surface heterogeneities were performed to compare the covariance-function approach against two conventional methods (bulk similarity and tile approach) by computing the aerodynamic resistance to heat transfer from the three different methods.
The thesis is organized as follows: In the subsequent sections of the first chapter, the theoretical background of the performed investigations is introduced. In the second chapter, the derivation of the two analytical models (canopy-edge-flow model and aerodynamic resistance model from covariance-function approaches) is outlined. In the third chapter, the numerical set-up of the performed LES is described, while the main results are summarized in the fourth chapter. The fifth section presents concluding remarks of this thesis.

1.1 Application of flow dynamics to atmospheric conditions

Throughout, quantities and equations are derived in a longitudinal $x_1 = x$, lateral $x_2 = y$, and elevation $x_3 = z$ Cartesian coordinate system (both index and meteorological notations are used). In this coordinate system, velocity components are defined as $u_1 = u$ along x, $u_2 = v$, along y and $u_3 = w$ along z. Surface quantities are indicated by subscript 0 unless otherwise stated.

1.1.1 Governing equations

To model atmospheric flow in micro-meteorological scenarios, the governing equations are expanded with respect to the synoptic background state. This state is described by incompressible, hydrostatic conditions, where synoptic-scale pressure gradients course a geostrophic wind speed due to the Coriolis force. When performing a first order expansion with respect to this background state, the three governing equations read

$$\partial_i u_i = 0, \tag{1.1}$$

which is referred to as the mass conservation equation,

$$\partial_t u_i + u_j \partial_j u_i = -\frac{1}{\rho_0}\partial_i p - \epsilon_{ijk} f_j u_k + \epsilon_{i3j} f_3 u_{g,j} + g\frac{\theta - \theta_0}{\theta_0}\delta_{i3} + \nu\partial^2 u_i, \tag{1.2}$$

which is referred to as the momentum conservation equation, and

$$\partial_t \theta + u_j \partial_j \theta = S, \tag{1.3}$$

which is referred to as the temperature equation. Throughout Eqs. (1.1), (1.2), (1.3), $u_i \in \{u, v, w\}$ denotes the three components of the velocity vector $\mathbf{u}$, ∂_t (∂_i) denotes temporal (spatial) partial derivatives, ρ_0 is the air density, p denotes the pressure fluctuations with respect to the background state, f_i denotes the Coriolis parameter, and $u_{g,i}$ denotes the components of the geostrophic wind vector $\mathbf{u}_g = (u_g, v_g, 0)$. Besides, g denotes the gravitational acceleration, and $\theta = T/\Pi$ denotes the potential temperature, where T is the absolute temperature and $\Pi = (p/p_0)^{R_d/c_p}$ is the Exner function (Pielke and Roger, 2013) relating the absolute temperature at a given pressure level p to a reference level p_0 (usually the surface value), θ_0 is a reference temperature (usually the surface value), R_d is the specific gas constant for dry air, and c_p is the specific heat for dry air. While the terms on the left hand side of Eq. (1.2) describe changes of the velocity field in time ($\partial_t u_i$) and advection ($u_j \partial_j u_i$), the terms on the right hand side describe the force due to pressure fluctuations ($-\partial_i p/\rho_0$), the Coriolis force ($-\epsilon_{ijk} f_j u_{g,j}$), the synoptic-scale pressure gradients ($\epsilon_{i3j} f_3 u_{g,j}$), buoyancy ($g\delta_{i3}\left(\theta - \theta_0\right)/\left(g\theta_0\right)$), and molecular dissipation ($\nu\partial^2 u_i$), where ν is the kinematic viscosity of air. Concerning Eq. (1.3), sources/sinks of potential temperature enter the equation through the source strength S. Besides, equations for passive scalars are used in addition to Eqs. (1.1), (1.2), (1.3), however these equations are constructed in analogy to Eq. (1.3) and are not relevant for this thesis.

After expanding the governing equations with respect to the synoptic background state, an additional separation of scales is usually performed. As several studies showed, the mean motion of fluids features an intrinsically different behavior than the random fluctuations, which are superimposed to this mean state. The random fluctuations, which are usually referred to as turbulent motions, are of significant importance for exchange processes between the surface and the atmo-

sphere. To separate the mean state from the turbulent motions, the flow variables are Reynolds-decomposed, e.g. $u_i = \overline{u}_i + u_i'$, where $\overline{u}_i$ denotes the mean state and u_i' fluctuations with respect to this mean state. Averaging Eqs. (1.1), (1.2), (1.3) and decomposing the flow variables into mean and turbulent fluctuations results in the governing equations for the mean flow variables

$$\partial_i \overline{u}_i = 0, \tag{1.4}$$

$$\partial_t \overline{u}_i + \overline{u}_j \partial_j \overline{u}_i = -\frac{1}{\rho_0}\partial_i \overline{p} - \epsilon_{ijk} f_j \overline{u}_k + \epsilon_{i3j} f_3 u_{g,j} + g\frac{\bar{\theta} - \theta_0}{\theta_0}\delta_{i3} + \nu \partial^2 \overline{u}_i - \partial_j \overline{u_i' u_j'}, \tag{1.5}$$

$$\partial_t \bar{\theta} + \overline{u}_j \partial_j \bar{\theta} = -\partial_j \overline{u_j' \theta'} + \bar{S}, \tag{1.6}$$

where the double moments $\overline{u_i' u_j'}$ and $\overline{u_i' \theta'}$ are covariances of the flow variables. These terms are usually referred to as turbulent fluxes or stresses, where $\overline{u_i' u_j'}$ denotes turbulent momentum fluxes and $\overline{u_i' \theta'}$ turbulent heat fluxes, and represent the effect of turbulent motions on the mean state.
Besides the equations for the mean variables, equations for the mean turbulent fluxes and the mean turbulent kinetic energy (TKE), defined by $\overline{e} = \frac{1}{2}\left(\overline{u'u'} + \overline{v'v'} + \overline{w'w'}\right)$, can also be derived from Eqs. (1.1), (1.2), (1.3). The TKE equation reads

$$\underbrace{\partial_t \overline{e}}_{I} = \underbrace{-\overline{u}_j \partial_j \overline{e}}_{II} \underbrace{- \partial_j \overline{u_j' e}}_{III} \underbrace{- \overline{u_i' u_j'} \partial_j \overline{u}_i}_{IV} + \underbrace{\frac{g}{\theta_0}\overline{w'\theta'}}_{V} \underbrace{- \frac{1}{\rho_0}\partial_j \overline{u_j' p'}}_{VI} \underbrace{- \epsilon}_{VII}, \tag{1.7}$$

where the TKE tendency (term I) is composed of advection with the mean flow (term II), turbulent transport of TKE (term III), mechanical production of TKE (term IV), buoyant production of TKE (term V), pressure de-correlation (term VI), and dissipation of TKE (term VII), where $\epsilon = -\nu\, \overline{u_i' \partial^2 u_i'}$.
When considering atmospheric measurements, e.g. using the eddy covariance method, the turbulent fluxes can be directly determined from calculating covariances of the flow variables. However, for analytical investigations or numerical approaches, the application of Reynolds decomposition leads to a series expansion of Eqs. (1.1), (1.2), (1.3) in orders of the turbulent fluctuations. While Eqs. (1.4), (1.5), (1.6) only depend on second moments, the calculation of these moments includes triple moments (Eq, 1.7) and so forth, which is usually referred to as "closure problem". To be able to make use of Eqs. (1.4), (1.5), (1.6), (1.7) in analytical and numerical investigations, the series expansion is truncated at a certain order and the unknown terms are expressed by the residual ones. In the majority of applications, the series expansion is truncated at the turbulent flux level and gradient approximations are used to express those fluxes as functions of the mean quantities. The main rational behind these approximations is that the turbulent flux of a certain flow variable $s \in \{u_i, \theta, e\}$ is proportional to the gradient of the corresponding mean quantity, however, oriented in opposite direction. The corresponding propor-

tionality constant is referred to as eddy diffusivity K_s. Therefore, the turbulent flux $\overline{u_i' s'}$ is approximated by

$$\overline{u_i' s'} \approx -K_s \partial_i \overline{s}, \tag{1.8}$$

where $[K_s] = \mathrm{m} \times \left(\mathrm{m\ s^{-1}}\right)$. Therefore, K_s can be expressed by the product of an eddy-specific length scale (mixing length) and an eddy-specific velocity.

1.1.2 Covariance functions and turbulence spectra

Covariance functions are often used to investigate turbulent motions, as these functions act as a generalization of the turbulent fluxes. The covariance function $\overline{E}_{V_1 V_2}$ of two flow variables V_1 and V_2 is defined by

$$\overline{E}_{V_1 V_2}\left(\left(\mathbf{r}, z\right), \hat{\mathbf{r}}\right) = \overline{V_1'\left(\mathbf{r}, z\right) V_2'\left(\mathbf{r} + \hat{\mathbf{r}}, z\right)}, \tag{1.9}$$

where $\mathbf{r}$ and $\hat{\mathbf{r}}$ are position vectors in the horizontal plane at altitude z. The covariance functions describe the structure of turbulence in the vicinity of the point $(\mathbf{r}, z)$, where the different scales of turbulence are represented by the distance vector $\hat{\mathbf{r}}$. Usually these scales of turbulent motion are investigated in spectral space by Fourier transforming Eq. (1.9) with respect to $\hat{\mathbf{r}}$. The resulting functions $\overline{F}_{V_1 V_2}\left(\mathbf{r}, \mathbf{k}\right) = \mathcal{F}_{\hat{\mathbf{r}} \rightarrow \mathbf{k}}\left[\overline{E}_{V_1 V_2}\right]$ are referred to as turbulence spectra. Fourier transforming the identity $\overline{E}_{V_1 V_2}\left(\left(\mathbf{r}, z\right), \hat{\mathbf{r}} = 0\right) = \overline{V_1' V_2'}\left(\mathbf{r}, z\right)$ yields

$$\overline{V_1' V_2'}\left(\mathbf{r}, z\right) = \int\limits_{\mathbb{R}^2} \frac{d^2\mathbf{k}}{\left(2\pi\right)^2}\, \overline{F}_{V_1 V_2}\left(\left(\mathbf{r}, z\right), \mathbf{k}\right) \cong \int\limits_0^\infty \frac{dk}{2\pi}\, k \overline{F}_{V_1 V_2}\left(\left(\mathbf{r}, z\right), k\right), \tag{1.10}$$

where k is the absolute value of $\mathbf{k}$ ($k = \|\mathbf{k}\|$) and the second expression holds true for isotropic spectra ($\overline{F}\left(\left(\mathbf{r}, z\right), \mathbf{k}\right) = \overline{F}\left(\left(\mathbf{r}, z\right), k\right)$). Equation (1.10) illustrates that the turbulent flux at a certain position $(\mathbf{r}, z)$ is composed of contributions from all scales of turbulent exchange, represented by the value of the spectrum for the corresponding wave vector. To derive an budget equation for the TKE spectrum $\overline{F}_e = \left(\overline{F}_{uu} + \overline{F}_{vv} + \overline{F}_{ww}\right)/2$, Eq. (1.10) is used to replace the turbulent fluxes in Eq. (1.7), which results in

$$\underbrace{\partial_t \overline{F}_e}_{I} = -\underbrace{\overline{u}_j \partial_j \overline{F}_e}_{II} + \underbrace{\mathcal{T}}_{III} - \underbrace{\overline{F}_{u_i u_j} \partial_j \overline{u}_i}_{IV} + \underbrace{\frac{g}{\theta_0} \overline{F}_{w\theta}}_{V} - \underbrace{\frac{2ik_j}{\rho_0} \overline{F}_{u_j p}}_{VI} - \underbrace{2\nu k^2 \overline{F}_e}_{VII}, \tag{1.11}$$

where I–VII correspond to the terms in Eq. (1.7) and $\mathcal{T} = -\partial_j \overline{u_j' F_e}$. Equation (1.11) shows that production and dissipation of turbulence occurs at different scales. While the pressure decorrelation (term VI) and the molecular dissipation (term VII) can be neglected against the production terms (terms IV and V) for $k \rightarrow 0$ (large scales), the reverse is true for $k \rightarrow \infty$ (small scales), as VI and VII are proportional to k_j and k^2. While the aforementioned terms describe production and

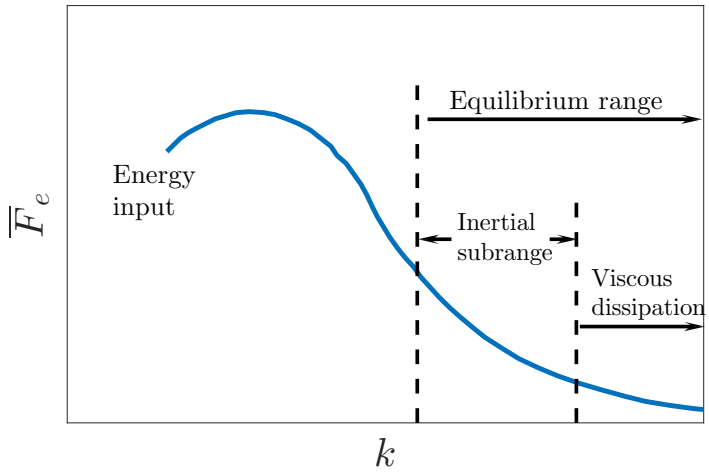

Figure 1.1: Cascade of turbulence after Garratt (1994), illustrating the different regimes of input, transfer, and dissipation of TKE ($\overline{F}_e$) as a function of the wavevector k.

dissipation of turbulence at a certain scale, term III describes energy transfer between scales, as several wave-vectors enter the budget equation of $\mathcal{T}$ (Spiegel, 2010). The combined picture of energy input from the mean flow at large scales followed by the transfer of energy to smaller scales till energy is transformed to heat by viscous dissipation, is usually referred to as "cascade of turbulence", which is depicted in Fig. 1.1. The spectral range in between, where neither production nor viscous dissipation to heat are relevant, is referred to as "inertial subrange". In this spectral range, the prevailing mechanism is the energy transfer across scales, which is entirely determined by ϵ. For the two cases of large scales, where dissipation can be neglected, and inertial scales, where energy input can be neglected, theories where developed based on dimensional analysis. These theories are presented in the next two subsections.

1.1.3 Kolmogorov theory

When considering the limit $k \to \infty$ the terms IV, V, and VI can be neglected from Eq. (1.11). When additionally changing to the Lagrangian reference frame and assuming stationary conditions Eq. (1.11) reduces to

$$\mathcal{T} = 2\nu k^2 \overline{F}_e = \hat{\epsilon}\left(\left(\mathbf{r}, z\right), \mathbf{k}\right), \tag{1.12}$$

where $\hat{\epsilon}$ denotes the contribution to ϵ from scale $\mathbf{k}$ ($\epsilon\left(\mathbf{r}, z\right) = \int_{\mathbb{R}^2} \frac{d^2\mathbf{k}}{(2\pi)^2}\ \hat{\epsilon}\left(\left(\mathbf{r}, z\right), \mathbf{k}\right)$). Equation (1.12) shows that the transfer of energy in the considered limit of small scales is entirely described by the dissipation, as the amount of energy, which leaves the considered scale ($\hat{\epsilon}$) is equal to the incoming energy ($\mathcal{T}$). When considering the cascade of energy (Fig. 1.1), this behavior describes the inertial subrange. To derive an expression for $\overline{F}_e$ is the inertial subrange, Kolmogorov (1941) assumed $\overline{F}_e$

to be homogeneous and isotropic ($\overline{F}_e\left(\left(\mathbf{r}, z\right), \mathbf{k}\right) = \overline{F}_e\left(k\right)$), which requires a sufficient distance to confining surfaces. However, a scale can be found for every confining surface, where the condition is met (Townsend, 1976). Therefore, TKE exchange in the inertial subrange is fully described by $\{\overline{F}_e, \epsilon, k\}$. From dimensional considerations using the Buckingham-π theorem (Buckingham, 1915), Kolmogorov (1941) concluded that

$$k\overline{F}_e = C_e \epsilon^{2/3} k^{-5/3}, \tag{1.13}$$

where C_e is a proportionality constant. Note that the left hand side of Eq. (1.13) reflects Eq. (1.10), concerning the integral measure k. Besides the TKE spectrum, the same arguments apply to $\overline{F}_{u_i u_j}$, however, a different proportionality constant has to be used. To derive a inertial subrange scaling for $\overline{F}_{\theta\theta}$, Corrsin (1951) extended the set of relevant quantities by a "thermal variance dissipation rate" N_θ with units $[N_\theta] = \mathrm{K}^2\ \mathrm{s}^{-1}$, resulting in

$$k\overline{F}_{\theta\theta} = C_{\theta\theta} N_\theta \epsilon^{-1/3} k^{-5/3}, \tag{1.14}$$

which again obeys the $k^{-5/3}$-law. This power-law behavior of the structure functions in the inertial subrange is supported by a large corpus of measurements of pipe, boundary layer and atmospheric flows (Pope, 2000; Saddoughi and Veeravalli, 1994; Cava and Katul, 2012), which were also used to determine the proportionality constants.

Besides determining expressions for the spectra in the inertial subrange, Kolmogorov (1941) additionally extracted the spatial and temporal scales at which TKE is dissipated to heat. At these scales, the incoming energy is described by ϵ, as this amount of TKE is emitted from the inertial subrange. On the other hand, the outgoing energy at those scales is dissipated to heat and is, therefore, described by ν. From these two parameters Kolmogorov (1941) constructed a length scale r_{Ko} and a time scale t_{Ko} from dimensional arguments:

$$\begin{aligned} r_{\mathrm{Ko}} &= \nu^{3/4} \epsilon^{-1/4}, \\ t_{\mathrm{Ko}} &= \nu^{1/2} \epsilon^{-1/2}. \end{aligned} \tag{1.15}$$

These scales are usually referred to as Kolmogorov microscales and can be of the orders of 0.1 mm and 10 ms for atmospheric flows.

1.1.4 Similarity theory

While Kolmogorov (1941) derived expressions for the turbulence spectra at small scales, Monin and Obukhov (1954) investigated Eq. (1.11) for the limit of large scales to derive equations for the mean flow, usually referred to as Monin–Obukhov similarity theory (MOST). In this limit of large scales ($k \to 0$), the pressure term (term VI) and the dissipation (term VII) can be neglected. Besides, Monin and Obukhov (1954) considered stationary turbulence and horizontally-homogeneous conditions,

which are defined by neglecting derivatives with respect to horizontal directions (x, y). Additionally aligning the reference system with the mean wind direction $\overline{u}$ and, therefore, eliminating the cross wind component ($\overline{v} = 0$) yields

$$\mathcal{T} = \overline{F}_{uw} \frac{d\overline{u}}{dz} - \frac{g}{\theta_0} \overline{F}_{w\theta}. \tag{1.16}$$

Equation (1.16) illustrates that the energy transfer for large scales is entirely determined by the mechanical and buoyant production of TKE. Therefore, the flow dynamics at large scales are described by $\{z, k, \overline{F}_{uw}, \overline{F}_{w\theta}, d_z\overline{u}, g/\theta_0\}$. This set can be simplified to $\{z, u_*, \overline{w'\theta'}, d_z\overline{u}, g/\theta_0\}$, when using dimensional arguments to replace $k^2\overline{F}$ by the corresponding turbulent flux and introducing the friction velocity $u_* = (\overline{u'w'}^2 + \overline{v'w'}^2)^{1/4}$. From this set of relevant quantities Monin and Obukhov (1954) derived the following expression for the gradient of the mean wind speed, applying the Buckingham-π theorem:

$$\frac{d\overline{u}}{dz} = \frac{u_*}{\kappa z} \phi_m \left(\frac{z}{L} \right), \tag{1.17}$$

where ϕ_m is the similarity function for momentum, L is the Obukhov length, defined by

$$L = -\frac{u_*^3}{\kappa g \, \overline{w'\theta'}/\theta_0}, \tag{1.18}$$

and $\kappa \approx 0.4$ is the von Kármán constant (Foken, 2006). The term $z/L \equiv \zeta$ is a measure of atmospheric stability, as $\zeta < 0$ describes unstable stratification, $\zeta = 0$ neutral, and $\zeta > 0$ stable conditions. For neutral stratification, $\phi_m \equiv 1$, to reproduce a logarithmic wind profile from Eq. (1.17).

Besides the mean wind gradient, a similar expression can be derived for the mean potential temperature gradient $d_z\bar{\theta}$, using the parameter set $\{z, u_*, d_z\overline{\theta}, \overline{w'\theta'}, g/\theta_0\}$, which results in

$$\frac{d\bar{\theta}}{dz} = \frac{\theta_*}{\kappa z} \phi_h \left(\frac{z}{L} \right), \tag{1.19}$$

where ϕ_h is the stability correction function for heat transfer and $\theta_* \equiv -\overline{w'\theta'}/u_*$ is a characteristic temperature scale. When determining the vertical profiles of $\overline{u}$ and $\overline{\theta}$, Eqs. (1.17) and (1.19) are integrated with respect to z, which requires an upper and a lower integration bound. However, as MOST is developed for the limit of large eddy scales, the theory becomes inaccurate at small elevations. This affects the choice of the lower integration bound, as the surface values of $\overline{u}$ ($\overline{u}_0 = 0$) and $\overline{\theta}$ ($\overline{\theta}_0$) are already attained at non-zero altitudes. These altitudes are usually referred to as roughness length for momentum (z_{0m}) and heat transfer (z_{0h}) respectively. Besides, $z - d$ is used as upper integration bound when integrating Eqs. (1.17) and (1.19), where z is the altitude, $\overline{u}$ and $\bar{\theta}$ are calculated at, and $d \approx (2/3)\, h_c$ (Thom, 1971) is the zero-plane displacement height, which is of relevance when describing flow above a canopy of height h_c. Integrating Eqs. (1.17) and (1.19) using the aforementioned integration

bounds yields

$$\overline{u}(z) = \frac{u_*}{\kappa} \int_{z_{0m}}^{z-d} d\tilde{z}\, \frac{\phi_m(\tilde{z}/L)}{\tilde{z}} = \frac{u_*}{\kappa} \left[\log\left((z-d)/z_{0m}\right) - \psi_m(\zeta_d, \zeta_{0m})\right], \tag{1.20}$$

and

$$\bar{\theta}(z) - \bar{\theta}_0 = \frac{\theta_*}{\kappa} \int_{z_{0h}}^{z-d} d\tilde{z}\, \frac{\phi_h(\tilde{z}/L)}{\tilde{z}} = \frac{\theta_*}{\kappa} \left[\log\left((z-d)/z_{0h}\right) - \psi_h(\zeta_d, \zeta_{0h})\right], \tag{1.21}$$

where $\zeta_d = (z-d)/L$, $\zeta_{0m(h)} = z_{0m(h)}/L$, and $\psi_{m(h)}$ are the integrated stability correction functions.
Besides calculating the mean wind and temperature profiles, Eqs. (1.20) and (1.21) can be used to derive an analytic expression of the aerodynamic resistance to heat transfer (r) for horizontally-homogeneous conditions. In analogy to the resistance of an electric circuit, r is defined as

$$r(z) = -\int_{z_{0h}}^{z-d} d\tilde{z}\, \frac{d_{\tilde{z}}\bar{\theta}}{\overline{w'\theta'}}, \tag{1.22}$$

where the temperature gradient corresponds to the difference in electric potential and the sensible heat flux to the current. The aerodynamic resistance is not only important for determining surface–atmosphere exchange of energy in meso-scale models, but is also used for calculating evaporation from eco-systems, e.g. by using the Penman–Monteith equation (Penman, 1948; Monteith, 1965). Equation (1.22) is further simplified when assuming $\overline{w'\theta'} = \overline{w'\theta'}_0 = \text{const.}$ within the surface layer (constant flux approximation), yielding

$$r(z) = \frac{\bar{\theta}_0 - \bar{\theta}(z)}{\overline{w'\theta'}_0}. \tag{1.23}$$

To determine an aerodynamic resistance parametrization for horizontally-homogeneous conditions (r_h, "h" $\equiv$ homogeneous), the MOST result for $d_z\bar{\theta}$ (Eq. 1.19) is applied to Eq. (1.22) and u_* is subsequently replaced by using Eq. (1.20), which yields

$$\begin{aligned} r_\mathrm{h} &= \frac{1}{\kappa^2 \overline{u}} \int_{z_{0m}}^{z-d} d\tilde{z}\, \frac{\phi_m}{\tilde{z}} \int_{z_{0h}}^{z-d} d\tilde{z}\, \frac{\phi_h}{\tilde{z}} \\ &= \frac{1}{\kappa^2 \overline{u}} \left[\log\left((z-d)/z_{0m}\right) - \psi_m(\zeta_d, \zeta_{0m})\right] \left[\log\left((z-d)/z_{0h}\right) - \psi_h(\zeta_d, \zeta_{0h})\right]. \end{aligned} \tag{1.24}$$

While the indirect proportionality between r_h and $\overline{u}$ is directly inferred from Eq. (1.24) the dependency on atmospheric stability is more complex. However, when using the ψ_m and ψ_h expressions of Liu et al. (2007), a decrease of r_h with increasing

atmospheric instability can be derived. This behavior of r_{h} was also supported by LES investigations of Banerjee et al. (2017).

1.2 Numerical approaches for modeling atmospheric flow

Even though Monin–Obukhov similarity and the Kolmogorov theory are frequently applied in micro-meterological investigations, the assumptions made to develop these theories (homogneity for MOST, inertial subrange scales for Kolmogorov, stationarity for both) are too limited for investigations of more realistic scenarios, like flow above heterogeneous forest or city canopies.
However, besides performing atmospheric measurements, numerical simulations greatly enhance understanding of atmospheric flow in various conditions. The main challenge for simulating atmospheric flow is the cascade of turbulence (Fig. 1.1), which connects all scales from the boundary layer thickness ($\approx \mathcal{O}\,(1\ \mathrm{km})$) to the Kolmogorov microscales ($\approx \mathcal{O}\,(0.1\ \mathrm{mm})$, Eq. (1.15)). This large number of relevant scales makes a direct application of Eqs. (1.1), (1.2), (1.3) quite expensive. Therefore, direct numerical simulations (DNS) are only computationally affordable for small domains or weakly turbulent flow. However, as these conditions are often not met when modeling atmospheric flow, other approaches like "Reynolds-averaged Navier–Stokes" (RANS) simulations are used. Within the RANS framework, Eqs. (1.4), (1.5), (1.6) are used to model the mean flow, where the entire effect of turbulence is parametrized. Therefore, RANS simulations are computationally cheap, however, parametrizing the entire turbulent exchange can lead to artefacts in the mean flow and only gives inaccurate predictions of turbulent fluxes.
Besides DNS and RANS, LES is frequently used to model atmospheric flow. These simulations are designed to combine the advantage of DNS and RANS by resolving many scales of atmospheric flow, while still keeping computational costs relativity low. The main idea of LES is the separation of the full range of scales into resolved (energy-containing) and parametrized (inertial sub-range and dissipative) scales by using a spatial filtering approach (Fig. 1.2). This spatial filtering is performed by explicitly resolving all scales larger than the grid-dimension Δ and parametrizing all subgrid scales. Therefore, the computational costs of LES largely depends on the chosen grid dimension. In the LES framework, Δ is chosen such that the parametrized scales mainly fall within the inertial subrange (Fig. 1.1), where the homogeneity and isotropy arguments of Kolmogorov (1941) apply (Section 1.1.3). Therefore, the same subgrid scale parametrization can be used for every grid-cell. Besides, Eqs. (1.4), (1.5), (1.6) are employed to describe the mean flow, where the applied averaging refers to spatial averaging for the grid cells in the case of LES. To distinguish between spatial and temporal averaging in the following, $\overline{u}$ and u' refers to temporal averages and fluctuations, while $\langle u \rangle$ and u'' refers to spatial averaging and spatial fluctuations respectively.

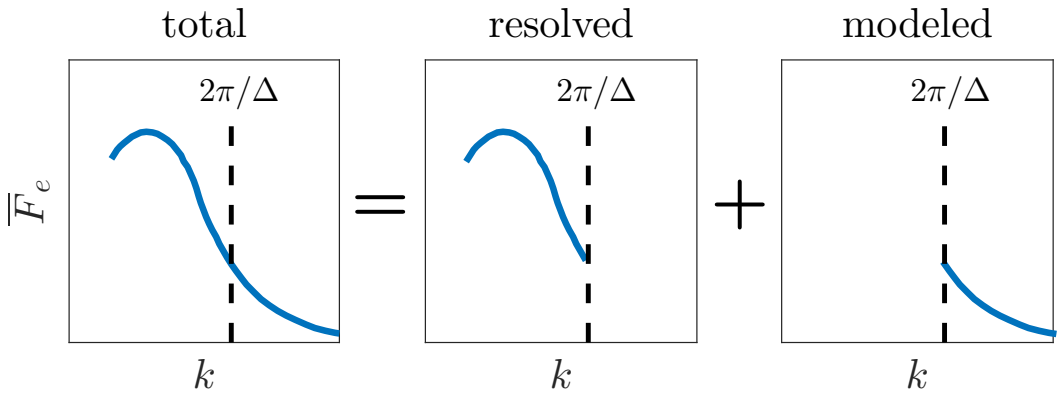

Figure 1.2: Filtering approach of LES: The total range of scales is seperated into resolved scales and modeled scales, where the grid spacing Δ is used as cutoff scale.

When performing atmospheric measurements, the turbulence statistics are usually calculated with respect to temporal averaging for a certain averaging period (often 30 min), which results in point measurements of the turbulent fluxes. To compare those fluxes to LES data, the contributions from the resolved and from the subgrid scales have to be added, as

$$\langle \overline{u_i u_j} \rangle - \langle \overline{u}_i \rangle \langle \overline{u}_j \rangle = \overline{\langle u_i \rangle' \langle u_j \rangle'} + \overline{\langle u_i'' u_j'' \rangle}, \tag{1.25}$$

where the left hand side is the LES counterpart of the measured fluxes, while the first/second term on the right hand side is the flux contribution of the resolved/subgrid scales.

While the spatial filtering approach is commonly used by all LES codes, the employed subgrid-scale parametrizations differ. Within the LES code PALM (Raasch and Schröter, 2001; Maronga et al., 2015), which was used throughout this thesis, the subgrid scale fluxes are modeled by employing Eq. (1.8) for momentum and heat fluxes. To parametrize the emerging eddy diffusivities, a characteristic length scale and velocity scale are needed, which describe the subgrid scale turbulence (see Section 1.1.1). While the length scale is determined from the vertical elevation of a certain grid cell and the grid spacing Δ, PALM uses $\sqrt{\langle e \rangle}$ as the velocity scale characterizing the subgrid-scale turbulence. To calculate the TKE, Eq. (1.7) is used, where the triple moments are also deduced from Eq. (1.8). The advantage of this turbulence closure scheme is that a bilateral coupling of the subgrid scales to the mean flow is achieved. While subgrid scale parametrizations relying on the gradient approach are usually referred to as first order closure schemes, the additional modeling of the TKE is referred to as 1.5^{th} order closure. As the aforementioned subgrid-scale parametrization depends on gradients of the mean flow (Eq. 1.8), no turbulent motions can emerge from fields that are homogeneous in all three spatial directions, however, homogeneous fields are often used to initialize LES. To solve this problem, PALM uses a random-number generator to apply fluctuations to the

mean flow until the simulation has reached a distinct turbulent state.

1.3 Canopy–atmosphere interactions

The land's surface is often covered by different kinds of canopies (e.g. forest or urban canopies). These canopies not only influence the atmospheric turbulence, but also act as sources or sinks for passive scalars and the potential temperature. To model the effect of a canopy on the atmospheric flow, new terms have to be added to the governing equations, which is presented in Section 1.3.1. In Section 1.3.2, the special case of a homogeneous canopy and the corresponding analytical theories are discussed.

1.3.1 Modified governing equations

When modeling the effect of a canopy on the atmospheric flow, new terms are added to Eqs. (1.2) and (1.3). Concerning the momentum conservation equation (Eq. 1.2), the drag of the canopy on the atmospheric flow is usually modeled by adding a drag force $\mathbf{f}_d$. Following Shaw and Schumann (1992) and Watanabe (2004), $\mathbf{f}_d$ is assumed to be antiparallel to the mean flow and proportional to the square of the mean wind speed, as the loss of momentum within a canopy is proportional to the incoming momentum. Besides, denser canopies feature a larger drag. Therefore, $\mathbf{f}_d$ is assumed to be proportional to the plant-area density (a), which is defined as the fraction of plant-area index (PAI) within a certain vertical slice, such that

$$\text{PAI} = \int_0^{h_c} dz\; a(z), \tag{1.26}$$

where the plant-area index is defined as the area of plant surfaces above a certain ground-surface area. Summarizing the aforementioned conditions, the components of the drag force (f_{di}) are defined by

$$f_{di} = -c_d a \|\overline{\mathbf{u}}\| u_i, \tag{1.27}$$

where the proportionality constant c_d is referred to as drag coefficient. When adding f_{di} to Eq. (1.2) and applying Reynolds averaging to defer the governing equations for the mean wind speed and TKE (Section 1.1.1), Eqs. (1.5) and (1.7) become

$$\partial_t \overline{u}_i + \overline{u}_j \partial_j \overline{u}_i = -\frac{1}{\rho_0}\partial_i \overline{p} - \epsilon_{ijk} f_j \overline{u}_k + \epsilon_{i3j} f_3 u_{g,j} + g\frac{\bar{\theta} - \theta_0}{\theta_0} + \nu \partial^2 \overline{u}_i - \partial_j \overline{u_i' u_j'} - \underline{c_d a \|\overline{\mathbf{u}}\| \overline{u}_i}, \tag{1.28}$$

and

$$\partial_t \overline{e} = -\overline{u}_j \partial_j \overline{e} - \partial_j \overline{u_j' e} - \overline{u_i' u_j'} \partial_j \overline{u}_i + \frac{g}{\theta_0}\overline{w'\theta'} - \frac{1}{\rho_0}\partial_j \overline{u_j' p'} - \epsilon - \underline{2 c_d a \|\overline{\mathbf{u}}\| \overline{e}}, \tag{1.29}$$

where the two additional terms, corresponding to the drag of the canopy, are underlined. While the additional term in Eq. (1.28) describes the attenuation of the mean wind speed by the drag of the canopy, the additional term in Eq. (1.29) describes the more rapid dissipation of TKE within the canopy due to the breaking up of eddies by roughness elements (Shaw and Patton, 2003).
Concerning the temperature equation (Eq. 1.3), the effect of the canopy is modeled by using a source term S, representing the warming of the air, which is in thermal contact with a canopy exposed to solar radiation. Following Brown and Covey (1966), the mean source term $\overline{S}$ of Eq. (1.6) is expressed through $\overline{S} = \partial_z \overline{Q}$, where $\overline{Q}$ is the source heat flux, modeled by

$$\overline{Q}(z) = \overline{Q}\,(h_c) \exp\left[-\alpha \int_z^{h_c} dz\; a(z)\right], \tag{1.30}$$

$\overline{Q}\,(h_c)$ is the source heat flux at canopy top, α is an extinction coefficient, and $\int_z^{h_c} dz\; a(z)$ describes the downward cumulative plant-area density. The exponential decrease of $\overline{Q}$ from the top to the bottom of the canopy, which is modeled by Eq. (1.30) represents the shadowing effect of the canopy concerning the incoming radiation. However, this functional dependency is only strictly valid for the attenuation of direct solar radiation by a horizontally-homogeneous canopy. When considering a canopy, which is heterogeneous in all three spatial directions, several additional contributions for the scattering of the incoming radiation on canopy elements have to be considered (Bailey et al., 2014; Matsuda et al., 2017).
When using Eqs. (1.28), (1.29), and (1.30) to model canopy–atmosphere interactions, two new length scales are introduced. The first length scale is the canopy height h_c, which describes the vertical extension of the direct canopy-atmosphere interaction. Besides, a second length scale enters by introducing the drag force (Eq. 1.27). This scale is usually referred to as adjustment length scale l_c (Belcher et al., 2003) and is defined by

$$l_c = (c_d a)^{-1}\,. \tag{1.31}$$

The adjustment length scale is a measure for the distance, unperturbed flow needs to adjust to a canopy, and becomes relevant for investigations of canopy edge flow (Section 1.4.1). As $l_c \sim a^{-1}$, a denser canopy features a smaller adjustment length.

1.3.2 Horizontally-homogeneous canopies

When considering a homogeneous canopy in terms of a horizontally-homogeneous $a\,(z)$ profile, assuming stationary flow, neutral stratification, neglecting the Coriolis terms, and neglecting molecular dissipation against turbulent dissipation, the governing equation for the mean wind (Eq. 1.28) reduces to

$$d_z \overline{u'w'}_{\mathrm{h}} = \overline{u}_{\mathrm{h}}^2 / l_c, \tag{1.32}$$

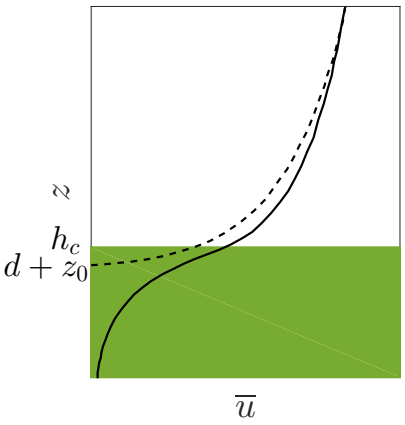

Figure 1.3: Mean wind profile (bold black line) within and above a homogeneous canopy (green square) of height h_c after Harman and Finnigan (2007). The MOST profile, depending on the roughness length z_0 and the displacement height d, is depicted as black dashed line.

where the coordinate system was rotated in mean wind direction, and the label "h" denotes homogeneous conditions. Further using a gradient approximation (Eq. 1.8) to express $\overline{u'w'}_\mathrm{h}$, and assuming the eddy diffusivity to be spatially constant within the canopy, Eq. (1.32) can be solved analytically (Albini, 1981; Massman, 1987, 1997), which results in

$$\begin{aligned} \overline{u}_\mathrm{h}(z) &= \overline{u}_\mathrm{h}(h_c) \exp\left[-n\left(1 - \frac{\int_0^z d\tilde{z}\, l_c^{-1}}{\int_0^{h_c} d\tilde{z}\, l_c^{-1}}\right)\right], \\ -\overline{u'w'}_\mathrm{h}(z) &= \overline{u}_\mathrm{h}^2(h_c) \left(\int_0^{h_c} d\tilde{z}\, l_c^{-1}\right) \exp\left[-2n\left(1 - \frac{\int_0^z d\tilde{z}\, l_c^{-1}}{\int_0^{h_c} d\tilde{z}\, l_c^{-1}}\right)\right] \end{aligned} \tag{1.33}$$

where n is dependent on l_c, $\overline{u}_\mathrm{h}(h_c)$, and $\overline{u'w'}_\mathrm{h}(h_c)$. Massman (1997) used this exponential $\overline{u}$ profile to calculate z_{0m} and d for a homogeneous canopy from the canopy parameters h_c and l_c in the case of neutral stratification. To generalize these results to arbitrary atmospheric stability, Harman and Finnigan (2007) derived the roughness lengths and the displacement height from combining the exponential $\overline{u}$ profile inside the canopy with MOST above the canopy by imposing continuity and differentiability on the $\overline{u}$ profile (Fig. 1.3).

1.4 Effect of surface heterogeneities on the atmospheric flow

While employing MOST to parametrize surface–atmosphere interactions can be a useful first-order approach, surface heterogeneities affect surface–atmosphere exchange on many scales. In the following section, two examples of heterogeneity-induced features of atmospheric flow are introduced, namely canopy-edge flow and secondary circulations.

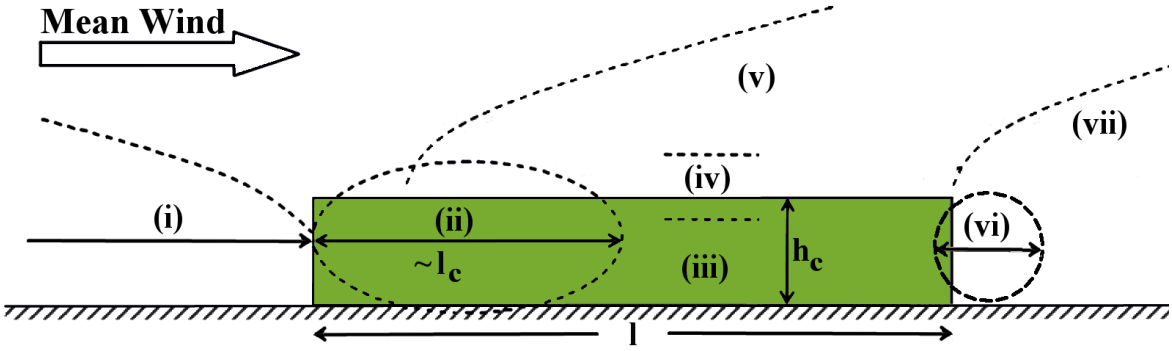

Figure 1.4: Schematic sketch of the important regions concerning edge-flow after Belcher et al. (2003): (i) impact region, (ii) adjustment region, (iii) canopy interior, (iv) canopy shear layer, (v) roughness change region, (vi) exit region, (vii) far wake. The quantities h_c, l and l_c denote canopy height, canopy length and adjustment length.

1.4.1 Canopy edge flow

When considering canopy–atmosphere interactions, edges and clearings in those canopies represent the sharpest transition in surface roughness (Belcher et al., 2012), and can, therefore, influence atmospheric measurements over large distances downstream of these heterogeneities (Dupont and Brunet, 2008; Kanani-Sühring and Raasch, 2014). Following Belcher et al. (2003), flow across leading and trailing canopy edges is described by seven different regions. These regions are illustrated in Fig. 1.4, where (i) labels the impact region before the leading edge, (ii) the adjustment region shortly past the leading edge, (iii) the canopy interior behind the adjustment region, (iv) the canopy shear layer located around the canopy top, (v) the roughness change region above the canopy, (vi) the exit region behind the trailing edge, and (vii) the far wake behind the canopy.

Concerning flow across leading canopy edges, Dupont et al. (2011) stated that one key issue for interpreting flux measurement near to those heterogeneities is the extension of the adjustment region. Even though this quantity is proportional to l_c, the actual extension of the adjustment region is, however, strongly dependent on the turbulent flow inside the canopy (Dupont et al., 2011). While the length of the adjustment region is not only important for performing atmospheric measurements or predictions of seed and pollen dispersal (Trakhtenbrot et al., 2014), scalar dynamics like greenhouse-gas fluxes inside the canopy also largely depend on this quantity (Launiainen et al., 2013; Kanani-Sühring and Raasch, 2014). Concerning trailing canopy edges, the impact on the atmospheric flow is mainly determined by re-circulations, which can be triggered in the exit region. These circulations are driven by vertical gradients in horizontal wind speed between the lee of the canopy and the flow above. Even though these re-circulation regions also occur in the canopy interior (Ross and Baker, 2013), they are much weaker in this region, due to the drag of the canopy (Dalpé and Masson, 2009). Besides affecting the mean wind speed, canopy edges also feature an effect on atmospheric pressure. While

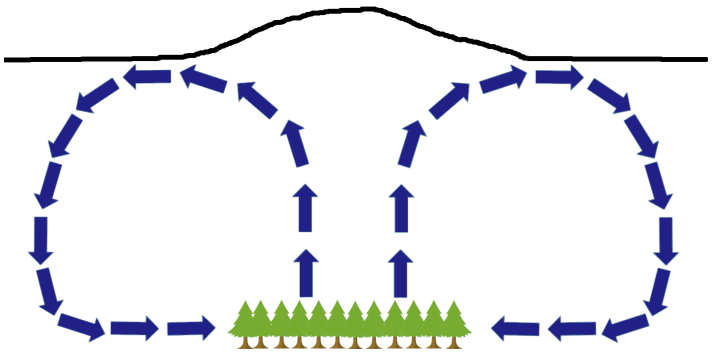

Figure 1.5: Illustration of secondary circulations coupling an isolated forest to the surrounding in a free-convection case. The height of the atmospheric boundary layer is depicted by the solid black line.

the deceleration of the mean wind past leading edges leads to an increase in atmospheric pressure within the canopy, the acceleration behind trailing canopy edges leads to a decrease in atmospheric pressure (Banerjee et al., 2013). However, the high pressure region downstream of leading canopy edges can feature an extend that is up to one order of magnitude smaller than the region of low pressure downstream of trailing edges (Cassiani et al., 2008; Banerjee et al., 2013).
While canopy-edge flow was mainly investigated by the comparison of numerical studies to wind tunnel measurements (Dupont and Brunet, 2008), field experiments (Dalpé and Masson, 2009; Schlegel et al., 2012; Kanani et al., 2014) or both (Yang et al., 2006; Banerjee et al., 2013), the number of analytical investigations is smaller. Besides one-dimenisonal descriptions of canopy flow for homogeneous canopies (Section 1.3.2), an two dimensional model of canopy edge flow was introduced by Belcher et al. (2003), who linearized the governing equations by assuming the wind-profile inside the canopy to be a small perturbation to the incoming logarithmic velocity profile. Even if this approach is only applicable to shallow canopies, it is able to describe the flow within all regions of Fig. 1.4.

1.4.2 Secondary circulations

Besides effects of micro-γ-scale heterogeneities on surface–atmosphere exchange, meso-γ-scale heterogeneities (of surface heating or roughness) also play a crucial role in affecting regional climate and weather (Garcia-Carreras et al., 2010, 2011). Due to Raupach and Finnigan (1995) and Patton et al. (2005), meso-γ-scale heterogeneities can trigger circulations, which influence the entire boundary layer and can even increase the boundary-layer height (Oke, 1982; Brugger et al., 2018), as illustrated in Fig. 1.5. These circulations are usually referred to as “secondary circulations” as they modulate the “primary circulations” on the synoptic scale. While Wang (2009) showed that secondary circulations can be triggered by heat-island effects of isolated cities, isolated semi-arid forests also have the capability to cause

these motions (Eder et al., 2015). One example of such an isolated semi-arid forest is the Yatir forest in Israel, which mainly consists of *Pinus halepensis* and is located at the northern edge of the Negev desert. As Rotenberg and Yakir (2010) hypothesized, albedo differences between the forest and the surrounding shrubland are able to cause extensive secondary circulations.
Due to the limited water availability besides the large net radiation at the Yatir forest, the survival of this ecosystem strongly depends on a cooling mechanism named "canopy-convector effect" (Rotenberg and Yakir, 2010). The canopy-convector effect describes an amplification of energy transport by enhanced sensible heat fluxes to compensate for the large net radiation values, especially in the dry summer periods (Rotenberg and Yakir, 2011; Eder et al., 2015). While an increase in heat flux for increasing atmospheric instability is already explained by means of aerodynamic resistance approaches for homogeneous canopies (Eq. (1.24), Banerjee et al., 2017), the interaction of the canopy-convector effect with secondary circulations might be crucial for the survival of the Yatir forest.

2 | Analytical models

To investigate the influence of surface heterogeneities on the atmospheric flow, the following two models were developed from analytical approaches: A model to calculate distributions of the mean wind speed and the mean pressure within a canopy past a leading forest edge (Section 2.1), which can be used to determine the influence of leading canopy edges on atmospheric measurements downstream of those edges, and an aerodynamic resistance parametrization for heterogeneous surfaces, applicable within meso-scale models (Section 2.2).

2.1 Effect of leading edges on the mean flow within a homogeneous canopy

As described in Section 1.3.2, several analytical theories for homogeneous canopies were developed in the past. However, these one-dimensional theories are insufficient for investigations of heterogeneous scenarios like canopy-edge flow. Improvements towards a two-dimensional analytical model were made by Belcher et al. (2003) through linearizing the governing flow equations for small perturbations added to an incoming logarithmic velocity profile, which is a valid assumption for shallow canopies (Section 1.4.1). To overcome the shallow-canopy limitation of this approach, Kröniger et al. (2018a) derived an analytical solution to the governing equations in the adjustment region (region (ii) in Fig. 1.4), which is presented in Appendix B. This analytical solution was developed for a leading canopy edge in a predefined background wind for neutral atmospheric stratification, where the canopy is homogeneous in crosswind direction (two-dimensional scenario) and is, therefore, defined by two length scales, the canopy height h_c and the adjustment length scale l_c (Section 1.3.1), where the latter was assumed to be vertically constant. When additionally neglecting molecular diffusion and the Coriolis terms, the mass-conservation (Eq. 1.4) and momentum-conservation equation (Eq. 1.28) reduce to

$$\begin{aligned} \partial_x \overline{u} + \partial_z \overline{w} &= 0 \\ \partial_x \overline{u}^2 + \partial_z (\overline{u}\,\overline{w}) &= -\tfrac{1}{\rho_0}\partial_x \overline{p} + \partial_j \overline{u' u'_j} - \tfrac{1}{l_c}\overline{u}^2 \\ \partial_x (\overline{u}\,\overline{w}) + \partial_z \overline{w}^2 &= -\tfrac{1}{\rho_0}\partial_z \overline{p} + \partial_j \overline{u'_j w'} - \tfrac{1}{l_c}\overline{u}\,\overline{w}, \end{aligned} \tag{2.1}$$

where $\overline{w} \ll \overline{u}$ was assumed to simplify the drag-force, which prevents the analytical model from predicting re-circulation regions (Section 1.4.1). Besides, (Kröniger et al., 2018a) neglected the influence of turbulent shear in Eq. (2.1) against the drag force, which is a valid approximation for the adjustment region (Townsend, 1972; Jackson and Hunt, 1975), while turbulent momentum fluxes play an important role within the canopy interior (Section 1.3.2).
By additionally assuming the vertical velocity component to be separable concerning the two spatial directions ($w\left(x,z\right) = -f\left(x\right) g\left(z\right)$), Eq. (2.1) can be solved analytically, yielding

$$\begin{aligned} \overline{u}(x,z) &= u_s \Lambda(x) \cosh(a_1 z/h_c), \\ \overline{w}(x,z) &= u_s \left(a_2 - a_3/\alpha \; e^{-x/l_c}\right) \Lambda(x) \sinh(a_1 z/h_c)/a_1, \\ \overline{p}(x,z)/p_s &= \textstyle\int_x^\infty \Lambda^2(\tilde{x}) d\tilde{x}/l_c - \Lambda^2/2 - \alpha a_2 \Lambda^2 \sinh^2(a_1 z/h_c)/\left(2a_1^2\right), \end{aligned} \tag{2.2}$$

where

$$\Lambda(x) = \exp\left(-a_2 x/h_c - a_3/\alpha^2 \; e^{-x/l_c}\right), \tag{2.3}$$

$\alpha = h_c/l_c$, a_1, a_2, and a_3 are dimensionless, positive parameters, and u_s and $p_s = \rho_0 u_s^2$ are velocity and pressure scales, determined from the incoming wind speed. As $\Lambda(x)$ exponentially decreases to zero with increasing distance from the leading edge, $\overline{u}$, $\overline{w}$, and $\overline{p}$ also feature this asymptotic behavior. Concerning $\overline{w}$, this result is in line with the one-dimensional theory for the canopy interior. However, concerning $\overline{u}$ and $\overline{p}$, the one-dimensional theory predicts horizontally constant (homogeneous) non-zero values due to momentum transport from the flow above into the canopy below. To solve this contradiction and to increase the applicability of the analytical model to the full canopy region, Kröniger et al. (2018a) subsequently combined the adjustment region model with Eq. (1.33) for the canopy interior, by imposing continuity on $\overline{u}$, using

$$\overline{u}\left(x,z\right) = u_s \Lambda\left(x\right) \cosh(a_1 z/h_c) \Theta\left(x_I - x\right) + \overline{u}_{\mathrm{h}}\left(z\right) \Theta\left(x - x_I\right), \tag{2.4}$$

where Θ is the Heaviside-step function and x_I is the distance from the leading edge, where the adjustment region passes into the canopy interior. Therefore, x_I also defines the length of the adjustment region. To derive an expression for x_I, Kröniger et al. (2018a) assumed this distance to be defined as the point, where the drag force decreased that far (due to a decrease of $\overline{u}$) that it equals the vertical gradient of $\overline{u'w'}$, which is the defining condition for the homogeneous scenario (Eq. 1.32). Therefore, the term $d_z \overline{u'w'}_{\mathrm{h}}$ in Eq. (1.32) is calculated from Eq. (1.33), while the drag force on the right hand side of Eq. (1.32) is calculated from using $\overline{u}$ from Eq. (2.4). This approach for determining x_I is illustrated in Fig. 2.1, where the intersections between the $\overline{u}^2/l_c$ term and the horizontally-constant $d_z \overline{u'w'}_{\mathrm{h}}$ term yields a height-

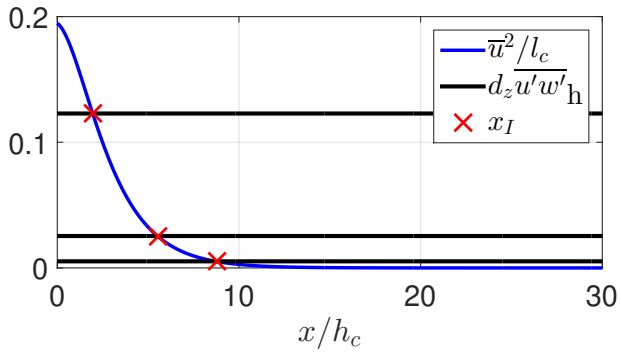

Figure 2.1: Illustration of the x_I calculation after Kröniger et al. (2018a). The height-dependent x_I (red crosses) is determined from intersecting the horizontal drag-force component of the adjustment region model $\overline{u}^2/l_c$ (blue lines) with the turbulent stress $d_z\overline{u'w'}_{\mathrm{h}}$ from the one-dimensional model for homogeneous canopies (Section 1.3.2, black lines). The profiles are normalized by u_s^2/l_c, while the elevations $0.2 \times h_c$, $0.5 \times h_c$ and $0.8 \times h_c$ are used.

dependent x_I. From this approach

$$a_2 x_I/h_c + a_3/\alpha^2 \exp\left(-x_I/l_c\right) = \log\left(u_s/u_{\mathrm{h}}\left(h_c\right)\right) + n\left(1 - z/h_c\right) \tag{2.5}$$

is derived, which implicitly defines x_I.

2.2 Aerodynamic resistance parametrization for heterogeneous surfaces

Besides the analytical investigations on canopy-edge flow, surface–atmosphere exchange of heterogeneous surfaces was also studied from developing an aerodynamic resistance parametrization for meso-scale models (Section 1.1.4) using a covariance-function (Section 1.1.2) approach in spectral space (Kröniger et al., 2018c, Appendix D). This covariance-function approach was employed to improve the representation of subgrid-scale heterogeneities with respect to other methods, like the bulk-similarity approach (e.g. Mahrt, 1996; Brutsaert, 1998) or the tile approach (Avissar and Pielke, 1989; Koster and Suarez, 1992; Stoll and Porté-Agel, 2009; de Vrese et al., 2016; de Vrese and Hagemann, 2016). The derivation of the aerodynamic-resistance parametrization from covariance functions (r_{cf}) is based on linking the covariance function of the heterogeneous scenario (label "nh" $\equiv$ non homogeneous) $\overline{E}^{\mathrm{nh}}_{V_1V_2}$ to the covariance function of the homogeneous bulk averaged scenario within the considered grid cell of the meso-scale model $\overline{E}^{\mathrm{h}}_{V_1V_2}$ by imposing

$$\overline{E}^{\mathrm{nh}}_{V_1V_2}\left(\left(\mathbf{r}, z\right), \hat{\mathbf{r}}\right) = \chi_{V_1V_2}\left(\mathbf{r} + \hat{\mathbf{r}}\right) \overline{E}^{\mathrm{h}}_{V_1V_2}\left(z, \hat{\mathbf{r}}\right), \tag{2.6}$$

where $\chi_{V_1V_2}$ represents the scale-wise distortions of heterogeneity on the planar-homogeneous covariance function. Following Kröniger et al. (2018c), an expression

for $\chi_{V_1V_2}$ can be derived from evaluating Eq. (2.6) at $\hat{\mathbf{r}} = 0$, which yields

$$\chi_{V_1V_2}(\mathbf{r}) = \overline{V_1'V_2'}\left(\mathbf{r}, z\right) / \langle \overline{V_1'V_2'} \rangle \left(z\right), \tag{2.7}$$

where it was assumed that $\overline{V_1'V_2'}$ and $\langle \overline{V_1'V_2'} \rangle$ feature the same dependence on z, which leads to a z-independent $\chi_{V_1V_2}$. To make use of Eq. (2.6), Kröniger et al. (2018c) simplified the governing equation for the $w\theta$ spectrum $\overline{F}^{\mathrm{nh}}_{w\theta}\left(\left(\mathbf{r}, z\right), \mathbf{k}\right)$ by assuming stationary flow, neglecting triple moments, molecular dissipation, dispersive fluxes and advection, and using a Rotta like closure for the pressure decorrelation, yielding

$$\overline{F}^{\mathrm{nh}}_{w\theta} \approx \left(-C_1 \overline{F}^{\mathrm{nh}}_{ww} \partial_z \bar{\theta} + C_2 \overline{F}^{\mathrm{nh}}_{\theta\theta} g/\theta_0\right) \tau, \tag{2.8}$$

where C_1 and C_2 are constants originating from the Rotta model and τ is the Rotta-time scale for relaxation. By additionally assuming that the spectral shapes for the bulk homogeneous scenario are based on Kolmogorovian power laws (Eqs. 1.13 and 1.14) for inertial scales and constant for the residual scales (Katul et al., 2013, 2014), the aerodynamic resistance to heat transfer is derived. As it turns out, this aerodynamic resistance r_{cf} can be calculated from Eq. (1.24) when replacing the usual similarity functions ϕ_m and ϕ_h through heterogeneity-corrected similarity functions ϕ^{cf}_m and ϕ^{cf}_h, which are defined by

$$\begin{aligned} \phi^{\mathrm{cf}}_m\left(\zeta\right) &= \phi_m\left(\zeta\right) I_{ww}\left(\phi_m^{-3/4}\left(\zeta\right) z\right), \\ \phi^{\mathrm{cf}}_h &= \left[\phi_m\left(\zeta\right) + \left(\phi_h\left(\zeta\right) - \phi_m\left(\zeta\right)\right) / I_{\theta\theta}\left(\phi_m^{-3/4}\left(\zeta\right) z\right)\right] I_{ww}\left(\phi_m^{-3/4}\left(\zeta\right) z\right), \end{aligned} \tag{2.9}$$

where the heterogeneity correction factors I_{ww} and $I_{\theta\theta}$ are defined by

$$I_{V_1V_2}(z) = \frac{7}{4}\left(2\pi\right)^{-7/3} z^{4/3} \left[\int_{\mathbf{k}} \int_{\tilde{\mathbf{k}}} \underbrace{\varphi_A\left(\tilde{\mathbf{k}}\right)}_{I} \underbrace{\hat{\chi}_{V_1V_2}\left(\tilde{\mathbf{k}}\right)}_{II} \underbrace{\frac{G_{-5/3}\left(z, \|\tilde{\mathbf{k}} - \mathbf{k}\|\right) G_{-2/3}\left(z, \|\mathbf{k}\|\right)}{\|\tilde{\mathbf{k}} - \mathbf{k}\|}}_{III}\right]^{-1}, \tag{2.10}$$

and $\int_{\mathbf{k}} \equiv \int \frac{d^2\mathbf{k}}{(2\pi)^2}$, $\varphi_A\left(\mathbf{k}\right) = \mathrm{sinc}\left(k_x \Delta x/2\right) \times \mathrm{sinc}\left(k_y \Delta y/2\right)$, $\mathrm{sinc}\left(x\right) = \sin\left(x\right)/x$, $A = \Delta x \times \Delta y$ is the area of the meso-scale-model grid cell, $\hat{\chi}_{V_1V_2}$ is the Fourier transform of $\chi_{V_1V_2}$ and G_α represents the assumed shapes of the homogeneous spectra (Kröniger et al., 2018c, Appendix D). Note that there are three different contributions to r_{cf} in Eq. (2.10). While term I (φ_A) represents the spatial averaging, dampening scales smaller than the grid dimensions of the meso-scale model, term II ($\hat{\chi}_{V_1V_2}$) represents the surface heterogeneity independent of the meso-scale-model grid. Term III illustrates the contribution of the bulk-averaged homogeneous scenario to r_{cf}.

3 | Numerical experiments

Besides investigating surface–atmosphere exchange of heterogeneous surfaces from analytical approaches (Chapter 2), three sets of LES were performed. The first set, consisting of eleven LES (Section 3.1), was used to calculate the parameters of the canopy-edge-flow model (Section 2.1) and to test the performance of this model against LES and the approach of Belcher et al. (2003). The second set, consisting of six LES (Section 3.2), was used to investigate surface–atmosphere exchange above the meso-γ-scale heterogeneity of the Yatir forest (Section 1.4.2), mainly by investigating secondary circulations between the forest and the surrounding shrubland. The third set, consisting of four LES (Section 3.3), was used to compare the performance of the aerodynamic resistance parametrization from structure functions (Section 2.2) against the bulk similarity and tile methods, by investigating three examples of idealized surface heterogeneities using six different test-meso-scale model grids.

3.1 Large-eddy simulations of flow across leading canopy edges

To test the performance of the developed canopy-edge-flow model and to determine the model parameters a_1, a_2 and a_3, Kröniger et al. (2018a) performed eleven LES of canopy stripes (Appendix B) using the LES code PALM (Section 1.2), which employs Eqs. (1.28), (1.29), and (1.30) to simulate the effect of the canopy on the atmospheric flow. To mimic a two-dimensional scenario in $x-z$, these canopy-stripes were taken to be homogeneous in y-direction. While the canopy drag coefficient was set constant throughout the simulations ($c_d = 0.2$), the three canopy length scales l, h_c, and l_c (Fig. 1.4) were varied, such that $l \in \{10, 20, 30, 500\}$ m, $h_c \in \{10, 15, 20\}$ m, and $l_c \in \{12.5, 16.7, 25\}$ m. For the sake of modeling neutral stratification, the surface heat flux was set to 0 throughout the simulation domain, which featured dimensions of $1025 \times 256 \times 128$ m in the x-, y-, and z-direction respectively. An uniform grid spacing of $\Delta x_{\mathrm{LES}} = \Delta y_{\mathrm{LES}} = \Delta z_{\mathrm{LES}} = 1$ m was used, yielding $1025 \times 256 \times 128$ grid cells. Throughout all simulations, a constant geostrophic wind speed $u_0 = 2$ m s^{-1} was used. At the top boundary, Dirichlet conditions were applied for the wind velocity and the pressure, while periodic boundary conditions were used in the horizon-

Table 3.1: Configuration of the preliminary simulations for modeling the Yatir forest.

Geostrophic wind speed u_0	5.7 m s^{-1}; 2.8 m s^{-1}; 0
Lapse rate of the inversion layer	7.25×10^{-4} K m^{-1}
Initial boundary-layer height	1000 m
Initial temperature	$34\,^{\circ}$ C
Roughness length	0.01 m
Kinematic heat flux at the surface	0.214 K m s^{-1}
Simulated time	2 h

tal directions. As initial conditions $\overline{u} = u_0$, $\overline{w} = 0$ and $\overline{p} = 0$ were set throughout the simulation domain. Due to starting from these constant profiles, a spin-up time is needed (Section 1.2). Kröniger et al. (2018a) used a spin-up time of 30 min, which was sufficient for the investigated canopy-edge flow scenarios featuring neutral stratification for the total modeling time of 1 h.

3.2 Large-eddy simulations of the Yatir forest

To investigate secondary circulations at the Yatir forest, Kröniger et al. (2018b) performed six LES (Appendix C), which were initialized from data of two measurement campaigns (Brugger et al., 2018; Kröniger et al., 2018b). The simulation set-up consists of both, three preliminary simulations and three corresponding main simulations. A dry atmosphere was modeled in all cases because of the negligible energy transport by latent heat fluxes at the Yatir forest (Rotenberg and Yakir, 2010; Eder et al., 2015). The bottom of the surface domain was taken as a flat surface because of the gentleness of the topography. The preliminary simulations were initialized by measurements from eddy-covariance and Doppler-lidar systems, located within the shrubland upstream to the forest, together with balloon measurements of the inversion above the atmospheric-boundary layer. This LES set-up did not feature a forest canopy and, therefore, simulates the shrubland surrounding the Yatir forest. The numerical values of the input quantities for the preliminary simulations are shown in Table 3.2, where the roughness length was chosen according to Eder et al. (2015), and the geostrophic wind speed was varied between the three preliminary simulations to model weakly-unstable (5.7 m s^{-1}), mildly-unstable (2.8 m s^{-1}), and strongly-unstable stratification (0). The main purpose of the preliminary simulations, which featured a simulation time of 2 h, was to decouple the spin-up needed to reach a stationary turbulent state (Section 1.2) from the main simulations.
The three main simulations were initialized by the prognostic variables at the end of the corresponding preliminary simulation at every grid point. Besides, the canopy of the Yatir forest was modeled by three-dimensional plant-area-density ($a(x, y, z)$) and source-heat-flux maps ($\overline{Q}\,(x, y, z)$) maps, which are required to apply Eqs. (1.28), (1.29), and (1.30) in the PALM canopy model. Kröniger et al. (2018b) derived those

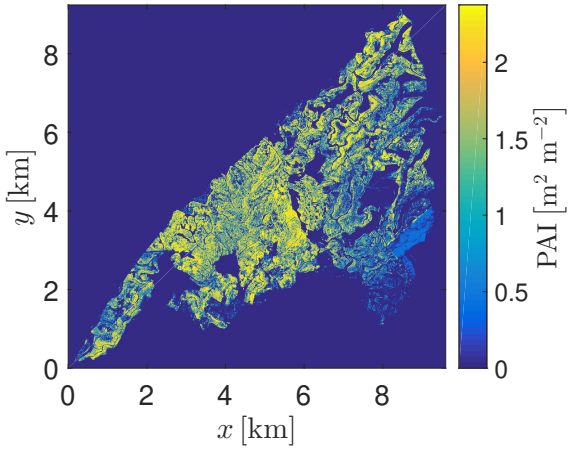

Figure 3.1: Plant-area-index map (PAI) of the Yatir forest, corresponding to the plant-area-density map used by Kröniger et al. (2018b). The map is rotated in mean-wind direction to model inflow from the left boundary of the modeling domain.

maps from combining satellite data with single-tree- and plot-PAI measurements. The corresponding two-dimensional PAI map (Eq. 1.26) is shown in Fig. 3.1, where the forest canopy was rotated in mean wind direction to simulate inflow from the left boundary of the modeling domain. Besides, the simulated time of the main simulations was 1 h, while data were extracted from the second 30-min period. All six LES featured the same grid resolution corresponding to $\Delta x_{\mathrm{LES}} \times \Delta y_{\mathrm{LES}} \times \Delta z_{\mathrm{LES}} = 5.0 \times 7.5 \times 2.5$ m, which enables the resolution of the forest canopy with up to six grid levels. Due to the periodic lateral boundary conditions used, the size of the domain had to be of a sufficient size to prevent the self-interaction of the forest. Therefore, a domain size of $30.72 \times 15.36 \times 2.56$ km was used for the weakly- and mildly-unstable LES, resulting in $6144 \times 2048 \times 1024$ grid points. Concerning the strongly-unstable LES, the grid dimensions were changed to $4096 \times 2816 \times 1024 \equiv 20.48 \times 21.12 \times 2.56$ km.

3.3 Large-eddy simulations to test the aerodynamic resistance parametrizations

To compare the aerodynamic resistance from the covariance functions method against the bulk and tile approaches, Kröniger et al. (2018c) performed one preliminary and three main LES of idealized surface heterogeneities (Appendix D). All four LES used a computational grid consisting of $2000 \times 2000 \times 400$ grid points in x-, y-, and z-direction respectively. The grid cells were equidistant in all three spatial directions, with $\Delta x_{\mathrm{LES}} = \Delta y_{\mathrm{LES}} = \Delta z_{\mathrm{LES}} = 4$ m, yielding a total modeling domain of $8 \times 8 \times 1.6$ km. A geostrophic wind of $u_g = 1$ m s^{-1} in x-direction was used to drive the simulations. In contrast to the previous LES featuring a canopy model (Sections 3.1 and 3.2), a roughness length model was applied to simulate the surface heterogeneity, by prescribing two-dimensional surface-heat-flux ($H_{0,\mathrm{LES}}$), and roughness-length maps

Table 3.2: Configuration of the preliminary simulation for testing aerodynamic resistance parametrizations.

Lapse rate of the inversion layer	$1.0 \cdot 10^{-2}$ K m^{-1}
Initial boundary-layer height	850 m
Initial temperature	27 ° C
Kinematic heat flux at the surface ($H_{0,\mathrm{LES}}$)	0.1 K m s^{-1}
Roughness length ($z_{0,\mathrm{LES}}$)	0.01 m
Simulated time	2 h

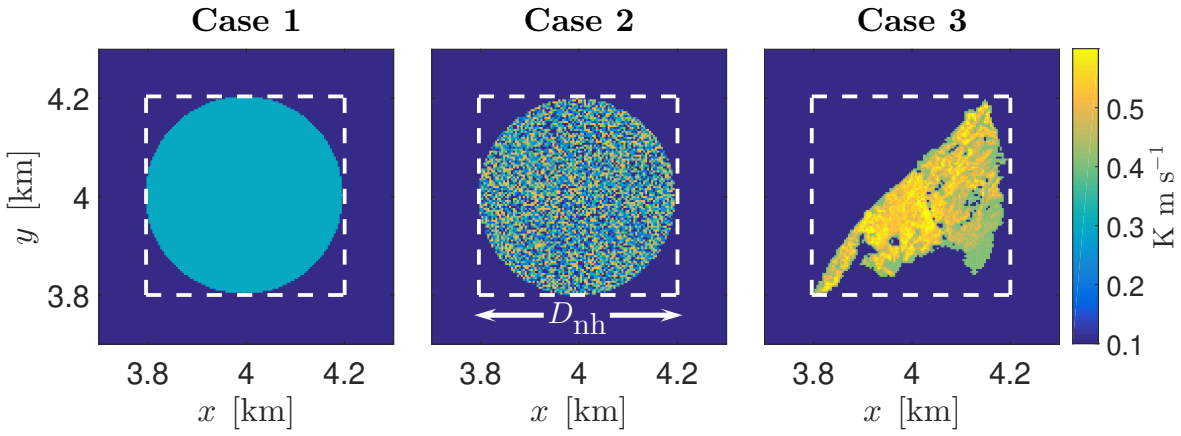

Figure 3.2: $H_{0,\mathrm{LES}}$ maps of the three test cases for investigating the performance of the covariance-function approach after Kröniger et al. (2018c) (Appendix D). The white dashed line indicates the dimension of the heterogeneity D_{nh}.

($z_{0,\mathrm{LES}}$). The homogeneous preliminary simulation, which was again used to decouple the turbulent spin-up from the main simulations (Section 3.2), was initialized by the values shown in Table 3.2, while the three main simulations were initialized by the output of this preliminary simulation at every grid point after an elapsed time of 2 h. The simulated time of the main simulations was also 2 h, were the data of the last 30 min was used for data output. The three considered heterogeneous scenarios were a disc-shaped heterogeneity of constant surface heat flux and roughness (Test case 1), a disc-shaped heterogeneity of randomly varying heat flux and roughness (Test case 2), and a realistic case, where a downscaled version of the Yatir forest was used by deriving $z_{0,\mathrm{LES}}$ and $H_{0,\mathrm{LES}}$ maps from the PAI and $\overline{Q}$ maps used by Kröniger et al. (2018b) (Test case 3). However, $H_{0,\mathrm{LES}}$ for case 3 was upscaled by a factor of 1.5 to guarantee that the total energy input, and therefore the boundary layer growth, is the same for all three test cases. The $H_{0,\mathrm{LES}}$ maps for the three test cases are shown in Fig. 3.2, where the white dashed line defines the size (diameter) of the heterogeneity $D_{\mathrm{nh}} = 400$ m. Besides, Kröniger et al. (2018c) used six different test-meso-scale-model grids to compare the aerodynamic resistance parametrization in the three LES test cases. Equilateral grid cells with dimensions $\Delta x/D_{\mathrm{nh}} = \Delta y/D_{\mathrm{nh}} = 0.1,\ 0.2,\ 0.4,\ 0.8,\ 2.0,\ 4.0$ were chosen for this purpose.

4 | Results and Discussion

After introducing the developed analytical models (Chapter 2) and performed numerical experiments (Chapter 3), which were used to study the effect of surface heterogeneity on the atmospheric flow, the results of those investigations are presented in this chapter. At first, the comparison of the analytical edge-flow model to LES and the model of Belcher et al. (2003) is discussed (Section 4.1). At second, the results of the investigations on secondary circulation above the Yatir forest are presented (Section 4.2). At third, the comparison of the aerodynamic resistance parametrization from structure function approaches against the bulk and tile approaches is discussed (Section 4.3).

4.1 Comparison of the canopy-edge-flow model against simulations

To compute the model parameters a_1, a_2, and a_3 (Section 2.1), Kröniger et al. (2018a) fitted Eq. (2.1) to a reference LES, which was defined by $l = 500$ m, $h_c = 10$ m, and $l_c = 16.7$ m (Appendix B). The least-squares fit of the analytical model to the reference simulation is shown in Fig. 4.1, with the corresponding model parameters $a_1 = 1.6 \times 10^{-3}$, $a_2 = 0.25$, and $a_3 = 0.13$. Figure 4.1 reveals discrepancies between the model and the LES result for two regions. While the deviations inside the canopy interior are due to neglecting the turbulent shear against the drag force, which is addressed by combining the model with the one-dimensional model for homogeneous canopies (Section 2.1), additional inaccuracies emerge in the inflow region shortly past the edge. In this region, the incoming $\overline{u}$-profile changes from a logarithmic form to a cosh-shaped one (Eq. 2.2), which contradicts the separability assumption used in the derivation (Section 2.1). To test the robustness of the derived model parameters, Kröniger et al. (2018a) further varied the three length scales l, h_c, and l_c by performing several LES. From comparison with those simulations, a good agreement between the analytical model using the aforementioned parameters and LES was deduced. By using the defining equation for the length of the adjustment region x_I (Eq. 2.5), which was derived from combining the adjustment region model with the model for the canopy interior (Section 2.1), Kröniger et al. (2018a) computed $x_I\,(h_c/2)$ for the simulated scenarios, resulting in distances that

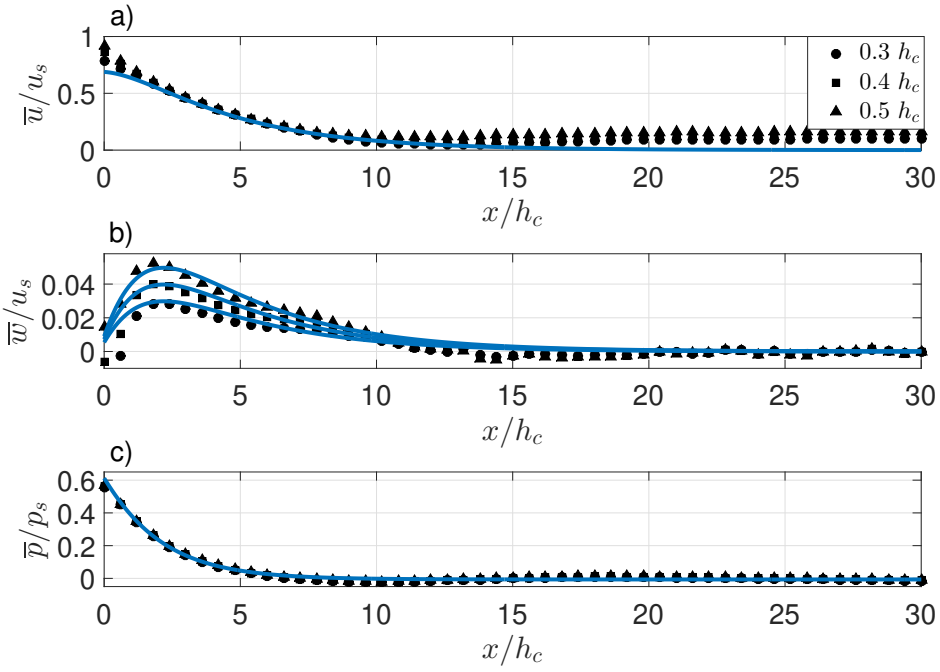

Figure 4.1: Fit of the Kröniger et al. (2018a) model to the reference LES after Kröniger et al. (2018a) (Appendix B). Three horizontal profiles are depicted for each of the three flow variables $\overline{u}$ (a), $\overline{w}$ (b) and $\overline{p}$ (c), corresponding to the height levels $0.3\ h_c$ (circles), $0.4\ h_c$ (squares) and $0.5\ h_c$ (triangles). The fitted model-curves are illustrated as blue solid lines.

ranged between $x_I\left(h_c/2\right)/l_c = 3.2$ for $(h_c, l_c) = (10, 25)$ m and $x_I\left(h_c/2\right)/l_c = 11.6$ for $(h_c, l_c) = (20, 16.7)$ m.

To compare the derived analytical model against the model of Belcher et al. (2003), Kröniger et al. (2018a) performed three additional LES, where $h_c = 10$ m, $l_c = 16.7$ m, and l/l_c was varied between 0.6, 1.2, and 1.8. The comparison of horizontal $\overline{u}(x, z = h_c/2)$ from the Kröniger et al. (2018a) model against the Belcher et al. (2003) model and LES are illustrated in Fig. 4.2. Figure 4.2 shows that the applicability of the Belcher et al. (2003) model is limited to small values of l/l_c, which is due to the shallow-canopy approximation used to derive this model from a linearization approach (Section 2.1). On the other hand, the LES results approach the Kröniger et al. (2018a) model for increasing l/l_c, which shows that this model is applicable for the reversed situation, as no linearization assumption was used for the derivation. As the length of the canopy (l) is not included in the derivation of the Kröniger et al. (2018a) model, the three corresponding curves collapse in Fig. 4.2.

4.2 Secondary circulations above the semi–arid forest Yatir

To investigate the relevance of secondary circulations for the surface–atmosphere exchange of the meso-γ scale heterogeneity Yatir forest, Kröniger et al. (2018b) analyzed the LES for the weakly-, mildly-, and strongly-convective scenarios, which

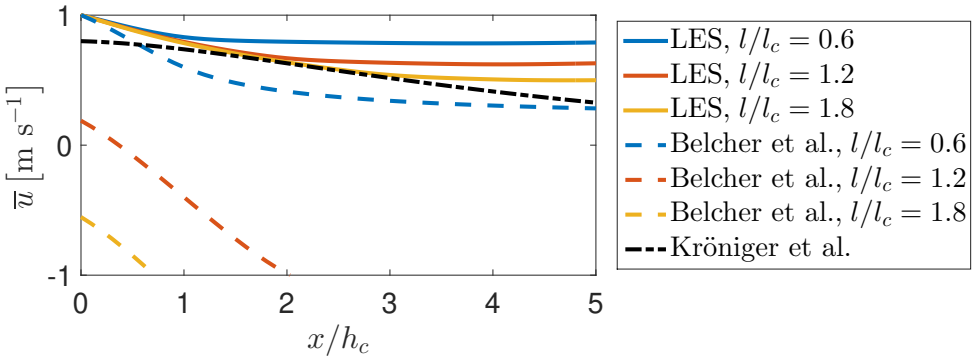

Figure 4.2: Comparison of horizontal $\overline{u}\,(x, z = h_c/2)$ past a leading forest edge, from LES (solid lines), from the Belcher et al. (2003) model (dashed lines) and from the Kröniger et al. (2018a) model (dashed-dotted line), for three different forest lengths l, constant forest height $h_c = 10$ m and adjustment length scale $l_c = 16.7$ m after Kröniger et al. (2018a) (Appendix B). The $l/l_c = 0.6$ profiles are colored red, the $l/l_c = 1.2$ profiles are colored blue and the $l/l_c = 1.8$ profiles are colored yellow. The l-independent model of Kröniger et al. (2018a) is colored black.

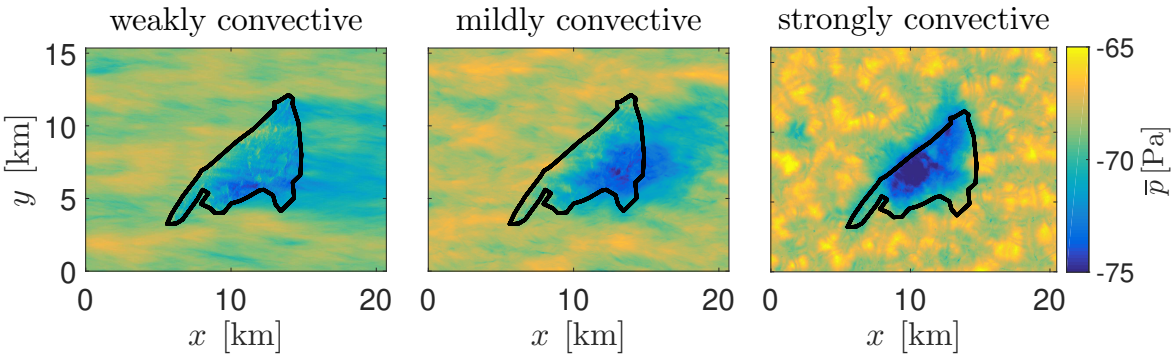

Figure 4.3: Pressure fluctuations at height $z = h_c$ for LES of the weakly-convective scenario (left), mildly-convective scenario (middle), and the strongly-convective scenario (right) according to Kröniger et al. (2018b) (Appendix C). The black dashed line illustrates the boundary of the Yatir forest.

are described in Section 3.2 (Appendix C). When using the canopy-edge-flow model (Eq. 2.5) to calculate the extension of the adjustment region for the Yatir forest, assuming a mean PAI of 1.6 m^2 m^{-2} and a mean tree height of 11 m (Sprintsin et al., 2007), it turns out that the effect of the leading edges on the atmospheric flow is $\sim \mathcal{O}\,(100$ m$)$. In comparison to the extension of the forest of up to 8 km in mean-wind direction this effect is of minor importance when considering surface–atmosphere exchange of the total forest. However, using Eq. (2.5) to calculate the extension of the adjustment region for Yatir forest can only serve as a first approximation, due to conditions like neutral stratification and a homogeneous canopy (Section 2.1). Therefore, Kröniger et al. (2018b) analyzed the mean pressure fluctuations $\overline{p}$ for the three scenarios of different atmospheric stability, which is illustrated in Fig. 4.3. On the one side, Fig. 4.3 shows that the effect of leading canopy edges on the pressure can be neglected, as these effects are hardly visible for the considered plot scale. One the other side, the $\overline{p}$ plots illustrate the occurrence of low-pressure

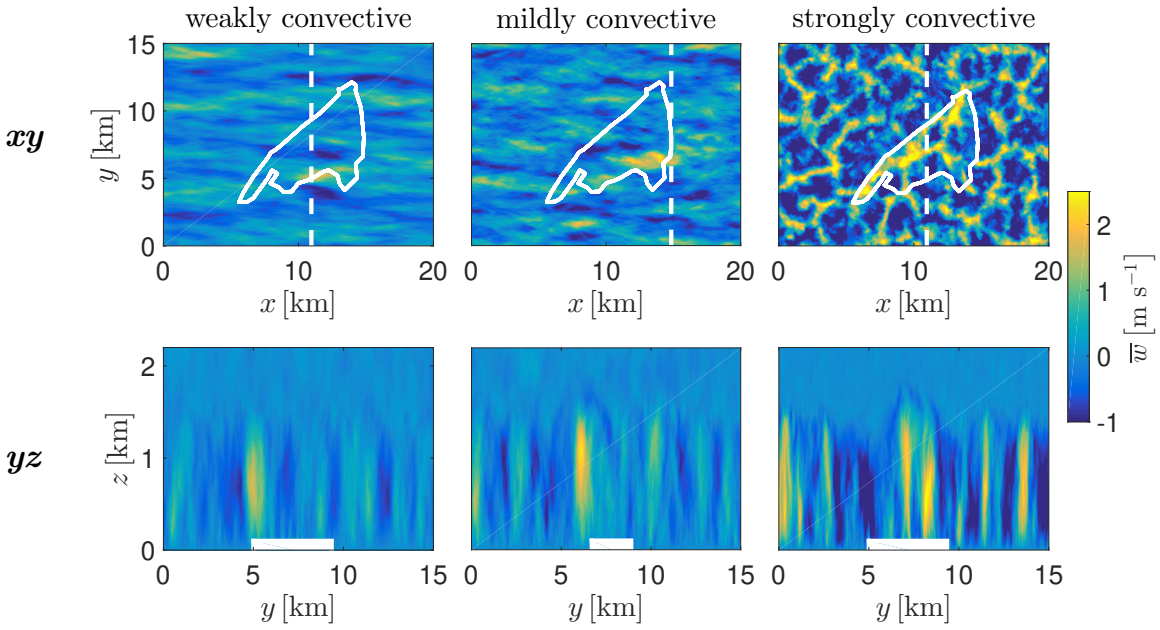

Figure 4.4: Horizontal (first row) and vertical cross-wind cross sections (second row) of the mean vertical velocity $\overline{w}$, for the weakly-convective (first column), mildly-convective (second column), and strongly-convective scenario (third column) after Kröniger et al. (2018b) (Appendix C). The location of the forest is depicted by the white solid lines in the first row and by white boxes in the second row. The horizontal cross sections are extracted at half of the boundary-layer height and the location of the vertical cross sections with respect to the forest is depicted by the white dashed lines in the first row.

regions in the lee of the densest part of Yatir forest (Fig. 3.1) for the weakly- and mildly-unstable scenarios, which is an effect of flow across the trailing edges of this region and affects the atmospheric flow for a distance of several kilometers (Section 1.4.1). For the strongly-convective case, buoyancy is the main mechanism affecting the pressure fluctuations, where the location of the region of low pressure is above the densest part of the forest, as this region also features the lowest albedo. Due to Kröniger et al. (2018b), these canopy-induced regions of low pressure cause secondary circulations above the Yatir forest, which is illustrated from investigating mean vertical wind speed $\overline{w}$ in Fig. 4.4. The emerging secondary circulations, which affect the whole boundary layer, were found to feature an extension that is too small to couple the whole forest to the sorrounding shrubland in all three scenarios, as regions of downdraft also appear above the forest. Besides, the effect of the secondary circulations on the incoming primary circulations (rolls for the weakly- and mildly-convective scenarios, fishnet structures for the strongly-convective scenario) was found to be most distinct for the strongly-convective scenario (yz-plots in Fig. 4.4), where also the height of the boundary layer is affected (Brugger et al., 2018). To quantify the effect of the secondary circulations on the surface–atmosphere exchange of energy ("canopy-convector effect", Section 1.4.2), Kröniger et al. (2018b) additionally investigated the aerodynamic resistance to heat transfer for the Yatir

forest and the surrounding shrubland. As discussed in Section 1.1.4, a reduction in aerodynamic resistance to heat transfer for increasing atmospheric instability can be explained for homogeneous canopies by employing MOST. Therefore, an increase in atmospheric instability should decrease the aerodynamic resistance for both regions, the Yatir forest and the surrounding shrubland, if the eco-systems could be described by MOST independently. Due to Kröniger et al. (2018b), a reduction in aerodynamic resistance can indeed be observed above the forest canopy, which is strongest for the densest part of the forest (Appendix C). However, the aerodynamic resistance above the surrounding shrubland was shown to increase with increasing atmospheric instability. This finding is explained by the fact that the secondary circulations affect the surface–atmosphere exchange of the Yatir forest by increasing the exchange in regions of updraft and decreasing the exchange in regions of downdraft. As most downdrafts are located above the shrubland, the reduction of the aerodynamic resistance, which would be observed for a homogeneous shrubland, is overcompensated by the increase of the aerodynamic resistance due to the effect of secondary circulations. Because of that, the increase in aerodynamic resistance above the shrubland for increasing atmospheric stability is a direct effect of surface heterogeneity and can, therefore, not be predicted from MOST.

4.3 Comparison of aerodynamic resistance from covariance-function, bulk, and tile approaches

To test the method of parametrizing surface heterogeneity by using the covariance-function approach in spectral space (Section 2.2), Kröniger et al. (2018c) compared the aerodynamic resistance from the covariance-function approach against the aerodynamic resistances from the bulk and from the tile approach by using the LES data of the three idealized heterogeneities (Section 3.3) as reference (Appendix D). This comparison was performed for the three surface heterogeneities, illustrated in Fig. 3.2, where the aerodynamic resistance was computed for all grid-cells of the six test-meso-scale-model grids (Section 3.3). To quantify the comparison of the three parametrizations against LES, Kröniger et al. (2018c) calculated the root-mean-square error (RMSE) between the aerodynamic resistance from these parametrizations and the LES data for the different LES test cases and meso-scale-model grids. The resulting RMSE values, as a function of the cell dimension Δx normalized by the size of the heterogeneity D_{nh} (Section 3.3), are depicted in Fig. 4.5. Figure 4.5 shows that the covariance-function approach mainly features smaller deviations from the LES than the tile approach, which itself shows smaller deviations than the bulk approach. Therefore, the covariance-function methods features the best ability of parametrizing surface heterogeneity in the considered scenarios. Besides, Fig. 4.5 shows that the RMSE for small Δx decreases from case 1 to case 2 and increases again from case 2 to case 3. This is explained by an decrease

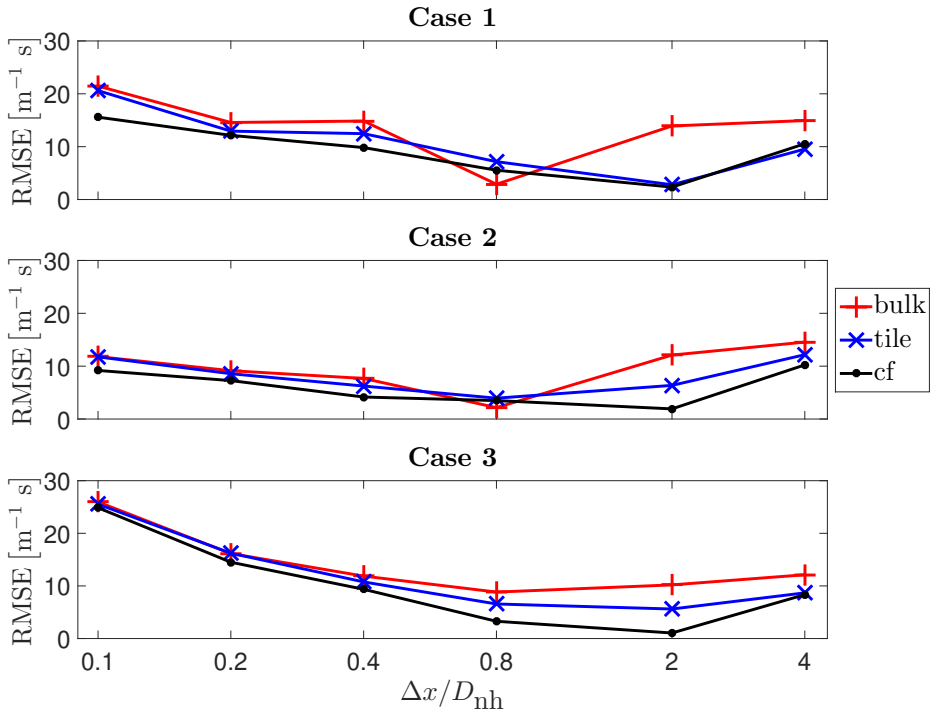

Figure 4.5: Root-mean-square-error (RMSE) plots between the bulk (red), tile (blue), and covariance-function (black) aerodynamic resistance parametrization and the LES results as a function of the meso-scale-model grid dimension Δx normalized by the heterogeneity size D_{nh} after Kröniger et al. (2018c) (Appendix D). The three subplots show the results for the three LES test cases, which were investigated by Kröniger et al. (2018c).

in heterogeneity from case 1 to case 2, as the edge between the disc and the surrounding is smoothed by randomizing the heat flux of the disc, and by an increase in heterogeneity when considering the most realistic test case 3. While the three methods feature large differences for $\Delta x = 2 \times D_{\mathrm{nh}}$, they approach each other again for the largest meso-scale-model grid with $\Delta x = 4 \times D_{\mathrm{nh}}$. The reason for this is the small extension of the heterogeneity in comparison to the grid-cell area in this case, which results in a small heterogeneity correction to the bulk approach. As the tile and the covariance-function methods both rely on MOST, the three curves have to approach each other in the limit of negligible heterogeneity. The fact that the smallest deviation from LES is achieved by the covariance-function approach in the most heterogeneous scenario ($\Delta x = 2 \times D_{\mathrm{nh}}$ for case 3) again shows the advantage of using the covariance-function approach for parametrizing surface heterogeneity with respect to the bulk and tile approaches.

5 | Summary and Conclusion

In this thesis the effect of surface heterogeneities on surface–atmosphere interactions at several scales was investigated by means of analytical approaches and LES. At first, meso-γ scale heterogeneities were analyzed by developing an analytical model to determine the spatial variation of the mean flow variables downstream of a leading canopy edge for neutral atmospheric stratification (Kröniger et al., 2018a, Appendix B). By neglecting the turbulent stresses against the drag force, which is a valid approximation for the flow adjustment region (Townsend, 1972; Jackson and Hunt, 1975), the governing equations were solved analytically. Through combining the analytical adjustment-region model with an one-dimensional model for the canopy interior (Massman, 1997), Kröniger et al. (2018a) derived a method for calculating the length of the adjustment region, which is an important quantity for determining the influence of leading canopy edges on atmospheric measurements above canopies (Chen et al., 1993; Cadenasso and Pickett, 2000; Dupont et al., 2011). To derive the emerging model parameters and to test the performance of the model, several LES of canopy stripes were performed, where the characteristic length scales for canopy-edge flow, namely the length of the canopy (l), the canopy height (h_c), and the adjustment length scale (l_c), were varied. Besides, the Kröniger et al. (2018a) model was also compared with the model of Belcher et al. (2003), which was developed for shallow canopies (small l/l_c) by treating the canopy as a first-order perturbation to the logarithmic wind profile. From comparison of the two models for three additional LES with varying l/l_c, it turned out that the two models act in different regimes. While the model of Belcher et al. (2003) is valid for small values of l/l_c, the Kröniger et al. (2018a) model shows the best results in the reversed case.

After studying the micro-γ-scale heterogeneity of leading forest edges, the atmospheric exchange of energy at the isolated meso-γ-scale heterogeneity Yatir forest was investigated by means of LES with varying atmospheric stability (weakly-convective, mildly-convective, and strongly-convective scenarios) (Kröniger et al., 2018b, Appendix C). Applying the canopy-edge-flow model of Kröniger et al. (2018a) to the leading edges of the Yatir forest, it turns out that those canopy edges have a minor effect on the surface-atmosphere exchange of the total forest. While this finding was supported by the aforementioned LES, these simulations also showed that

trailing forest edges, mainly downstream of the densest part of the forest, have a major effect on surface–atmosphere exchange of the Yatir forest by triggering regions of low pressure for the weakly-convective and mildly-convective scenarios. However, the secondary circulations, which were caused by these regions of low pressure, were not able to couple the total forest area to the surrounding shrubland due to their small horizontal extension. Even in the strongly-convective case, where the low albedo of the densest part of the forest triggered the most intense secondary circulations, the horizontal extension was not sufficient. However, from investigating the aerodynamic resistance to heat transfer for the forest and the surrounding shrubland, Kröniger et al. (2018b) deduced that the aforementioned secondary circulations affect the surface–atmosphere exchange of the Yatir forest despite of their small horizontal extension. While aerodynamic resistance parametrizations for homogeneous surfaces predict a decrease of the aerodynamic resistance with increasing atmospheric instability, the aerodynamic resistance of the shrubland in fact increased in the considered numerical simulations. The reason for this is that the downdrafts of the heterogeneity-induced secondary circulations reduced surface–atmosphere exchange above the shrubland and, therefore, increased the aerodynamic resistance. As this effect is a distinct feature of surface heterogeneity, it cannot be predicted by homogeneous parametrizations.

However, parametrizing surface heterogeneity is an important task when considering numerical weather, climate or hydrological simulations, as those meso-scale models usually feature grid resolutions of one to several hundred kilometers (e.g., Fujita, 1986; King et al., 2007), which prevents these models from resolving fine-scaled heterogeneity (e.g., forest patches, mountains, lakes). As the surface interacts with the spectrum of atmospheric turbulence on many different scales, heterogeneity parametrizations have to respect all spatial scales of the surface. To account for those scales, Kröniger et al. (2018c) developed a novel parametrization from a covariance-function approach in spectral space, which is the third part of this thesis (Appendix D). The approach of Kröniger et al. (2018c) links the covariance function of the actual heterogeneous scenario to the covariance functions of the bulk averaged scenario for a certain grid cell of the meso-scale model. By neglecting advection and dispersive fluxes, and assuming that the spectral shapes for the bulk homogeneous scenario are based on Kolmogorovian power laws for inertial scales (Katul et al., 2013, 2014), Kröniger et al. (2018c) derived heterogeneity corrections to the bulk stability correction functions. These correction terms are calculated from the used meso-scale-model grid, the spectral shape of the homogeneous structure functions, and a map, which represents the scale-wise distortions of heterogeneity on the planar-homogeneous covariance function. To compare the covariance function approach against the conventional bulk similarity (e.g. Mahrt, 1996; Brutsaert, 1998) and tile approaches (Avissar and Pielke, 1989; Koster and Suarez, 1992; Stoll and Porté-Agel, 2009; de Vrese et al., 2016; de Vrese and Hagemann, 2016), LES

of idealized surface heterogeneities were performed. The aerodynamic resistances from the three aforementioned approaches were subsequently tested against the LES reference by resolving the surface heterogeneities with six different test-meso-scale-model grids of varying cell dimension. The results of this comparison showed that the covariance-function approach yields the smallest deviations from the LES reference. In addition, the least difference of the covariance-function approach to the reference was observed for the LES with the most heterogeneous surface, which illustrates the advantage of using this novel parametrization for meso-scale models.

Therefore, the covariance-function approach proposes a framework for determining correction factors to MOST, which might even have several applications besides improving subgrid scale parametrizations. However, additional investigations (analytical, numerical, measurements) are still needed to judge the influence of advection and dispersive fluxes on the proposed method for parametrizing surface heterogeneity.

6 | Bibliography

Albertson, J. D. and Parlange, M. B. (1999). Surface length scales and shear stress: Implications for land-atmosphere interaction over complex terrain. *Water. Resour. Res.*, 35(7):2121–2132.

Albini, F. A. (1981). A phenomenological model for wind speed and shear stress profiles in vegetation cover layers. *J. Appl. Meteorol.*, 20(11):1325–1335.

Avissar, R., Eloranta, E. W., Gürer, K., and Tripoli, G. J. (1998). An evaluation of the large-eddy simulation option of the regional atmospheric modeling system in simulating a convective boundary layer: a FIFE case study. *J. Atmos. Sci.*, 55(7):1109–1130.

Avissar, R. and Pielke, R. A. (1989). A parameterization of heterogeneous land surfaces for atmospheric numerical models and its impact on regional meteorology. *Mon. Weather Rev.*, 117(10):2113–2136.

Bailey, B. N., Overby, M., Willemsen, P., Pardyjak, E. R., Mahaffee, W. F., and Stoll, R. (2014). A scalable plant-resolving radiative transfer model based on optimized GPU ray tracing. *Agric. For. Meteorol.*, 198:192–208.

Banerjee, T., De Roo, F., and Mauder, M. (2017). Explaining the convector effect in canopy turbulence by means of large-eddy simulation. *Hydrol. Earth. Syst. Sci.*, pages 1–20.

Banerjee, T., Katul, G., Fontan, S., Poggi, D., and Kumar, M. (2013). Mean flow near edges and within cavities situated inside dense canopies. *Boundary-Layer Meteorol.*, 149(1):19–41.

Belcher, S. E., Harman, I. N., and Finnigan, J. J. (2012). The wind in the willows: flows in forest canopies in complex terrain. *Annu. Rev. Fluid Mech.*, 44:479–504.

Belcher, S. E., Jerram, N., and Hunt, J. C. R. (2003). Adjustment of a turbulent boundary layer to a canopy of roughness elements. *J. Fluid. Mech.*, 488:369–398.

Bou-Zeid, E., Meneveau, C., and Parlange, M. B. (2004). Large-eddy simulation of neutral atmospheric boundary layer flow over heterogeneous surfaces: Blending height and effective surface roughness. *Water Resour. Res.*, 40(2).

Brown, K. W. and Covey, W. (1966). The energy-budget evaluation of the micrometeorological transfer processes within a cornfield. *Agric. Meteorol.*, 3(1-2):73–96.

Brugger, P., Banerjee, T., De Roo, F., Kröniger, K., Qubaja, R., Rohatyn, S., Rotenberg, E., Tatarinov, F., Yakir, D., Yang, F., and Mauder, M. (2018). Effect of surface heterogeneity on the boundary layer height: a case study at a semi-arid forest. *Boundary-Layer Meteorol.*, (In press).

Brutsaert, W. (1998). Land-surface water vapor and sensible heat flux: Spatial variability, homogeneity, and measurement scales. *Water Resour. Res.*, 34(10):2433–2442.

Buckingham, E. (1915). The principle of similitude. *Nature*, 96(2406):396.

Cadenasso, M. L. and Pickett, S. T. A. (2000). Linking forest edge structure to edge function: mediation of herbivore damage. *J. Ecol.*, 88(1):31–44.

Cassiani, M., Katul, G. G., and Albertson, J. D. (2008). The effects of canopy leaf area index on airflow across forest edges: Large-eddy simulation and analytical results. *Boundary-Layer Meteorol.*, 126(3):433–460.

Cava, D. and Katul, G. G. (2012). On the scaling laws of the velocity-scalar cospectra in the canopy sublayer above tall forests. *Boundary-Layer Meteorol.*, 145(2):351–367.

Chen, J., Franklin, J. F., and Spies, T. A. (1993). Contrasting microclimates among clearcut, edge, and interior of old-growth douglas-fir forest. *Agric. For. Meteorol.*, 63(3-4):219–237.

Corrsin, S. (1951). On the spectrum of isotropic temperature fluctuations in an isotropic turbulence. *J. Appl. Phys.*, 22(4):469–473.

Dalpé, B. and Masson, C. (2009). Numerical simulation of wind flow near a forest edge. *J. Wind Eng. Ind. Aerodyn.*, 97(5-6):228–241.

de Vrese, P. and Hagemann, S. (2016). Explicit representation of spatial subgrid-scale heterogeneity in an ESM. *J. Hydrometeorol.*, 17(5):1357–1371.

de Vrese, P., Schulz, J.-P., and Hagemann, S. (2016). On the representation of heterogeneity in land-surface–atmosphere coupling. *Boundary-Layer Meteorol.*, 160(1):157–183.

Dupont, S., Bonnefond, J.-M., Irvine, M. R., Lamaud, E., and Brunet, Y. (2011). Long-distance edge effects in a pine forest with a deep and sparse trunk space: In situ and numerical experiments. *Agric. For. Meteorol.*, 151(3):328–344.

Dupont, S. and Brunet, Y. (2008). Edge flow and canopy structure: A large-eddy simulation study. *Boundary-Layer Meteorol.*, 126(1):51–71.

Eder, F., De Roo, F., Rotenberg, E., Yakir, D., Schmid, H. P., and Mauder, M. (2015). Secondary circulations at a solitary forest surrounded by semi-arid shrubland and their impact on eddy-covariance measurements. *Agric. For. Meteorol.*, 211-212:115–127.

Foken, T. (2006). 50 years of the Monin–Obukhov similarity theory. *Boundary-Layer Meteorol.*, 119(3):431–447.

Fujita, T. (1986). Mesoscale classifications: their history and their application to forecasting. In *Mesoscale Meteorol. Forecast.*, pages 18–35. Springer.

Garcia-Carreras, L., Parker, D. J., and Marsham, J. H. (2011). What is the mechanism for the modification of convective cloud distributions by land surface–induced flows? *J. Atmos. Sci.*, 68(3):619–634.

Garcia-Carreras, L., Parker, D. J., Taylor, C. M., Reeves, C. E., and Murphy, J. G. (2010). Impact of mesoscale vegetation heterogeneities on the dynamical and thermodynamic properties of the planetary boundary layer. *J. Geophys. Res. Atmos.*, 115(D3).

Garratt, J. R. (1994). The atmospheric boundary layer. *Earth-Science Rev.*, 37(1-2):89–134.

Harman, I. N. and Finnigan, J. J. (2007). A simple unified theory for flow in the canopy and roughness sublayer. *Boundary-Layer Meteorol.*, 123(2):339–363.

Hechtel, L. M., Stull, R. B., and Moeng, C.-H. (1990). The effects of nonhomogeneous surface fluxes on the convective boundary layer: A case study using large-eddy simulation. *J. Atmos. Sci.*, 47(14):1721–1741.

Huang, H.-Y. and Margulis, S. A. (2009). On the impact of surface heterogeneity on a realistic convective boundary layer. *Water Resour. Res.*, 45(4).

Huang, H.-Y. and Margulis, S. A. (2010). Evaluation of a fully coupled large-eddy simulation–land surface model and its diagnosis of land-atmosphere feedbacks. *Water Resour. Res.*, 46(6).

Jackson, P. S. and Hunt, J. C. R. (1975). Turbulent wind flow over a low hill. *Quart. J. Roy. Meteorol. Soc.*, 101(430):929–955.

Kanani, F., Träumer, K., Ruck, B., and Raasch, S. (2014). What determines the differences found in forest edge flow between physical models and atmospheric measurements? – an LES study. *Meteorol. Z.*, 23(1):33–49.

Kanani-Sühring, F. and Raasch, S. (2014). Spatial variability of scalar concentrations and fluxes downstream of a clearing-to-forest transition: A large-eddy simulation study. *Boundary-Layer Meteorol.*, 155(1):1–27.

Katul, G. G., Porporato, A., Manes, C., and Meneveau, C. (2013). Co-spectrum and mean velocity in turbulent boundary layers. *Phys. Fluids*, 25(9):091702.

Katul, G. G., Porporato, A., Shah, S., and Bou-Zeid, E. (2014). Two phenomenological constants explain similarity laws in stably stratified turbulence. *Phys. Rev. E*, 89(2):023007.

Kenny, W. T., Bohrer, G., Morin, T. H., Vogel, C. S., Matheny, A. M., and Desai, A. R. (2017). A numerical case study of the implications of secondary circulations to the interpretation of eddy-covariance measurements over small lakes. *Boundary-Layer Meteorol.*, 165(2):311–332.

King, J. C., Jrrar, A., and Connolley, W. M. (2007). Sensitivity of modelled atmospheric circulation to the representation of stable boundary layer processes. *Geophys. Res. Lett.*, 34(6).

Kolmogorov, A. N. (1941). The local structure of turbulence in incompressible viscous fluid for very large Reynolds numbers. In *Dokl. Akad. Nauk SSSR*, volume 30, pages 299–303.

Koster, R. D. and Suarez, M. J. (1992). A comparative analysis of two land surface heterogeneity representations. *J. Clim.*, 5(12):1379–1390.

Kröniger, K., Banerjee, T., De Roo, F., and Mauder, M. (2018a). Flow adjustment inside homogeneous canopies after a leading edge–An analytical approach backed by LES. *Agric. For. Meteorol.*, 255:17–30. Honoring W.J. Massman's Discoveries: Bringing Physics to Agriculture.

Kröniger, K., De Roo, F., Brugger, P., Huq, S., Banerjee, T., Zinsser, J., Rotenberg, E., Yakir, D., Rohatyn, S., and Mauder, M. (2018b). Effect of secondary circulations on surface–atmosphere exchange of energy at an isolated semi-arid forest. *Boundary-Layer Meteorol.*

Kröniger, K., Katul, G. G., De Roo, F., Brugger, P., and Mauder, M. (2018c). Aerodynamic resistance parametrization for heterogeneous surfaces using structural function approaches. *J. Atmos. Sci.*, (under review).

Launiainen, S., Katul, G. G., Grönholm, T., and Vesala, T. (2013). Partitioning ozone fluxes between canopy and forest floor by measurements and a multi-layer model. *Agric. For. Meteorol.*, 173:85–99.

Liu, S., Lu, L., Mao, D., and Jia, L. (2007). Evaluating parameterizations of aerodynamic resistance to heat transfer using field measurements. *Hydrol. Earth Syst. Sci.*, 11(2):769–783.

Mahrt, L. (1996). The bulk aerodynamic formulation over heterogeneous surfaces. *Boundary-Layer Meteorol.*, 78:87–119.

Maronga, B., Gryschka, M., Heinze, R., Hoffmann, F., Kanani-Sühring, F., Keck, M., Ketelsen, K., Letzel, M. O., Sühring, M., and Raasch, S. (2015). The parallelized large-eddy simulation model (PALM) version 4.0 for atmospheric and oceanic flows: model formulation, recent developments, and future perspectives. *Geosci. Model Dev.*, 8(8):2515–2551.

Maronga, B. and Raasch, S. (2013). Large-eddy simulations of surface heterogeneity effects on the convective boundary layer during the LITFASS-2003 experiment. *Boundary-Layer Meteorol.*, 146(1):17–44.

Massman, W. (1987). A comparative study of some mathematical models of the mean wind structure and aerodynamic drag of plant canopies. *Boundary-Layer Meteorol.*, 40(1-2):179–197.

Massman, W. (1997). An analytical one-dimensional model of momentum transfer by vegitation of arbitrary structure. *Boundary-Layer Meteorol.*, 83(3):407–421.

Matsuda, K., Onishi, R., and Takahashi, K. (2017). Tree-crown-resolving large-eddy simulation coupled with three-dimensional radiative transfer model. *J. Wind Eng. Ind. Aerodyn.*, 173:53–66.

Miller, N. E. and Stoll, R. (2013). Surface heterogeneity effects on regional-scale fluxes in the stable boundary layer: Aerodynamic roughness length transitions. *Boundary-Layer Meteorol.*, 149(2):277–301.

Monin, A. S. and Obukhov, A. M. F. (1954). Basic laws of turbulent mixing in the surface layer of the atmosphere. *Contrib. Geophys. Inst. Acad. Sci. USSR*, 151(163):e187.

Monteith, J. (1965). Evaporation and environment. The state and movement of water in living organisms. Symposium of the society of experimental biology, volume 19 (pp. 205-234).

Oke, T. R. (1982). The energetic basis of the urban heat island. *Q. J. R. Meteorol. Soc.*, 108(455):1–24.

Orlanski, I. (1975). A rational subdivision of scales for atmospheric processes. *Bull. Am. Meteorol. Soc.*, pages 527–530.

Patton, E. G., Sullivan, P. P., and Moeng, C.-H. (2005). The influence of idealized heterogeneity on wet and dry planetary boundary layers coupled to the land surface. *J. Atmos. Sci.*, 62(7):2078–2097.

Penman, H. L. (1948). Natural evaporation from open water, bare soil and grass. *Proc. R. Soc. Lond. A*, 193(1032):120–145.

Pielke, S. and Roger, A. (2013). *Mesoscale meteorological modeling*, volume 98. Academic press.

Pope, S. (2000). *Turbulent Flows*. p. 771. Cambridge University Press, Cambridge, UK.

Prabha, T. V., Karipot, A., and Binford, M. W. (2007). Characteristics of secondary circulations over an inhomogeneous surface simulated with large-eddy simulation. *Boundary-Layer Meteorol.*, 123(2):239–261.

Raasch, S. and Schröter, M. (2001). PALM–a large-eddy simulation model performing on massively parallel computers. *Meteorol. Z.*, 10(5):363–372.

Raupach, M. R. and Finnigan, J. J. (1995). Scale issues in boundary-layer meteorology: Surface energy balances in heterogeneous terrain. *Hydrol. Proc.*, 9(5-6):589–612.

Ross, A. N. and Baker, T. P. (2013). Flow over partially forested ridges. *Boundary-Layer Meteorol.*, 146(3):375–392.

Rotenberg, E. and Yakir, D. (2010). Contribution of semi-arid forests to the climate system. *Science*, 327(5964):451–454.

Rotenberg, E. and Yakir, D. (2011). Distinct patterns of changes in surface energy budget associated with forestation in the semiarid region. *Glob. Change Biol.*, 17(4):1536–1548.

Saddoughi, S. G. and Veeravalli, S. V. (1994). Local isotropy in turbulent boundary layers at high Reynolds number. *J. Fluid Mech.*, 268:333–372.

Schlegel, F., Stiller, J., Bienert, A., Maas, H.-G., Queck, R., and Bernhofer, C. (2012). Large-eddy simulation of inhomogeneous canopy flows using high resolution terrestrial laser scanning data. *Boundary-Layer Meteorol.*, 142(2):223–243.

Schlegel, F., Stiller, J., Bienert, A., Maas, H.-G., Queck, R., and Bernhofer, C. (2015). Large-eddy simulation study of the effects on flow of a heterogeneous forest at sub-tree resolution. *Boundary-Layer Meteorol.*, 154(1):27–56.

Shaw, R. H. and Patton, E. G. (2003). Canopy element influences on resolved-and subgrid-scale energy within a large-eddy simulation. *Agric. For. Meteorol.*, 115(1-2):5–17.

Shaw, R. H. and Schumann, U. (1992). Large-eddy simulation of turbulent flow above and within a forest. *Boundary-Layer Meteorol.*, 61(1-2):47–64.

Spiegel, E. A. (2010). *The Theory of Turbulence: Subrahmanyan Chandrasekhar's 1954 Lectures*, volume 810. Springer, Dordrecht.

Sprintsin, M., Karnieli, A., Berliner, P., Rotenberg, E., Yakir, D., and Cohen, S. (2007). The effect of spatial resolution on the accuracy of leaf area index estimation for a forest planted in the desert transition zone. *Remote Sens. Environ.*, 109(4):416–428.

Stoll, R. and Porté-Agel, F. (2009). Surface heterogeneity effects on regional-scale fluxes in stable boundary layers: surface temperature transitions. *J. Atmos. Sci.*, 66(2):412–431.

Thom, A. (1971). Momentum absorption by vegetation. *Q. J. R. Meteorol. Soc.*, 97(414):414–428.

Townsend, A. A. (1972). Flow in a deep turbulent boundary layer over a surface distorted by water waves. *J. Fluid Mech.*, 55(4):719–735.

Townsend, A. A. (1976). *The structure of turbulent shear flow*. Cambridge university press, Cambridge, UK, 2nd ed. edition.

Trakhtenbrot, A., Katul, G. G., and Nathan, R. (2014). Mechanistic modeling of seed dispersal by wind over hilly terrain. *Ecol. Modell.*, 274:29–40.

Verma, S. B. (1990). Micrometeorological methods for measuring surface fluxes of mass and energy. *Remote Sens. Rev.*, 5(1):99–115.

Wang, W. (2009). The influence of thermally-induced mesoscale circulations on turbulence statistics over an idealized urban area under a zero background wind. *Boundary-Layer Meteorol.*, 131(3):403–423.

Watanabe, T. (2004). Large-eddy simulation of coherent turbulence structures associated with scalar ramps over plant canopies. *Boundary-Layer Meteorol.*, 112(2):307–341.

Yang, B., Morse, A. P., Shaw, R. H., and U, K. T. P. (2006). Large-eddy simulation of turbulent flow across a forest edge. Part II: Momentum and turbulent kinetic energy budgets. *Boundary-Layer Meteorol.*, 121(3):433–457.

Appendices

A | Individual contributions to the joint publications

This thesis is presented in cumulative form and consists of three publications that were composed together with other researchers. Within this chapter, the contributions of the different authors are specified, where the first paragraph highlights my own contribution and the second paragraph the contribution of the other authors for every single manuscript.

Appendix B

Kröniger, K., Banerjee, T., De Roo, F., and Mauder, M. (2018). Flow adjustment inside homogeneous canopies after a leading edge–An analytical approach backed by LES. *Agric. For. Meterorol.*, 255:17–30. Honoring W.J. Massman's Discoversies: Bringing Physics to Agriculture, doi: 10.1016/j.agrformet.2017.09.019

I came up with the basic idea of solving the two-dimensional governing equations of canopy-edge flow using the separability approach and performed all analytical derivations, corresponding to the canopy-edge-flow model. Besides, I designed and performed the LES and conducted the comparisons of the model with the LES results and the Belcher et al. (2003) model. I also wrote the first version of the entire manuscript.

Tirtha Banerjee motivated me to investigate leading canopy edges, referring to Banerjee et al. (2013), were canopy-edge flow was studied by means of LES. Tirtha Banerjee also brought up the idea of extending the adjustment region model to a model of the full canopy. From this discussion, the method of combining the adjustment region model with the model of Massman (1997) originated. Frederik De Roo cross-checked my LES set-up and every single line of the derivation and gave important comments on the presentation of the derivation within the manuscript. Besides, Tirtha Banerjee, Frederik De Roo, and Matthias Mauder contributed through various correction and comments to improve the writing of the manuscript. They also provided me a lot of literature concerning flow across leading canopy edges.

Appendix C

Kröniger, K., De Roo, F., Brugger, P., Huq, S., Banerjee, T., Zinsser, J., Rotenberg, E., Yakir, D., Rohatyn, S., and Mauder, M. (2018). Effect of secondary circulations on surface–atmosphere exchange of energy at an isolated semi-arid forest. *Boundary-Layer Meteorol.*, doi: 10.1007/s10546-018-0370-6

I designed the LES set-up and wrote a proposal to the super-computing facility SuperMUC to apply for core hours. Besides, I performed the simple mapping of the satellite image to the PAD and $\overline{Q}_{h_c}$ maps. I also analysed the LES data, performed the comparison to the measured lidar profiles, selected the cross-section locations, and conducted the aerodynamic resistance comparison. Besides, I wrote the entire first version of the manuscript.

Frederik De Roo helped me with the proposal to SuperMUC, cross-checked the LES set-up and provided many comments concerning the performed LES along the way. Sadiq Huq helped a lot with problems concerning compiling/data output and managed to get to run PALM at SuperMUC at the desired number of grid cells. Peter Brugger performed the measurement campaign in 2015, with the help of Eyal Rotenberg, Dan Yakir, Shani Rohatyn, and Matthias Mauder. Peter Brugger also performed the measurement campaign in 2016 together with Judith Zinsser, which was again supported by Eyal Rotenberg and Dan Yakir. Besides, Frederik De Roo, Peter Brugger, Tirtha Banerjee, and Matthias Mauder helped improving the manuscript by multiple comments and corrections.

Appendix D

Kröniger, K., Katul, G. G., De Roo, F., Brugger, P., and Mauder, M. (2018). Aerodynamic resistance parametrization for heterogeneous surfaces using structural function approaches. *J. Atmos. Sci.*, (under review)

I performed the entire analytic derivation, including setting up of the covariance-function approach and the derivation of the aerodynamic resistance from this method. I also performed all LES to compare the several aerodynamic resistance parametrizations, and conducted the whole analysis connected to this comparison. Besides, I wrote the entire first draft of the manuscript.

Gabriel G. Katul came up with the idea to employ the homogeneous structure functions of Katul et al. (2014) and to combine them with the surface heterogeneity in spectral space. Gabriel G. Katul also cross-checked all equations in the derivation of the aerodynamic resistance, together with Frederik De Roo. Gabriel G. Katul, Frederik De Roo, Peter Brugger, and Matthias Mauder helped me with improving the writing of the manuscript through multiple comments and corrections. Gabriel G. Katul also intended adding Fig. 5 to quantify the heterogeneity of the investigated test cases.

B | Flow adjustment inside homogeneous canopies after a leading edge–An analytical approach backed by LES

Kröniger, K., Banerjee, T., De Roo, F., and Mauder, M. (2018). Flow adjustment inside homogeneous canopies after a leading edge–An analytical approach backed by LES. *Agric. For. Meterorol.*, 255:17–30. Honoring W.J. Massman's Discoversies: Bringing Physics to Agriculture, doi: 10.1016/j.agrformet.2017.09.019

Agricultural and Forest Meteorology 255 (2018) 17–30

Contents lists available at ScienceDirect

Agricultural and Forest Meteorology

journal homepage: www.elsevier.com/locate/agrformet

Flow adjustment inside homogeneous canopies after a leading edge – An analytical approach backed by LES

Konstantin Kröniger[a,*], Tirtha Banerjee[a,b], Frederik De Roo[a], Matthias Mauder[a]

[a] Institute of Meteorology and Climate Research, Atmospheric Environmental Research (IMK-IFU), Karlsruhe Institute of Technology (KIT), Kreuzeckbahnstrasse 19, 82467 Garmisch-Partenkirchen, Germany

[b] Current affiliation: Earth and Environmental Sciences Division, Los Alamos National Laboratory, Los Alamos, New Mexico, USA

ARTICLE INFO

Keywords:
Canopy edge
Analytical model
Adjustment region
Large eddy simulations

ABSTRACT

A two-dimensional analytical model for describing the mean flow behavior inside a vegetation canopy after a leading edge in neutral conditions was developed and tested by means of large eddy simulations (LES) employing the LES code PALM. The analytical model is developed for the region directly after the canopy edge, the adjustment region, where one-dimensional canopy models fail due to the sharp change in roughness. The derivation of this adjustment region model is based on an analytic solution of the two-dimensional Reynolds averaged Navier–Stokes equation in neutral conditions for a canopy with constant plant area density (PAD). The main assumptions for solving the governing equations are separability of the velocity components concerning the spatial variables and the neglection of the Reynolds stress gradients. These two assumptions are verified by means of LES. To determine the emerging model parameters, a simultaneous fitting scheme was applied to the velocity and pressure data of a reference LES simulation. Furthermore a sensitivity analysis of the adjustment region model, equipped with the previously calculated parameters, was performed varying the three relevant length, the canopy height (h), the canopy length and the adjustment length (L_c), in additional LES. Even if the model parameters are, in general, functions of h/L_c, it was found out that the model is capable of predicting the flow quantities in various cases, when using constant parameters. Subsequently the adjustment region model is combined with the one-dimensional model of Massman [*Bound. Layer Meteorol.*, 83(3):407–421, 1997], which is applicable for the interior of the canopy, to attain an analytical model capable of describing the mean flow for the full canopy domain. Finally the model is tested against an analytical model based on a linearization approach.

1. Introduction

In canopy turbulence, flow across edges and clearings is a field of particular interest, as the largest perturbations in the flow quantities can be encountered in the vicinity of such sharp transitions in surface roughness (Belcher et al., 2012). As pointed out by Dupont and Brunet (2008), these perturbations can influence the flow over distances of several tree heights downwind from canopy edges. Therefore, measurements inside and above canopies, e.g. of scalar fluxes like greenhouse gases, can also be influenced by edges over similar distances (Kanani-Sühring and Raasch, 2014). Due to the fact that these measurements mainly rely on the eddy covariance (EC) technique, heterogeneities in the measurement footprint play an even more important role, due to the requirements of the standard EC technique (Aubinet et al., 2012; Burba, 2013). While the effects of forest edges on flux measurements were already investigated in several studies (Chen et al., 1993; Cadenasso and Pickett, 2000; Dupont et al., 2011) stated that one key issue for interpreting flux measurement near to edges is the distance required by the flow to fully adjust with the canopy, which depends on the character of turbulent flow inside of the canopy.

To investigate turbulent flow inside canopies and close to canopy-edges, various approaches have been used in the past. While canopy-edge scenarios were mainly investigated by the comparison of numerical studies to wind tunnel measurements (Dupont and Brunet, 2008), field experiments (Dalpé and Masson, 2009; Schlegel et al., 2012; Kanani et al., 2014) or both (Yang et al., 2006; Banerjee et al., 2013), the number of analytical investigations is smaller. However, interpretation of EC measurements could benefit from the prediction of analytical models for the influence of edges at the measurement location. Apart from that, the determination of properties like the aerodynamic resistance of heterogeneous canopies can benefit from analytical models, as approaches for homogeneous canopies, like the one of

* Corresponding author.
E-mail address: konstantin.kroeniger@kit.edu (K. Kröniger).

http://dx.doi.org/10.1016/j.agrformet.2017.09.019
Received 17 November 2016; Received in revised form 4 September 2017; Accepted 24 September 2017
Available online 06 October 2017

Yang et al. (2001), might fail for canopies, which are mainly under the influence of edges.

Concerning analytical investigations of canopy flow, several studies, based on one-dimensional approaches were performed (Massman, 1987, 1997; Harman and Finnigan, 2007). These models, which are applicable for horizontally homogenous condition, resulted in the analytical solution of an exponentially decaying velocity profile inside the canopy. However these one-dimensional approaches are too limited to describe the effect of forest edge flow.

Improvements towards a two-dimensional analytical model were made by Belcher et al. (2003), where the governing flow equations were linearized on small perturbations, added to an incoming logarithmic velocity profile. The advantage of this approach was that the mean velocities could be calculated for all distinct regions of the canopy-edge-flow-scenario.

These regions are shown in Fig. D.1, where (i) labels the impact region before the edge, (ii) the adjustment region shortly past the edge, (iii) the canopy interior behind the adjustment region, (iv) the canopy shear layer located around the canopy top and (v) the roughness change region above the canopy. The adjustment region, where the unperturbed flow adapts to the canopy, and the canopy interior, where the flow has fully adapted to the canopy, are the two regions of major interest in the following work.

An essential ingredient of the linearization approach is the much smaller magnitude of the velocity perturbations in comparison to the incoming wind profile. As Belcher et al. (2003) stated, this translates to the requirement of a canopy that is either sparse or short enough that the flow is never able to fully adjust to it.

The aim of the presented work is to overcome this issue of a linearization approach. Therefore we derived an analytic solution to the governing flow equations in the adjustment region, where one-dimensional models fail. Studying the aforementioned adjustment zone is of interest, as a plethora of applications rely on the flow within this region. These applications include seed and pollen dispersal from adjacent areas into the canopy zone and conversely (Trakhtenbrot et al., 2014), determination of forest-floor fluxes of CO_2 or O_3 using micrometeorological methods (Launiainen et al., 2013), or separating aerosol-sized particle deposition onto foliage and forest floor in patchy forested environments (Grönholm et al., 2009; Huang et al., 2014; Katul et al., 2010), to name a few.

The analytical solution was developed for a neutral canopy-stripe-scenario in a predefined background wind, where the canopy stripe is homogeneous in crosswind direction (two-dimensional scenario) and is, therefore, defined by three length scales, the canopy length L, the canopy height h and the adjustment length scale L_c, which are also depicted in Fig. D.1. The adjustment length scale can be used to describe the width of the adjustment region, which can reach an extension of up to $15L_c$ (Dupont and Brunet, 2008).

Besides gaining a functional description of the velocity components and the pressure, another important outcome of the presented analytical investigation is the insight on the interplay of the three involved length scales L, h and L_c.

To determine the occurring model parameters (integration constants) a large eddy simulation (LES) of a reference canopy was performed employing the LES code PALM (Maronga et al., 2015). In Section 4, the analytical model for the adjustment region, equipped with these parameters, is subsequently tested on variations of the three defining length scales by performing further LES.

To gain an analytical model for the full range of the canopy and to deduce an expression for the length of the adjustment region, subsequently the adjustment region model was combined with the model of Massman (1997) for the canopy interior.

Finally the current model is compared with the model of Belcher et al. (2003) for increasing length L of the investigated canopy.

2. Derivation

2.1. Background

The basis of the subsequent analytical investigation of flow across a canopy edge are the Reynolds averaged continuity and momentum equation for an incompressible 2D flow when neglecting Coriolis and buoyancy effects (neutral case) within a canopy

$$\partial_i u_i = 0, \tag{1}$$

$$\partial_t u_i + \partial_j (u_i u_j) = -\frac{1}{\rho}\partial_i p + \partial_j \tau_{ij} - F_{di}, \tag{2}$$

where u_i is the mean velocity component in direction x_i, $\partial_j(u_i u_j)$ describes the advection of the flow field, ρ the mean fluid density, p the mean perturbation of the hydrostatic pressure, τ_{ij} the Reynolds stress tensor and F_{di} the drag force, the latter modeling the effect of the canopy on the flow. The drag force is defined according to Shaw and Schumann (1992) and Watanabe (2004) as

$$F_{di} = 1/L_c \|\vec{u}\| u_i \Theta(x/h)\Theta(1 - z/h), \tag{3}$$

where the adjustment length scale is defined following Belcher et al. (2003, 2012) through $L_c = 1/(C_d a)$ with the drag coefficient C_d and the PAD a, $\|\vec{u}\|$ is the wind speed, $x = x_1$, $z = x_3$ and Θ is the Heaviside step function ensuring the drag force to be zero outside of the canopy. The definition of the drag force, presented here, describes a canopy with constant canopy height h and with a canopy-edge located at $x = 0$.

To simplify the analysis a constant a was considered throughout the canopy, defined by

$$a = \mathrm{PAI}/h \tag{4}$$

with the canopy height h and the plant area index PAI.

Focusing on a steady state scenario, the flow quantities were considered to be time independent ($\partial_t u_i = 0$). Therefore, Eqs. (1) and (2) in terms of the velocity components $u = u_1$ and $w = u_3$ inside the canopy are given by

$$\partial_x u + \partial_z w = 0 \tag{5}$$

$$\partial_x u^2 + \partial_z (uw) = -\frac{1}{\rho}\partial_x p + \partial_j \tau_{1j} - \frac{1}{L_c}\left\|\vec{u}\right\| u \tag{6}$$

$$\partial_x (uw) + \partial_z w^2 = -\frac{1}{\rho}\partial_z p + \partial_j \tau_{3j} - \frac{1}{L_c}\left\|\vec{u}\right\| w \tag{7}$$

Following the argument of Belcher et al. (2003), which relies on Townsend (1972) and Jackson and Hunt (1975), it becomes apparent that the Reynolds stress gradients have just a small impact in Eqs. (6) and (7) when compared to the remaining terms. In Appendix A this assumption is proven by comparing the magnitudes of the several terms for a LES of a canopy stripe with $h = 10$ m and $L_c = 16.7$ m, showing that the gradients of the Reynolds stress are mostly smaller than 5% of the residual terms. Therefore the Reynolds stress gradient terms will be neglected in Eqs. (6) and (7) in the subsequent investigations, which results in a turbulently inviscid scenario (Banerjee et al., 2013). Furthermore, following Banerjee et al. (2013), the pressure was eliminated from these two equations by computing their curl, which finally results in

$$\partial_x \partial_z u^2 + \partial_z^2 (uw) - \partial_x^2 (uw) - \partial_x \partial_z w^2 + 1/L_c [\partial_z (\|\vec{u}\| u) - \partial_x (\|\vec{u}\| w)] = 0. \tag{8}$$

To non-dimensionalize the spatial variables x/z, they were re-scaled by h through the introduction of the new variables x and z by

$$x = x/h \quad \text{and} \quad z = z/h \tag{9}$$

Rewriting Eqs. (5) and (8), in these re-scaled quantities gives

$$\partial_x u + \partial_z w = 0, \tag{10}$$

$$\partial_x\partial_z u^2 + \partial_z^2(uw) - \partial_x^2(uw) - \partial_x\partial_z w^2 + \alpha\partial_z(\|\vec{u}\|u) - \alpha\partial_x(\|\vec{u}\|w) = 0, \tag{11}$$

where $\alpha = h/L_c$. h was selected for the re-scaling, on the one hand, as it is the natural length scale for normalizing distances inside a canopy, one the other hand, as this re-scaling allows for the elimination of h from the drag force term (inside the Heaviside step function), yielding a canopy defined for $z \in [0;1]$.

2.2. Analytic derivation of the adjustment region flow field

The following discussion is based on the finding that the vertical profiles of the velocity component w are approximately described by a constant function multiplied with a x-dependent scaling factor for heights below the shear layer. This behavior is depicted in Fig. D.2, where the vertical profiles of w at distances of $2h$, $3h$, $4h$ and $5h$ from the canopy edge for the LES with $h = 10$ m and $L_c = 16.7$ m are shown. This observation justifies separation of variables w

$$w(x, z) = -f'(x)g(z), \tag{12}$$

where f and g are solely dependent on x and z and the prime denotes a total derivative of the respective function. The boundary condition $w(x, z = 0) = 0$ implies that $g(0) = 0$. Applying the continuity equation, $u(x, z)$ can be determined

$$u(x, z) = f(x)g'(z) + g_\infty(z), \tag{13}$$

where g_∞ is solely depending on z. As shown in several publications (Raupach et al., 1987; Dupont and Brunet, 2008), the u-profile inside the canopy approaches a horizontally constant value, which also justifies the one-dimensional approach of Massman (1997) for the canopy interior. Transferring this knowledge to Eq. (13) results in $\lim_{x\to\infty} u(x, z) = g_\infty(z)$, as the x-dependence of u has to vanish for large values of x. Therefore g_∞ can be seen as the vertical u-profile in the canopy interior. However it was only possible to deduce an analytical solution assuming $g_\infty = 0$, which turns out to be a sufficient approximation in the adjustment region. This finding can be explained by the derivation of Massman (1997), where the vertical gradient of the Reynolds stress tensor component τ_{13} is of major importance for the calculation of the u-profile. However, as stated in the previous section, the gradients of τ_{ij} can be neglected in the adjustment region, which justifies neglecting of g_∞ in Eq. (13).

Additionally it is assumed that the horizontal wind component, is much larger than the vertical wind component, w, in the adjustment region.

$$|u| >> |w| \tag{14}$$

This assumption is realistic, as the mean wind component w is mostly more than one order of magnitude smaller than the mean wind component u for the investigated neutral scenario. This assumption on the velocity components allows to apply a power-series expansion in w to the drag force.

$$\begin{aligned} F_{d1} &= \|\vec{u}\|u = \sqrt{1 + (w/u)^2}\; u^2 \simeq u^2 + \tfrac{1}{2}w^2 + \mathcal{O}(w^3) \\ F_{d2} &= \|\vec{u}\|w = \sqrt{1 + (w/u)^2}\; uw \simeq uw + \mathcal{O}(w^3) \end{aligned} \tag{15}$$

Using this expansion for the drag force and the decomposition of u and w in f and g functions in Eq. (11) gives

$$-ff'gg'' + (ff' + 2\alpha f^2)g'g'' + (ff'' - f'f'' + \alpha(ff'' + 2(f')^2))gg' = 0. \tag{16}$$

One z-integration can be applied to this equation, yielding

$$-ff'gg' + (ff' + \alpha f^2)(g')^2 + \frac{1}{2}(ff'' - f'f'' + \alpha(ff'' + 2(f')^2))g^2 = C(x), \tag{17}$$

where C is a purely x-dependent function originating from the z-integration. This function can be determined using the boundary condition $g(0) = 0$, which results in

$$C(x) = (ff' + \alpha f^2)(g'(0))^2. \tag{18}$$

Plugging this result into Eq. (17) and dividing by f^2 yields

$$-\frac{f'}{f}g'g + \left(\frac{f'}{f} + \alpha\right)((g')^2 - (g'(0))^2) + \frac{1}{2}\left(\left(\frac{f''}{f}\right)' + \alpha\frac{f''}{f} + 2\alpha\left(\frac{f'}{f}\right)^2\right)g^2 = 0. \tag{19}$$

It is found out that there exist three solutions for g which satisfy Eq. (19) and the given boundary condition. These three solutions are of sinusoidal, hyperbolic sinusoidal and linear shape. However it was also found out, when performing the fit to LES data (Section 4.1) that the three solutions in fact coincide in the modeled canopy scenarios. Therefore only the hyperbolic sine solution will be used in the subsequent derivation, while the concurrence of the three solutions for g will be discussed in Section 4.1. The hyperbolic sine solution has the form

$$g(z) = \frac{g'(0)}{a_1}\sinh(a_1 z), \tag{20}$$

where a_1 is a model parameter introduced for the sake of generality of the solution. Applying this form of g to Eq. (19) results in a differential equation for f

$$\left(\frac{f''}{f}\right)' + \alpha\frac{f''}{f} + 2\alpha\left(\frac{f'}{f}\right)^2 + 2\alpha a_1^2 = 0. \tag{21}$$

The procedure for solving this equation is presented in Appendix B. However two further approximations were needed to deduce an analytical solution. The first approximation relies on the finding that $|\partial_x^2 u/u| \gg (\partial_x u/u)^2$ in the adjustment region. An investigation of this approximation by means of LES is shown in Appendix C. The second approximation relies on the negligible magnitude of a_1 in comparison to the residual terms, which will be verified by LES in Section 4.1.

The final solution of Eq. (21) for f is given by

$$f(x) = f_s\exp(-a_2 x - a_3/\alpha^2 e^{-\alpha x}) \equiv f_s F(x), \tag{22}$$

where f_s, a_2 and a_3 are integration constants and the x-dependent function $F(x)$ is introduced to reduce the complexity of the final expressions. Plugging in the expressions for f and g into Eqs. (12) and (13) finally gives u and w.

$$u(x, z) = u_s F(x)\cosh(a_1 z), \tag{23}$$

$$w(x, z) = u_s(a_2 - a_3/\alpha\; e^{-\alpha x})F(x)\sinh(a_1 z)/a_1, \tag{24}$$

where $u_s \equiv f_s g'(0)$ is the velocity scale.

As the inflow in the discussed scenario is oriented in positive x-direction, the horizontal velocity component u has to be positive at the canopy edge. Therefore u_s also has to be positive, due to Eq. (23) and the functional expression of $F(x)$. However, from the expression of $F(x)$ it then also follows that $u > 0$ in the full adjustment region.

A positive value of u inside the canopy is a valid prediction, as long as no re-circulation develops, as this can lead to negative u-values. The dimension and strength of these re-circulation zones are highly dependent on factors like canopy drag coefficient, PAI and PAD shape. While Dalpé and Masson (2009) and Dupont et al. (2011) showed that re-circulation zones are strongly suppressed for canopies with a shallow trunk space, also scenarios with constant or nearly constant PAD profiles were investigated. Cassiani et al. (2008) found out that for dense canopies with PAI $\geq 6\ \mathrm{m^2 m^{-2}}$ re-circulations start to develop at distances of approximately 10–15h from the canopy edge. This result is in line with the work of Dupont and Brunet (2008), where no re-circulation zones were spotted for PAI $\leq 5\ \mathrm{m^2 m^{-2}}$. On the other hand, Ross and Baker (2013), which were investigating flow over partially forested ridges already found re-circulations for PAI $\approx 3\ \mathrm{m^2 m^{-2}}$, but again in

distances of $\sim 10h$ from the canopy edge. However Ross and Baker (2013) also stated, that the re-circulation effects might be dependent on the used model turbulence scheme next to the details of the canopy structure. All the investigations mentioned before were performed with approximately the same values for h and C_d as in the current work.

Due to the discussion above, it can be seen that the $u > 0$ assumption of the current model works for moderate canopies. However for very dense canopies, the current model is still able to describe the region between the edge and the onset of the re-circulation. This can be deferred from Cassiani et al. (2008), who defines the onset of a re-circulation zone in his analytical model as the point, where u starts to attain negative values, which is not included in the current model.

Having found analytical expressions for u and w, the pressure p can be computed by solving Eqs. (6) and (7), which is shown in Appendix D. The final expression is given by

$$p(x, z) = p_\infty - p_s(F^2/2 + \alpha \int_0^x d\tilde{x}\ F^2(\tilde{x})) - p_s \alpha a_2 F^2 \sinh^2(a_1 z)/2a_1^2, \tag{25}$$

where $p_s = \rho u_s^2$ is the pressure scale and p_∞ is the emerging integration constant. This constant can be defined by claiming $\lim_{x\to\infty} p = 0$, which reflects the vanishing influence of the canopy-edge when diverging from it. Therefore p_∞ is given by

$$p_\infty = p_s \alpha \int_0^\infty \mathrm{dx}\ F^2. \tag{26}$$

Plugging this expression into Eq. (25) results in

$$p(x, z)/p_s = \alpha \int_x^\infty F^2(\tilde{x}) d\tilde{x} - F^2/2 - \alpha a_2 F^2 \sinh^2(a_1 z)/2a_1^2. \tag{27}$$

To depict these analytical results, Fig. D.3 shows the graphical representation of u/u_s, w/w_s and p/p_s, where the change in line style from solid to dashed illustrates the restricted range of validity of the developed expressions, which will be discussed in Section 4. Two different coordinate scales were used as w/u_s is one order of magnitude smaller than u/u_s and p/p_s.

When investigating these final results, it is recognized that $\lim_{x\to\infty} u = 0$ and $\lim_{x\to\infty} w = 0$. Concerning the w-component this makes sense, as the influence of the canopy-edge vanishes with increasing x and a homogeneous canopy is considered. However the vanishing u-component is a direct effect of the approximation $g_\infty = 0$ and limits the applicability of the attained solutions to the adjustment region.

2.3. Model parameters

To investigate the emerging model parameters, as a first step the final results are re-scaled to the physical coordinates x and z (see Eq. (9)).

$$u(\mathrm{x}, \mathrm{z}) = u_s F(\mathrm{x}) \cosh(a_1 \mathrm{z}/h), \tag{28}$$

$$w(\mathrm{x}, \mathrm{z}) = u_s (a_2 - a_3/\alpha\ e^{-\mathrm{x}/L_c}) F(\mathrm{x}) \sinh(a_1 \mathrm{z}/h)/a_1, \tag{29}$$

$$p\left(\mathrm{x}, \mathrm{z}\right)/p_s = L_c^{-1} \int_{\mathrm{x}}^\infty F^2(\tilde{\mathrm{x}}) d\tilde{\mathrm{x}} - F^2/2 - \alpha a_2 F^2 \sinh^2\left(a_1 \mathrm{z}/h\right)/2a_1^2, \tag{30}$$

where

$$F(\mathrm{x}) = \exp(-a_2 \mathrm{x}/h - a_3/\alpha^2\ e^{-\mathrm{x}/L_c}). \tag{31}$$

The usual procedure for determining the parameters a_1, a_2 and a_3 would be the application of boundary conditions, i.e. points where the velocity components are known. Due to the fact that the equations were solved in a certain part of the total domain (i.e. the adjustment region), the only given boundary is $w(\mathrm{x}, \mathrm{z} = 0) = 0$, which was used already.

Nevertheless it can be stated that the model parameters a_1, a_2 and a_3 are in general dependent on the canopy length scales and the roughness properties of the region upstream to the canopy, where the influence of the latter is negligible for the LES performed in the presented work (Section 3.1). As a_1, a_2 and a_3 are dimensionless parameters, the dependency on the two canopy length scales h and L_c leads to a dependency on $\alpha = h/L_c$. However, it turned out that this α-dependency is quite weak, as an application of constant a_1, a_2 and a_3 already produces satisfactory results (Section 4.2). Therefore the following investigations were performed assuming α-independent parameters.

3. Methods

3.1. PALM and numerical set up

To test the developed analytical model and to determine the model parameters a_1, a_2 and a_3, numerical simulations were performed, employing the LES code PALM (version 4.0) developed at the University of Hanover. In PALM, the canopy drag force is implemented corresponding to Eq. (3), while the default-canopy-setting inserts a canopy, spanning the full model domain. Therefore, for setting up simulations on canopy-stripes, additional user code was needed. To mimic a two-dimensional scenario in x and z, these canopy-stripes were taken to be homogeneous in y-direction. While the canopy drag coefficient was set constant throughout the simulations ($C_d = 0.2$), the other canopy parameters (L, h and L_c) were varied. The simulated values of those canopy parameters are summarized in Table D.1, grouped by the corresponding section label. For the sake of modeling neutral stratification, the surface heat flux was set to 0 throughout the simulation domain, which had the dimensions of 1025 m in x, 256 m in y and 128 m in z-direction respectively. An uniform grid spacing of 1 m was taken in all spatial directions, yielding a number of $1025 \times 256 \times 128$ grid cells. In all modeled scenarios a constant geostrophic background wind $u_{bg} = 2\ \mathrm{ms}^{-1}$ was used to drive the simulations. At the top boundary, Dirichlet conditions were applied for the wind velocity and the pressure, while periodic boundary conditions were used in the horizontal directions. Due to these horizontal boundary conditions, the discussed scenario is rather a periodic series of alternating canopy stripes of width L and clearings with a width of 1025 m-L and a roughness length of 0.1 m to model grassland. As shown by Cassiani et al. (2008), the clearing width is large enough for the velocity profile to fully readjust to the grassland before entering the canopy again. A simulation time of 1 h was chosen, while the length of the time-steps, Δt, was dynamically computed using a Courant–Friedrichs–Lewy (CFL) factor of 0.90, yielding $\Delta t \approx 0.3$ s. As initial conditions $u = u_{bg}$, $w = 0$ and $p = 0$ were set throughout the simulation domain. Due to starting from these constant profiles, the system needs some time to reach a steady state. By extracting the wind components and the pressure for a sampling time of 5 s, it was found out that a time interval of half an hour is sufficient for this purpose. Therefore, the data of the first half hour was discarded. The LES-output-data of u, w and p for the second half hour was subsequently averaged in time and spatially in y.

3.2. Fitting procedure

To infer the model parameters a_1, a_2 and a_3, a simultaneous fitting scheme was developed using MATLAB (version R2015a).

The u, w and p data of the canopy region defined by $\mathrm{x} \in [0, 30h]$ and $\mathrm{z} \in [0.3h, 0.6h]$ were used as input data for the fitting procedure. An illustration of this region can be seen in Fig. D.4, where the boundaries of the canopy (canopy edge and canopy top) are depicted by black solid lines, the boundaries of the fitting region by black dotted lines. This region was selected as its x-extension ensures that the full effect of the canopy-edge is covered, while its z-boundaries were taken central inside the canopy. This is rather important as, on the one side, the analytical model is expected to become inaccurate when entering the canopy shear layer, due to the separability assumption on w, while, on the other side, the LES is expected to be deficient close to the bottom. The optimization process was subsequently implemented to simultaneously

fit Eq. (28) to u, Eq. (29) to w and Eq. (30) to p by varying u_s, a_1, a_2 and a_3 to achieve a minimal relative error between the fits and the corresponding input data in the considered region of interest. Application of the relative error, instead of the absolute error, is an important ingredient of this fitting procedure, as u/u_s and p/p_s attain values that are one order of magnitude larger than the ones of w/u_s. Therefore using the absolute error would imply w to have a lot less influence in the optimization process than u and p, while an equal partition of the three observables is favored.

4. Results and discussion

In the derivation of the analytical model for the adjustment region, two length scales were considered, the canopy height h and the adjustment length scale L_c. However, when approaching more realistic conditions, a third length scale, the elongation of the canopy in x-direction, L, enters. To be able to test the model's capability of predicting the flow quantities for varying length scales L, h and L_c, the model parameters are needed. These parameters are derived from fits of the model to the data of one selected canopy LES, which is named reference case. Subsequently the derived analytical model for the adjustment region is combined with the one-dimensional model of Massman (1997) for the canopy interior to get a model which is applicable to the full range of the canopy. Finally the current model is tested against the model of Belcher et al. (2003).

4.1. Determination of model parameters for a reference case

To compute the model parameters, the fitting procedure described in Section 3.2 was applied to a reference simulation. This simulation includes a canopy stripe defined by $L = 500$ m, $h = 10$ m and $L_c = 16.7$ m, where the last value is corresponding to PAI $= 3\ \mathrm{m^2 m^{-2}}$ and $C_d = 0.2$. The choice of C_d and PAI was motivated by the sensitivity analysis of Dalpé and Masson (2009) to insure that no re-circulation develops and, therefore, that $u > 0$ in the investigated domain. This can be also seen in Fig. D.5, where a contour plot of the horizontal velocity component u of the reference case LES is shown. The model parameters are subsequently derived by performing a simultaneous fit on the flow quantities of the reference scenario.

The parameter values are shown in Table D.2, where the small value of a_1 has to be noticed. This small value, on the one hand, justifies neglecting a_1 in the derivation of f in Appendix B and, on the other hand, allows for expanding the flow quantities in powers of a_1. Performing an expansion to first order in a_1 gives $\sinh(a_1 z/h)/a_1 \to z/h$ and $\cosh(a_1 z/h) \to 1$, resulting in a z-independent u in the adjustment region. As mentioned in Section 2.2, there exist two other solutions for the basic Eq. (19), a sinusoidal and a linear one. Due to the fact that $\sin(a_1 z/h)/a_1 \to z/h$ and $\cos(a_1 z/h) \to 1$ when expanding to first order in a_1, the sinusoidal and the hyperbolic sinusoidal solutions both converge to a linear solution, which leads to a concurrence of the three solutions in the limit of small a_1 and therefore justifies the approach of selecting only one of them for the analytical derivation.

In Fig. D.6 the three horizontal LES-profiles (at height levels $0.3h$, $0.4h$ and $0.5h$) are compared with the fitted model (blue solid lines). Due to the performed fit, the three model curves for u and p cannot be separated in the adjustment region. Concerning p, the z-independence in the adjustment region is in line with the discussion by Belcher et al. (2003). This shows that the z-dependent term in Eq. (30) is negligible against the residual terms. However, concerning the z-independence of u, which is mainly due to the small value of a_1, the fitted model shows inacurracies in two regions.

The first one is the inflow region past the edge, where the incoming u-profile has to change it's shape from a logarithmic form to a cosh-shaped (constant) one, leading to the deviations in u and w past the edge, visible in Fig. D.6. These inaccuracies are a drawback of the separability approach that the model is based upon.

The second region is close to the surface, where u should get smaller rather than staying constant due to the surface roughness. This drawback of the model fit, in favor of reproducing the z-independence of the pressure term, is accepted, as neglecting the Reynolds stress gradients also fails for height values smaller than $\approx 0.2h$ (see Fig. D.13). However, one can see that the model quite nicely matches the pressure data in the whole range, being the upside of the current model fit.

Again looking at the comparison of the u-components in Fig. D.6, it can be seen that the analytical model starts to deviate from the LES profiles at $x \sim 10h$ at the considered heights, as expected from the approximation $g_\infty = 0$. For the canopy interior, w and p show small deviations from the LES data, while u is shown to attain a constant value.

These deviations between u from the LES and the model lead to a fundamental change in the form of the streamlines, as depicted in Fig. D.7. This figure shows a comparison of the LES-streamlines (solid lines) and model-streamlines (dashed lines) for the reference case, while the boundary of the canopy is depicted by black solid lines. From this figure several conclusions can be drawn. First, as expected from Dalpé and Masson (2009) no re-circulation develops for the LES, due to the chosen C_d and PAI values. Second, it can be seen that the streamlines of the LES level off horizontally inside the canopy, while the analytical curves follow the shape of the LES streamlines behind the forest edge, but start to diverge from them when the bending of the LES-streamlines sets in. This finding nicely illustrates the region of applicability of the derived model and demonstrates the importance of combining the derived model with the solution of Massman (1997) in the canopy interior.

4.2. Sensitivity analysis of the adjustment region model

4.2.1. Varying the canopy length

To test the developed model for changes in the canopy length L, the reference case simulation was compared to three further LES with variable L ($4L_c$, $8L_c$ and $15L_c$), while the canopy height and the adjustment length scale were kept constant. These values of L were selected as they guarantee that the major part of the adjustment region is covered (Dupont and Brunet, 2008).

A comparison of horizontal profiles of the flow quantities at height $0.5h$ can be seen in Fig. D.8, where the u and w profiles were normalized by the u-value at the canopy edge, u_0, and the p-profiles by ρu_0^2, in analogy to the definition of p_s by u_s in Eq. (25). As depicted in this figure, the profiles show a proper match to each other as long as they do not reach the right edge of the canopy. From this result it can be seen that an analytical model, which is set up to describe the flow behavior in the adjustment region, should not depend on the canopy length, L, as the LES also shows no dependency for a huge range of canopy lengths. In the development of the current model, no canopy length scale did enter, as an infinitely elongated canopy was assumed. Therefore application of the prescribed analytical model to canopy-scenarios with $L \geq 4L_c$, is shown to be valid. The performance of the model for smaller forest length will be discussed in Section 4.4.

4.2.2. Varying the canopy height

As a second test the effect of altering canopy height h on the model is investigated. For this reason, the next two LES were performed, one with $h = 15$ m and PAI $= 4.5\ \mathrm{m^2 m^{-2}}$ and the other with $h = 20$ m and PAI $= 6\ \mathrm{m^2 m^{-2}}$. These PAI-values were chosen to ensure that the two simulations have the same L_c as in the reference simulation for the sake of comparability. The results of this investigation can be seen in Fig. D.9 where horizontal u, w and p profiles at the corresponding half-canopy-height are depicted for the reference case (a), (b) and (c) with $h = 10$ m, the $h = 15$ m case (d), (e) and (f) and the $h = 20$ m case (g), (h) and (i). The data of the three LES simulations are shown as black squares, the model prediction as blue solid lines. For the model set up the calculated reference-case-parameters a_1, a_2 and a_3 were used (see Table D.2). The velocity scale u_s, and therefore p_s, were determined

Table D.1
Used canopy parameters (L, h, L_c) for the LES simulations, discussed in the corresponding sections.

Section	L[m]	h[m]	L_c[m]
4.1	500	10	16.7
4.2.1	64	10	16.7
	126	10	16.7
	250	10	16.7
4.2.2	500	15	16.7
	500	20	16.7
4.2.3	500	10	12.5
	500	10	25
4.4	10	10	16.7
	20	10	16.7
	30	10	16.7

Table D.2
Fitting parameters for a simultaneous fit of the analytical model to the LES data of the reference scenario.

u_s [ms^{-1}]	a_1	a_2	a_3
0.64	1.6×10^{-3}	0.25	0.13

Table D.3
Calculated $x_i(h/2)$ values from Eq. (41) for the discussed LES with varying h and L_c length scales.

Section	h[m]	L_c[m]	$x_i(h/2)/L_c$
4.1	10	16.7	5.7
4.2.2	15	16.7	8.3
	20	16.7	11.6
4.2.3	10	12.5	8
	10	25	3.2

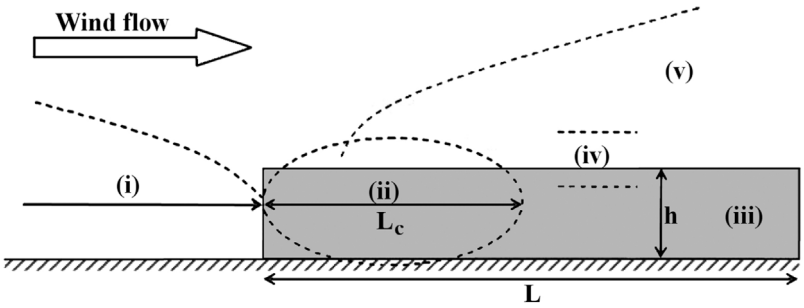

Fig. D.1. Schematic sketch of the important regions concerning edge-flow after Belcher et al. (2003): (i) impact region, (ii) adjustment region, (iii) canopy interior, (iv) canopy shear layer, (v) roughness change region. The quantities h, L and L_c denote canopy height, canopy length and adjustment length.

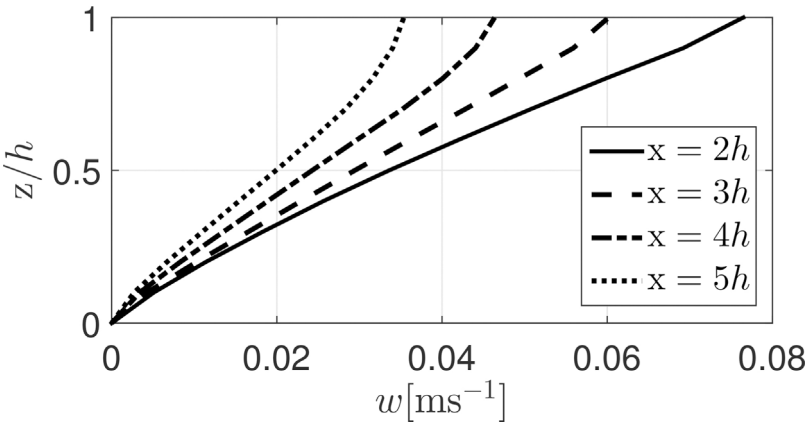

Fig. D.2. Vertical wind profiles of the w-component inside the adjustment region for distances of 2h, 3h, 4h and 5h from the canopy-edge for a LES with L_c = 16.7 m and h = 10 m.

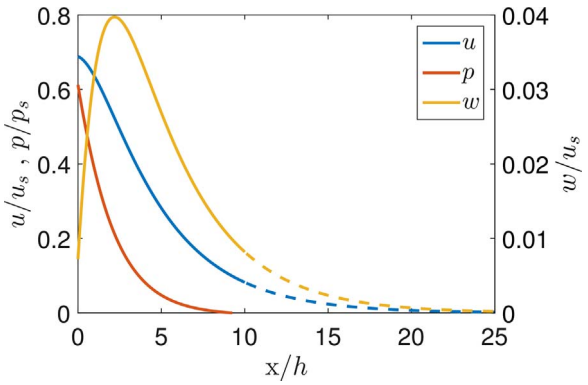

Fig. D.3. Graphical representation of the derived analytical expressions for u/u_s (blue line), w/w_s (yellow line) and p/p_s (red line) at half the canopy height, where the linestyle is solid in the region where the analytical solution is valid, dashed for the residual region. (For interpretation of the references to color in this figure legend, the reader is referred to the web version of the article.)

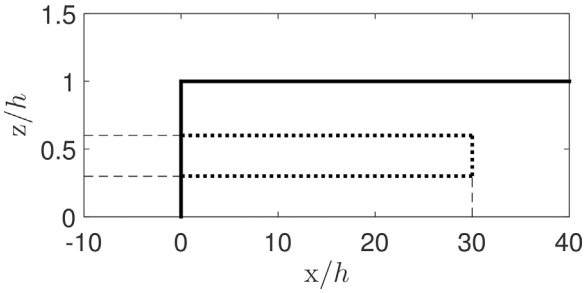

Fig. D.4. Illustration of the region used for the simultaneous fitting approach. The boundaries of the canopy (canopy edge and canopy top) are depicted by black solid lines, the boundary of the fitting region by black dotted lines.

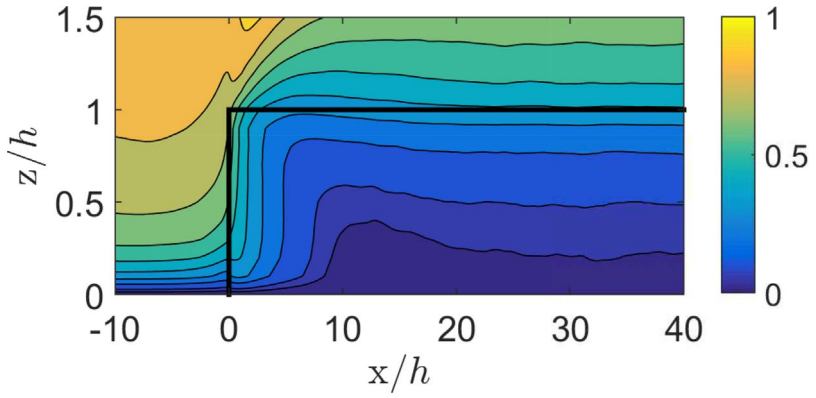

Fig. D.5. Contour plot of the horizontal velocity component u in m/s for the reference case LES. The canopy boundary (canopy edge and canopy top) is indicated by the black solid lines.

separately in the other two cases, as $u_s \sim u(x = 0)$ and the initial velocity was varying between the three LES. Due to application of the reference-case-parameters, the mismatch of the model to the LES data is lowest in this case. As a general trend it can be seen, that the mismatch in the peak region of w is increasing with increasing canopy height, however when passing the peak, the overall behavior of decrease is again nicely described by the model. When investigating the behavior of u, it can be seen that the deviations in the region shortly behind the canopy-edge are approximately of same size in the three cases, even so the deviations of the model and the LES data of u get smaller in the canopy interior with increasing h, which has to be covered by models for the canopy interior. Last but not least, the comparison of p between LES and the model shows a nice agreement for all three investigated cases.

4.2.3. Varying the adjustment length scale

As a last test, the adjustment length scale, L_c, was varied. Also for this purpose, two additional LES were performed and compared to the reference case. One equipped with a PAI = 2 m^2m^{-2} canopy, and the other one with a PAI = 4 m^2m^{-2} canopy. As carried out in the previous sections, the other length scale, h, was kept constant (h = 10 m) in addition to a constant C_d. Therefore a L_c-calculation of the three cases is yielding L_c = 25 m for the first additional LES, L_c = 16.7 m for the reference case (PAI = 3 m^2m^{-2}) and L_c = 12.5 m for the second additional LES.

Fig. D.10 shows the comparison of the model to the LES data for horizontal profiles of the flow quantities taken at half the canopy height for the three canopies. As depicted there, the largest mismatch between the model and the LES data appears in the L_c = 25 m case for all three observables (subplots (g,h,i)). While the largest differences in u appear close to the canopy-edge in this case, a horizontal shift of the peak values by $\sim h$ can be spotted in the corresponding w-profiles. Again the pressure distribution shows the best qualitative match. For the reference case (subplots (d,e,f)) the mismatch is naturally minimal due to the usage of the reference-case-parameters, but also for the L_c = 12.5 m scenario (subplots (a,b,c)) the model matches the LES data quite nicely

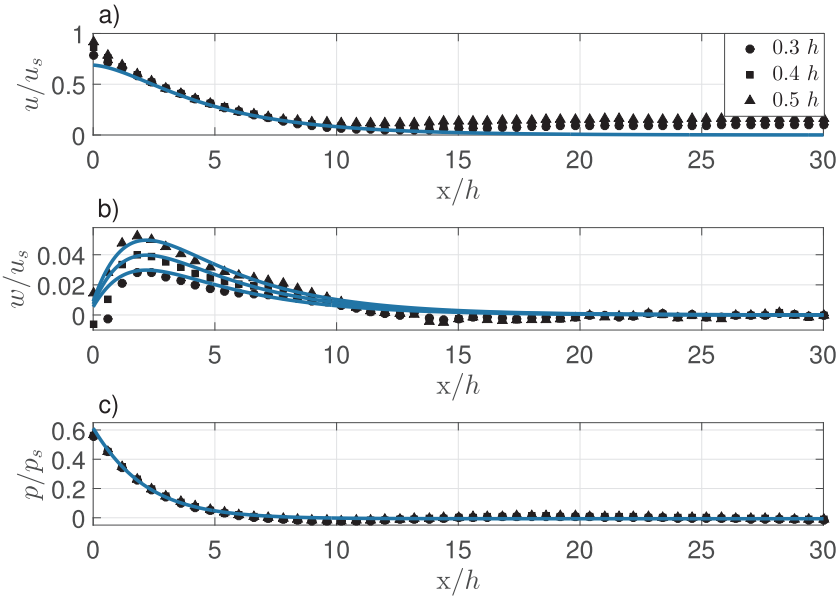

Fig. D.6. Fit of the analytical model to the LES data of the reference case. Three horizontal profiles are depicted for each of the three flow quantities u (a), w (b) and p (c), corresponding to the heights $0.3h$ (circles), $0.4h$ (squares) and $0.5h$ (triangles). The fitted model-curves are illustrated as blue solid lines. (For interpretation of the references to color in this figure legend, the reader is referred to the web version of the article.)

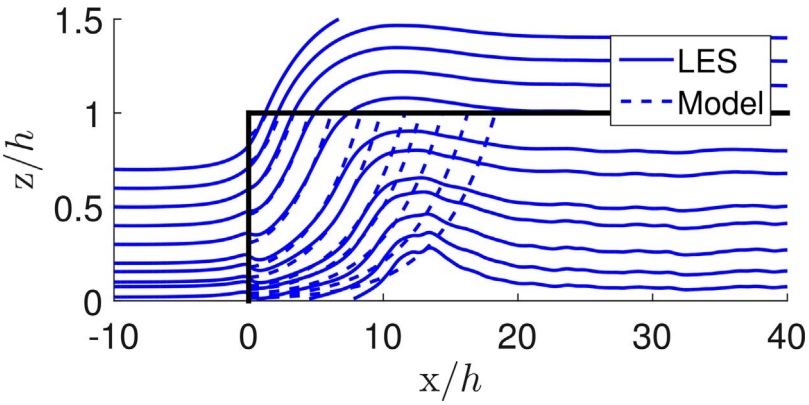

Fig. D.7. Comparison of the LES-streamlines (blue solid lines) to the ones of the analytical model (blue dashed lines) for the reference case. The canopy boundary (canopy edge and canopy top) is indicated by the black solid lines. (For interpretation of the references to color in this figure legend, the reader is referred to the web version of the article.)

except for the small differences close to the canopy-edge in u and w. Aside from these findings it is again recognized that the value, u levels off to in the canopy interior, is indirect proportional to L_c. In conclusion it can be stated that the analytical model, equipped with α-independent parameters, is also capable of describing variations in the adjustment length scale L_c.

4.3. An analytical model for the full canopy domain

To get a model for the full canopy region, Eqs. (28), (29) and (30) have to be combined with the one-dimensional analytical description of Massman (1997) for the canopy interior. This combination additionally yields an expression for the length of the adjustment region x_I.

The solution of Massman (1997), is based on assuming neutral and homogeneous conditions and, therefore, neglecting all horizontal derivatives and setting the mean vertical wind, w, to zero. Application of this conditions to the momentum Eqs. (6) and (7) results in

$$\frac{d\tau_{13}}{dz} = F_{d1} = \frac{u^2}{L_c}, \tag{32}$$

and

$$\frac{dp}{dz} = \rho\frac{d\tau_{33}}{dz}, \tag{33}$$

meaning that the turbulent shear stress is given by the drag force and the pressure by the variance of the vertical velocity in this scenario.

From Eq. (32), Massman (1997) calculated expression for u and τ_{13}. Adapting these analytical solutions to the discussed case of a constant PAI results in

$$u_\infty(z) = u_\infty(h)\exp(-n(1 - z/h)), \tag{34}$$

and

$$\tau_{13} = (u_\infty(h))^2\frac{\alpha}{2n}\exp(-2n(1 - z/h)) \tag{35}$$

where $u_\infty(h)$ is the velocity at the canopy top,

$$n = \frac{\alpha}{2(c_1 - c_2\exp(-c_3\alpha))}, \tag{36}$$

and c_1, c_2, c_3 are constants determined in the work of Massman (1997).

Solving Eq. (33), allows for calculation of the pressure from the vertical velocity variance $\tau_{33} = \sigma_w^2$ with the standard deviation σ_w. However, an functional expression for $\sigma_w(z)$ could not be determined by the approach of Massman (1997).

To combine the analytical model for the adjustment region and the model for the homogeneous canopy, it is assumed that the adjustment region model is valid for $x \in [0; x_I(z)]$, while the homogeneous model is valid for $x \in]x_I(z); \infty[$.

Therefore the final set of equations is given by:

$$u(x, z) = u_s F(x)\Theta(x_I(z) - x) + u_\infty(z)\Theta(x - x_I(z)), \tag{37}$$

$$w(x, z) = u_s(a_2 - a_3/\alpha e^{-x/L_c})F(x)z/h, \tag{38}$$

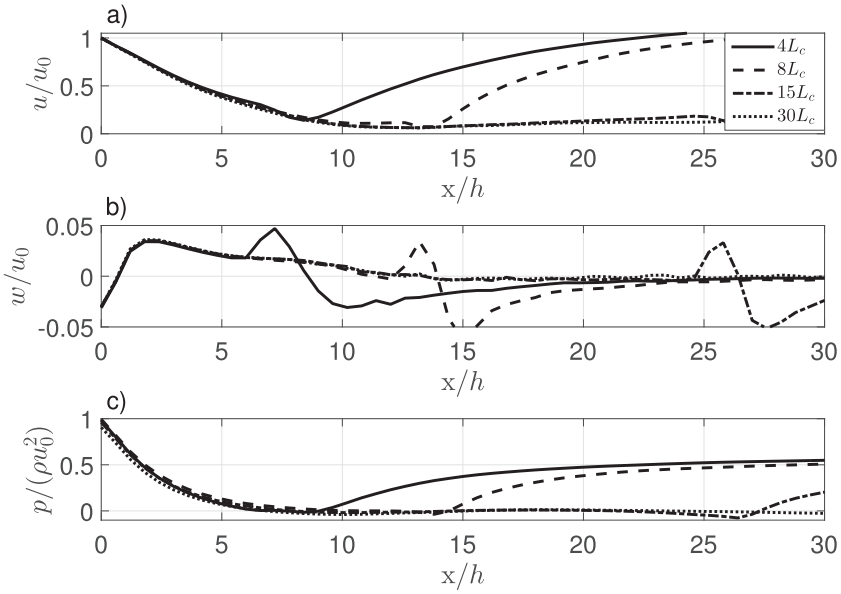

Fig. D.8. Comparison of horizontal u-profiles (a), w-profiles (b) and p-profiles (c) at a height of $0.5h$ for four LES with different canopy length $L = 4L_c$ (solid line), $L = 8L_c$ (coarse dashed line), $L = 15L_c$ (ordinary dashed line) and $L = 30L_c$ (fine dashed line).

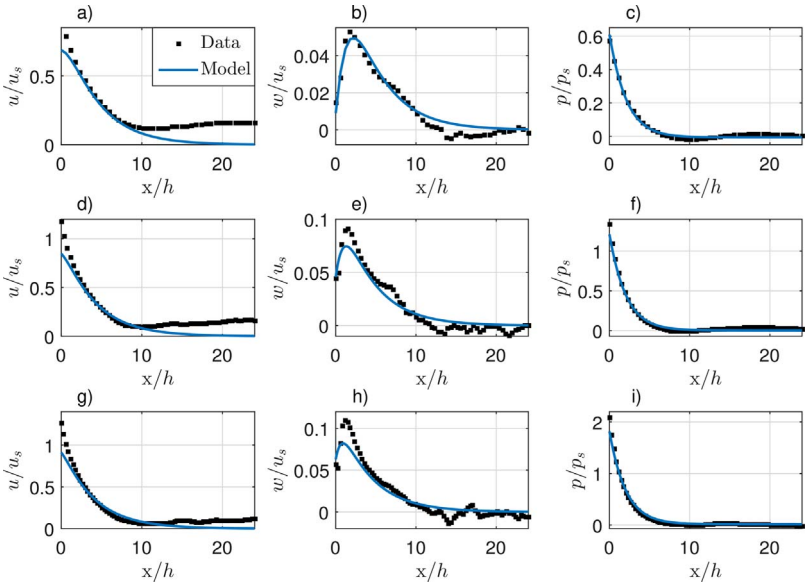

Fig. D.9. Application of the analytical model to three scenarios with variable canopy height h. The subplots (a)–(c) depict horizontal profiles of u, w and p for the reference case with $h = 10$ m, the subplots (d)–(f) show the profiles of the $h = 15$ m case and the subplots (g)–(i) the profiles of the $h = 20$ m case. All horizontal profiles were taken at half the corresponding canopy height. The LES data sets are depicted as black squares, the model prediction as blue solid lines.

$$p\left(\mathrm{x},\mathrm{z}\right) = p_s\,[L_c^{-1}\int_{\mathrm{x}}^{\infty} d\tilde{\mathrm{x}}\; F^2(\tilde{\mathrm{x}}) - F^2(\mathrm{x})/2]\Theta\left(\mathrm{x}_I(\mathrm{z}) - \mathrm{x}\right) + \rho\sigma_w^2(\mathrm{z})\Theta\left(\mathrm{x} - \mathrm{x}_I(\mathrm{z})\right), \tag{39}$$

where

$$F(\mathrm{x}) = \exp(-a_2\mathrm{x}/h - a_3/\alpha^2 e^{-\mathrm{x}/L_c}), \tag{40}$$

$\Theta(*)$ is the Heaviside step function, $p_s = \rho u_s^2$, the parameters a_2 and a_3 are given in Table D.2. As described in Section 4.1, the equations were expanded in a_1 and the z-dependent term in the adjustment region pressure was neglected.

The z-dependent boundary between the two regions, x_I, is further on defined as the distance from the canopy edge, where the horizontal wind component u decreased that far, that Eq. (32) is fulfilled. For this reason, the drag force component F_{d1}, is calculated from the adjustment region model, while the vertical gradient of the stress tensor, $d(\tau_{13})/dz$, of the Massman (1997) model is used (Eq. (35)).

By this approach, a defining equation for x_I can be derived

$$a_2\mathrm{x}_I(\mathrm{z})/h + a_3/\alpha^2\exp(-\mathrm{x}_I(\mathrm{z})/L_c) = \log(u_s/u_\infty(h)) + n(1 - \mathrm{z}/h), \tag{41}$$

which has to be solved numerically for $\mathrm{x}_I(\mathrm{z})$ at all investigated height levels z.

This approach is illustrated in Fig. D.11, where the horizontal F_{d1}-profiles of the adjustment region model are depicted as blue lines, the $d\tau_{13}/dz$-profiles of the canopy interior model as black lines. The profiles were normalized by u_s^2/L_c and taken at the heights $0.2h$, $0.5h$ and $0.8h$. The red crosses depict the intersection points $\mathrm{x}_I(\mathrm{z})$, showing a height dependent behavior.

In Table D.3, the calculated $\mathrm{x}_I(h/2)$ values for the discussed LES simulations with varying h and L_c length scales are summarized.

From this table it can be seen, that the length of the adjustment region is not just proportional to L_c as the normalized values $\mathrm{x}_I(h/2)/L_c$ still show h and L_c dependency. However the values are in line with the investigations of Cassiani et al. (2008) and Dupont and Brunet (2008) and are also capable of describing the points, where the adjustment region model starts to deviate from the LES in Figs. D.6, D.9 and D.10.

When plugging the defining equation for x_I into the final equation for u (Eq. (37)), it can be seen that x_I guaranties continuity of this expression.

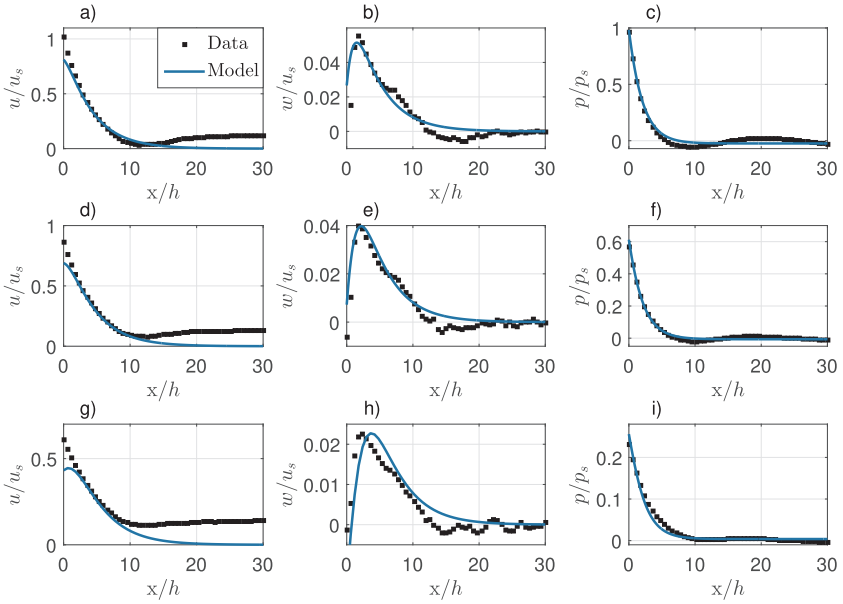

Fig. D.10. Application of the analytical model to three scenarios with different adjustment length scale L_c. The three subplots (a)–(c) depict horizontal profiles of u, w and p of the LES with L_c = 12.5 m, the subplots (d)–(f) show the reference-case profiles (L_c = 16.7 m) and the subplots (g)–(i) the profiles of the L_c = 25 m-case. All profiles were taken at 0.5h. The LES data sets are depicted as black squares, the model prediction as blue solid lines. (For interpretation of the references to color in this figure legend, the reader is referred to the web version of the article.)

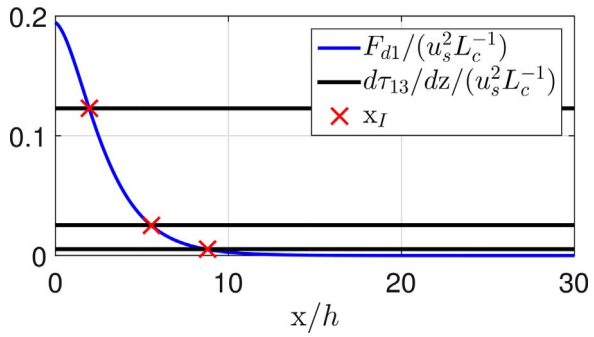

Fig. D.11. Illustration of the x_I-calculation, where $x_I(z)$ (red crosses) is determined by intersecting the horizontal F_{d1}-profiles of the adjustment region model (blue lines) with the $d\tau_{13}/dz$-profiles of the canopy interior model (Massman, 1997) (black lines). The profiles are normalized by u_s^2/L_c and are taken at the heights 0.2h, 0.5h and 0.8h, from the lowest to the largest u-value respectively. (For interpretation of the references to color in this figure legend, the reader is referred to the web version of the article.)

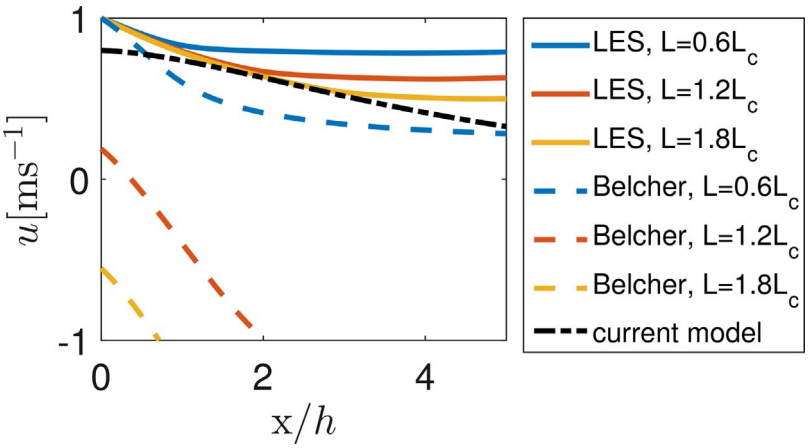

Fig. D.12. Comparison of u-profiles at half canopy height past the edge, from LES simulations (solid lines), from the Belcher et al. (2003) model (dashed lines) and from the current model (dashed-dotted line), for three different forest lengths L, constant forest height h = 10 m and adjustment length scale L_c = 16.7 m. The $L = 0.6L_c$ profiles are colored red, the $L = 1.2L_c$ profiles are colored blue and the $L = 1.8L_c$ profiles are colored yellow. The L-independent current model is colored black. (For interpretation of the references to color in this figure legend, the reader is referred to the web version of the article.)

Also requiring continuity for the pressure at $x = x_I$, an functional expression for the vertical velocity variance σ_w^2 in the canopy interior can be derived

$$\sigma_w^2(z) = u_s^2/L_c \int_{x_I(z)}^{\infty} F^2(x)dx - u_\infty^2/2 \exp(-2n(1 - z/h)) \tag{42}$$

For the final application of the combined model, it might be sensible to express the velocity scale u_s by flow quantities at the canopy edge. As it was shown in the sections before, the pressure distribution should be used for this purpose as it is works best in reproducing the LES results at the edge. Using Eq. (39) and the definition of $p_s = \rho u_s^2$, we get

$$u_s^2 = p_0/\rho (L_c^{-1} \int_0^{\infty} F^2(x)dx - F^2(0)/2)^{-1} \tag{43}$$

where $p_0 = p(x = 0)$ is the pressure at the canopy edge.

Taking this definition into account, the final input parameters for the analytical model are the mean perturbation of the hydrostatic pressure at the canopy edge p_0, the horizontal velocity component close

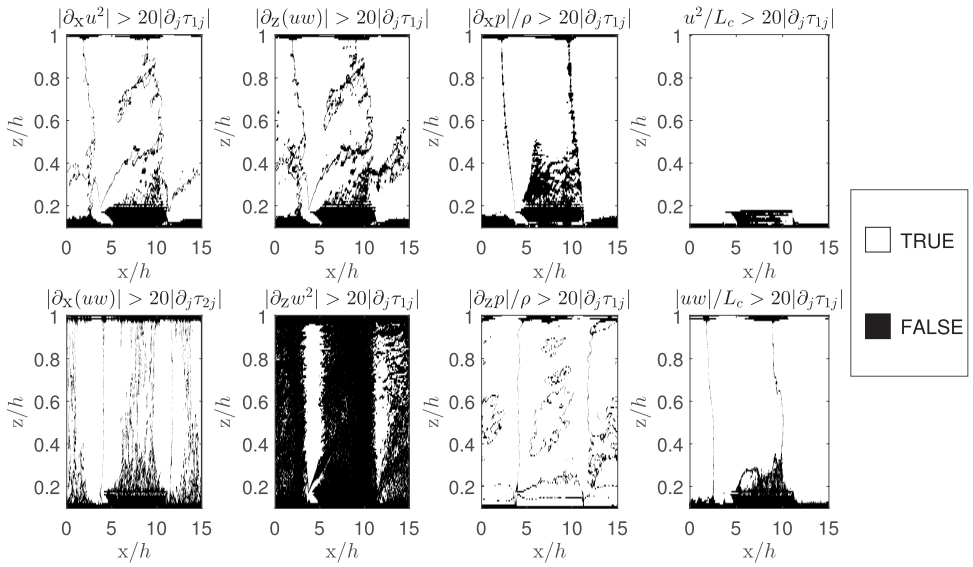

Fig. D.13. Comparison of the Reynolds stress gradient $\partial_j \tau_{1j}$ and $\partial_j \tau_{2j}$ to the remaining terms in Eqs. (6) and (7). The subplots show binary maps, of white and black pixels. If a pixel of a certain subplot is white, the inequality in the title of this subplot is fulfilled. If a pixel is black, the inequality is violated.

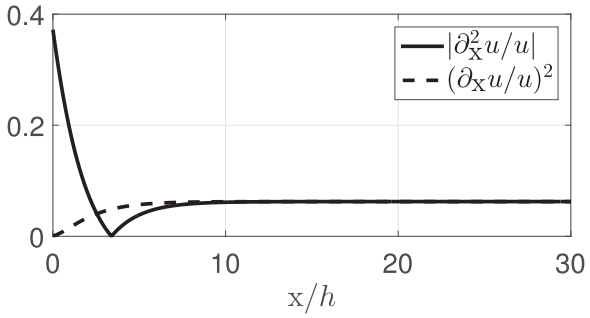

Fig. D.14. Comparison of the magnitudes of $(\partial_x u/u)^2$ (solid line) and $|\partial_x^2 u/u|$ (dashed line) for the parameters of Table D.2.

to the ground of the canopy interior $u_\infty(0)$, the air density ρ, the canopy height h and the adjustment length scale L_c, next to the model parameters a_2, a_3, c_1, c_2 and c_3.

4.4. Comparison to a linearized analytical model

Belcher et al. (2003) derived a two dimensional analytical model by linearizing the governing equations in fluctuations, which are superimposed on a mean background wind field and by neglecting the Reynolds stress gradients.

The well functioning of this linearization approach is based on the smallness of the before mentioned fluctuations in comparison to the mean background wind. Belcher et al. (2003) showed that this transfers to

$$L << L_c, \tag{44}$$

which either means that the horizontal extent of the canopy has to be very short, or that it has to be very sparse. Therefore the Belcher et al. (2003) model describes a flow that is not fully adjusted to the canopy, as the width of the adjustment region, which is of order L_c, is larger than the length of the forest. Because of that, the Belcher et al. (2003) model cannot be compared to the Massman (1997) model, as these two models work in disjoint regions. On the other hand, the current model technically describes an infinitely elongated forest ($L \rightarrow \infty$), which leads to the fact that the canopy length L does not enter as an input parameter. Therefore it can be seen that the two models describe different regimes of forest edge flow.

This finding is illustrated in Figure D.12, where horizontal u-profiles at half canopy height, originating from LES simulations, from the Belcher et al. (2003) model and from the current model are compared downwind of the forest edge. This is done by investigating three scenarios, where $h = 10$ m and $L_c = 16.7$ m were kept constant, while the length of the forest L was varied between h, $2h$ and $3h$, which is corresponding to $L = 0.6L_c$ for the first, $L = 1.2L_c$ for the second and $L = 1.8L_c$ for the third scenario. The LES profiles are depicted by solid lines, the Belcher et al. (2003) profiles by dashed lines and the u-profile of the current model by the dashed-dotted line, while the different scenarios are distinguished through coloring. Blue labels the $L = 0.6L_c$ scenario, red the $L = 1.2L_c$ scenario and yellow the $L = 1.8L_c$ scenario. Due to the fact that the current model is independent of L, there is just one line representing the result from this model, which is colored black.

By varying the ratio L/L_c in the three scenarios it is possible to distinguish the regimes of applicability of the Belcher et al. (2003) model and the current model. In the first scenario, the ratio $L/L_c = 0.6$, which is still in favor of inequality (44). A similar scenario with $L/L_c = 0.5$ and a canopy of constant PAD was also discussed by Belcher et al. (2003). In this scenario it can be seen that the model of Belcher et al. (2003) (dashed blue line) attains similar values as the LES result close to the edge, however after that it levels off too rapidly. Albeit the qualitative behavior of the LES result is covered. The curve of the current model (black dashed-dotted line) also underestimates the results given by LES. However, the prediction of this model improves performance with increasing length of the forest, as the red line ($L = 2h$) and the yellow line ($L = 3h$) match the model better and better, which is expected due to the $L \rightarrow \infty$ condition. On the other hand the Belcher et al. (2003) model is no longer able to reproduce the LES u-profiles, which is also expected, as the condition for the well functioning of the linearization approach, (inequality (44)) is violated by the L/L_c values of 1.2 and 1.8.

In conclusion, the comparison of the model of Belcher et al. (2003)

and the current model for the interior of the canopy shows that the first one is better applicable for canopy edge scenarios, where the flow is not able to fully adjust to the canopy, while the latter one can be used for the reversed case.

5. Conclusion

An analytical solution to the two-dimensional Reynolds averaged Navier–Stokes equations was developed in the adjustment region of a canopy-edge scenario in neutral conditions and tested on variations of the relevant length scales by means of LES. The adjustment region was chosen for the derivation, as the values of the flow quantities in this region show the largest deviation from the respective values in the canopy interior, where one-dimensional models apply. The one-dimensional model of Massman (1997) was subsequently combined with the derived analytical solution for the adjustment region to attain a model for the full canopy interior. The current model was finally tested against the analytical model of Belcher et al. (2003) for varying canopy lengths.

In the derivation of the analytical solution for the adjustment region, several approximations were applied. The most important ones were neglecting the Reynolds stress gradients against the residual terms in the governing equations, the assumption of a constant plant area density and canopy height throughout the canopy, the separability of the vertical velocity component concerning the spatial variables and the neglection of a height-dependent additional term in the horizontal velocity component. We found out that the fourth assumption is responsible for the limitation of the approach to the adjustment region, as it relates to the neglection of the Reynolds stress gradients, which play a major role in the canopy interior. Because the final solution yields $u > 0$ for the full canopy domain, the model cannot reproduce recirculation zones that appear in very dense canopies.

For calculation of the occurring model parameters and for testing the model in several canopy cases, LES runs were performed, while varying the three defining length scales of the canopies, the canopy length L, the canopy height h and the adjustment length scale L_c. Treating the model parameters as constants, deferred from a fit to a reference LES, turned out to give satisfactory model-predictions in all considered cases, even if these parameters are in general dependent on h/L_c. Therefore an investigation on the h/L_c-behavior of the model parameters would further improve the model's performance. This kind of study will also be of importance when investigating canopy scenarios with highly non-constant plant area densities, as the flow behavior in this case will strongly differ from the one inside a canopy of constant plant area density, as shown by Dupont and Brunet (2008).

Comparison of the current model with the analytical model of Belcher et al. (2003) shows that both models act in different regimes. While the model of Belcher et al. (2003) should be used for canopies that are too short or shallow that the flow can adjust to them ($L \ll L_c$), the current model should be applied for the reversed scenario.

Besides of increasing the understanding of canopy-edge flow, the current analytical model can be used to calculated the length of the adjustment region, which might be used to judge the possible influence of edges on EC measurements performed inside or above canopies. Furthermore being able to compute the velocity field inside a given canopy can have an impact on predictions of seed dispersal or scalar dynamics inside the canopy. The combined model may also be used for developing a spatially inhomogeneous aerodynamic resistance applicable to the so-called "canopy convector effect" problem in isolated forest patches situated in arid environments (Rotenberg and Yakir, 2010). Besides these applications, a comparison between the proposed model and field experiments must be performed to evaluate its utility in realistic conditions.

Acknowledgements

This research was supported by the German Research Foundation (DFG) as part of the project "Climate feedbacks and benefits of semi-arid forests (CliFF)" and the project "Capturing all relevant scales of biosphere-atmosphere exchange – the enigmatic energy balance closure problem", which is funded by the Helmholtz-Association through the President's Initiative and Networking Fund, and by KIT. We thank the PALM group at Leibniz University Hannover for their open-source PALM code and their support.

Appendix A. Comparison of Reynolds stress gradients to residual terms

To justify neglecting the Reynolds stress gradients in Eqs. (6) and (7) against the residual terms, the magnitudes of all entering contributions were extracted from a canopy stripe LES with $h = 10$ m and $L_c = 16.7$ m. In Fig. D.13 Eqs. (6) and (7) are investigated by comparing the magnitude of the Reynolds stress gradients ($\partial_j \tau_{1j}$ and $\partial_j \tau_{2j}$) to the remaining terms. The white pixels in this binary plots label positions, where the Reynolds stress gradients are smaller than 5% ($= 1/20$) of the terms, which are displayed in the title of the respective subplot. The residual pixels are colored black.

From investigating these two figures, it can be seen that, apart from the top or bottom of the canopy, the Reynolds stress terms are mostly smaller than 5% of the remaining terms. The only exception to this trend is the term $\partial_z w^2$, as the main part of the surface is colored black in this plot. However, most of the area becomes white again when extending the threshold to 10% in this selected case. This is still a reasonable value for neglecting of the Reynolds stress gradients in the derivation of the analytical model.

Appendix B. Adjustment region solution of the horizontal velocity

To solve the differential Eq. (21), two approximations are applied. The first one is $|\partial_x^2 u/u| \gg (\partial_x u/u)^2$, which translates to $|f''/f| \gg (f'/f)^2$, the second one is $|f''/f| \gg 2a_1^2$. The validity of both equations is investigated in Appendix C by means of LES.

Applying these approximations to Eq. (21), the $(f'/f)^2$-terms and $2a_1^2$ are neglected against the f''/f-terms, which results in

$$\left(\frac{f''}{f}\right)' + \alpha\frac{f''}{f} = 0, \tag{B.1}$$

which can be integrated to give

$$f''/f = -a_3 \exp(-\alpha x), \tag{B.2}$$

where a_3 is the emerging integration constant. The term f''/f can now be reformed using the approximation $|f''/f| \gg (f'/f)^2$ to give

$$f''/f \approx f''/f - (f'/f)^2 = (f'/f)'. \tag{B.3}$$

By inserting (B.3) into (B.2), and performing the two remaining integrations, f can be calculated

$$f(x) = f_s \exp(-a_2 x - a_3/\alpha^2 e^{-\alpha x}), \tag{B.4}$$

where a_2 and f_s are also integration constants. As u has to be positive at the canopy edge, f_s has to be positive and as u has to decrease in amplitude when entering the canopy, a_2 has to be positive, too.

Appendix C. Validity of the approximations in the velocity derivation

To test the first approximations applied in the velocity derivation (Appendix B), i.e. $|\partial_x^2 u/u| \gg (\partial_x u/u)^2$, the derived model parameters of Section 4.1 (Table D.2) were inserted in the first and second derivative of Eq. (23). This approach yields a self-consistency check, as (23) was derived assuming the approximation to hold true.

The comparison of the two contributions, $(\partial_x u/u)^2$ and $|\partial_x^2 u/u|$, is depicted in Fig. D.14. It can be seen from this graph that $|\partial_x^2 u/u| \gg (\partial_x u/u)^2$ past the canopy edge as demanded for the derivation of f presented in Appendix B. When the two terms reach comparable magnitudes ($x \sim 2.5h$), the inequality breaks down and it is, strictly speaking, not longer possible to describe u by Eq. (23). However it was shown in Section 4, that the model is capable in describing the flow till $x \sim 10h$.

The second approximation used in the derivation of the velocity, $|\partial_x^2 u/u| \gg 2a_1^2$, is validated by inserting the a_1 from Table D.2. It can be seen that the left hand side is of order 10^{-1} in magnitude, while the right hand side is of order 10^{-6}, which allows for neglecting of the $2a_1^2$-term in the velocity derivation.

Appendix D. Calculation of the pressure

To calculate the pressure p, the momentum equations are used, where the Reynolds stress gradients were neglected (see Appendix A), the drag force was expanded (see Eq. (15)) and u and w were decomposed (see Eqs. (12) and (13)), yielding

$$\partial_x \frac{p}{\rho} = ff' gg'' - \left(ff' + \alpha f^2\right)(g')^2 - \frac{\alpha}{2}(f')^2 g^2, \tag{D.1}$$

$$\partial_z \frac{p}{\rho} = ((ff')' - 2(f')^2 + \alpha ff')gg'. \tag{D.2}$$

Eq. (D.1) originates from Eq. (6) and Eq. (D.2) from Eq. (7). Eq. (D.2) can be directly integrated in z, giving

$$\frac{p}{\rho} = C(x) + \frac{1}{2}((ff')' - 2(f')^2 + \alpha ff')g^2, \tag{D.3}$$

with a x-dependent function $C(x)$. To determine $C(x)$, we plug in p from (D.3) into (D.1), yielding

$$C' = ff' gg'' - \left(ff' + \alpha f^2\right)(g')^2 - \frac{1}{2}(ff''' - f'f'' + \alpha(ff'' + 2(f')^2))g^2 \tag{D.4}$$

From comparison with Eq. (19), it can be seen that

$$C' = -(ff' + \alpha f^2)(g'(0))^2 \tag{D.5}$$

which yields the following result for p:

$$\frac{p}{\rho} = \frac{p_\infty}{\rho} - \left(\frac{1}{2}f^2 + \alpha \int_0^x f^2(\tilde{x})d\tilde{x}\right)(g'(0))^2 + \frac{1}{2}((ff')' - 2(f')^2 + \alpha ff')g^2 \tag{D.6}$$

where p_∞ is the integration constant emerging when integrating (D.5). Eq. (25) is subsequently obtained when plugging in the derived expressions for f and g.

References

Aubinet, M., Vesala, T., Papale, D., 2012. Eddy Covariance: A Practical Guide to Measurement and Data Analysis. Springer, Netherlands.

Banerjee, T., Katul, G., Fontan, S., Poggi, D., Kumar, M., 2013. Mean flow near edges and within cavities situated inside dense canopies. Bound. Layer Meteorol. 149 (1), 19–41. http://dx.doi.org/10.1007/s10546-013-9826-x.

Belcher, S.E., Jerram, N., Hunt, J.C.R., 2003. Adjustment of a turbulent boundary layer to a canopy of roughness elements. J. Fluid Mech. 488, 369–398. http://dx.doi.org/10.1017/s0022112003005019.

Belcher, S.E., Harman, I.N., Finnigan, J.J., 2012. The wind in the willows: flows in forest canopies in complex terrain. Ann. Rev. Fluid Mech. 44 (1), 479–504. http://dx.doi.org/10.1146/annurev-fluid-120710-101036.

Burba, G., 2013. Eddy Covariance Method for Scientific, Industrial, Agricultural, and Regulatory Applications: A Field Book on Measuring Ecosystem Gas Exchange and Areal Emission Rates. LI-COR Biosciences, Lincoln, NE, USA.

Cadenasso, M.L., Pickett, S.T.A., 2000. Linking forest edge structure to edge function: mediation of herbivore damage. J. Ecol. 88 (February (1)), 31–44. http://dx.doi.org/10.1046/j. 1365-2745.2000.00423.x.

Cassiani, M., Katul, G.G., Albertson, J.D., 2008. The effects of canopy leaf area index on airflow across forest edges: large-eddy simulation and analytical results. Bound. Layer Meteorol. 126 (3), 433–460. http://dx.doi.org/10.1007/s10546-007-9242-1.

Chen, J., Franklin, J.F., Spies, T.A., 1993. Contrasting microclimates among clearcut, edge, and interior of old-growth douglas-fir forest. Agric. For. Meteorol. 63 (March (3–4)), 219–237. http://dx.doi.org/10.1016/0168-1923(93)90061-l.

Dalpé, B., Masson, C., 2009. Numerical simulation of wind flow near a forest edge. J. Wind Eng. Ind. Aerodyn. 97 (5–6), 228–241. http://dx.doi.org/10.1016/j.jweia.2009.06.008.

Dupont, S., Brunet, Y., 2008. Edge flow and canopy structure: a large-eddy simulation study. Bound. Layer Meteorol. 126 (1), 51–71. http://dx.doi.org/10.1007/s10546-007-9216-3.

Dupont, S., Bonnefond, J.-M., Irvine, M.R., Lamaud, E., Brunet, Y., 2011. Long-distance edge effects in a pine forest with a deep and sparse trunk space: in situ and numerical experiments. Agric. For. Meteorol. 151 (March (3)), 328–344. http://dx.doi.org/10.1016/j.agrformet.2010.11.007.

Grönholm, T., Launiainen, S., Ahlm, L., Mårtensson, E.M., Kulmala, M., Vesala, T., Nilsson, E.D., 2009. Aerosol particle dry deposition to canopy and forest floor measured by two-layer eddy covariance system. J. Geophys. Res. D: Atmos. 114 (D4). http://dx.doi.org/10.1029/2008JD010663.

Harman, I.N., Finnigan, J.J., 2007. A simple unified theory for flow in the canopy and roughness sublayer. Bound. Layer Meteorol. 123 (March (2)), 339–363. http://dx.doi.org/10.1007/s10546-006-9145-6.

Huang, C.-W., Launiainen, S., Grönholm, T., Katul, G.G., 2014. Particle deposition to

forests: an alternative to k-theory. Atmos. Environ. 94, 593–605. http://dx.doi.org/10.1016/j.atmosenv.2014.05.072.
Jackson, P.S., Hunt, J.C.R., 1975. Turbulent wind flow over a low hill. Q. J. R. Meteorol. Soc. 101 (430), 929–955. http://dx.doi.org/10.1002/qj.49710143015.
Kanani, F., Träumer, K., Ruck, B., Raasch, S., 2014. What determines the differences found in forest edge flow between physical models and atmospheric measurements? – An LES study. Meteorol. Z. 23 (1), 33–49. http://dx.doi.org/10.1127/0941-2948/2014/0542.
Kanani-Sühring, F., Raasch, S., 2014. Spatial variability of scalar concentrations and fluxes downstream of a clearing-to-forest transition: a large-eddy simulation study. Bound. Layer Meteorol. 155 (December (1)), 1–27. http://dx.doi.org/10.1007/s10546-014-9986-3.
Katul, G.G., Grönholm, T., Launiainen, S., Vesala, T., 2010. Predicting the dry deposition of aerosol-sized particles using layer-resolved canopy and pipe flow analogy models: role of turbophoresis. J. Geophys. Res. D: Atmos. 115 (D12). http://dx.doi.org/10.1029/2009JD012853.
Launiainen, S., Katul, G.G., Grönholm, T., Vesala, T., 2013. Partitioning ozone fluxes between canopy and forest floor by measurements and a multi-layer model. Agric. For. Meteorol. 173, 85–99. http://dx.doi.org/10.1016/j.agrformet.2012.12.009.
Maronga, B., Gryschka, M., Heinze, R., Hoffmann, F., Kanani-Sühring, F., Keck, M., Ketelsen, K., Letzel, M.O., Sühring, M., Raasch, S., 2015. The parallelized large-eddy simulation model (PALM) version 4.0 for atmospheric and oceanic flows: model formulation, recent developments, and future perspectives. Geosci. Model Dev. 8 (8), 2515–2551. http://dx.doi.org/10.5194/gmd-8-2515-2015.
Massman, W., 1997. An analytical one-dimensional model of momentum transfer by vegitation of arbitrary structure. Bound. Layer Meteorol. 83 (3), 407–421. http://dx.doi.org/10.1023/a:1000234813011.
Massman, W., 1987. A comparative study of some mathematical models of the mean wind structure and aerodynamic drag of plant canopies. Bound. Layer Meteorol. 40 (1-2), 179–197. http://dx.doi.org/10.1007/bf00140075.
Raupach, M.R., Bradley, F., Ghadiri, H., 1987. A wind tunnel investigation into the aerodynamic effect of forest clearings on the nesting of abbott's booby on Christmas Island. Internal report. CSIRO Centre for environmental Mechanics, Canberra 21 p.
Ross, A.N., Baker, T.P., 2013. Flow over partially forested ridges. Bound. Layer Meteorol. 146 (3), 375–392. http://dx.doi.org/10.1007/s10546-012-9766-x.
Rotenberg, E., Yakir, D., 2010. Contribution of semi-arid forests to the climate system. Science 327 (5964), 451–454. http://dx.doi.org/10.1126/science.1179998.
Schlegel, F., Stiller, J., Bienert, A., Maas, H.-G., Queck, R., Bernhofer, C., 2012. Large-eddy simulation of inhomogeneous canopy flows using high resolution terrestrial laser scanning data. Bound. Layer Meteorol. 142 (2), 223–243. http://dx.doi.org/10.1007/s10546-011-9678-1.
Shaw, R.H., Schumann, U., 1992. Large-eddy simulation of turbulent flow above and within a forest. Bound. Layer Meteorol. 61 (1–2), 47–64. http://dx.doi.org/10.1007/bf02033994.
Townsend, A.A., 1972. Flow in a deep turbulent boundary layer over a surface distorted by water waves. J. Fluid Mech. 55 (4), 719–735. http://dx.doi.org/10.1017/s0022112072002101.
Trakhtenbrot, A., Katul, G.G., Nathan, R., 2014. Mechanistic modeling of seed dispersal by wind over hilly terrain. Ecol. Model. 274, 29–40. http://dx.doi.org/10.1016/j.ecolmodel.2013.11.029.
Watanabe, T., 2004. Large-eddy simulation of coherent turbulence structures associated with scalar ramps over plant canopies. Bound. Layer Meteorol. 112 (2), 307–341. http://dx.doi.org/10.1023/b:boun.0000027912.84492.54.
Yang, B., Morse, A.P., Shaw, R.H., Paw U, K.T., 2006. Large-eddy simulation of turbulent flow across a forest edge. Part II: momentum and turbulent kinetic energy budgets. Bound. Layer Meteorol. 121 (3), 433–457. http://dx.doi.org/10.1007/s10546-006-9083-3.
Yang, K., Tamai, N., Koike, T., 2001. Analytical solution of surface layer similarity equations. J. Appl. Meteorol. 40 (September (9)), 1647–1653. http://dx.doi.org/10.1175/1520-0450(2001)040<1647:asosls>2.0.co;2.

C | Effect of secondary circulations on surface–atmosphere exchange of energy at an isolated semi-arid forest

Kröniger, K., De Roo, F., Brugger, P., Huq, S., Banerjee, T., Zinsser, J., Rotenberg, E., Yakir, D., Rohatyn, S., and Mauder, M. (2018). Effect of secondary circulations on surface–atmosphere exchange of energy at an isolated semi-arid forest. *Boundary-Layer Meteorol.*, doi: 10.1007/s10546-018-0370-6

Boundary-Layer Meteorology
https://doi.org/10.1007/s10546-018-0370-6

RESEARCH ARTICLE

Effect of Secondary Circulations on the Surface–Atmosphere Exchange of Energy at an Isolated Semi-arid Forest

Konstantin Kröniger[1] · Frederik De Roo[1] · Peter Brugger[1] · Sadiq Huq[1] · Tirtha Banerjee[1,2] · Judith Zinsser[1] · Eyal Rotenberg[3] · Dan Yakir[3] · Shani Rohatyn[3] · Matthias Mauder[1]

Received: 22 November 2017 / Accepted: 14 June 2018

Abstract

Afforestation in semi-arid regions can potentially enhance the global carbon sink by increasing the terrestrial biomass. However, the survival of planted forests under such extreme environmental conditions is not guaranteed a priori, and critically depends on the surface–atmosphere exchange of energy. We investigate the pine forest Yatir in Israel, an example of a man-made semi-arid ecosystem, by means of large-eddy simulations. We focus on the interaction between surface–atmosphere exchange and secondary circulations that couple the isolated forest to the surrounding shrubland. The large-eddy simulations feature a grid resolution that resolves the forest canopy in several layers, and are initialized by satellite data and Doppler lidar, eddy-covariance and radiosonde measurements. We perform three large-eddy simulations with different geostrophic wind speeds to investigate the influence of those wind speeds on the surface–atmosphere exchange. We reproduce the measured mean updrafts above the forest and mean downdrafts above the shrubland, which increase in strength with decreasing geostrophic wind speed. The largest updrafts emerge above the older, denser part of the forest, triggering secondary circulations. The spatial extent of these circulations does not cover the entire forest area, although we observe a reduced aerodynamic resistance in the regions of updraft. Our simulations indicate that the enhanced surface–atmosphere exchange of the Yatir forest is not sufficient to compensate for the increased net radiation, due to the lower albedo of the forest with respect to the surroundings, resulting in higher air temperatures inside the forest. However, the difference between the forest and shrubland temperatures decreases with increasing geostrophic wind speed due to reduction in the aerodynamic resistance.

Konstantin Kröniger
Konstantin.Kroeniger@kit.edu

1 Institute of Meteorology and Climate Research, Atmospheric Environmental Research (IMK-IFU), Karlsruhe Institute of Technology (KIT), Kreuzeckbahnstrasse 19, 82467 Garmisch-Partenkirchen, Germany

2 Present Address: Earth and Environmental Sciences Division, Los Alamos National Laboratory, Los Alamos, NM, USA

3 Department of Earth and Planetary Sciences, Faculty of Chemistry, Weizmann Institute of Science, 234 Herzl Street, 7610001 Rehovot, Israel

Published online: 07 July 2018

Keywords Aerodynamic resistance · Large-eddy simulation · Secondary circulations · Virtual canopy construction · Yatir forest

1 Introduction

Afforestation efforts in semi-arid regions is a field of active research in terms of land and forest management, ecosystem services, and the mitigation of anthropogenic climate change. However, complex processes and trade-offs are often involved regarding ecosystem–atmosphere interactions (Bonan 2008; Anderson-Teixeira et al. 2011). Positive effects, such as enhanced carbon uptake or increased humidity, possibly leading to cloud formation, are opposed by negative effects, such as enhanced water use or a lowered albedo (Betts 2000; Arneth et al. 2010). Lowering the albedo by artificially planting trees in semi-arid regions, combined with high incoming radiation can lead to a substantial increase in available energy (Rotenberg and Yakir 2011; Eder et al. 2015). To guarantee the survival of the artificial ecosystem, this energy load has to be removed, mainly by transport to the atmosphere. However, due to the limited water availability in semi-arid regions, the common pathway of evaporative cooling can often not be applied. Rotenberg and Yakir (2010) discovered an alternative cooling mechanism for semi-arid ecosystems from investigations of the isolated, semi-arid pine forest Yatir (predominantly *Pinus halepensis*), which is located at the northern edge of the Negev desert in Israel, naming this mechanism the "canopy-convector effect". The canopy-convector effect describes an amplification of energy transport by enhanced sensible heat fluxes to compensate for large net radiation, especially in dry summer periods.

While an enhancement of the heat flux with instability can already be explained for homogeneous canopies by means of the aerodynamic resistance based on Monin–Obukhov similarity theory (Banerjee et al. 2017b), the heterogeneous nature of the isolated Yatir forest can also influence energy transport by generating secondary circulations between the forest and the surrounding shrubland, similar to the secondary circulations around heat islands, such as isolated cities and the surrounding rural area (Wang 2009). As hypothesized by Rotenberg and Yakir (2010), these secondary circulations are mainly due to albedo differences between the forest and the surrounding shrubland. Due to the horizontal extent of the Yatir forest canopy of 2800 ha, emerging circulations are very likely to influence the entire atmospheric boundary layer (ABL) (Raupach and Finnigan 1995; Patton et al. 2005), which can affect weather and climate at the regional scale (Garcia-Carreras et al. 2010, 2011).

The first extensive investigations of secondary circulations above the Yatir forest were conducted by Eder et al. (2015), featuring eddy-covariance and Doppler lidar measurements. From investigations of the energy balance closure, and by performing large-eddy simulations (LES) using a roughness-length parametrization, Eder et al. (2015) were able to detect secondary circulations. However, persistent updrafts above the Yatir forest were not always measured. As pointed out by them, this could be due to the measurement locations and additionally due to the strong geostrophic flow, which is mainly the result of the Persian trough system (Dayan and Levy 2002). Additionally, Eder et al. (2015) were neither able to determine the occurrence and extension of these secondary circulations in detail, nor identify the mechanisms triggering such circulations in the LES results due to the coarse model resolution. A second measurement campaign was conducted by Brugger et al. (2018), using eddy-covariance, Doppler lidar and ceilometer systems located upstream, inside, and downstream of the Yatir forest. From these measurements, the impact of the Yatir forest on the

boundary-layer height z_i was characterized, and the suppressing effect of the geostrophic wind speed on boundary-layer development was also observed and characterized.

To investigate the canopy-convector effect and its interplay with secondary circulations for the isolated Yatir forest, single-point or profile measurements have to be accompanied by additional spatial information. Large-eddy simulations have been established as a suitable research approach to model surface–atmosphere exchange for heterogeneous surfaces (e.g., Hechtel et al. 1990; Avissar et al. 1998; Albertson and Parlange 1999; Bou-Zeid et al. 2004; Prabha et al. 2007; Huang and Margulis 2009, 2010; Maronga and Raasch 2013; Miller and Stoll 2013; Schlegel et al. 2015; Kenny et al. 2017), as LES has the advantage of resolving turbulent transport on multiple scales. An important aspect for modelling canopy turbulence is the model resolution, which has to be fine enough to resolve the canopy in several layers, since representing the canopy as a vertically-distributed momentum sink results in a more realistic implementation of the momentum sink than a simplified roughness-length parametrization (e.g., Finnigan et al. 2009; Grant et al. 2016).

We have simulated the flow above the Yatir forest and the surrounding shrubland, by employing the "PArallelized Large eddy simulation Model" (PALM) (Maronga et al. 2015). Using a vertical resolution of 2.5 m enabled us to resolve the Yatir forest canopy with up to six grid levels. Initialization of the model required a three-dimensional map of the plant area density (PAD) of the forest canopy, which we constructed by combining a simple threshold-based approach for extracting the tree density from satellite data, together with measurements of the mean plant area index (PAI) at several plots and *PAD* profiles of single trees. We also initialized the LES model using eddy-covariance and meteorological measurements upstream and inside the Yatir forest, as well as from lidar profiles for the time of the largest incoming solar radiation. In addition to the simulation of the observed conditions, we performed two additional simulations with the same set-up as the first, but with the geostrophic wind speed reduced by 50% and then set to zero. Further, we assume a flat surface in all three simulations since, to first order, the effect of topography on boundary-layer turbulence can be neglected for the Yatir forest scenario (slope $< 2\%$).

The three simulations enable analysis of the nature of secondary circulations, including their extent and strength, their triggering mechanisms, as well as their spatial structure by inspection of horizontal and vertical cross-sections. Furthermore, we determine the effect of secondary circulations on the aerodynamic resistance, and the extent to which surface–atmosphere exchange and the incoming energy jointly affect the air temperature inside the Yatir forest.

2 Material and Methods

2.1 Model Description

The non-hydrostatic incompressible Boussinesq-approximated Navier–Stokes equations are calculated numerically with the PALM software, which solves for six prognostic equations: the three components of the velocity field, the potential temperature, the humidity or total water content, and the subgrid-scale turbulent kinetic energy (TKE). The subgrid-scale turbulence is modelled according to the method proposed by Deardorff (1980). Equations are discretized on a staggered Arakawa C-grid (Harlow and Welch 1965; Arakawa and Lamb 1977), and are integrated in time using a third-order Runge–Kutta scheme. The Poisson

equation for pressure is solved with the fast Fourier transform method for periodic lateral boundary conditions.

We used PALM version 4.0 together with the PALM canopy scheme to simulate the flow above the Yatir forest, which uses two prognostic equations for momentum and TKE modified to account for the aerodynamic drag of the canopy via a drag force term. The i'th component of the drag force F_{di} is, according to Shaw and Schumann (1992) and Watanabe (2004), defined by

$$F_{di} = U u_i / L_c, \tag{1}$$

where U is the mean wind speed, u_i is the i'th component of the velocity vector $\mathbf{u} = (u, v, w)$, and $L_c = 1/(C_d\ PAD)$ is the adjustment length scale of the canopy (Belcher et al. 2003), which is defined by the drag coefficient C_d, and the spatially-varying plant area density. As the drag coefficient has not been determined for *Pinus halepensis*, we used the lodgepole pine value $C_d = 0.2$ (Mayhead 1973) throughout all simulations.

The prognostic equation of the potential temperature θ inside the canopy is

$$\partial_t \theta = -u_i \partial_i \theta - \partial_i \overline{u_i' \theta'} + \partial_z Q, \tag{2}$$

where $\partial_t \theta$ is the tendency term, $u_i \partial_i \theta$ is the term for transport by mean advection, $\partial_i \overline{u_i' \theta'}$ is the turbulent transport term, and $\partial_z Q$ is a source term for the additional heat flux to account for the interaction of the canopy with direct solar radiation. Referring to Brown and Covey (1966), the source heat flux Q is modelled by an exponentially decreasing profile from canopy top to bottom,

$$Q = Q_{h_c} \exp(-\eta F), \tag{3}$$

where Q_{h_c} is the source heat flux at the canopy top h_c, η is the extinction coefficient set to 0.6 (Maronga et al. 2015), and F is the downwards cumulative plant area density $F = \int_z^{h_c} d\tilde{z}\ PAD(x, y, \tilde{z})$. However, this functional dependency is only strictly valid for the attenuation of direct solar radiation by a homogeneous canopy. When considering a canopy, which is heterogeneous in all three spatial directions, several additional contributions for the scattering of the incoming radiation on canopy elements have to be considered (Bailey et al. 2014; Matsuda et al. 2017). However, for computational purposes, we use the simple model of Eq. 3.

2.2 Measurement Campaigns

Two measurement campaigns were performed to collect the data necessary for initialization and validation of the LES model. The first campaign took place in August 2015 and the second in September 2016.

2.2.1 Campaign 2015

During the dry season from 16 to 29 August 2015, Brugger et al. (2018) employed eddy-covariance and lidar measurements at one forest and at one shrubland site. The shrubland site is located upstream of the Yatir forest at a distance of 1.6 km from the forest edge, while the forest site is located above the canopy of the most mature part of the Yatir forest. The eddy-covariance measurements were performed at a height of 9 m above ground for the shrubland site, and at 19 m above ground for the forest site, which is approximately 10 m above, and twice the height of, the canopy top. The turbulence statistics were calculated from 30-min averages of the 20-Hz eddy-covariance data using TK3 software (Mauder et al. 2013). In

Table 1 The *PAI* values for the three measurement plots from the 2016 campaign

Plot index	*PAI* ($m^2\ m^{-2}$)
1	1.73
2	1.87
3	2.45

addition to the eddy-covariance systems, one Doppler lidar was used at the shrubland site L_1, and another at the forest site L_2.

The lidars were operated in two modes, the first being a vertical stare mode that measures profiles of the vertical velocity component with a frequency of 1 Hz for a time interval of 30 min. This mode is followed by a velocity-azimuth-display scan for generating instantaneous profiles of the horizontal wind speed and wind direction, assuming horizontal homogeneity and negligible vertical motions within the confined measurement cone (Browning and Wexler 1968). These assumptions become more valid for a larger elevation angle (cone angle), but with the trade-off of an increased error propagation on the measurement accuracy. The velocity-azimuth-display scans were performed at an elevation angle of 70° and with 18 azimuthal points at a separation of 20°. A similar set-up by Päschke et al. (2015) with an elevation angle of 75° and 24 points was found to agree well with a wind-speed profiler. The spatial resolution of the lidars is 18 m, where the three lowest levels were discarded due to measurement inaccuracies. We temporally averaged the eddy-covariance and lidar data for all days from 22 to 29 August, excluding 25 August (technical malfunction of the forest eddy-covariance station). To investigate the time of peak radiation and, therefore, of a strong canopy-convector effect, we chose a daily time-averaging interval of 1000–1200 UTC, an interval during which the incoming radiation also stays approximately constant.

To deduce the stratification of the free atmosphere, we used data from radiosonde launches at Beit Dagan (station number 40179) located approximately 75 km away from the Yatir forest, which uses radiosondes model RS92/DigiCORA II from Vaisala, Finland. The measurements were performed by the Israel Meteorological Service at 1200 UTC for all seven days. The data were distributed via the World Meteorological Organization network, which we accessed with a web-tool provided by the University of Wyoming (www.weather.uwyo.edu).

2.2.2 Campaign 2016

In September 2016, we measured the mean *PAI* value for three different plots and *PAD* profiles of seven single trees using the plant canopy analyzer LAI-2200 (LI-COR, Lincoln, USA; control unit SN: PCA-2270) and two optical sensors (SN: PCH-3743 and SN: PCH-3744), which employ an optical technique for the calculation of *PAI* values from attenuation of the total amount of radiation by foliage elements based on the Beer–Lambert law. The three plots, which were already used by Sprintsin et al. (2011), are located in the most mature part of the Yatir forest, and feature an approximate size of 1000 m^2 each (Fig. 1a). To capture the spatial variability, we sampled each plot in regular intervals of 8 m. Furthermore, we applied a clumping-index correction to the measured *PAI* values (Chen 1996; Leblanc et al. 2005), which was derived by Sprintsin et al. (2011) for the Yatir forest. The resulting *PAI* values for the three plots are shown in Table 1.

Besides the plot-averaged *PAI* value, we also inferred *PAD* profiles of seven individual trees (Fig. 1b) using LAI-2200 measurements on up to six height levels, which yielded integrated *PAI* values between the corresponding height level and tree top, where we again

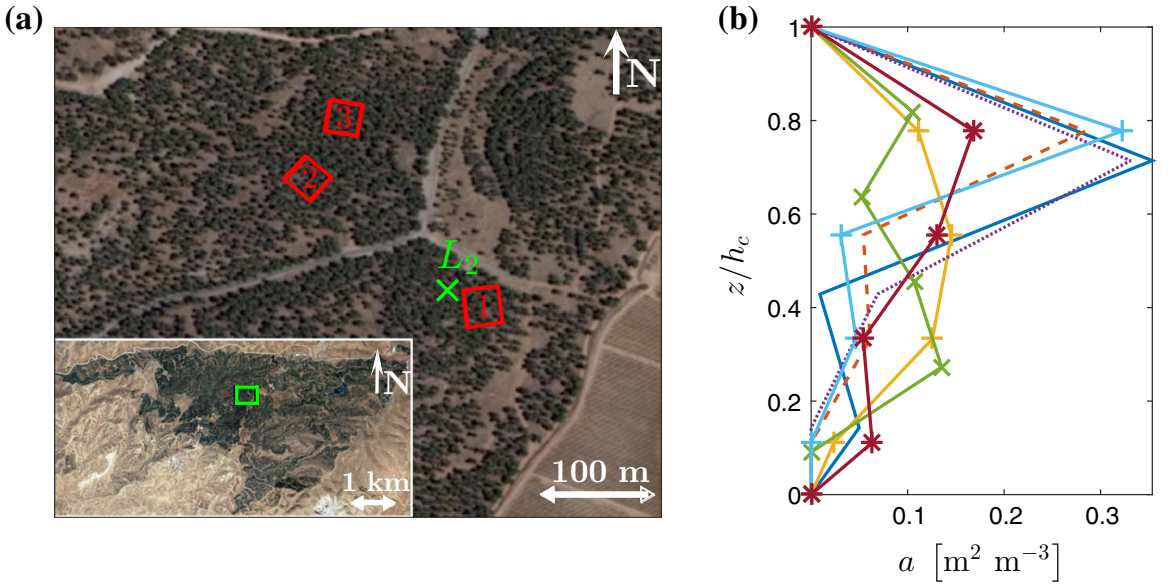

Fig. 1 The measurements of *PAI* and *PAD* values in the 2016 campaign: **a** Position of the three plots used for the determination of *PAI* values (red squares), which are labelled by their respective plot index and position of the forest lidar L_2 (green cross). The inset shows the location of the large map with respect to the full forest. **b** Normalized *PAD* profiles ($\int_0^{h_c} dz\, a = 1$) for seven selected single trees. The measurement levels are normalized by the respective tree heights

used the optical gap-fraction method. However, distance vectors were applied for each sensor ring to adjust the measurements to the specific tree shape. The *PAD* value was, thereafter, calculated by subtracting the *PAI* values for subsequent levels. The seven single trees were selected to adhere to the requirements of this method and the proximity to the forest site. Plots and single-tree *PAD* values were computed using the FV2200 software of LI-COR. The shapes of the resulting *PAD* profiles compare well with the *PAD* profiles of conifer Japanese larches, which were obtained by Takeda et al. (2008) using a ground-based laser scanner.

2.3 Values of Plant-Area Density and Heat-Source Calculations from Satellite and In Situ Data

To obtain a three-dimensional model of the Yatir forest canopy, we first decomposed the *PAD* value into a product of the local $PAI(x, y)$ value and the normalized *PAD* profile $a(x, y, z)$,

$$PAD(x, y, z) = PAI(x, y)a(x, y, z), \tag{4}$$

and then assumed a direct proportionality between the *PAI* value and the tree density $\rho_T(x, y)$,

$$PAI(x, y) = \beta\rho_T(x, y), \tag{5}$$

where β is the mean *PAI* value per tree. To determine $\rho_T(x, y)$, we used a satellite map of the Yatir forest with a resolution of 1 m in the x and y directions. As the trees have a dark greenish colour, while the surface is shaded brownish, the red, green and blue values of the tree and non-tree pixels are different. To calculate the thresholds for the three colour channels, we analyzed a small region of approximately 660 × 600 m from the satellite map, which features regions of tree pixels and non-tree pixels (Fig. 2a). The two distinct maxima in the histogram of the red component (Fig. 2c) illustrate these colour differences between tree and non-tree pixels (left = tree, right = non-tree), and the distinct maxima occur for all

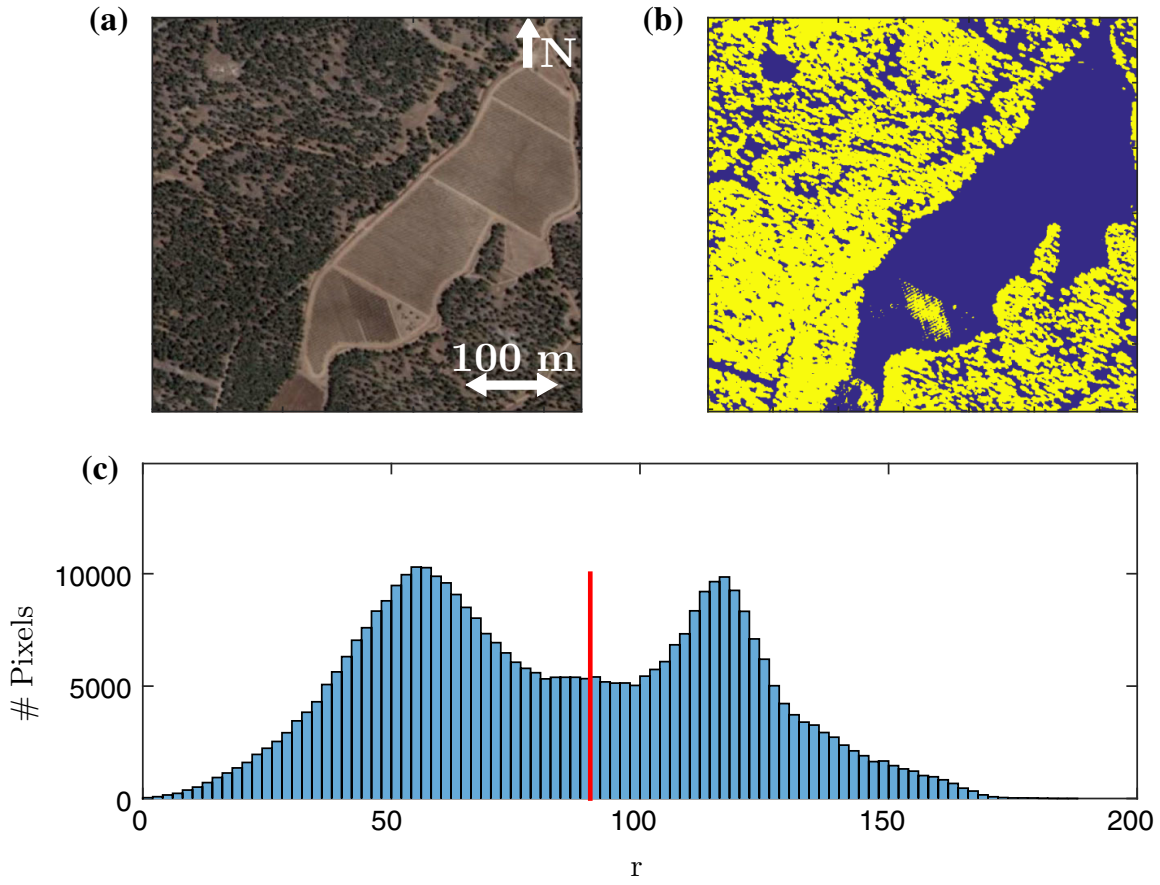

Fig. 2 Calculation of colour thresholds to transfer satellite images to tree density maps. **a** Satellite image (Google maps, 24 November 2016) used for the threshold calculation. **b** Binary tree density map from applying the threshold approach to **a**. **c** Histogram of red colour component r of the top left, where the threshold for separating tree and non-tree pixels is depicted by the vertical red line

three colour channels. To distinguish between tree and non-tree pixels, we defined a threshold separating the two maxima for every colour channel (Fig. 2c), with the described procedure resulting in the binary map shown in Fig. 2b. Artefacts such as the agricultural area, which is partly transferred into tree pixels, are later removed by visual inspection and comparison with Sprintsin et al. (2007). Subsequently, we calculated the tree-density map ρ_T by applying this approach to the image of the entire Yatir forest.

To calculate the scaling factor β, we used the measured PAI values for the three plots (Sect. 2.2), and by mapping these values to the mean ρ_T value for the three plot areas, we inferred the factor β to further calculate the value of $PAI(x, y)$. Defining the forest area through all pixels with a non-zero PAI value leads to a total forest area of 3500 ha, which is a value larger than the 2800 ha mentioned by Rotenberg and Yakir (2010). However, the difference is basically due to areas of small PAI values on the trailing edge of the Yatir forest, which can be seen from a comparison with the maps of the leaf area index of Sprintsin et al. (2007). Finally, we employed Eq. 4 to compute the three-dimensional PAD map by randomly assigning the normalized measured PAD profiles (Sect. 2.2) to tree pixels to model the natural variability of tree shapes and foliage density within the forest.

To simulate heating of the modelling domain by solar radiation, a two-dimensional map of the source heat flux at the canopy top $\overline{Q_{h_c}}(x, y)$, in addition to a two-dimensional map of the kinematic heat flux at the surface $\overline{w'\theta'}|_{z=0}(x, y)$, is needed. Both quantities are kept constant during the simulation so as to assume a constant net radiation, which corresponds to

Table 2 Configuration of the preliminary simulation

Geostrophic wind speed u_0	5.7 m s^{-1}
Lapse rate of the inversion layer	7.25×10^{-4} K m^{-1}
Initial z_i	1000 m
Initial temperature	34 °C
Roughness length	0.01 m
Kinematic heat flux at the surface	0.214 K m s^{-1}
Simulated time	2 h

the measurements that are extracted shortly after noon (Sect. 2.2.1). We deduced the value of Q_{h_c} by setting $Q_{h_c} = Q_f$ for tree pixels and $Q_{h_c} = Q_s = H_s$ for non-tree pixels of the ρ_{h_c} map, where H_s is the measured heat flux at the shrubland eddy-covariance site (Sect. 2.2). To determine Q_f from H_s and the measured heat flux at the forest site H_f, we calculated the footprint of the forest eddy-covariance tower for the period of the measurements using the TK3 software (Mauder et al. 2013) and the fraction p of tree pixels in that footprint. Further, we used

$$H_f = pQ_f + (1 - p)H_s, \tag{6}$$

and set $\overline{w'\theta'}_0 = Q(z = 0)$, where Q is calculated from Q_{h_c} and the *PAD* map using Eq. 3.

2.4 Numerical Set-up

The simulation set-up consists of both a preliminary simulation and the main simulation. We modelled a dry atmosphere in all cases because of the negligible energy transport by latent heat fluxes at the Yatir forest (Rotenberg and Yakir 2010; Eder et al. 2015). The bottom of the surface domain was taken as a flat surface because of the gentleness of the topography. The preliminary simulation was initialized by the measurements from the shrubland eddy-covariance system and of L_1, together with the balloon measurements of the inversion above the ABL (Sect. 2.2). This LES set-up did not feature a forest canopy and, therefore, simulates the shrubland surrounding the Yatir forest. The numerical values of the input quantities for the preliminary simulation are shown in Table 2, where the roughness length was chosen according to Eder et al. (2015), and the geostrophic wind speed u_0 was calculated from vertically averaging the measured horizontal wind speed at L_1. The geostrophic wind speed, which is also used as an upper boundary condition for the horizontal wind speed, was kept constant to model a constant pressure gradient driving the simulation. The main purpose of the preliminary simulation, whose simulation time was 2 h, was to decouple the spin-up needed to reach a stationary turbulent state from the main simulation.

The main simulation was initialized by the prognostic variables at the end of the preliminary simulation at every grid point, the *PAD* values, and the Q map, which were both rotated into the mean wind direction (315°), while the Coriolis parameters were also adjusted accordingly. The simulated time of the main simulation is 1 h, and data were extracted from the second 30-min period. Due to the applied constant surface heat flux, the value of z_i increases during the simulations. Therefore, we chose the initial z_i value of the preliminary simulation so that the mean measured value of 1402 m (Sect. 2.2) is reproduced in the main simulation. Using $z_i = 1000$ m to initialize the preliminary simulation leads to $z_i = 1350$ m at the start and $z_i = 1450$ m at the end of the main simulation, which satisfied this aim.

Both simulations feature the same grid resolution corresponding to $dx \times dy \times dz = 5.0\ \text{m} \times 7.5\ \text{m} \times 2.5\ \text{m}$, which enables the resolution of the forest canopy with up to six grid levels, and gives reasonable values for the aspect ratios dx_i/dx_j (Maronga et al. 2015). We chose $dx < dy$, as the larger gradients at the forest edges appear along the mean wind direction. Due to the periodic lateral boundary conditions used, the size of the domain had to be of a sufficient size to prevent the self-interaction of the forest. Therefore, we used a domain size of 30.72 km × 15.36 km × 2.56 km, resulting in $6144 \times 2048 \times 1024 \approx 1.3 \times 10^{10}$ grid points. Due to the large amount of grid cells, the simulations were performed at the supercomputing facility SuperMUC (Leong and Kranzlmüller 2015).

Besides the reference LES set-up featuring a geostrophic wind speed of 5.7 m s^{-1}, we also performed two main and corresponding preliminary simulations for geostrophic wind speeds of 2.8 m s^{-1} and zero, keeping constant the other input values as defined in Table 2. We additionally changed the grid dimensions to $4096 \times 2816 \times 1024 \equiv 20.48\ \text{km} \times 21.12\ \text{km} \times 2.56\ \text{km}$ in the latter case to prevent self-interaction from the periodic boundary conditions.

2.5 Structure of Modelling Results

We extracted five different fields from the model results:

- Instantaneous profiles at the positions L_1 and L_2.
- Spatially- and temporally-averaged profiles for six distinct regions: total forest area ($A_{\text{f,tot}}$), total shrubland area ($A_{\text{s,tot}}$), the area of the new, less dense part of the Yatir forest ($A_{\text{f,new}}$), the area of the old, densest part of the Yatir forest ($A_{\text{f,old}}$), a circular area (A_{C1}) centred around L_1 and a circular area (A_{C2}) centred around L_2. Both circles have a diameter of 3 km.
- Temporally-averaged horizontal cross-sections for the total modelling domain with a horizontal resolution of $\Delta x \times \Delta y = 15\ \text{m} \times 15\ \text{m}$.
- Temporally-averaged horizontal cross-sections for a 9 km × 8 km region centred around the Yatir forest at grid resolution.
- Temporally-averaged vertical cross-wind cross-sections, upstream to the Yatir forest ($x = x_u$), intersecting with L_2 ($x = x_{L_2}$), at the trailing forest edge ($x = x_e$), and downstream of the Yatir forest ($x = x_d$). The cross-sections have a resolution $\Delta y \times \Delta z = 15\ \text{m} \times 15\ \text{m}$.

The time averages were performed for the second 30 min of the main simulations. The location of the lidars and the several averaging regions within the modelling domain are depicted in Fig. 3.

3 Results

3.1 Reference Simulation

3.1.1 Comparison with Lidar Data

At first, we compared the measured lidar profiles for the mean horizontal wind speed $\overline{U}$, the mean vertical velocity component $\overline{w}$, and its standard deviation σ_w, with the single profile and spatially-averaged LES profiles at locations L_1 and L_2 (Fig. 4). While the measured profiles were averaged over the early afternoon of the total measurement campaign (Sect. 2.2), the simulated profiles were averaged over 30 min. The standard deviations were calculated with

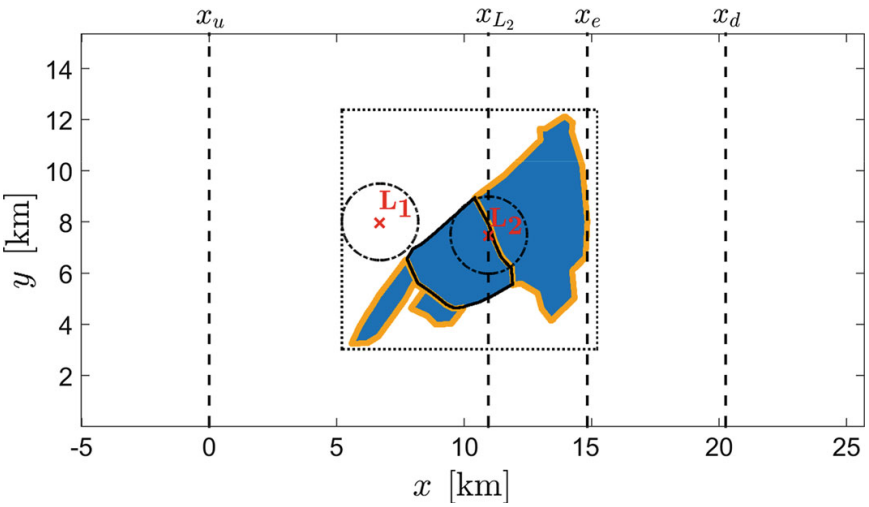

Fig. 3 Location of the LES data fields within the modelling domain. The total forest area $A_{\mathrm{f,tot}}$ is coloured blue and the total shrubland area $A_{\mathrm{s,tot}}$ white. The area of the older part of the Yatir forest $A_{\mathrm{f,old}}$ is bounded by the black solid line, the area of the newer part of the Yatir forest $A_{\mathrm{f,new}}$ by the orange line. The dashed circles around the lidar positions L_1 and L_2 depict the areas A_{C1} and A_{C2}, respectively. The fine dashed line depicts the central region for cross-section data with the grid resolution. The vertical dashed lines depict the positions of the $y{-}z$ planes, labelled by x_u (upstream to the Yatir forest), x_{L_2} (intersecting with L_2), x_e (at the trailing edge of the Yatir forest), and x_d (downstream of the Yatir forest)

respect to time averaging for the single profiles at L_1 and L_2, and with respect to spatial averaging for the areas A_{C1} and A_{C2}.

We find that the simulated values of $\overline{U}$ underestimate the observed values by approximately 1.5 m s^{-1} for $z < 500$ m, and show an opposite behaviour above that height at both lidar positions. The simulated single profiles and the spatially-averaged profiles agree well over the full height range. The strong fluctuations of the measured profiles above 1000 m reflect a weak signal-to-noise ratio and missing data at these altitudes. All three $\overline{U}$ profiles at both lidar positions remain within the standard deviation of the spatially-averaged LES profiles. The $\overline{w}$ profiles show large differences between all three profiles recorded by both lidar instruments. While the measurements show downdrafts for L_1 and updrafts for L_2 nearly throughout the entire ABL, the smoother simulated profiles show downdrafts for both positions. Once more, all three $\overline{w}$ profiles remain within the standard deviation of the spatially-averaged LES profiles, as the standard deviations (σ_w for $\langle L^{\mathrm{sim}} \rangle_C$) are up to one order of magnitude larger than for the $\overline{w}$ profiles. The three σ_w profiles agree well for both lidar positions. However, the maximum amplitude of the measured profile at L_1 is attained at lower heights in comparison with the simulated profiles.

3.1.2 Spatially-Averaged Profiles

Besides the investigation of single profiles at the locations L_1 and L_2 and the areas A_{C1} and A_{C2}, we averaged $\overline{U}$, $\overline{w}$, σ_w, the standard deviation of the horizontal wind speed σ_U, the mean potential temperature $\overline{\theta}$, the vertical turbulent kinematic heat flux $\overline{w'\theta'}$, the friction velocity u_*, and TKE values, $\overline{e}$, for the areas $A_{\mathrm{f,tot}}$, $A_{\mathrm{s,tot}}$, $A_{\mathrm{f,old}}$ and $A_{\mathrm{f,new}}$ (Sect. 2.5), and present them in Fig. 5. All second-order statistics are presented as 30-min time averages of the spatial (co-)variances.

The $\overline{U}$ values are smaller close to the ground for the forest regions, while the profiles converge at a larger altitude. The $\overline{w}$ plot shows updrafts for all three forest areas, where $\langle \overline{w} \rangle_{A_{\mathrm{f,old}}}$ reaches the largest values. The $\langle \overline{w} \rangle_{A_{\mathrm{s,tot}}}$ profile values are one order of magnitude

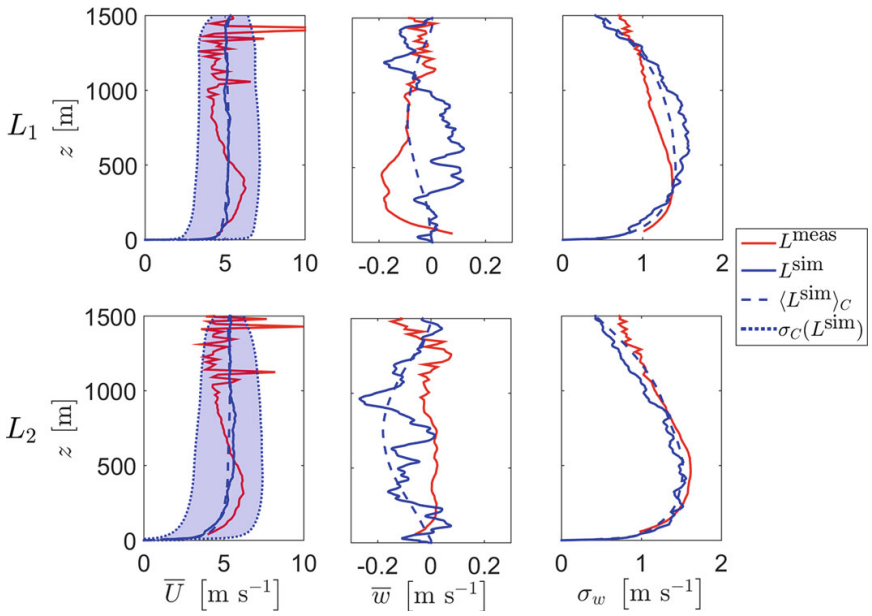

Fig. 4 Comparison of temporally-averaged lidar profiles (red) to temporally-averaged single LES profiles (solid blue) and temporally- and spatially-averaged LES profiles (dashed blue). The time average is performed over the early afternoon of the total measurement campaign in the case of the lidar measurements, and over 30 min in the case of the model results. The spatial averaging is performed for the areas A_{C1} and A_{C2}. The upper row shows $\overline{U}$, $\overline{w}$ and σ_w at L_1 the lower row at L_2. The standard deviations σ_w are calculated with respect to time averaging for L^{meas} and L^{sim}, while the standard deviations for $\langle L^{\mathrm{sim}}\rangle_C$ are calculated with respect to spatial averaging. The light blue domain, which is bounded by the dotted blue lines, depicts the spatial standard deviation of the $\langle L^{\mathrm{sim}}\rangle_C$ profiles for $\overline{U}$

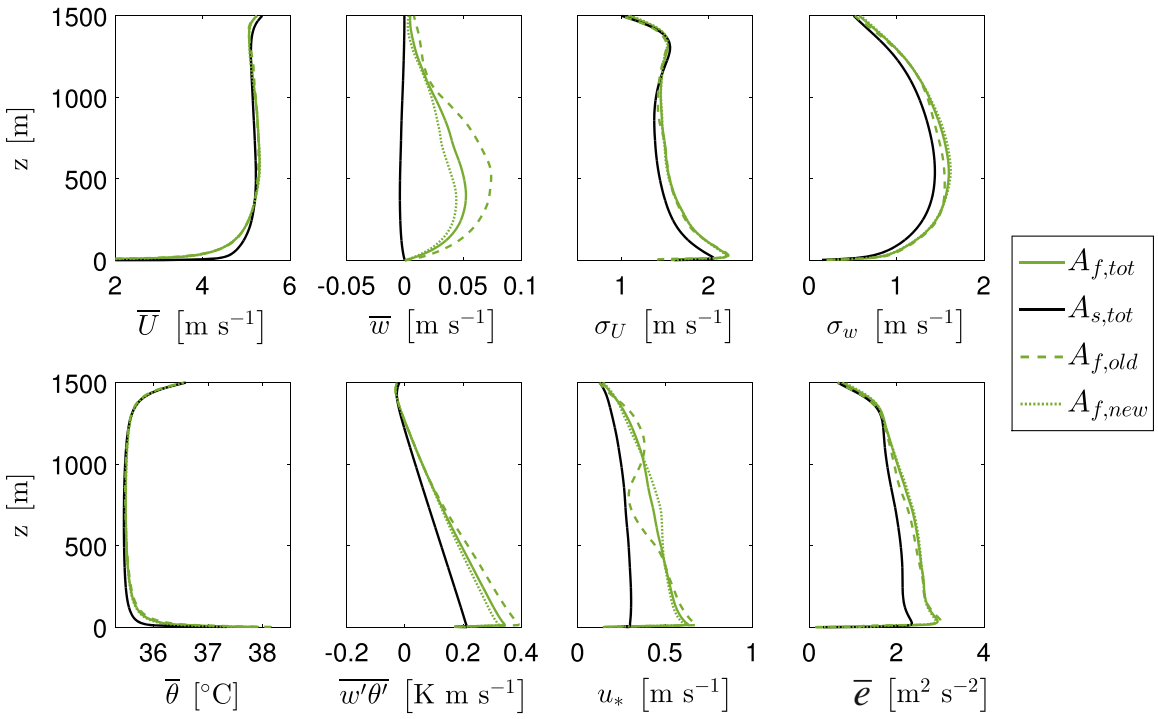

Fig. 5 Comparison of spatially-averaged profiles of $\overline{U}$, $\overline{w}$, σ_U, σ_w, $\overline{\theta}$, $\overline{w'\theta'}$, u_*, and TKE $\overline{e}$ for the four averaging regions $A_{\mathrm{f,tot}}$ (solid green), $A_{\mathrm{s,tot}}$ (solid black), $A_{\mathrm{f,old}}$ (coarse dashed green), and $A_{\mathrm{f,new}}$ (fine dashed green). The second-order statistics are calculated with respect to spatial averaging. Additionally, a 30-min time average was applied to the profiles

smaller than the forest profiles, but show downdrafts over the full range of heights. The potential temperature above the Yatir forest is up to 2 K higher than above the shrubland, where the differences between the individual forest profiles are quite small. The sensible heat flux is up to twice as large above the Yatir forest than above the shrubland, where the largest fluxes occur above the area $A_{\mathrm{f,old}}$ close to the ground. The standard deviations σ_U and σ_w are higher for the forest than for the shrubland, where the difference between the forest patches are small. The profiles of u_* and TKE also attain larger values for the forest than for the shrubland throughout the ABL, where the largest differences appear for u_* values close to the surface.

3.1.3 Horizontal Cross-Sections

Besides one-dimensional profiles, we also extracted horizontal cross-sections of the prognostic variables at different levels above ground, which are resolved on a 15 m × 15 m grid. The temporally-averaged cross-sections of $\overline{u}$, $\overline{v}$, $\overline{w}$ values, and the perturbation of the hydrostatic pressure $\overline{p^*}$ at heights h_c, $z_i/2$, and z_i are shown in Fig. 6. The $\overline{u}$ velocity component experiences a strong dampening shortly above the canopy, which disappears for the other levels. However, a slightly smaller $\overline{u}$ value occurs at height z_i downstream of the area $A_{\mathrm{f,old}}$. A region of roll-like convergence appears for the $\overline{v}$ value at height h_c, again downstream of the area $A_{\mathrm{f,old}}$. This structure, which disappears at height $z_i/2$, becomes a divergence region at z_i. The vertical velocity component $\overline{w}$ does not show features of large-scale circulations at heights h_c and z_i. However, elongated regions of updrafts and downdrafts emerge for the central height, where the location of the largest updrafts coincides with the convergence/divergence region in $\overline{v}$. A reduced $\overline{p^*}$ value occurs in the lee of the Yatir forest at the canopy top with the largest decrease downstream of the area $A_{\mathrm{f,old}}$. At height z_i, a high-pressure region emerges downstream of $A_{\mathrm{f,old}}$.

Figure 7 shows the vertical velocity component at the canopy top ($\overline{w}_{h_c}$) and the lowest-level pressure fluctuations ($\overline{p^*}_0$) at the grid resolution for a smaller horizontal area. For $\overline{w}_{h_c}$, updrafts emerge behind the leading canopy edges, with downdrafts behind the trailing edges, but the updraft regions are smaller. These edge effects occur either at the boundary of the forest (dashed black line in Fig. 7) or at clearings inside the forest (compare with the inset in Fig. 1a). A similar behaviour appears for $\overline{p^*}_0$ values, with larger and lower values behind leading and trailing edges, respectively. However, the extended area of low pressure downstream of the area $A_{\mathrm{f,old}}$ (Fig. 6) is superimposed on those edge effects.

3.2 Variation of the Geostrophic Wind Speed

To investigate the effect of the geostrophic wind speed and, therefore, of atmospheric stability on secondary circulations and surface–atmosphere exchange, we performed two additional simulations using the same set-up as the weakly-convective reference case (see Sect. 2.4), but with the geostrophic wind speeds set to $u_0/2 = 2.85\ \mathrm{m\ s^{-1}}$ and zero to represent mildly- and strongly-convective conditions, respectively. At first we investigated $\overline{w}$ values for the two additional simulations and different averaging regions (Fig. 8), where updrafts above the Yatir forest and downdrafts above the shrubland occur for the entire ABL in both scenarios. The updrafts are approximately twice as strong (in terms of the vertical velocity) for the mildly-convective case than for the weakly-convective case, and one order of magnitude larger for the strongly-convective case (compare Fig. 5). While the value of $\langle\overline{w}\rangle_{A_{\mathrm{f,new}}}$ is larger than $\langle\overline{w}\rangle_{A_{\mathrm{f,old}}}$

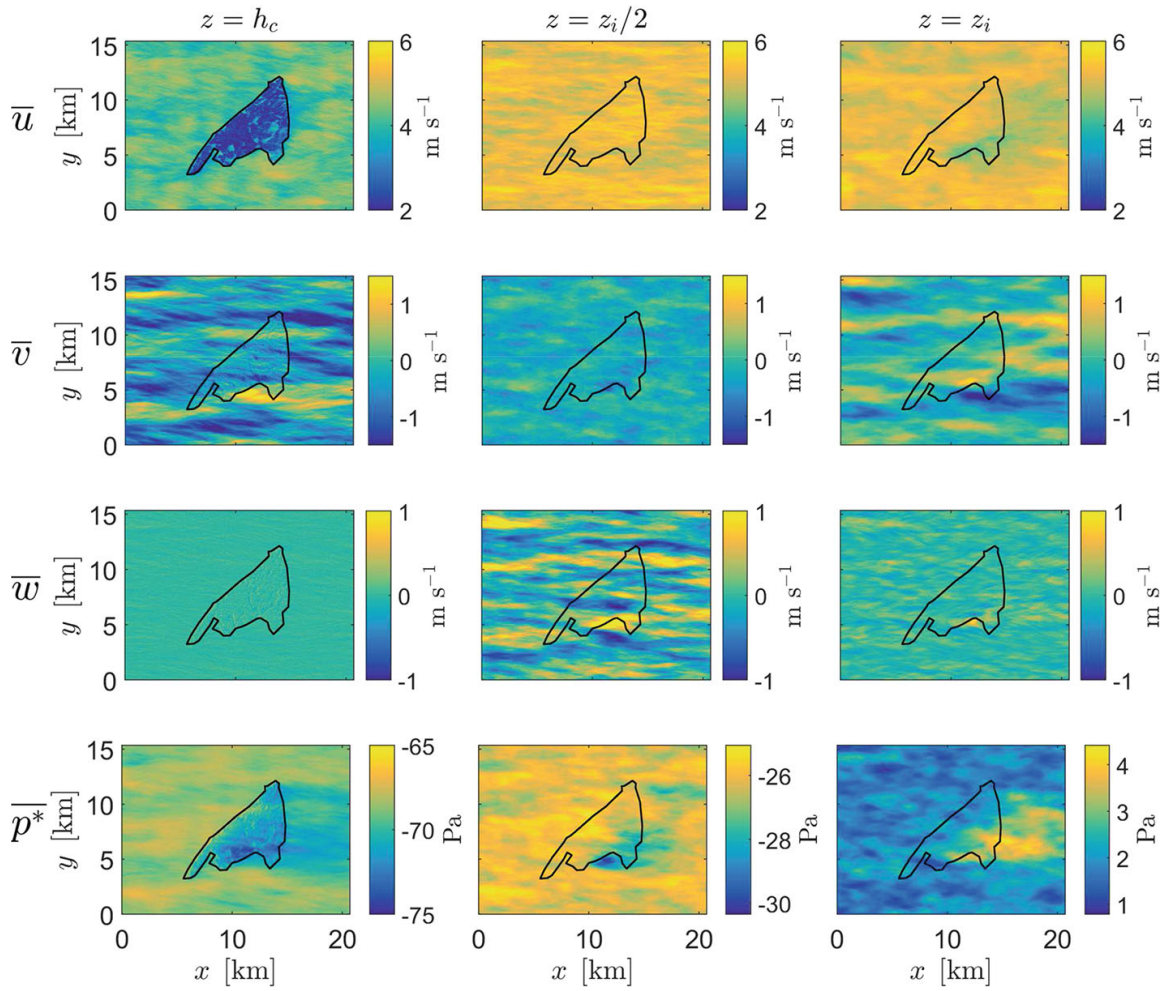

Fig. 6 Horizontal cross-sections of the 30-min time averages of u, v, w, and of the pressure perturbation p^*, at the heights h_c, $z_i/2$ and z_i. Different scales were used for the $\overline{p^*}$ plots. The black solid line depicts boundary of the Yatir forest

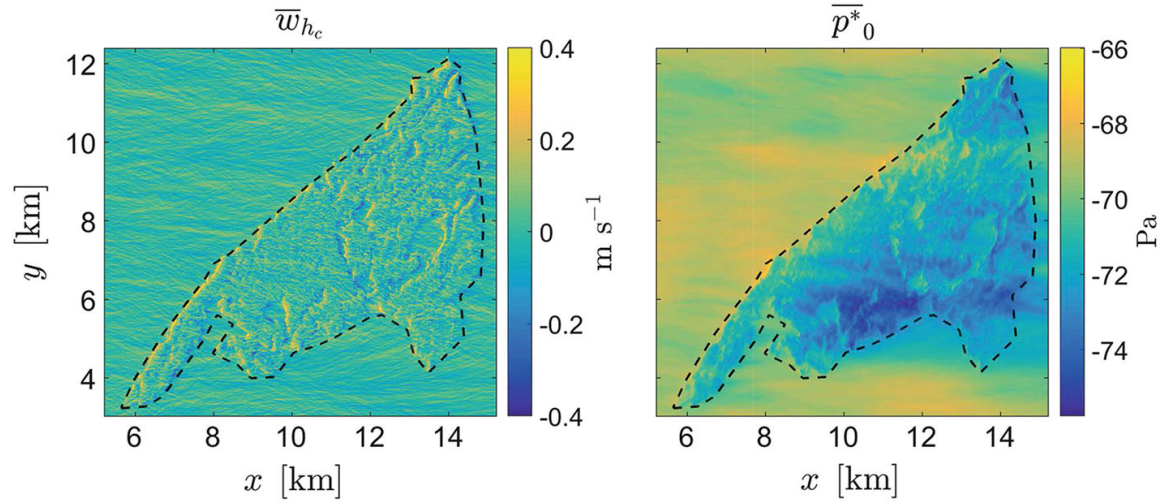

Fig. 7 Horizontal cross-sections of 30-min averages of w_{h_c} and p_0^* at the grid resolution. The black dashed line illustrates the boundary of the Yatir forest

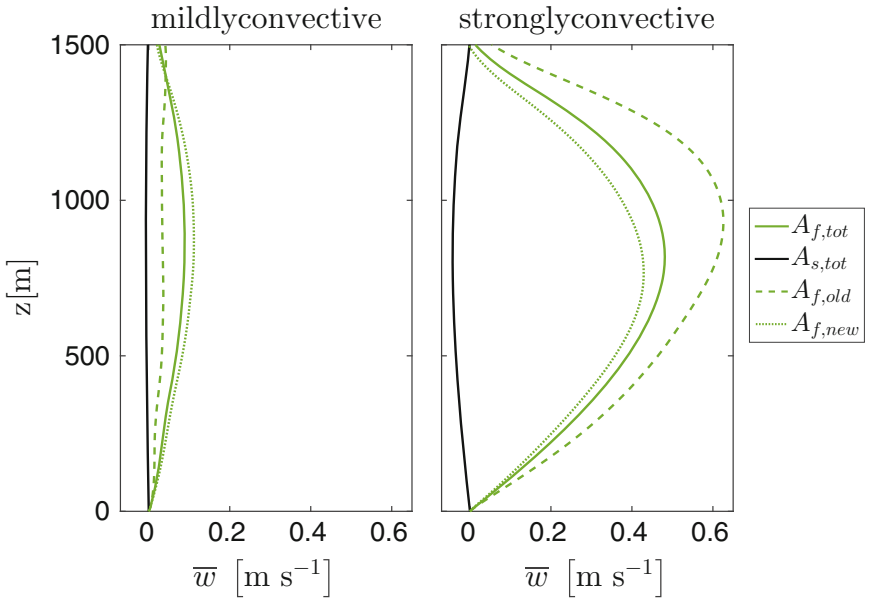

Fig. 8 Profiles of the vertical velocity component $\overline{w}$, spatially-averaged for the regions $A_{\mathrm{f,tot}}$ (solid green), $A_{\mathrm{s,tot}}$ (solid black), $A_{\mathrm{f,old}}$ (coarse dashed green) and $A_{\mathrm{f,new}}$ (fine dashed green). The left and right panels show profiles for the mildly- and strongly-convective cases, respectively

in the mildly-convective case, an opposite relation emerges for the strongly-convective case. The largest updrafts of up to 0.6 m s^{-1} also occur for the strongly-convective simulation.

The investigation of secondary circulations for the two additional simulations by inspection of horizontal cross-sections (Fig. 9) reveals a region of convergence in $\overline{v}$ values downstream of the area $A_{\mathrm{f,old}}$ for the mildly-convective case at height h_c, which is accompanied by an area of low pressure. However, the horizontal distance from the area $A_{\mathrm{f,old}}$ is smaller, and the amplitudes of the velocity fields are larger in comparison with the weakly-convective case. Again, updrafts at height $z_i/2$ and divergence at height z_i appear. In the strongly-convective scenario, the area of low pressure, as well as the secondary circulation, are centred directly above the area $A_{\mathrm{f,old}}$. For $\overline{w}_{z_i/2}$ values, hexagonal cells with strong updrafts above the area $A_{\mathrm{f,old}}$ occur. Besides the extended circulation above the area $A_{\mathrm{f,old}}$, a second circulation appears above the upper right part of the area $A_{\mathrm{f,new}}$, but it is smaller and weaker.

Investigation of the effect of the Yatir forest on the incoming circulations (rolls for the weakly- and mildly-convective cases, and cells for the strongly-convective case) is enabled by plotting in Fig. 10 $y-z$ cross-sections of $\overline{w}$ at the three different x-positions upstream of ($x = x_u$), within ($x = x_{L_2}$ for the weakly- and strongly-convective cases, $x = x_e$ for the mildly-convective case), and downstream from (x_d) the forest as defined in Fig. 3. For the weakly- and mildly-convective cases, the incoming circulations show a similar shape, featuring four regions of updrafts and downdrafts, while the pattern for the strongly-convective case shows eight regions of updrafts and downdrafts, featuring a smaller spatial extension. Strong updrafts emerge at the planes intersecting the forest in all three cases, while the y-position of these updrafts drifts from the forest edge for the weakly-convective case to the forest centre for the strongly-convective case, reaching the largest amplitudes of all considered cases. The x_d cross-sections show similar structures as the corresponding cross-sections for x_u.

Investigation of the heat exchange between the ground and atmosphere from profiles of $\overline{\theta}$, $\overline{w'\theta'}$ and the aerodynamic resistance $r_{aH} = \left[\overline{\theta}_0 - \overline{\theta}(z)\right]/\overline{w'\theta'}$ (Fig. 11) reveals a potential temperature above the Yatir forest exceeding the shrubland values for an increasing

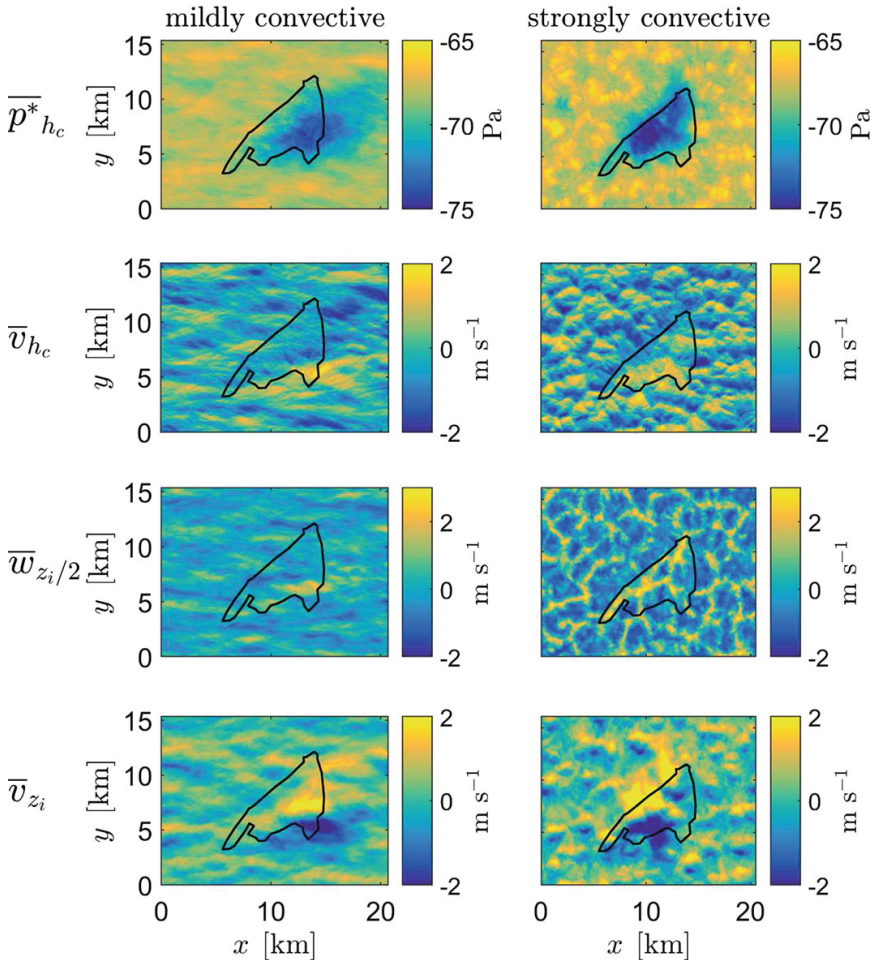

Fig. 9 Investigation of secondary circulations for the mildly- (left column) and strongly-convective (right column) simulations by horizontal cross-sections of the pressure fluctuations ($\overline{p^*}_{h_c}$) and the cross-wind direction ($\overline{v}_{h_c}$) at canopy top (first and second row), the vertical velocity component at $z_i/2$ ($\overline{w}_{z_i/2}$, third row), and the cross-wind direction at z_i ($\overline{v}_{z_i}$, fourth row). The Yatir forest is depicted by the black solid line

height range with decreasing geostrophic wind speed. While the three $\overline{\theta}$ profiles of the forest converge in all three scenarios, clear differences between the scenarios and averaging regions appear for $\overline{w'\theta'}$ values, with $\langle\overline{w'\theta'}\rangle_{A_{\mathrm{f,old}}}$ attaining the largest values throughout the ABL, where the distance to the other forest profiles grows with decreasing geostrophic wind speed; $\langle\overline{w'\theta'}\rangle_{A_{\mathrm{s,tot}}}$ is the smallest for all scenarios. The aerodynamic resistance profiles are larger for the shrubland than for the Yatir forest in all considered cases. While the r_{aH} profiles of the forest converge for the weakly- and mildly-convective cases, the value of $r_{aH}|_{A_{\mathrm{f,old}}}$ is up to 50% smaller than the value of $r_{aH}|_{A_{\mathrm{f,new}}}$ for the strongly-convective scenario, where it remains constant.

Investigation of the temperature differences at the lowest grid level between the Yatir forest and the shrubland (Fig. 12) reveals generally larger forest temperatures than the mean shrubland temperature for all three scenarios, but temperature differences are reduced with decreasing geostrophic wind speed. The reduction is largest for the new part of the forest, and smallest for the old part of the forest, as also indicated in Table 3. Here we have excluded the clearings inside the forest, which show a similar behaviour to the surrounding shrubland, and considered the lowest-level air temperatures at the tree pixels for the different forest patches. The aforementioned decrease of the lowest-level air temperature of the forest with

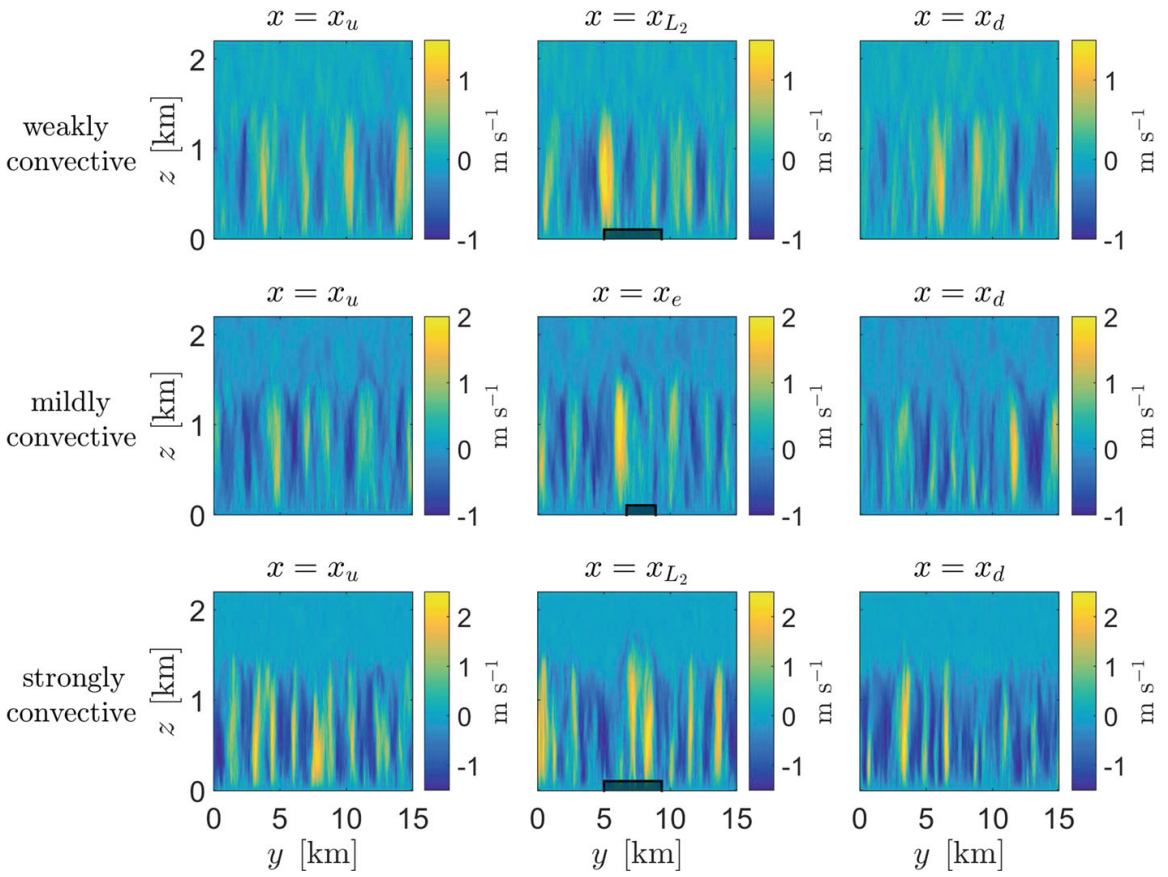

Fig. 10 Vertical $y-z$ cross-sections of $\overline{w}$ values for the weakly-convective (first row), mildly-convective (second row) and strongly-convective (third row) cases upstream of (first column), within (second column), and downstream from (third row) the forest. For the weakly- and strongly-convective cases, the plane intersecting with the location L_2 is used in the second column. For the mildly-convective case, the plane intersecting with the trailing edge of the forest is used. The grey boxes at the bottom of the subplots in the second column depict the extension of the Yatir forest for this specific x-value

Table 3 Fraction of the forest area with a smaller lowest-level air temperature than the mean shrubland value in percent. The first/second/third columns are normalized by $A_{\mathrm{f,tot}}/A_{\mathrm{f,old}}/A_{\mathrm{f,new}}$, respectively

$\Delta\overline{\theta}_0 < 0$	$A_{\mathrm{f,tot}}$	$A_{\mathrm{f,old}}$	$A_{\mathrm{f,new}}$
Weakly convective	0.02	0.01	0.21
Mildly convective	0.65	0.39	0.80
Strongly convective	2.1	0.6	2.9

decreasing geostrophic wind speed leads to a change from 0.01 to 0.6% for the older part, and from 0.21 to 2.9% for the newer part of the forest.

4 Discussion

While we approximately reproduced the observed profiles of $\overline{U}$ and σ_w in the reference simulation (Fig. 4), we were not able to simulate the observed downdrafts and updrafts at the locations L_1 and L_2, respectively, even when applying a spatial average for the circular regions A_{C1} and A_{C2}. However, the observed $\overline{U}$ and $\overline{w}$ profiles remain within a margin of one standard deviation within the simulated profiles for the regions A_{C1} and A_{C2}, which shows a strong spatial variation of the velocity components. To further investigate surface–

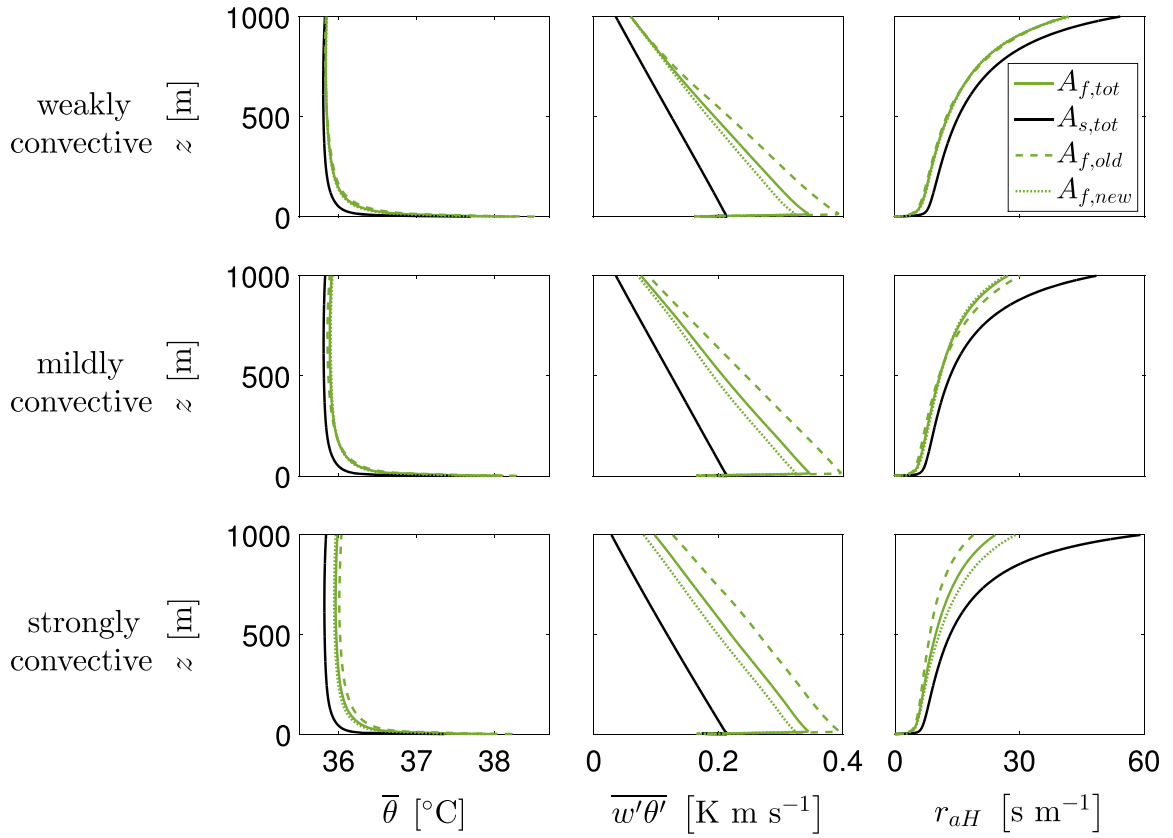

Fig. 11 Comparison of spatially-averaged profiles of $\overline{\theta}$, $\overline{w'\theta'}$ and r_{aH} for the weakly-convective (first row), the mildly-convective (second row) and the strongly-convective (third row) cases. The profiles are averaged for the regions $A_{\mathrm{f,tot}}$ (solid green), $A_{\mathrm{s,tot}}$ (solid black), $A_{\mathrm{f,old}}$ (coarse dashed green), and $A_{\mathrm{f,new}}$ (fine dashed green)

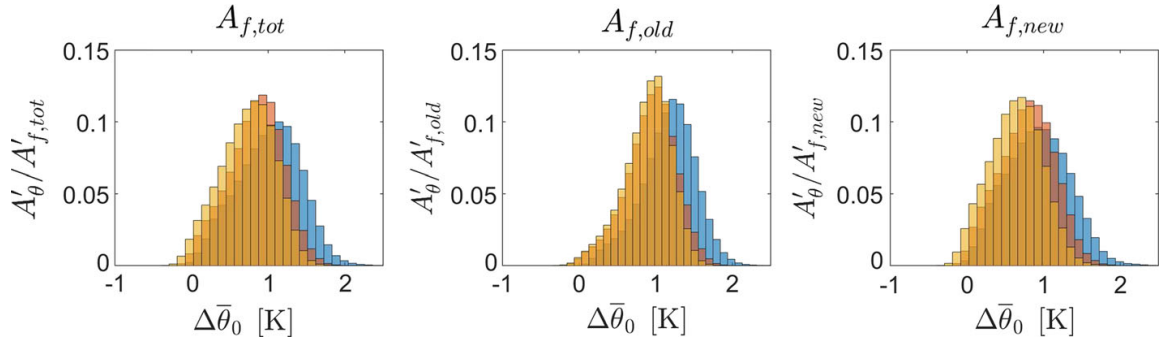

Fig. 12 Air-temperature differences between forest pixels and the mean shrubland temperature at the lowest grid level for the weakly-convective (blue), mildly-convective (orange), and strongly-convective (yellow) simulations. The left, central and right subplots show tree pixels located within the areas $A_{\mathrm{f,tot}}$, $A_{\mathrm{f,old}}$ and $A_{\mathrm{f,new}}$, respectively. The areas of a certain temperature value A'_θ are normalized by the respective total areas of tree pixels ($A'_{\mathrm{f,tot}}$, $A'_{\mathrm{f,old}}$, $A'_{\mathrm{f,new}}$) for the three subplots

atmosphere exchange of the total forest and the total shrubland, we applied a spatial average for the corresponding areas $A_{\mathrm{f,tot}}$ and $A_{\mathrm{s,tot}}$, resulting in updrafts above the Yatir forest and downdrafts above the shrubland (Fig. 5). We also find that the older and denser area of the Yatir forest $A_{\mathrm{f,old}}$ has a larger effect on the updrafts and energy transport by means of the vertical heat flux than the newer and less-dense area $A_{\mathrm{f,new}}$. The larger $\overline{w'\theta'}$ value at the canopy top is mainly explained by stronger heat sources due to the larger tree density of the area $A_{\mathrm{f,old}}$. The stronger heat sources of the forest in comparison with the shrubland also lead

to higher temperatures near the surface inside the Yatir forest. Smaller values of $\overline{U}$ and larger values of σ_U, σ_w, u_* and TKE for the Yatir forest are mainly explained by a larger roughness, the consequent attenuation of the geostrophic wind speed, and mechanical production of turbulence (Banerjee et al. 2017a). Another effect of this canopy-induced attenuation is the occurrence of low-pressure regions in the lee of the Yatir forest (Fig. 6), which is consistent with Cassiani et al. (2008), who performed LES investigations of flow past leading and trailing forest edges in neutral conditions. However, the applied surface heating reduces the region of negative $\overline{w}$ values (Fig. 7) in comparison with the region of lower pressure. As the area $A_{\mathrm{f,old}}$ features the largest *PAI* values, the pressure in the lee of the older part of the forest attains the lowest values (Cassiani et al. 2008; Banerjee et al. 2013; Chatziefstratiou et al. 2014). This low-pressure region downstream of the area $A_{\mathrm{f,old}}$ subsequently triggers convergence (in the $\overline{v}$ component), which leads to the observed updrafts at height $z_i/2$ and divergence at height z_i. Due to its location, this secondary circulation is unable to couple the total forest with the surrounding shrubland to enhance energy transport. Besides the effects due to trailing canopy edges, we also encountered the effects of leading edges (Fig. 7). Strong attenuation of the incoming flow leads to enhanced pressure and updrafts past those edges. However, this effect only features a small horizontal extension of 50–100 m for the *PAD* values of the Yatir forest, which is consistent with numerical studies (Dupont and Brunet 2008; Belcher et al. 2012) and analytical investigations (Belcher et al. 2003; Kröniger et al. 2018) of canopy-edge flow, making it, therefore, of minor importance for surface–atmosphere exchange of the entire forest.

Reducing the geostrophic wind speed from u_0 (weakly-convective scenario) to $u_0/2$ (mildly-convective scenario) and to zero (strongly-convective scenario) in two additional simulations reveals a strong impact on the updrafts above the Yatir forest, with the largest updrafts of 0.06 m s^{-1} for the weakly-convective case (Fig. 5), 0.1 m s^{-1} for the mildly-convective case, and 0.5 m s^{-1} for the strongly-convective case (Fig. 8). An increase in updraft velocity with decreasing geostrophic wind speed is consistent with the discussion of Eder et al. (2015). Considering the different forest patches, stronger updrafts above the area $A_{\mathrm{f,old}}$ than $A_{\mathrm{f,new}}$ are found for the weakly- and strongly-convective cases, which is explained by a larger convective velocity $w_* = \left(g z_i H_0/\overline{\theta}_0\right)^{1/3}$ (Lenschow et al. 1980) above the area $A_{\mathrm{f,old}}$ due to the larger sensible heat fluxes there. However, the value of $\langle\overline{w}\rangle_{A_{\mathrm{f,old}}}$ is smaller than the value of $\langle\overline{w}\rangle_{A_{\mathrm{f,new}}}$ for the mildly-convective scenario as revealed by horizontal $\overline{w}$ cross-sections in Fig. 9. In comparison with the weakly-convective case, the downstream advection of the secondary circulation is reduced. Therefore, the region of strong updrafts is relocated above the area $A_{\mathrm{f,new}}$, while a region of slight downdrafts is located above the area $A_{\mathrm{f,old}}$. Hence, the secondary circulation counteracts the larger w_* above the area $A_{\mathrm{f,old}}$, leading to smaller updrafts. While the secondary circulation for the mildly-convective case is still generated by mechanical effects, buoyancy is the driving force of surface–atmosphere exchange for the strongly-convective scenario, which leads to hexagonal "fishnet" structures (Schmidt and Schumann 1989; Kanak et al. 2000; Fujiwara et al. 2011; Patton et al. 2016; Salesky et al. 2017) for $\overline{w}_{z_i/2}$, and to strong updrafts above the Yatir forest, especially above the area $A_{\mathrm{f,old}}$ (Fig. 9).

The influence of the Yatir forest on the incoming circulations was investigated by inspection of $y{-}z$ cross-sections of $\overline{w}$ upstream of ($x = x_u$), within ($x = x_{L_2}$ for the weakly- and strongly-convective cases, and $x = x_e$ for the mildly-convective case), and downstream from ($x = x_d$) the forest, as shown in Fig. 10. The different structure of the undisturbed velocity field for the weakly-convective/mildly-convective cases and the strongly-convective cases at x_u is again explained by a transition from roll-like circulations for the weakly-

and mildly-convective cases, to fishnet structures for the case of strong convection (Etling and Brown 1993; Maronga and Raasch 2013). The lateral dimensions of these circulations are mainly defined by the boundary-layer height z_i for the fishnet structures, while for the weakly- and mildly-convective cases, larger circulations also appear. The general structure of these circulations is recovered at the downstream plane in all three cases. The impact of the Yatir forest on incoming circulations is influenced by the different driving mechanism for the three cases as depicted by the cross-sections intersecting with the forest. For the weakly- and mildly-convective cases, the secondary circulations are induced by the region of low pressure downstream of the area $A_{\mathrm{f,old}}$ (Fig. 6), while the secondary circulation is mainly driven by buoyancy for the strongly-convective case, which explains the central location, the extension of the updraft region, and the larger values of boundary-layer height above the Yatir forest. The reason why we chose the x_{L_2} plane for the weakly-convective/strongly-convective case and the $x = x_e$ plane for the mildly-convective case is for their exact correspondence to the location of the secondary circulation (Fig. 9). For the weakly- and mildly-convective cases, the secondary circulations are mainly located between the x_{L_2} and x_d planes. However, for the weakly-convective case, the x_{L_2} plane intersects with the uppermost part of the corresponding circulation, while the x_d plane intersects with the lowermost part for the mildly-convective case.

Investigation of the influence of the secondary circulations on surface–atmosphere exchange by analysis of the aerodynamic resistance (Fig. 11) reveals that the value of r_{aH} for the Yatir forest is smaller than for the shrubland in all investigated scenarios because of the larger value of u_* above the forest, and r_{aH} is indirectly proportional to this quantity (Yang et al. 2001). There is a decrease in the value of $r_{aH}|_{A_{\mathrm{f,tot}}}$ for decreasing geostrophic wind speed, which is explained (Banerjee et al. 2017b) by the decrease in the aerodynamic resistance with increasing atmospheric instability, while we expect the same argument to apply to the value $r_{aH}|_{A_{\mathrm{s,tot}}}$. However, while reducing the geostrophic wind speed from u_0 to $u_0/2$ leads to a decrease in the value of $r_{aH}|_{A_{\mathrm{s,tot}}}$, an increase of approximately the same amount occurs for the strongly-convective case resulting from secondary circulations, which are strong enough to decrease the sensible heat flux above the shrubland, leading to an increase of the value of r_{aH} there. Furthermore, the secondary circulations also affect the values of $r_{aH}|_{A_{\mathrm{f,old}}}$ and $r_{aH}|_{A_{\mathrm{f,new}}}$. While the two profiles converge for the weakly- and mildly-convective cases, the value of $r_{aH}|_{A_{\mathrm{f,old}}}$ is nearly 50% smaller than the value of $r_{aH}|_{A_{\mathrm{f,new}}}$ for the strongly-convective scenario. In this case, the updrafts above the area $A_{\mathrm{f,old}}$ and slight downdrafts above the area $A_{\mathrm{f,new}}$ (Fig. 9) affect the value r_{aH} in opposite ways. While the exchange increases above the area $A_{\mathrm{f,old}}$, the downdrafts above the area $A_{\mathrm{f,new}}$ counteract the decrease in r_{aH} resulting from the increase in atmospheric instability, leading to a constant value.

While the surface–atmosphere exchange at the Yatir forest is of sufficient strength to increase the air temperatures above the forest throughout the ABL (Fig. 11), on average, the strength of the exchange is insufficient to fully offset the difference in net radiation to the extent that it may reduce the averaged lowest-level air temperature of the forest below the shrubland value. However, we find that the fraction of the forest featuring lower temperatures than the shrubland increases with decreasing geostrophic wind speed (Fig. 12 and Table 3). In addition, we also find that the lowest temperatures occurred for the area $A_{\mathrm{f,new}}$ and not for the area $A_{\mathrm{f,old}}$, despite the 50% lower r_{aH} values, which also shows that the incoming energy to the Yatir forest cannot be completely compensated by the enhanced surface–atmosphere exchange.

5 Summary and Conclusions

We investigated the influence of secondary circulations on the surface–atmosphere exchange of the isolated semi-arid Yatir forest by means of the LES approach by using the PALM software, and deduced the location and extension of those circulations, including their triggering mechanisms for varying geostrophic wind speeds. We also extracted the effect of the secondary circulations on the updrafts above different regions of the forest, and quantified the effects of the secondary circulations on the surface–atmosphere exchange of energy by investigating the aerodynamic resistance and the impact on air temperatures inside the Yatir forest.

To construct a virtual copy of the Yatir forest canopy, we used a threshold-based approach to infer the tree density from satellite data alongside the measurements of *PAI* and *PAD* values. A vertical grid spacing of 2.5 m enabled the resolution of the forest canopy in to several layers, and the application of the PALM canopy scheme (Brown and Covey 1966; Shaw and Schumann 1992; Watanabe 2004; Bohrer et al. 2009; Maronga et al. 2015). We initialized the simulations with lidar, eddy-covariance and radiosonde measurements described by Brugger et al. (2018) averaged for 2-h intervals in the early afternoon of seven consecutive days. We performed three LES set-ups with varying geostrophic wind speed to investigate the impact on the surface–atmosphere exchange, with the reference simulation based on the actual geostrophic wind speed u_0 according to lidar measurements, and reduced to values of $u_0/2$ and zero for the other two simulations corresponding to weakly-, mildly-convective and strongly-convective conditions, respectively. As atmospheric stability significantly affects the boundary-layer dynamics above canopies (Patton et al. 2016), the three scenarios also represent surface–atmosphere interactions at the Yatir forest at different times of the day.

Due to the large computational demand of the LES approach, we extracted data for a single 30-min interval. This short-term statistical approach prevented reproduction of the observed updrafts above the Yatir forest, as well as the observed downdrafts above the shrubland from the reference simulation. However, the spatial standard deviation of the LES results within 3 km of the lidars indicates large spatial fluctuations of the flow variables. From investigation of the flow variables above the total forest area $A_{\mathrm{f,tot}}$, as well as above the total shrubland area $A_{\mathrm{s,tot}}$, updrafts above the forest, and downdrafts above the shrubland were replicated. A decrease in geostrophic wind speed increases the strength of these updrafts and downdrafts, which is consistent with Eder et al. (2015), with the strongest updrafts occurring above the region of the older, denser part of the Yatir forest $A_{\mathrm{f,old}}$.

Besides investigating secondary circulations by means of spatially-averaged $\overline{w}$ profiles, we also investigated cross-sections of the prognostic variables, illustrating horizontally-extended secondary circulations spanning the full ABL for all three LES set-ups. These secondary circulations are mainly produced by mechanical effects for the weakly- and mildly-convective cases, while buoyancy is the driving force in the strongly-convective case. In all three cases, the secondary circulations do not couple the full forest to the shrubland due to the location and size of these structures, which indicates that the Yatir forest is too large to interact with the surrounding shrubland by a single secondary circulation. Therefore, downdrafts also appear above the Yatir forest, decreasing the surface–atmosphere exchange of energy with respect to a smaller forest, and resulting in the interaction with the atmosphere by a single circulation. While the flow across the trailing edge of the old part of the forest triggers the secondary circulations in the weakly- and mildly-convective cases, we find that the leading canopy edges have a minor effect on the surface–atmosphere exchange of the Yatir forest. From investigation of the vertical cross-sections upstream of, within, and downstream from

the forest, we identified the influence of the forest canopy on the incoming circulations, with the largest impact detected for the strongly-convective scenario, where the updrafts have a significant effect on the height of the boundary layer above the Yatir forest.

To quantify the influence of secondary circulations on the surface–atmosphere exchange, we investigated profiles of aerodynamic resistance, detecting a higher resistance for the shrubland than for the Yatir forest in all investigated cases, and finding a decreasing aerodynamic resistance with decreasing geostrophic wind speed from a value of u_0 to $u_0/2$. These findings are again consistent with Banerjee et al. (2017b) and the statement of Eder et al. (2015) concerning the suppressing mechanism of the geostrophic wind speed on the canopy-convector effect. However, for the strongly-convective scenario, we encountered a strong influence of the secondary circulations on aerodynamic resistance, leading to an increase in r_{aH} above the shrubland for increasing atmospheric instability. In contrast, the secondary circulations enhance the surface–atmosphere exchange in the updraft regions, mainly above the area $A_{\mathrm{f,old}}$. We also find that the heat exchange of different forest regions with the atmosphere is still not sufficiently strong to counteract the incoming radiative energy, which results in higher mean air temperatures inside the Yatir forest than for the shrubland in all cases. However, there is an increased effect of the forest area with a lower air temperature than the shrubland for a decreasing geostrophic wind speed, which is a signature of the canopy-convector effect. The result that the surface–atmosphere exchange is unable to overcome the incoming radiative energy also explains the higher air temperatures inside the older than inside the newer, less dense, part of the Yatir forest, despite the lower r_{aH} values.

For the special case of the Yatir forest, our case study gives a good understanding of the processes affecting energy transport between the forest canopy and the atmosphere. The effect of secondary circulations on the surface–atmosphere exchange on the temperatures inside the forest could also be considered in further studies of isolated ecosystems, or be used for recommendations for successful afforestation efforts in semi-arid regions. Moreover, idealized studies on the aerodynamic resistance of heterogeneous surfaces should be helpful for gaining a deeper understanding of the effect of secondary circulations on the surface–atmosphere exchange for isolated ecosystems, such as the Yatir forest.

Acknowledgements We are grateful to Michael Sprintsin of the Jewish National Fund (KKL-JNF) for his advice and infrastructure regarding the PAI measurements. We are also grateful to the team of the Earth and Planetary Sciences Department of the Weizmann Institute for Science for providing the eddy-covariance data used to initialize the LES model. We also thank the PALM group at Leibniz University Hannover for their open-source PALM code and their support. Furthermore, the authors gratefully acknowledge the Gauss Centre for Supercomputing e.V. (http://www.gauss-centre.eu) for funding this project by providing computing time on the GCS Supercomputer SuperMUC at the Leibniz Supercomputing Centre (LRZ, www.lrz.de). This research was supported by the German Research Foundation (DFG) as part of the project "Climate feedbacks and benefits of semiarid forests (CliFF)" and the project "Capturing all relevant scales of biosphere–atmosphere exchange—the enigmatic energy balance closure problem", which is funded by the Helmholtz-Association through the President's Initiative and Networking Fund, and by KIT.

References

Albertson JD, Parlange MB (1999) Surface length scales and shear stress: Implications for land-atmosphere interaction over complex terrain. Water Resour Res 35(7):2121–2132. https://doi.org/10.1029/1999WR900094

Anderson-Teixeira KJ, Delong JP, Fox AM, Brese DA, Litvak ME (2011) Differential responses of production and respiration to temperature and moisture drive the carbon balance across a climatic gradient in new mexico. Glob Change Biol 17(1):410–424. https://doi.org/10.1111/j.1365-2486.2010.02269.x

Arakawa A, Lamb VR (1977) Computational design of the basic dynamical processes of the UCLA general circulation model. Methods Comput Phys 17:173–265. https://doi.org/10.1016/B978-0-12-460817-7.50009-4

Arneth A, Harrison SP, Zaehle S, Tsigaridis K, Menon S, Bartlein PJ, Feichter J, Korhola A, Kulmala M, O'donnell D et al (2010) Terrestrial biogeochemical feedbacks in the climate system. Nat Geosci 3(8):525. https://doi.org/10.1038/ngeo905

Avissar R, Eloranta EW, Gürer K, Tripoli GJ (1998) An evaluation of the large-eddy simulation option of the regional atmospheric modeling system in simulating a convective boundary layer: a FIFE case study. J Atmos Sci 55(7):1109–1130. https://doi.org/10.1175/1520-0469(1998)055<1109:AEOTLE>2.0.CO;2

Bailey BN, Overby M, Willemsen P, Pardyjak ER, Mahaffee WF, Stoll R (2014) A scalable plant-resolving radiative transfer model based on optimized GPU ray tracing. Agric For Meteorol 198:192–208. https://doi.org/10.1016/j.agrformet.2014.08.012

Banerjee T, Katul G, Fontan S, Poggi D, Kumar M (2013) Mean flow near edges and within cavities situated inside dense canopies. Boundary-Layer Meteorol 149(1):19–41. https://doi.org/10.1007/s10546-013-9826-x

Banerjee T, Brugger P, De Roo F, Kröniger K, Yakir D, Rotenberg E, Mauder M (2017a) Turbulent transport of energy across a forest and a semi-arid shrubland. Atmos Chem Phys Discuss pp 1–21. https://doi.org/10.5194/acp-2017-159

Banerjee T, De Roo F, Mauder M (2017b) Explaining the convector effect in canopy turbulence by means of large-eddy simulation. Hydrol Earth Syst Sci pp 1–20. https://doi.org/10.5194/hess-2017-4

Belcher SE, Jerram N, Hunt JCR (2003) Adjustment of a turbulent boundary layer to a canopy of roughness elements. J Fluid Mech 488:369–398. https://doi.org/10.1017/s0022112003005019

Belcher SE, Harman IN, Finnigan JJ (2012) The wind in the willows: flows in forest canopies in complex terrain. Annu Rev Fluid Mech 44:479–504. https://doi.org/10.1146/annurev-fluid-120710-101036

Betts RA (2000) Offset of the potential carbon sink from boreal forestation by decreases in surface albedo. Nature 408(6809):187. https://doi.org/10.1038/35041545

Bohrer G, Katul GG, Walko RL, Avissar R (2009) Exploring the effects of microscale structural heterogeneity of forest canopies using large-eddy simulations. Boundary-Layer Meteorol 132(3):351–382. https://doi.org/10.1007/s10546-009-9404-4

Bonan GB (2008) Forests and climate change: forcings, feedbacks, and the climate benefits of forests. Science 320(5882):1444–1449. https://doi.org/10.1126/science.1155121

Bou-Zeid E, Meneveau C, Parlange MB (2004) Large-eddy simulation of neutral atmospheric boundary layer flow over heterogeneous surfaces: Blending height and effective surface roughness. Water Resour Res 40(2). https://doi.org/10.1029/2003WR002475

Brown KW, Covey W (1966) The energy-budget evaluation of the micrometeorological transfer processes within a cornfield. Agric Meteorol 3(1–2):73–96. https://doi.org/10.1016/0002-1571(66)90006-9

Browning KA, Wexler R (1968) The determination of kinematic properties of a wind field using doppler radar. J Appl Meteorol 7(1):105–113. https://doi.org/10.1175/1520-0450(1968)007<0105:TDOKPO>2.0.CO;2S

Brugger P, Banerjee T, De Roo F, Kröniger K, Qubaja R, Rohatyn S, Rotenberg E, Tatarinov F, Yakir D, Yang F, Mauder M (2018) Effect of surface heterogeneity on the boundary layer height: a case study at a semi-arid forest. Boundary-Layer Meteorol. https://doi.org/10.1007/s10546-018-0371-5

Cassiani M, Katul GG, Albertson JD (2008) The effects of canopy leaf area index on airflow across forest edges: large-eddy simulation and analytical results. Boundary-Layer Meteorol 126(3):433–460. https://doi.org/10.1007/s10546-007-9242-1

Chatziefstratiou EK, Velissariou V, Bohrer G (2014) Resolving the effects of aperture and volume restriction of the flow by semi-porous barriers using large-eddy simulations. Boundary-Layer Meteorol 152(3):329–348. https://doi.org/10.1007/s10546-014-9923-5

Chen JM (1996) Optically-based methods for measuring seasonal variation of leaf area index in boreal conifer stands. Agric For Meteorol 80(2–4):135–163. https://doi.org/10.1016/0168-1923(95)02291-0

Dayan U, Levy I (2002) Relationship between synoptic-scale atmospheric circulation and ozone concentrations over Israel. J Geophys Res Atmos 107(D24). https://doi.org/10.1029/2002JD002147

Deardorff JW (1980) Stratocumulus-capped mixed layers derived from a three-dimensional model. Boundary-Layer Meteorol 18(4):495–527. https://doi.org/10.1007/BF00119502

Dupont S, Brunet Y (2008) Edge flow and canopy structure: a large-eddy simulation study. Boundary-Layer Meteorol 126(1):51–71. https://doi.org/10.1007/s10546-007-9216-3

Eder F, De Roo F, Rotenberg E, Yakir D, Schmid HP, Mauder M (2015) Secondary circulations at a solitary forest surrounded by semi-arid shrubland and their impact on eddy-covariance measurements. Agric For Meteorol 211–212:115–127. https://doi.org/10.1016/j.agrformet.2015.06.001

Etling D, Brown RA (1993) Roll vortices in the planetary boundary layer: a review. Boundary-Layer Meteorol 65(3):215–248. https://doi.org/10.1007/BF00705527

Finnigan JJ, Shaw RH, Patton EG (2009) Turbulence structure above a vegetation canopy. J Fluid Mech 637:387–424. https://doi.org/10.1017/S0022112009990589

Fujiwara C, Yamashita K, Nakanishi M, Fujiyoshi Y (2011) Dust devil-like vortices in an urban area detected by a 3d scanning doppler lidar. J Appl Meteorol Clim 50(3):534–547. https://doi.org/10.1175/2010JAMC2481.1

Garcia-Carreras L, Parker DJ, Taylor CM, Reeves CE, Murphy JG (2010) Impact of mesoscale vegetation heterogeneities on the dynamical and thermodynamic properties of the planetary boundary layer. J Geophys Res Atmos 115(D3). https://doi.org/10.1029/2009JD012811

Garcia-Carreras L, Parker DJ, Marsham JH (2011) What is the mechanism for the modification of convective cloud distributions by land surface-induced flows? J Atmos Sci 68(3):619–634. https://doi.org/10.1175/2010JAS3604.1

Grant ER, Ross AN, Gardiner BA (2016) Modelling canopy flows over complex terrain. Boundary-Layer Meteorol 161(3):417–437. https://doi.org/10.1007/s10546-016-0176-3

Harlow FH, Welch JE (1965) Numerical calculation of time-dependent viscous incompressible flow of fluid with free surface. Phys Fluids 8(12):2182–2189. https://doi.org/10.1063/1.1761178

Hechtel LM, Stull RB, Moeng CH (1990) The effects of nonhomogeneous surface fluxes on the convective boundary layer: a case study using large-eddy simulation. J Atmos Sci 47(14):1721–1741. https://doi.org/10.1175/1520-0469(1990)047<1721:TEONSF>2.0.CO;2

Huang HY, Margulis SA (2009) On the impact of surface heterogeneity on a realistic convective boundary layer. Water Resour Res 45(4). https://doi.org/10.1029/2008WR007175

Huang HY, Margulis SA (2010) Evaluation of a fully coupled large-eddy simulation-land surface model and its diagnosis of land-atmosphere feedbacks. Water Resour Res 46(6). https://doi.org/10.1029/2009WR008232

Kanak KM, Lilly DK, Snow JT (2000) The formation of vertical vortices in the convective boundary layer. Q J R Meteorol Soc 126(569):2789–2810. https://doi.org/10.1002/qj.49712656910

Kenny WT, Bohrer G, Morin TH, Vogel CS, Matheny AM, Desai AR (2017) A numerical case study of the implications of secondary circulations to the interpretation of eddy-covariance measurements over small lakes. Boundary-Layer Meteorol 165(2):311–332. https://doi.org/10.1007/s10546-017-0268-8

Kröniger K, Banerjee T, De Roo F, Mauder M (2018) Flow adjustment inside homogeneous canopies after a leading edge-An analytical approach backed by LES. Agric For Meteorol 255:17–30. https://doi.org/10.1016/j.agrformet.2017.09.019

Leblanc SG, Chen JM, Fernandes R, Deering DW, Conley A (2005) Methodology comparison for canopy structure parameters extraction from digital hemispherical photography in boreal forests. Agric For Meteorol 129(3):187–207. https://doi.org/10.1016/j.agrformet.2004.09.006

Lenschow DH, Wyngaard JC, Pennell WT (1980) Mean-field and second-moment budgets in a baroclinic, convective boundary layer. J Atmos Sci 37(6):1313–1326. https://doi.org/10.1175/1520-0469(1980)037<1313:MFASMB>2.0.CO;2

Leong SH, Kranzlmüller D (2015) A case study–cost of preemption for urgent computing on SuperMUC. In: Kunkel J, Ludwig T (eds) High performance computing. ISC High Performance 2015. Lecture Notes in Computer Science, Springer, vol 9137

Maronga B, Raasch S (2013) Large-eddy simulations of surface heterogeneity effects on the convective boundary layer during the LITFASS-2003 experiment. Boundary-Layer Meteorol 146(1):17–44. https://doi.org/10.1007/s10546-012-9748-z

Maronga B, Gryschka M, Heinze R, Hoffmann F, Kanani-Shring F, Keck M, Ketelsen K, Letzel MO, Shring M, Raasch S (2015) The parallelized large-eddy simulation model (PALM) version 4.0 for atmospheric and oceanic flows: model formulation, recent developments, and future perspectives. Geosci Model Dev 8(8):2515–2551. https://doi.org/10.5194/gmd-8-2515-2015

Matsuda K, Onishi R, Takahashi K (2017) Tree-crown-resolving large-eddy simulation coupled with three-dimensional radiative transfer model. J Wind Eng Ind Aerodyn 173:53–66. https://doi.org/10.1016/j.jweia.2017.11.015

Mauder M, Cuntz M, Drüe C, Graf A, Rebmann C, Schmid HP, Schmidt M, Steinbrecher R (2013) A strategy for quality and uncertainty assessment of long-term eddy-covariance measurements. Agric For Meteorol 169:122–135. https://doi.org/10.1016/j.agrformet.2012.09.006

Mayhead GJ (1973) Some drag coefficients for British forest trees derived from wind tunnel studies. Agric Meteorol 12:123–130. https://doi.org/10.1016/0002-1571(73)90013-7

Miller NE, Stoll R (2013) Surface heterogeneity effects on regional-scale fluxes in the stable boundary layer: aerodynamic roughness length transitions. Boundary-Layer Meteorol 149(2):277–301. https://doi.org/10.1007/s10546-013-9839-5

Päschke E, Leinweber R, Lehmann V (2015) An assessment of the performance of a 1.5 μm doppler lidar for operational vertical wind profiling based on a 1-year trial. Atmos Meas Tech 8(6):2251. https://doi.org/10.5194/amt-8-2251-2015

Patton EG, Sullivan PP, Moeng CH (2005) The influence of idealized heterogeneity on wet and dry planetary boundary layers coupled to the land surface. J Atmos Sci 62(7):2078–2097. https://doi.org/10.1175/JAS3465.1

Patton EG, Sullivan PP, Shaw RH, Finnigan JJ, Weil JC (2016) Atmospheric stability influences on coupled boundary layer and canopy turbulence. J Atmos Sci 73(4):1621–1647. https://doi.org/10.1175/JAS-D-15-0068.1

Prabha TV, Karipot A, Binford MW (2007) Characteristics of secondary circulations over an inhomogeneous surface simulated with large-eddy simulation. Boundary-Layer Meteorol 123(2):239–261. https://doi.org/10.1007/s10546-006-9137-6

Raupach MR, Finnigan JJ (1995) Scale issues in boundary-layer meteorology: surface energy balances in heterogeneous terrain. Hydrol Proc 9(5–6):589–612. https://doi.org/10.1002/hyp.3360090509

Rotenberg E, Yakir D (2010) Contribution of semi-arid forests to the climate system. Science 327(5964):451–454. https://doi.org/10.1126/science.1179998

Rotenberg E, Yakir D (2011) Distinct patterns of changes in surface energy budget associated with forestation in the semiarid region. Glob Change Biol 17(4):1536–1548. https://doi.org/10.1111/j.1365-2486.2010.02320.x

Salesky ST, Chamecki M, Bou-Zeid E (2017) On the nature of the transition between roll and cellular organization in the convective boundary layer. Boundary-Layer Meteorol 163(1):41–68. https://doi.org/10.1007/s10546-016-0220-3

Schlegel F, Stiller J, Bienert A, Maas HG, Queck R, Bernhofer C (2015) Large-eddy simulation study of the effects on flow of a heterogeneous forest at sub-tree resolution. Boundary-Layer Meteorol 154(1):27–56. https://doi.org/10.1007/s10546-014-9962-y

Schmidt H, Schumann U (1989) Coherent structure of the convective boundary layer derived from large-eddy simulations. J Fluid Mech 200:511–562. https://doi.org/10.1017/S0022112089000753

Shaw RH, Schumann U (1992) Large-eddy simulation of turbulent flow above and within a forest. Boundary-Layer Meteorol 61(1–2):47–64. https://doi.org/10.1007/bf02033994

Sprintsin M, Karnieli A, Berliner P, Rotenberg E, Yakir D, Cohen S (2007) The effect of spatial resolution on the accuracy of leaf area index estimation for a forest planted in the desert transition zone. Remote Sens Environ 109(4):416–428. https://doi.org/10.1016/j.rse.2007.01.020

Sprintsin M, Cohen S, Maseyk K, Rotenberg E, Grünzweig J, Karnieli A, Berliner P, Yakir D (2011) Long term and seasonal courses of leaf area index in a semi-arid forest plantation. Agric For Meteorol 151(5):565–574. https://doi.org/10.1016/j.agrformet.2011.01.001

Takeda T, Oguma H, Sano T, Yone Y, Fujinuma Y (2008) Estimating the plant area density of a Japanese larch (Larix kaempferi Sarg.) plantation using a ground-based laser scanner. Agric For Meteorol 148(3):428–438. https://doi.org/10.1016/j.agrformet.2007.10.004

Wang W (2009) The influence of thermally-induced mesoscale circulations on turbulence statistics over an idealized urban area under a zero background wind. Boundary-Layer Meteorol 131(3):403–423. https://doi.org/10.1007/s10546-009-9378-2

Watanabe T (2004) Large-eddy simulation of coherent turbulence structures associated with scalar ramps over plant canopies. Boundary-Layer Meteorol 112(2):307–341. https://doi.org/10.1023/b:boun.0000027912.84492.54

Yang K, Tamai N, Koike T (2001) Analytical solution of surface layer similarity equations. J Appl Meteorol 40(9):1647–1653 https://doi.org/10.1175/1520-0450(2001)040<1647:ASOSLS>2.0.CO;2

D | Aerodynamic resistance parametrization for heterogeneous surfaces

Kröniger, K., Katul, G. G., De Roo, F., Brugger, P., and Mauder, M. (2018). Aerodynamic resistance parametrization for heterogeneous surfaces using structural function approaches. *J. Atmos. Sci.*, (under review)

JOURNAL OF THE ATMOSPHERIC SCIENCES

Aerodynamic resistance parametrization for heterogeneous surfaces using a covariance function approach in spectral space

KONSTANTIN KRÖNIGER* AND GABRIEL G. KATUL† AND FREDERIK DE ROO AND PETER BRUGGER AND MATTHIAS MAUDER

Institute of Meteorology and Climate Research, Atmospheric Environmental Research, Karlsruhe Institute of Technology

ABSTRACT

Simulating the influence of heterogeneous surfaces on atmospheric flow using meso-scale models (MSM) remains a challenging task, as the resolution of these models usually prohibits resolving important scales of surface heterogeneity. However, surface heterogeneities strongly impact fluxes of momentum, heat or moisture, which act as boundary conditions for MSM. Even though several approaches for parametrizing subgrid-scale heterogeneities in MSM exist, many of these approaches rely on Monin–Obukhov similarity theory, preventing those models from resolving all scales of surface heterogeneity. To include these residual heterogeneity scales, we derive a novel heterogeneity parametrization by linking the heterogeneous covariance function in spectral space to an associated homogeneous one. This covariance function approach is subsequently used to derive a parametrization of the aerodynamic resistance to heat transfer. Here the effect of surface heterogeneity enters as a factor applied to the stability correction functions of the bulk similarity approach. To compare the covariance function approach against the conventional bulk similarity and tile approaches, large-eddy simulations (LES) of distinct surface heterogeneities are performed. The aerodynamic resistances from these three parametrizations are subsequently tested against the LES reference by resolving the surface heterogeneities with six different test-MSM grids of varying cell dimension. The results of this comparison show that the covariance function approach yields the smallest deviations from the LES reference. In addition, the smallest deviation of the covariance function approach to the reference is observed for the LES with the largest surface heterogeneity, which illustrates the advantage of using this novel parametrization for MSM.

1. Introduction

While the significance of surface-atmosphere exchanges of momentum, heat, or moisture is rarely in dispute, their representation in numerical weather, climate or hydrological simulations remains a subject of inquiry. The barrier to progress in representing these exchanges in large-scale models are linked to non-linearities associated with the underlying processes and the multi-scaled heterogeneity of the land surface itself. Meso-scale models (MSM) usually feature grid resolutions of one to several hundred kilometers (e.g., Fujita 1986; King et al. 2007), which prevents these numerical models from resolving fine-scaled heterogeneity (e.g., forest patches, mountains, lakes) that interact with or influence the spectrum of turbulence. To account for such 'subgrid-scale' heterogeneities, several parametrizations are used in MSM. The common one employs Monin-Obukhov similarity theory (MOST) to link a local flux to a meteorological variable such as mean velocity or scalar concentration, even if this theory applies to planar homogeneous surfaces. A straight forward application of MOST to cell-averaged surface parameters (bulk similarity) continues to be in use within many MSM (e.g. Mahrt 1996; Brutsaert 1998). However, there is mounting evidence from large-eddy simulation (LES) studies that such usage of bulk similarity may be problematic (Stoll and Porté-Agel 2009) with increasing surface heterogeneity.

To improve bulk similarity arguments, "discrete approaches" are often used to parametrize subgrid scale heterogeneity (Giorgi and Avissar 1997). These parametrizations rely on a fragmentation of the MSM grid cells into several surface "patches", where MOST is applied to individual patches. The overall impact of the surface on the atmosphere is subsequently aggregated from these patches. Within discrete approaches, different methods also exist

*Corresponding author address: Institute of Meteorology and Climate Research, Atmospheric Environmental Research (IMK-IFU), Karlsruhe Institute of Technology (KIT), Kreuzeckbahnstrasse 19, 82467 Garmisch-Partenkirchen, Germany
E-mail: konstantin.kroeniger@kit.edu

†Current affiliation: Nicholas School of the Environment and Earth Sciences, Duke University

based on the definition of surface patch. While in "mosaic" approaches, subgrid scale models are operated on actual surface patches within a grid cell (Koster and Suarez 1992; Giorgi and Avissar 1997; de Vrese et al. 2016), in "tile" or "mixture" approaches only the area fraction of a certain surface type, irrespective of the spatial organisation, is considered (Avissar and Pielke 1989; Koster and Suarez 1992; Stoll and Porté-Agel 2009; de Vrese et al. 2016; de Vrese and Hagemann 2016). Even if the mosaic approach was shown to yield better results than the tile approach (e.g., Koster and Suarez 1992), it is computationally much more expensive. Besides the definition of the surface patches, the aggregation of the patches to the overall effect of the grid cell is performed in two different manners. Either by aggregating the turbulent fluxes of the patches to the flux of the whole cell (flux aggregation), or by aggregating the surface parameters of the patches to a single effective parameter (parameter aggregation). Comparing to numerical simulations featuring finer grid resolutions, Heinemann and Kerschgens (2005) showed that aggregating fluxes is preferable to aggregating parameters. Even though discrete methods lead to improvements in representing subgrid-scale heterogeneity with respect to bulk similarity, MOST is applied to different surface patches, actually requiring homogeneity either at the tile- or patch- scales. Besides, discrete parametrization treat every MSM grid cell independently of the neighboring cells. Therefore, cell–cell interactions are not taken into account, which is especially important when strong heterogeneities appear close to cell boundaries or when advective effects impact a large portion of the cell.

To overcome these drawbacks in current approaches, a novel way to parametrizing subgrid-scale heterogeneity in MSM models is proposed here that incorporates all scales of the surface heterogeneity. This parametrization is derived analytically from linking the covariance function of the heterogeneous scenario to the covariance of the bulk averaged scenario within the MSM cell. By assuming the spectral shape of the covariance functions for the bulk averaged surface (Katul et al. 2013, 2014), heterogeneity corrections to bulk similarity can be derived. To test the covariance function approach against the tile approach for flux aggregation and bulk similarity, three LES runs of distinct surface heterogeneities are conducted. These heterogeneities are characterized by a different surface heat flux and roughness length when compared to the surrounding background. We further compared the different parametrizations with the LES as a 'reference' by computing the effective aerodynamic resistance to heat transfer using the different aggregation methods, as this quantity is a necessary parameter for MSM (Liu et al. 2007; Banerjee et al. 2017). In addition, comparisons are performed for six different grid dimensions to investigate the effects of grid resolution of the numerical models on the aggregate outcome.

The manuscript is organized as follows: In the second section, a derivation of the covariance function approach is presented for calculating the aerodynamic resistance in a heterogeneous MSM cell. In the third section, the LES and the calculation of the aerodynamic resistances from the bulk and tile approaches are presented. In the fourth section, different aggregation methods are compared against the LES runs. The fifth section presents a summary and the main findings.

2. Theory

Throughout, quantities and equations are derived in a longitudinal $x_1 = x$, lateral $x_2 = y$, and elevation $x_3 = z$ Cartesian coordinate system (both index and meteorological notations are used). In this coordinate system, velocity components are defined as $u_1 = u$ along x, $u_2 = v$, along y and $u_3 = w$ along z. Time averaging is indicated by overline and fluctuations from this averaging are indicated by primed quantities. The bracketed quantities $\langle\cdot\rangle = \int_A dxdy$ denote spatial averaging over surface area A. Because the interest is in MSM parameterizations, the vertical structure of land-surface features are not explicitly considered and are surrogated to a roughness length. Hence, A does not include multiply connected spaces (as inside canopies) and the usual Reynolds decomposition rules apply. Potential temperature T is the key scalar being analyzed. Surface quantities are indicated by subscript 0 unless otherwise stated.

a. Aerodynamic resistance to heat transfer

In MSM, the aerodynamic resistance to heat transfer (r) links the sensible heat flux ($\overline{w'T'}$) emitted from A to a mean temperature difference ($\Delta\overline{T} = \overline{T}_0 - \overline{T}(z)$) between the surface ($\overline{T}_0$) and height z ($\overline{T}(z)$). The altitude z is usually set to the vertical resolution of the numerical model. The integral form of the aerodynamic resistance is given by:

$$r(z) = -\int_{z_{0h}}^{z-d} d\tilde{z} \frac{\langle\Gamma\rangle(\tilde{z})}{\langle\overline{w'T'}\rangle(\tilde{z})}, \tag{1}$$

where d is the displacement height, z_{0h} is the roughness length to heat transfer, $\Gamma = \partial_z\overline{T}$ is the gradient of the mean vertical potential temperature. Usually, $\langle\overline{w'T'}\rangle$ is assumed to be constant with height in the surface layer (constant flux approximation), which allows for evaluating the integral in Eq. 1, yielding

$$r(z) = \frac{\langle\overline{T}\rangle(z_{0h}) - \langle\overline{T}\rangle(z-d)}{\langle\overline{w'T'}\rangle}. \tag{2}$$

When applying MOST to Eq. 2, the following parametrization for the homogeneous aerodynamic resistance (r_h) can be derived (Yang et al. 2001; Banerjee et al.

2017):

$$r_{\mathrm{h}}(z) = \frac{1}{\kappa^2 \overline{u}(z)} \left[\log\left(\frac{z-d}{z_{om}}\right) - \psi_m\left(\zeta_d, \zeta_{0m}\right) \right] \times \\ \times \left[\log\left(\frac{z-d}{z_{oh}}\right) - \psi_h\left(\zeta_d, \zeta_{0h}\right) \right], \tag{3}$$

where $\kappa = 0.4$ is the von Karman constant, $\overline{u}(z)$ is the mean velocity at height z, z_{0m} is the roughness length for momentum transfer, ψ_m and ψ_h are integral stability correction functions (Banerjee et al. 2017), $\zeta_d = (z-d)/L$, $\zeta_{0m} = z_{0m}/L$ (ζ_{0h} accordingly), and $L = -u_*^3 \overline{T}_0 / \left(\kappa g \overline{w'T'}_0\right)$ is the Obukhov length (e.g., Foken 2006), where u_* is the friction velocity and g is the gravitational acceleration. Besides, Eq. 3 can also be expressed in integral form containing the stability correction functions ϕ_m and ϕ_h:

$$r_{\mathrm{h}}(z) = \frac{1}{\kappa^2 \overline{u}(z)} \int_{z_{0m}}^{z-d} d\tilde{z}\, \frac{\phi_m(\zeta)}{\tilde{z}} \int_{z_{0h}}^{z-d} d\tilde{z}\, \frac{\phi_h(\zeta)}{\tilde{z}}, \tag{4}$$

where $\zeta = z/L$ is the stability parameter.

b. Budget equations for covariance functions

Because the interest here is integration across all possible interactions between turbulence and ground inhomogeneity at height z, the theoretical tactic is as follows. It is assumed that ground heterogeneity distorts the shapes of the vertical velocity and potential temperature spectra from their planar homogeneous counterparts. Next, a co-spectral budget model is used to link these distortions to the sensible heat flux co-spectrum, which when integrated across scales, provides the sensible heat flux at z. It is assumed that the heterogeneity is not too fine-scaled and severe to distort inertial subrange scales of turbulent quantities so that the Kolmogorovian (Kolmogorov 1941) description still holds for the finest scales resolved by the LES. Turbulent motions that are subject to mean gradients in the vertical direction are now considered and are characterized by the covariance function $\overline{E}_{V_1V_2}$ of two field variables V_1 and V_2 defined as

$$\overline{E}_{V_1V_2}\left(\left(\mathbf{r},z\right),\hat{\mathbf{r}}\right) = \overline{V_1'\left(\mathbf{r},z\right) V_2'\left(\mathbf{r}+\hat{\mathbf{r}},z\right)} \tag{5}$$

where $\mathbf{r} = (x,y)$, $\hat{\mathbf{r}} = (\hat{x},\hat{y})$ are vectors within the horizontal plane at altitude z. The corresponding covariance function in spectral space ($\overline{F}_{V_1V_2}$) is defined as the two-dimensional Fourier transform of $\overline{E}_{V_1V_2}$ with respect to the distance vector $\hat{\mathbf{r}}$. Therefore, the expression $\overline{V_1'V_2'}(\mathbf{r},z) = \overline{E}_{V_1V_2}\left(\left(\mathbf{r},z\right),\hat{\mathbf{r}}=\mathbf{0}\right)$ becomes

$$\overline{V_1'V_2'}\left(\mathbf{r},z\right) = \int_{\mathbf{k}} \overline{F}_{V_1V_2}\left(\left(\mathbf{r},z\right),\mathbf{k}\right), \tag{6}$$

where $\int_{\mathbf{k}} \equiv \int \frac{d^2\mathbf{k}}{(2\pi)^2}$. By using Eq. 6, budget equations for the turbulent fluxes can be transferred to budget equations for the covariance function in spectral space. The budget equation for $\overline{F}_{wT}$ therefore reads

$$\partial_t \overline{F}_{wT} = \left[-\Gamma \overline{F}_{ww} + \beta \overline{F}_{TT} - \partial_z \overline{w'F_{wT}} + \overline{\Pi}_T - \nu k^2 \overline{F}_{wT} \right] + \\ + \left[-\overline{u}_j \partial_j \overline{F}_{wT} - \partial_l \overline{u_l' F_{wT}} - \overline{F}_{u_jT}\, \partial_j \overline{w} - \overline{F}_{u_lw}\, \partial_l \overline{T} \right], \tag{7}$$

where $\beta = g/\overline{T}$ is the buoyancy parameter, the pressure term $\overline{\Pi}_T = -ik_z \overline{F}_{pT}/\rho$, ρ is the density of air, k is the norm of $\mathbf{k}$ ($k = \|\mathbf{k}\|$) , the j-summations include all three spatial dimensions ($j \in \{1,2,3\}$), and the l-summations are defined for the horizontal dimensions ($l \in \{1,2\}$). The terms of Eq. 7 are ordered in a way that the first line includes terms relevant for a horizontally-homogeneous scenario, while the terms in the second line are corrections due to: advection with the mean wind and subsidence (first term), horizontal flux divergence (second term), mechanical production/dissipation from gradients of the mean vertical wind speed (third term), and production/dissipation from horizontal gradients of the mean temperature (fourth term). While the two last correction terms are usually small with respect to the terms in the first line, we also neglect advection and flux divergence in the following derivation for analytical tractability. The motivation for this is that spatial averages with respect to aggregate surface area A have to be applied to Eq. 7 when deriving the aerodynamic resistance (Eq. 1). However, area averaging the corrections due to advection and flux divergence is equivalent to evaluating these terms at the surface boundaries and dividing the result by A. Therefore, corrections due to advection and flux divergence become negligible for a sufficiently large surface area A on the area-averaged quantities though this argument need not hold at a given scale or spatial location. To keep the following derivation clear, advection and flux divergence terms are neglected prior to performing spatial averages.

Considering homogeneous conditions, Katul et al. (2014) simplified the $\overline{F}_{wT}$ budget equation by assuming stationary flow, neglecting dissipation ($-\nu k^2 \overline{F}_{wT}$) and the flux transfer terms across scales $\partial_z \overline{w'F_{wT}}$ (a reasonable assumption for scalar co-spectra but not energy spectra), and employing a Rotta type closure model for the pressure term that includes both a slow- and a fast- part linked to the isotropization of the production term, yielding

$$\overline{\Pi}_T = -A_T \frac{\overline{F}_{wT}}{\tau} - C_{IT} \Gamma \overline{F}_{ww}, \tag{8}$$

where A_T and C_{IT} are constants (≈ 1.8 and $3/5$), and τ is the relaxation time of the Rotta model. Employing the aforementioned assumptions of Katul et al. (2014) to Eq. 7 results in

$$\overline{F}_{wT}\left(\left(\mathbf{r},z\right),\mathbf{k}\right) \approx \Big[-C_1 \Gamma\left(\mathbf{r},z\right) \overline{F}_{ww}\left(\left(\mathbf{r},z\right),\mathbf{k}\right) + \\ + C_2 \beta\left(\mathbf{r},z\right) F_{TT}\left(\left(\mathbf{r},z\right),\mathbf{k}\right) \Big] \tau\left(z,\mathbf{k}\right), \tag{9}$$

where $C_1 = (1+C_{IT})A_T^{-1}$, and $C_2 = A_T^{-1}$. The relaxation time scale for the heterogeneous scenario is assumed to be independent of $\mathbf{r}$. A plausibility argument is that τ is defined as a ratio of two covariance functions (Eq. 8) that include similar $\mathbf{r}$-dependency to yield a τ not sensitive to $\mathbf{r}$ variations.

c. Linking homogeneous and heterogeneous covariance functions

A general V_1V_2 function for a heterogeneous (non-homogeneous $\equiv$ "nh") scenario ($\overline{E}^{\mathrm{nh}}_{V_1V_2}$) is now considered. The associated homogeneous ("ah") covariance function ($\overline{E}^{\mathrm{ah}}_{V_1V_2}$), which is defined for a homogeneous scenario, is constructed from the bulk average of the heterogeneous scenario for area A. It follows from this definition that a certain flow variable of the associated homogeneous scenario V_{ah} is given by $V_{\mathrm{ah}} = \langle V \rangle$. In analogy to the concept of 'transfer function' in systems theory, the homogeneous and non-homogeneous covariance functions can be related by:

$$\overline{E}^{\mathrm{nh}}_{V_1V_2}\left((\mathbf{r},z),\hat{\mathbf{r}}\right) = \chi_{V_1V_2}\left(\mathbf{r}+\hat{\mathbf{r}},z\right)\overline{E}^{\mathrm{ah}}_{V_1V_2}\left(z,\hat{\mathbf{r}}\right), \qquad (10)$$

where $\chi_{V_1V_2}$ represents the scale-wise distortions of heterogeneity on the planar-homogeneous covariance function at height z. Equation 10 was motivated from investigating covariance functions by means of LES (Fig. 1). Figure 1 shows $\overline{E}^{\mathrm{nh}}_{TT}$ for a disc-shaped surface heterogeneity of diameter D_{nh} (dashed white circles) for nine fixed values of $\mathbf{r}$. As apparent from this plot, $\overline{E}^{\mathrm{nh}}_{TT}$ is composed of a function representing the underlying surface heterogeneity (disc-shaped irregularities), which is shifted to $-\mathbf{r}$ in each case ($\chi_{V_1V_2}(\mathbf{r}+\hat{\mathbf{r}})$), and a second function, which causes the maximum of the distribution at $\hat{\mathbf{r}} = \mathbf{0}$ ($\overline{E}^{\mathrm{ah}}_{wT}$). To derive an expression for $\chi_{V_1V_2}$, Eq. 10 is first evaluated at $\hat{\mathbf{r}} = \mathbf{0}$. Equation 5 is then employed along with the definition $\overline{V_1'V_2'}_{\mathrm{ah}} = \langle \overline{V_1'V_2'} \rangle$ to arrive at

$$\chi_{V_1V_2}(\mathbf{r},z) = \overline{V_1'V_2'}(\mathbf{r},z) \,/\, \langle \overline{V_1'V_2'} \rangle (z). \qquad (11)$$

This equation implies a normalization condition for $\chi_{V_1V_2}$, as spatially averaging Eq. 11 for the considered grid cell yields

$$\langle \chi_{V_1V_2} \rangle = 1. \qquad (12)$$

In the following, we additionally assume that $\overline{V_1'V_2'}$ and $\langle \overline{V_1'V_2'} \rangle$ feature the same dependence on z, which leads to a z-independent $\chi_{V_1V_2}$.
Fourier transforming Eq. 10 with respect to $\hat{\mathbf{r}}$ gives

$$\overline{F}^{\mathrm{nh}}_{V_1V_2}\left((\mathbf{r},z),\mathbf{k}\right) = \int_{\tilde{\mathbf{k}}} \exp\left(i\tilde{\mathbf{k}}\mathbf{r}\right)\hat{\chi}_{V_1V_2}\left(\tilde{\mathbf{k}}\right)\overline{F}^{\mathrm{ah}}_{V_1V_2}\left(z,\mathbf{k}-\tilde{\mathbf{k}}\right), \qquad (13)$$

where $\hat{\chi}_{V_1V_2}$ is the Fourier transform of $\chi_{V_1V_2}$. In the following derivation, we will use the spatial average of Eq. 13 for the grid cell area $A = \Delta x \times \Delta y$, where Δx and Δy denote the MSM grid spacing in x and y direction respectively. Applying $\langle\cdot\rangle$ to Eq. 13 yields

$$\langle \overline{F}^{\mathrm{nh}}_{V_1V_2} \rangle (z,\mathbf{k}) = \int_{\tilde{\mathbf{k}}} \varphi_A\left(\tilde{\mathbf{k}}\right)\hat{\chi}_{V_1V_2}\left(\tilde{\mathbf{k}}\right)\overline{F}^{\mathrm{ah}}_{V_1V_2}\left(z,\mathbf{k}-\tilde{\mathbf{k}}\right), \qquad (14)$$

where

$$\varphi_A(\mathbf{k}) = \langle \exp(i\mathbf{k}\mathbf{r}) \rangle = \mathrm{sinc}(k_x\Delta x/2)\,\mathrm{sinc}(k_y\Delta y/2), \qquad (15)$$

and $\mathrm{sinc}(x) = \sin(x)/x$. When $x \to 0$, $\mathrm{sinc}(x) \to 1$ and $\varphi_A \to 1$ (i.e. a desirable unity value is guaranteed in the limit of $\Delta x = \Delta y = 0$ at all scales).

d. Aerodynamic resistance from the covariance function approach

To derive the aerodynamic resistance from the covariance function approach, we first express $\overline{w'T'}$ through $\overline{F}^{\mathrm{nh}}_{wT}$ using Eq. 6:

$$\overline{w'T'}(\mathbf{r},z) = \int_{\mathbf{k}} \overline{F}^{\mathrm{nh}}_{wT}\left((\mathbf{r},z),\mathbf{k}\right). \qquad (16)$$

Subsequently, we use Eq. 9 to replace $\overline{F}^{\mathrm{nh}}_{wT}$

$$\overline{w'T'} = -C_1\Gamma\int_{\mathbf{k}} \overline{F}^{\mathrm{nh}}_{ww}\tau_{\mathrm{ah}} + C_2\beta\int_{\mathbf{k}} \overline{F}^{\mathrm{nh}}_{TT}\tau_{\mathrm{ah}}, \qquad (17)$$

where we omitted the dependencies of the specific terms for the sake of readability and replaced τ by the τ_{ah}, as this $\mathbf{r}$-independent function is directly associated with the heterogeneous scenario. To derive the aerodynamic resistance using Eq. 1, the spatially averaged sensible heat flux is needed. When spatially averaging Eq. 17, we encounter averages of two product terms, $\langle \Gamma\overline{F}^{\mathrm{nh}}_{ww} \rangle$ and $\langle \beta\overline{F}^{\mathrm{nh}}_{TT} \rangle$. Even though dispersive fluxes might have a valid contribution close to the surface, when a canopy is present (Harman et al. 2016), we approximate the averages of the products by the products of the averaged terms, resulting in

$$\langle \overline{w'T'} \rangle = -C_1\langle\Gamma\rangle\int_{\mathbf{k}} \langle \overline{F}^{\mathrm{nh}}_{ww} \rangle\tau_{\mathrm{ah}} + C_2\langle\beta\rangle\int_{\mathbf{k}} \langle \overline{F}^{\mathrm{nh}}_{TT} \rangle\tau_{\mathrm{ah}}. \qquad (18)$$

Further, we divide Eq. 18 by $\langle\Gamma\rangle$ and employ Eq. 1, which yields

$$(d_z r)^{-1} = C_1\int_{\mathbf{k}} \langle \overline{F}^{\mathrm{nh}}_{ww} \rangle\tau_{\mathrm{ah}} - C_2\beta_{\mathrm{ah}}/\Gamma_{\mathrm{ah}}\int_{\mathbf{k}} \langle \overline{F}^{\mathrm{nh}}_{TT} \rangle\tau_{\mathrm{ah}}, \qquad (19)$$

were d_z denotes the total derivative with respect to z and we employed the definition of the associated heterogeneous scenario for $\langle\Gamma\rangle$ and $\langle\beta\rangle$ (Section 2c). To derive the aerodynamic resistance from the covariance function approach (r_{cf}), we further replace $\langle \overline{F}^{\mathrm{nh}}_{ww} \rangle$ and $\langle \overline{F}^{\mathrm{nh}}_{TT} \rangle$ using Eq. 14:

$$\begin{aligned}(d_z r_{\mathrm{cf}})^{-1} = \int_{\mathbf{k}}\int_{\tilde{\mathbf{k}}} \varphi_A\left(\tilde{\mathbf{k}}\right)\Big[&C_1\hat{\chi}_{ww}\left(\tilde{\mathbf{k}}\right)\overline{F}^{\mathrm{ah}}_{ww}\left(\mathbf{k}-\tilde{\mathbf{k}}\right) - \\ &-C_2\beta_{\mathrm{ah}}/\Gamma_{\mathrm{ah}}\,\hat{\chi}_{TT}\left(\tilde{\mathbf{k}}\right)\overline{F}^{\mathrm{ah}}_{TT}\left(\mathbf{k}-\tilde{\mathbf{k}}\right)\Big]\tau_{\mathrm{ah}}(\mathbf{k}),\end{aligned} \qquad (20)$$

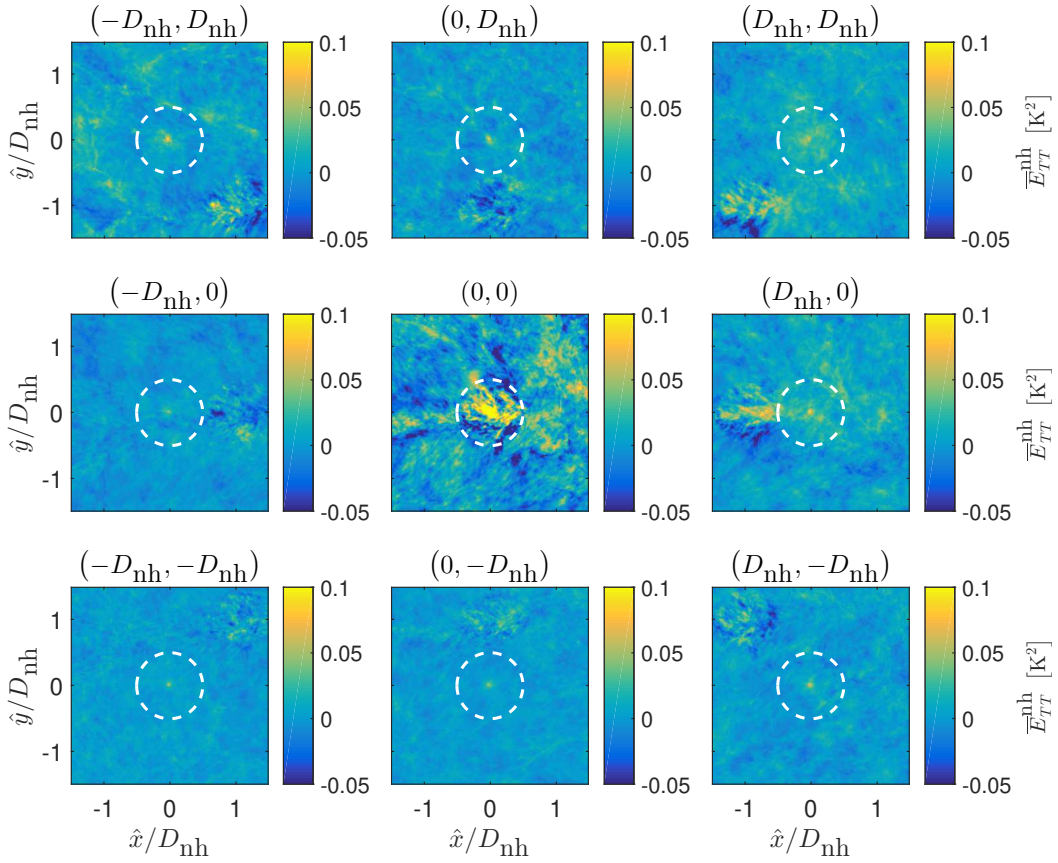

FIG. 1. Horizontal cross sections of $\overline{E}^{\mathrm{nh}}_{TT}$ at $z = 10$ m as a function of $\hat{\mathbf{r}} = (\hat{x}, \hat{y})$, where $\hat{x}$ and $\hat{y}$ are normalized by the heterogeneity diameter D_{nh}. The position vector $\mathbf{r}$ is varied between the nine subplots as indicated in the titles. The white circles indicate the modeled disc-shaped surface heterogeneity of diameter D_{nh}.

where we still omit the dependencies on z. Note that there are three different contributions to r_{cf}. While φ_A represents the spatial averaging, dampening scales smaller than the MSM grid dimensions, $\hat{\chi}_{ww}$ and $\hat{\chi}_{TT}$ represent the surface heterogeneity independent of the MSM grid. The residual terms are the contribution of the bulk averaged homogeneous scenario to r_{cf}.

e. *Homogeneous covariance function approach and application to the aerodynamic resistance*

To complete the r_{cf} derivation, distributions for the associated homogeneous covariance functions $\overline{F}^{\mathrm{ah}}_{ww}$, $\overline{F}^{\mathrm{ah}}_{TT}$, and τ_{ah} have to be assumed. For this purpose, the approach of Katul et al. (2014) is adopted. In this approach, the spectral functions are assumed only dependent on $k = \|\mathbf{k}\|$ (isotropy), to follow the Kolmogorovian power-laws for $k > k_a$, and to be constant for $k \leq k_a$ (Fig. 2). Furthermore, Katul et al. (2014) employed Townsends attached eddy hypothesis (Townsend 1976) to determine the cut-off wave vector $k_a = 2\pi/z$ for a neutrally stratified atmosphere. Formally, these spectral functions are defined by:

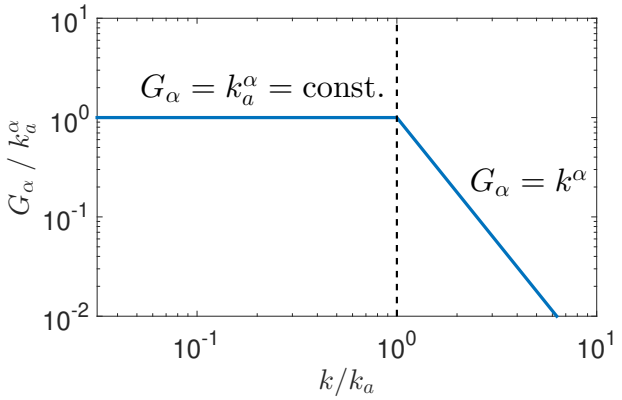

FIG. 2. G_α distribution as function of $\hat{k}$ and the cut-off wave vector k_a, according to Katul et al. (2014). The slope of the plotted G_α corresponds to $G_{-5/3}$.

$$
\begin{aligned}
\overline{F}^{\mathrm{ah}}_{ww}(z,\mathbf{k}) &= C_0\,(\varepsilon_{\mathrm{ah}}(z))^{2/3}\,G_{-5/3}(z,k)/k,\\
\overline{F}^{\mathrm{ah}}_{TT}(z,\mathbf{k}) &= C_T N_T^{\mathrm{ah}}\,(\varepsilon_{\mathrm{ah}}(z))^{-1/3}\,G_{-5/3}(z,k)/k,\\
\tau_{\mathrm{ah}}(z,\mathbf{k}) &= (\varepsilon_{\mathrm{ah}}(z))^{-1/3}\,G_{-2/3}(z,k),
\end{aligned}
\tag{21}
$$

where

$$G_\alpha(z,k) = k_a^\alpha\,\Theta(k_a-k) + k^\alpha\,\Theta(k-k_a), \qquad (22)$$

C_0 and C_T are constants, ε is the mean turbulent kinetic energy dissipation rate, N_T is the thermal variance dissipation rate, and $\Theta(\cdot)$ is the Heaviside step function. Besides, we introduced k^{-1}-normalisations for $\overline{F}^{\rm ah}_{ww}$ and $\overline{F}^{\rm ah}_{TT}$ to cancel the measure of the two dimensional $\int_{\mathbf{k}}$ integrals. Following Katul et al. (2014), the dissipation of the thermal variance is given by

$$N_T^{\rm ah} = \Gamma_{\rm ah}\overline{w'T'}_{\rm ah} = \Gamma_{\rm ah}^2\left(d_z r_{\rm cf}\right)^{-1}, \qquad (23)$$

where we used Eq. 1 in the second step to replace $\overline{w'T'}_{\rm ah}$. When inserting the homogeneous covariance functions of Eq. 21 into Eq. 20, using $N_T^{\rm ah}$ from Eq. 23, $d_z r_{\rm cf}$ appears on both sides of the equation. Subsequently solving for $d_z r_{\rm cf}$ yields

$$d_z r_{\rm cf} = \delta_{TT}\, d_z r_{{\rm cf},ww}, \qquad (24)$$

where $r_{{\rm cf},ww}$ is the aerodynamic resistance, originating from the ww term in Eq. 20, given by

$$d_z r_{{\rm cf},ww} = \frac{4}{7}\left(2\pi\right)^{7/3}\left(C_1C_0\right)^{-1}\,\varepsilon_{\rm ah}^{-1/3} z^{-4/3}\, I_{ww}(z), \qquad (25)$$

and δ_{TT} is a correction to $r_{{\rm cf},ww}$ due to the TT part (i.e. temperature spectrum) in Eq. 20, given by

$$\delta_{TT}(z) = 1 + \frac{7}{4}\left(2\pi\right)^{-7/3} C_2C_T\beta_{\rm ah}\Gamma_{\rm ah}\,\varepsilon_{\rm ah}^{-2/3} z^{4/3}\, I_{TT}^{-1}(z). \qquad (26)$$

The contribution of the surface heterogeneity to the aerodynamic resistance enters through the correction factors I_{ww} and I_{TT}, which are defined by

$$I_{V_1V_2}(z) = \frac{7}{4}\left(2\pi\right)^{-7/3} z^{4/3}\left[\int_{\mathbf{k}}\int_{\tilde{\mathbf{k}}} \varphi_A\left(\tilde{\mathbf{k}}\right)\hat{\chi}_{V_1V_2}\left(\tilde{\mathbf{k}}\right)\times \right.$$
$$\left.\times\frac{G_{-5/3}\left(z,\|\mathbf{k}-\tilde{\mathbf{k}}\|\right)G_{-2/3}\left(z,\|\mathbf{k}\|\right)}{\|\mathbf{k}-\tilde{\mathbf{k}}\|}\right]^{-1}, \qquad (27)$$

where we normalised $I_{V_1V_2}$ such that $I_{V_1V_2}=1$ for homogeneous conditions.

To determine the turbulent dissipation for the associated homogeneous scenario $\varepsilon_{\rm ah}$, we apply MOST for a neutrally stratified atmosphere (though generalization to non-neutral conditions can be readily conducted):

$$\varepsilon_{\rm ah}(z) = \frac{\left(u_{*,\rm ah}\right)^3}{\kappa z}, \qquad (28)$$

where $u_{*,\rm ah}$ is the friction velocity of the associated homogeneous scenario. When inserting Eq. 28 into Eqs. 25 and 26 and subsequently integrating Eq. 24, the following can be derived:

$$r_{\rm cf} = \frac{1}{\tilde{C}_1 u_{*,\rm ah}}\int_{z_{0h}}^{z-d} d\tilde{z}\;\delta_{TT}(\tilde{z})\frac{I_{ww}(\tilde{z})}{\tilde{z}}, \qquad (29)$$

where δ_{TT} is given by

$$\delta_{TT}(z) = 1 + \tilde{C}_2\frac{\beta_{\rm ah}(z)\Gamma_{\rm ah}(z)z^2}{\left(u_{*,\rm ah}\right)^2}\, I_{TT}^{-1}(z) \equiv 1 + \eta(z) I_{TT}^{-1}(z), \qquad (30)$$

$\tilde{C}_1 = \frac{7}{4}\left(2\pi\right)^{-7/3} C_1C_0\kappa^{1/3}$, $\tilde{C}_2 = \frac{7}{4}\left(2\pi\right)^{-7/3} C_2C_T\kappa^{2/3}$, and we introduced η.

As $u_{*,\rm ah}$ is often not available in MSM, we replace the friction velocity by an expression containing the mean wind speed $\overline{u}_{\rm ah}$, which is derived in the Appendix following the rationale of the last sections, when starting from the uw budget equation. This expression is given by:

$$u_{*,\rm ah}^{-1} = \left(\tilde{C}_3\overline{u}_{\rm ah}\right)^{-1}\int_{z_{0m}}^{z-d} d\tilde{z}\,\frac{I_{ww}(\tilde{z})}{\tilde{z}}, \qquad (31)$$

where $\tilde{C}_3$ is a constant, defined in analogy to $\tilde{C}_1$ and $\tilde{C}_2$. Inserting $u_{*,\rm ah}$ from Eq. 31 into Eq. 29 yields

$$r_{\rm cf} = \frac{1}{\tilde{C}_1\tilde{C}_3\overline{u}_{\rm ah}}\int_{z_{0m}}^{z-d} d\tilde{z}\,\frac{I_{ww}}{\tilde{z}}\int_{z_{0h}}^{z-d} d\tilde{z}\;\delta_{TT}\,\frac{I_{ww}}{\tilde{z}}. \qquad (32)$$

f. Incorporating atmospheric stratification and final form of r_{cf}

In a last step, the expression for $r_{\rm cf}$ can be generalized by including atmospheric stability corrections. To a leading order, atmospheric stability generates eddy anisotropy that impacts the overall mixing length (Mahrt and Gamage 1987) as well as the cross-over transition from production to inertial scales. To include the emerging difference between horizontal and vertical eddy dimensions for non-neutral conditions, an approach of maximum simplicity requires altering the cut-off wave vector $k_a \sim 1/z$ by including a stability dependent correction factor $f(\zeta)$ (Katul et al. 2011):

$$k_a(\zeta) = 2\pi/\left(f(\zeta)z\right). \qquad (33)$$

Inserting Eq. 33 into Eq. 32 while preserving the normalisation of $I_{V_1V_2}$ yields

$$r_{\rm cf} = \frac{1}{\tilde{C}_1\tilde{C}_3\overline{u}_{\rm ah}}\int_{z_{0m}}^{z-d} d\tilde{z}\,\frac{f^{-4/3}\left(\tilde{\zeta}\right)I_{ww}(fz)}{\tilde{z}}\times$$
$$\times\int_{z_{0h}}^{z-d} d\tilde{z}\;\delta_{TT}(\tilde{\zeta})\frac{f^{-4/3}\left(\tilde{\zeta}\right)I_{ww}(fz)}{\tilde{z}}, \qquad (34)$$

where $\tilde{\zeta} = \tilde{z}/L$ and $\delta_{TT}(\zeta) = 1 + \eta(fz) f^{4/3} I_{TT}^{-1}(fz)$. To determine $\tilde{C}_1\tilde{C}_3$, f, and η, we evaluate Eq. 34 for homogeneous conditions ($I_{ww} = I_{TT} = 1$) and compare to the homogeneous expression Eq. 4. This comparison yields $\tilde{C}_1\tilde{C}_3 = \kappa^2$, $f = \phi_m^{-3/4}$, and $\eta = \phi_h - \phi_m$. Therefore, the final form of r_{cf} is given by

$$r_{\mathrm{cf}} = \frac{1}{\kappa^2 \langle \overline{u} \rangle} \int_{z_{0m}}^{z-d} d\tilde{z}\, \frac{\phi_m^{\mathrm{cf}}\left(\tilde{\zeta}\right)}{\tilde{z}} \int_{z_{0h}}^{z-d} d\tilde{z}\, \frac{\phi_h^{\mathrm{cf}}\left(\tilde{\zeta}\right)}{\tilde{z}}, \qquad (35)$$

where we defined the stability correction functions including the heterogeneity corrections from the covariance function approach (ϕ_m^{cf}, ϕ_h^{cf}) by:

$$\phi_m^{\mathrm{cf}}(\zeta) = \phi_m(\zeta) I_{ww}\left(\phi_m^{-3/4}(\zeta) z\right),$$

$$\phi_h^{\mathrm{cf}} = \left[\phi_m(\zeta) + \left(\phi_h(\zeta) - \phi_m(\zeta)\right) / I_{TT}\left(\phi_m^{-3/4}(\zeta) z\right)\right] \times \times I_{ww}\left(\phi_m^{-3/4}(\zeta) z\right). \qquad (36)$$

3. Methods

a. LES code PALM

The LES code PALM (version 4.0.) (Raasch and Schröter 2001; Maronga et al. 2015) is a finite difference solver for the non-hydrostatic incompressible Boussinesq-approximated Navier-Stokes equations. PALM solves for six prognostic equations: the three components of the velocity field, the potential temperature, the humidity or total water content and the sub-grid scale turbulent kinetic energy. The sub-grid scale turbulence is modeled according to the method proposed by Deardorff (1980). The equations are discretized on a staggered Arakawa C-grid (Harlow and Welch 1965; Arakawa and Lamb 1977). The prognostic equations are integrated in time using a third order Runge-Kutta scheme. The Poisson equation for pressure is solved with the Fast Fourier Transform method for the employed periodic lateral boundary conditions. To determine the surface boundary values of the turbulent fluxes and the prognostic variables, MOST is applied locally between $z = 0$ and $z = \Delta z_{\mathrm{LES}}/2$, where Δz_{LES} is the vertical grid spacing. This calculation requires input of the roughness lengths for momentum ($z_{0m,\mathrm{LES}}$), while PALM uses $z_{0h,\mathrm{LES}} = z_{0m,\mathrm{LES}} \equiv z_{0,\mathrm{LES}}$ as default setting. The surface heat flux $\overline{w'T'}_0 \equiv H_{0,\mathrm{LES}}$ is also needed for the different scenarios. To model a net radiation, which is constant in time, we used a temporally constant $H_{0,\mathrm{LES}}$ and Neumann conditions for the potential temperature at the surface. Besides, the height of the atmospheric boundary layer within PALM is defined by the onset of a potential temperature inversion. While the onset and strength of this positive temperature gradient have to be prescribed when the LES runs are initialized, the boundary layer grows during the simulations due to surface heating. Further, the simulations are driven by a constant geostrophic wind, which models a constant synoptic mean pressure gradient. This geostrophic wind is additionally used as the top boundary condition for the horizontal velocity components. As the LES are initialized by spatially constant prognostic variables, a certain spin-up time is required to generate a distinct turbulent state from applying random fluctuation to the prognostic variables. To decouple this spin up from the main simulations, a homogeneous preliminary simulation was used to initialize the heterogeneous main simulations (Kröniger et al. 2018). The heterogeneous surfaces of the main simulations are defined by heterogeneous $H_{0,\mathrm{LES}}$ and $z_{0,\mathrm{LES}}$ maps, which are read in at initialization.

TABLE 1. Configuration of the preliminary simulation.

Lapse rate of the inversion layer	$1.0 \cdot 10^{-2}$ K m^{-1}
Initial boundary layer height	850 m
Initial temperature	27° C
Roughness length ($z_{0,\mathrm{LES}}$)	0.01 m
Surface heat flux ($H_{0,\mathrm{LES}}$)	0.1 K m s^{-1}
Simulated time	2 h

b. Numerical set up of LES test cases

All performed LES used a computational grid consisting of $2000 \times 2000 \times 400$ grid points in x, y, and z-direction respectively. The grid cells were equidistant in all three spatial directions, with $\Delta x_{\mathrm{LES}} = \Delta y_{\mathrm{LES}} = \Delta z_{\mathrm{LES}} =$ 4 m, yielding a total modeling domain of 8 km $\times$ 8 km $\times$ 1.6 km. A geostrophic wind of $u_g = 1$ m s^{-1} in x-direction was used to drive the simulations. Preliminary simulations were initialized by the values shown in Table 1, while the three main simulations were subsequently initialized by the output of this preliminary simulation at every grid point after an elapsed time of 2 h. The simulated time of the main simulations was also 2 h, were the data of the last 30 min was used for data output. The three considered heterogeneous scenarios are a disc-shaped heterogeneity of constant surface heat flux and roughness (Test case 1), a disc-shaped heterogeneity of randomly varying heat flux and roughness (Test case 2), and a realistic case, where we used a downscaled version of data collected above a semi-arid forest detailed elsewhere (Rotenberg and Yakir 2010) (Test case 3). The $H_{0,\mathrm{LES}}$ maps for the three test cases are shown in Fig. 3, where the white dashed line defines the size (diameter) of the heterogeneity (D_{nh}). These surface heat flux maps were chosen such that the total energy input, and therefore the boundary layer growth, is the same for all three test cases. Besides, we chose $D_{\mathrm{nh}} = 400$ m

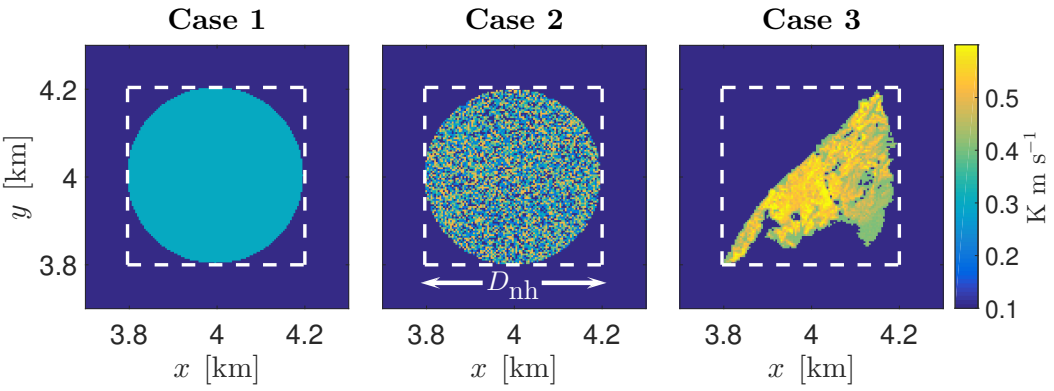

FIG. 3. $H_{0,\mathrm{LES}}$ maps of the three test cases from left to right. The white dashed line indicates the dimension of the heterogeneity D_{nh}.

to prevent self interaction of the forest due to the non-zero geostrophic wind and the periodic boundary conditions within the simulated time of 2 h. The corresponding $z_{0,\mathrm{LES}}$ maps were subsequently constructed, applying a linear mapping to $H_{0,\mathrm{LES}}$, were $z_{0,\mathrm{LES}} = 0.01$ m corresponds to $H_{0,\mathrm{LES}} = 0.1$ K m s^{-1} and $z_{0,\mathrm{LES}} = 1.44$ m to $H_{0,\mathrm{LES}} = 0.3$ K m s^{-1}. For $H_{0,\mathrm{LES}} > 0.3$ K m s^{-1} we kept $z_{0,\mathrm{LES}}$ constant set to 1.44 m, as the application of MOST as surface boundary condition becomes unstable if the roughness length approaches $\Delta z_{\mathrm{LES}}/2$.
To construct $H_{0,\mathrm{LES}}$ for test case 3, we used the surface heat flux map of Kröniger et al. (2018), which we scaled down by a factor of 20 in the lateral dimensions to model the same D_{nh} in all three test cases. We additionally scaled $H_{0,\mathrm{LES}}$ by a factor of 1.5 to guarantee the same energy input in all three test cases.

c. *Calculating aerodynamic resistances from LES data*

To test the aerodynamic resistance parametrization from the covariance function approach (r_{cf}) against bulk similarity (r_{bulk}) and tile (r_{tile}) aggregation approaches, the aerodynamic resistance directly calculated from the LES (r_{LES}) is used as reference. The required mean values and covariances for this calculation were derived from 30 min time averages of the LES data. To determine the four aerodynamic resistances for a given averaging area A (MSM grid cell), the following procedure is employed:

r_{LES}: To calculate r_{LES}, Eq. 1 is used for the spatially averaged LES profiles of Γ and $\overline{w'T'}$.

r_{bulk}: To calculate r_{bulk}, the r-parametrization for homogeneous conditions in the integral form (Eq. 4) is used. Here, spatial averages of the flow quantities are employed to determine L and $\langle\overline{u}\rangle$. Note that this approach recovers the covariance function approach for $I_{ww} = I_{TT} = 1$.

r_{cf}: To calculate r_{cf}, Eq. 35 is used with ϕ_m^{cf} and ϕ_h^{cf} from Eq. 36. Again spatial averages of the flow quantities are used to determine L and $\langle\overline{u}\rangle$. Further, we assumed $I_{TT} = I_{ww} = I_{wT}$, and calculated I_{wT} from Eq. 27. To obtain χ_{wT}, we used the surface heat flux maps $H_{0,\mathrm{LES}}$ (Fig. 3), which we normalized using Eq. 12. We conducted these approximations as $\overline{T'T'}$ and $\overline{w'w'}$ (needed for χ_{TT} and χ_{ww}) are not available for MSM on the subgrid scale but H_0 might be available from satellite data. As the lower boundaries of the $\mathbf{k}$ integrals in Eq. 27, these are defined by the dimension of the used χ maps, a larger map allows smaller wave numbers to contribute to the integrals. Due to computational issues, we defined the dimensions of χ_{wT} to be $1.5\,\Delta x \times 1.5\,\Delta y = 2.25\,A$, which allows the neighboring cells to contribute to the aerodynamic resistance of the given cell.

r_{tile}: To calculate r_{tile} using flux aggregation, the mean vertical heat flux of the MSM cell is quantified by

$$\langle\overline{w'T'}\rangle = \sum_{n\in\mathrm{tiles}} \nu_n \langle\overline{w'T'}\rangle_n, \tag{37}$$

where ν_n is the area fraction of a certain surface type n and $\langle\cdot\rangle_n$ denotes spatial averaging over the area of the surface type n. Subsequently, $\langle\overline{w'T'}\rangle$ and $\langle\overline{w'T'}\rangle_n$ are determined assuming vertically constant fluxes of momentum and heat and applying Eq. 2 for every surface type independently:

$$\frac{\langle\overline{T}\rangle(z_{0h}) - \langle\overline{T}\rangle(z-d)}{r_{\mathrm{tile}}} = \sum_{n\in\mathrm{tiles}} \nu_n \times \times \frac{\langle\overline{T}\rangle_n(z_{0h}) - \langle\overline{T}\rangle_n(z-d)}{r_n}, \tag{38}$$

where $\langle\overline{T}\rangle(z_{0h})$ and $\langle\overline{T}\rangle(z-d)$ are available from the MSM, and $\langle\overline{T}\rangle_n(z_{0h})$ is also known. Furthermore, it is assumed that surface heterogeneity is blended at

$z-d$, and therefore, $\langle\overline{T}\rangle_n(z-d) \approx \langle\overline{T}\rangle(z-d)$ (Stoll and Porté-Agel 2009). To determine r_n, MOST is employed for every tile independently (Eq. 4). For defining the different surface tiles, we subdivided $H_{0,\mathrm{LES}}$ within the MSM cell into areas of the same surface heat flux (up to a difference of 1 %). To calculate ν_n, we subsequently divided the number of LES cells belonging to a certain tile by the total number of LES cells within the MSM cell.

For determining the aerodynamic resistances, z-integrations have to be performed above and beyond the scale-wise integration (Eqs. 1, 4, 35). However, the modeled roughness lengths, which also define the lower integration boundaries of the z-integrals, are smaller than the lowest grid level at $\Delta z_{\mathrm{LES}}/2$ (Section 3b), which prohibits correct evaluation of the integrals. To avoid inaccuracies due to this issue, we increased the lower integration boundaries to $\Delta z_{\mathrm{LES}}/2$ for both z-integrals in Eqs. 1, 4, and 35. While the shift from z_{0h} to $\Delta z_{\mathrm{LES}}/2$ in the second z-integral only represents calculation of the aerodynamic resistance with respect to a different surface level, shifting the lower integration boundary of the first integral from z_{0m} to $\Delta z_{\mathrm{LES}}/2$ introduces an error, as $\langle\overline{u}\rangle(\Delta z_{\mathrm{LES}}/2) \neq 0$. To compensate for this error, we replaced $\langle\overline{u}\rangle(z)$ by $\langle\overline{u}\rangle(z) - \langle\overline{u}\rangle(\Delta z_{\mathrm{LES}}/2)$ in Eqs. 1, 4, and 35. For the upper boundary of the z-integrations, we used $z = 102$ m for all aerodynamic resistances, to capture most part of the surface layer. The reason why we chose the integral approach for r_{bulk} and r_{tile} (Eq. 4), instead of directly applying Eq. 3 is that the above mentioned method of calculation can be used for all four aerodynamic resistances, which increases their comparability upon comparisons. Besides, the zero-plane displacement d was set to zero here, as PALM uses this assumption for the calculation of the surface boundary conditions from MOST (Maronga et al. 2015).

d. MSM grid effects on aggregated aerodynamic resistances

Six different test-MSM grid sizes are used to compare the aerodynamic resistance parametrization in the three LES test cases. Equilateral grid cells with dimensions $\Delta x/D_{\mathrm{nh}} = \Delta y/D_{\mathrm{nh}} = 0.1,\ 0.2,\ 0.4,\ 0.8,\ 2.0,\ 4.0$ are chosen for this purpose. Further, we defined the extension of the test-MSM grids such that every line and row of the grid intersects with the heterogeneity with one cell at least. This procedure yields 144, 36, 16, 4, 4, and 4 grid cells for the different grid dimensions respectively. The position of the test-MSM grids with respect to the $H_{0,\mathrm{LES}}$ maps of the LES test cases is illustrated in Fig. 4.

To quantify the heterogeneity of the three test cases for the six test-MSM grids, we further computed the intra-cell variance of χ_{wT} (σ_χ) from the $H_{0,\mathrm{LES}}$ maps of the three test cases for every grid cell of Fig. 4 employing Eq. 12. Further, we calculated the mean value of σ_χ ($\mu(\sigma_\chi)$) over all MSM cells for a certain grid dimension Δx. The mean values of σ_χ as a function of the grid resolution are illustrated in Fig. 5, where the errorbars denote the standard deviation from $\mu(\sigma_\chi)$. This figure is interpreted as follows: While $\mu(\sigma_\chi)$ is a measure for the intra-cell heterogeneity, the errorbars represent the inter-cell heterogeneity for the three cases and six test-MSM grid dimensions. Therefore, all three test cases feature the largest intra-cell heterogeneites for $\Delta x = 0.8 \times D_{\mathrm{nh}}$, while smaller and larger grid dimensions are more homogeneous in this aspect. However, the smaller intra-cell heterogeneity for the finest grid is a result of the coarse LES resolution, while the smaller values for $\Delta x = 4.0 \times D_{\mathrm{nh}}$ are due to the small area coverage of the heterogeneity with respect to the cell area ($\approx 1.2\%$). Further, test case 1 features the smallest intra- and inter-cell heterogeneity, while test case 3 features the largest inter-cell heterogeneity. Concerning intra-cell heterogeneity, test case 2 is more heterogeneous than test case 1 for the three finer grid dimensions, which is reversed for the three coarser grids. The reason for that is the large fine-scale heterogeneity of the randomly applied heat fluxes in test case 2 for fine grid resolutions, which averages out when increasing the grid-cell dimensions.

4. Results and discussion

a. LES test case 1

At first, the different aerodynamic resistance parametrization for the disc-shaped heterogeneity with constant surface heat flux (Fig. 3, left) are compared using the test-MSM grids of Fig. 4. The results of this comparison are presented in Fig. 6, where the investigated parametrization (r_{bulk}, r_{tile}, r_{cf}) are featured against the LES reference (r_{LES}) for the six grid cell dimensions. Figure 6 shows a separation of r_{bulk}, r_{tile}, and r_{cf} into two clusters for the three smaller grid resolutions (marked by the dashed ellipses), where the ellipses in the left side of the panels represent grid cells containing at least 25% of the heterogeneity (outer cells), while grid cells with more than 25% of the heterogeneity belong to the ellipses in the right side of the panels (inner cells). While all three parametrization mainly overestimate r_{LES} for the outer cells, they underestimate the reference for the inner cells, where the over/underestimation can be up to one order of magnitude. The scatter of the data decreases with increasing Δx, which is explained by an increased spatial averaging of the heterogeneous surface and relates to the decrease of inter-cell heterogeneity with increasing Δx (Fig. 5). However, even for the largest grid dimension of $\Delta x = 4.0 \times D_{\mathrm{nh}}$, differences between the three parametrization cases exist, which shows that the surface heterogeneity even matters in the case where it only covers 1.2% of the cell area.

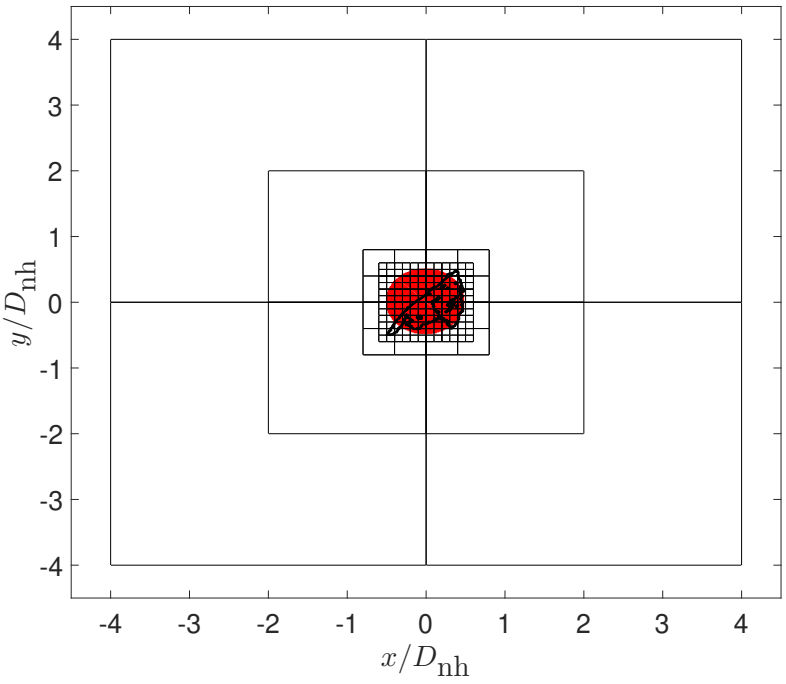

FIG. 4. MSM test grids used for the comparison of the different aerodynamic resistance parametrization. The thin black lines depict the boundaries of the grid cells, the red circle depicts $H_{0,\mathrm{LES}}$ of LES test case 1, and the fat black line depicts the contour of $H_{0,\mathrm{LES}}$ of LES test case 3.

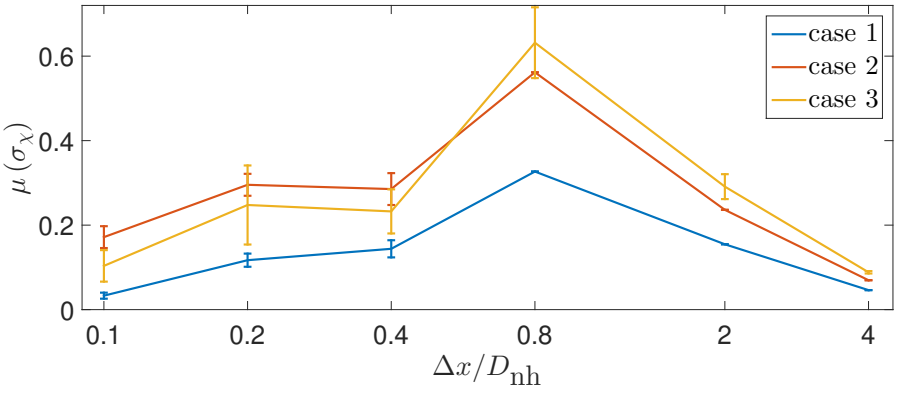

FIG. 5. Mean values of the intra-cell variance σ_χ of the $H_{0,\mathrm{LES}}$ maps as a function of the test-MSM grid resolution Δx for test case 1 (blue), test case 2 (red), and test case 3 (yellow). The errorbars denote the standard deviation of σ_χ from $\mu\,(\sigma_\chi)$.

Besides, the number of isolated cells (cyan dots), which feature $r_{\mathrm{iso}} = r_{\mathrm{bulk}} = r_{\mathrm{tile}} = r_{\mathrm{cf}}$, decreases with increasing Δx. While r_{tile} and r_{bulk} already coincide when the grid cell is homogeneous, r_{cf} only agrees with the two other parametrization if the homogeneity extents to the neighboring grid cells (size of χ_{wT} in Section 3c). As the probability for such a homogeneous area decreases for increasing Δx (Fig. 4), the number of isolated cells also has to decrease. Besides the isolated cells, there exists a larger number of cells with $r_{\mathrm{tile}} = r_{\mathrm{bulk}} \neq r_{\mathrm{cf}}$, where r_{cf} agrees better with the reference. These cells directly illustrate the importance of neighboring cells for the surface atmosphere exchange of the considered MSM cell.

To quantify the quality of the different parametrization, we further computed the root-mean-square error (RMSE) of the bulk, tile, and covariance function approach with respect to the reference LES case, which is illustrated in Fig. 7. This figure shows that the tile and covariance function approaches mainly produced better results than the bulk parametrization, achieving RMSE values up to one order of magnitude smaller then $\mathrm{RMSE}_{\mathrm{bulk}}$. The

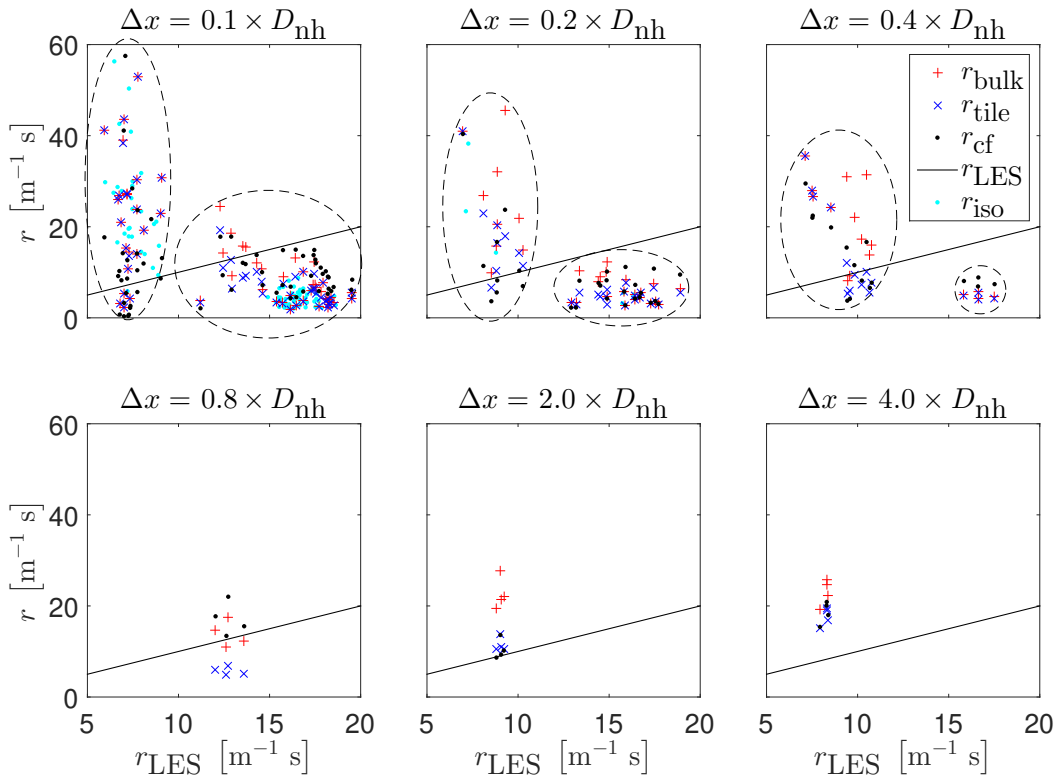

FIG. 6. Scatter plots of r_{bulk} (red crosses), r_{tile} (blue crosses), and r_{cf} (black dots) against the LES reference r_{LES} (black solid line) for the test case 1 and varying test-MSM grid cell dimensions (different subplots). The isolated cells, defined by $r_{\mathrm{iso}} = r_{\mathrm{bulk}} = r_{\mathrm{tile}} = r_{\mathrm{cf}}$, are displayed by cyan dots. The dashed ellipses separate inner cells (right ellipses) from outer cells (left ellipses) for the three finer test-MSM grids.

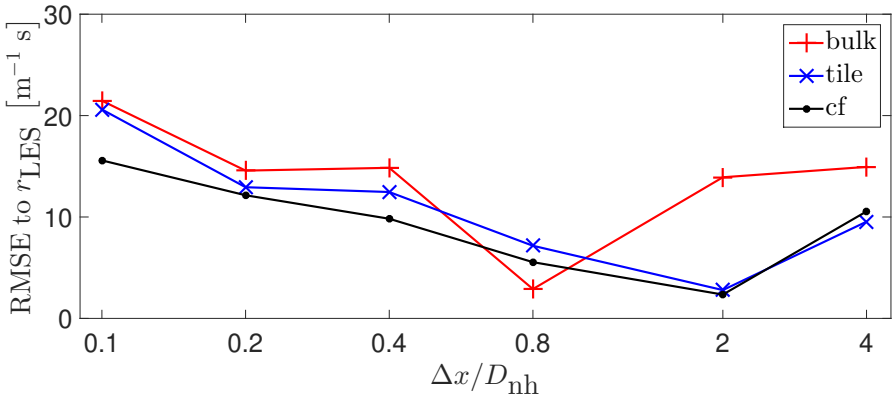

FIG. 7. Root-mean-square error (RMSE) of the bulk (red line), tile (blue line), and covariance function approaches (black line) with respect to the LES reference r_{LES} as a function of the test-MSM grid dimensions for the LES test case 1.

only exception is the $\Delta x = 0.8 \times D_{\mathrm{nh}}$ case, where the tile approach resulted in twice as large RMSE than the bulk approach. While the errors of the tile and the bulk approach are similar for small Δx, which is due to the large number of cells with $r_{\mathrm{tile}} = r_{\mathrm{bulk}}$ (Fig. 6), the errors of the tile and the covariance function approaches decrease with increasing Δx, featuring a minimal value of 2.3 m^{-1} s for the covariance function approach at $\Delta x = 2.0 \times D_{\mathrm{nh}}$. However, the errors of both parametrizations increase again for $\Delta x = 4.0 \times D_{\mathrm{nh}}$ by a factor of five. The reason for this is that the intra- and inter-cell heterogeneity in this particular case are small enough (Fig. 5) that the corrections with respect to the bulk method decrease, which leads to the occurring approach of the three methods. This resolution is additionally the only case, where the errors of the tile approach are smaller than the errors of the covariance function approach. Otherwise,

the errors of the covariance function approach are up to 35% smaller than $\mathrm{RMSE}_{\mathrm{tile}}$.

b. LES test case 2

The different aerodynamic resistance parametrizations for the disc-shaped heterogeneity with a random heat flux (Fig. 3, centre) are now compared using the test-MSM grids of Fig. 4. The results of this comparison are depicted in Fig. 8, in analogy to Fig. 6. Figure 8 shows that inner and outer cells cluster again for the three finer resolutions, where the inner/outer cells under/overestimate the LES reference. However, less scatter of the three parametrization for the outer cells occurs for these grid dimensions. This finding can be explained by the less sharp transition between the surrounding and the randomly assigned heat fluxes with respect to the constant heat flux in test case 1. Besides, the number of cyan cells within the left ellipses agrees with test case 1, as we used the same test-MSM grids and the two test cases feature the same size (disc-shaped heterogeneities of diameter D_{nh}). However, the increased intra-cell heterogeneity of the randomly assigned heat flux (Fig. 5) inhibits homogeneous cells within the disc-shaped region, which inhibits isolated cells within the right ellipses of Fig. 8. Despite this fact, the three parametrization still feature similar values for the largest part of the inner cells (right ellipsis for $\Delta x = 0.1 \times D_{\mathrm{nh}}$). For the three larger Δx, the differences between the methods and the offset to the reference are similar to test case 1. This can be explained by the fact that the spatial average of the full area of randomly assigned surface heat fluxes in test case 2 equals the constant surface heat flux of test case 1 (Section 3b), and that the surface-atmosphere exchange, therefore, becomes similar in both cases for large grid cells.

In analogy to test case 1, we further computed the RMSE of the three parametrization and r_{LES} for test case 2, which is illustrated in Fig. 9. As apparent from this figure, the errors of the different parametrization are reduced for the three finer resolutions, which reflects the smaller scatter in Fig. 8. Even though $\mathrm{RMSM}_{\mathrm{tile}}$ again coincides with $\mathrm{RMSE}_{\mathrm{bulk}}$ for the finer grid resolutions, the tile approach shows larger errors for the coarser grid dimensions in comparison to test case 1. This can be explained by the fact that MOST is employed independently for every surface tile within the tile approach (Section 3c), which is an inferior approximation to the randomly assigned surface heat fluxes than for the constant one. Besides, the covariance function method now features smaller errors than the tile approach for all considered resolutions, where the smallest value of 1.9 m^{-1} s is still achieved for $\Delta x = 2.0 \times D_{\mathrm{nh}}$. However, due to the poorer performance of the tile approach for this resolution, $\mathrm{RMSE}_{\mathrm{cf}}$ decreased $\mathrm{RMSE}_{\mathrm{tile}}$ by a factor of three and $\mathrm{RMSE}_{\mathrm{bulk}}$ by a factor of six. The root-mean-square error of the bulk approach still decreased when compared to the other two methods for $\Delta x = 0.8 \times D_{\mathrm{nh}}$. However, the difference between the three parametrization is halved with respect to test case 1. For the coarsest grid resolution, all three parametrization converge, which is due to the smaller effect of the heterogeneity correction to the bulk parametrization for this grid cell dimension, as discussed for test case 1 (Section 4a).

c. LES test case 3

The different aerodynamic resistance parametrization for the models applied to the semi-arid forest (Fig. 3, right) are considered using the test-MSM grids of Fig. 4. The results of this comparison are depicted in Fig. 10. As already discussed for the other two test cases, the separation of inner and outer cells is also apparent for test case 3, where the inner/outer cells again mainly under/overestimate the reference. However, the scatter of the three parametrization for the outer cells is largest for case 3, which is due to the fact that test case 3 features the largest inter-cell heterogeneity (Fig. 5). Besides, the clustering now also appears for $\Delta x = 0.8 \times D_{\mathrm{nh}}$, which is due to the fact that the forest covers a smaller area than the disc-shaped heterogeneities (Fig. 4). This different area coverage also affects the number of isolated cells (cyan dots), which is larger within the group of outer cells with respect to the other test cases. However, due to the heterogeneity of the forest (Fig. 5), isolated cells are again suppressed within the group of inner cells. While the parametrization results are in general different for the three test cases at finer resolution, case 3 shows similar values as the other two test cases for the largest Δx. This is again due to the fact that the spatial average of the surface heat flux and the heterogeneity size D_{nh} is the same for all three test cases, which yields similar results for larger grid cell dimensions (Section 4a).

In analogy to the other two test cases, we further computed the RMSE of the three parametrization and r_{LES} for test case 3, which is illustrated in Fig. 11. As already apparent from Fig. 10, the larger scatter of all three parametrization for the finer resolutions causes a RMSE, which is two times larger than for test case 2. Errors of all three parametrization are of similar magnitude for the finest grid resolution, which is explained by the larger number of isolated cells. Different from the two previous cases, the bulk approach yielded larger errors than the two other approaches for all grid resolutions, where $\mathrm{RMSE}_{\mathrm{cf}}$ is always smaller than $\mathrm{RMSE}_{\mathrm{tile}}$. The smallest $\mathrm{RMSE}_{\mathrm{cf}}$ is again achieved for $\Delta x = 2.0 \times D_{\mathrm{nh}}$, however the corresponding value of 1.1 m^{-1} s is the smallest error throughout all three test cases and is smaller than the corresponding error of the tile/bulk approach by a factor of 6/10. For $\Delta x = 4.0 \times D_{\mathrm{nh}}$ the errors of the three parametrization are similar to the other test cases, which is again due to the

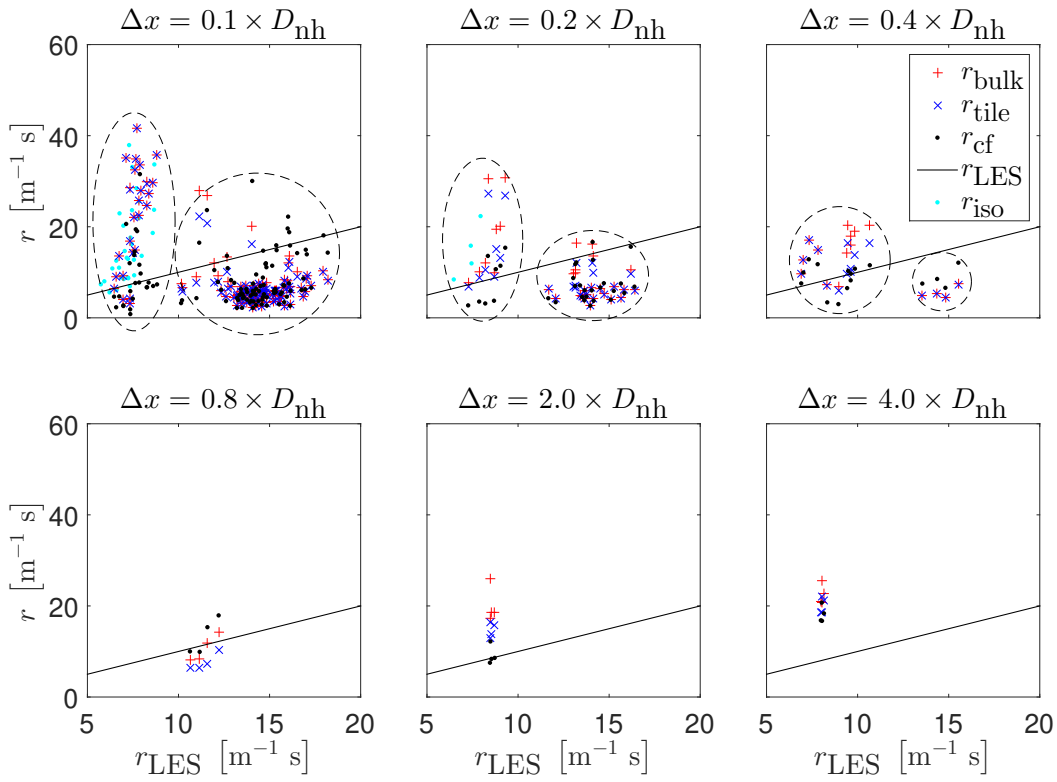

FIG. 8. Scatter plots of r_{bulk} (red crosses), r_{tile} (blue crosses), and r_{cf} (black dots) against the LES reference r_{LES} (black solid line) for the test case 2 and varying test-MSM grid cell dimensions (different subplots). The isolated cells, defined by $r_{\mathrm{iso}} = r_{\mathrm{bulk}} = r_{\mathrm{tile}} = r_{\mathrm{cf}}$, are displayed by cyan dots. The dashed ellipses separate inner cells (right ellipses) from outer cells (left ellipses) for the three finer test-MSM grids.

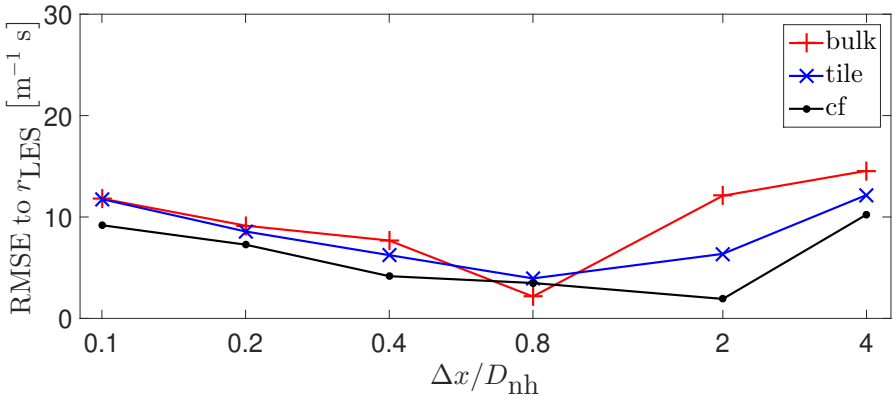

FIG. 9. Root-mean-square error (RMSE) of the bulk (red line), tile (blue line), and covariance function approaches (black line) with respect to the LES reference r_{LES} as a function of the test-MSM grid dimensions for the LES test case 2.

small effect of the heterogeneity for large MSM cell grid dimension (Section 4a).

5. Conclusion

A novel analytical method for parametrization of subgrid-scale heterogeneity in meso-scale models is proposed. The derivation is based on linking the covariance functions of the actual heterogeneous scenario to the covariance functions of the bulk averaged scenario for a certain test-MSM grid cell. Assuming stationary flow, neglecting triple moments, using a Rotta like closure for the pressure decorrelation, neglecting dispersive fluxes and advection, and assuming the spectral shapes for the bulk homogeneous scenario are based on Kolmogorovian power laws (Katul et al. 2013, 2014) for inertial scales, the aerodynamic resistance to heat transfer is derived. To incorporate arbitrary atmospheric stability, eddy anisotropy is added to the cross-over from produc-

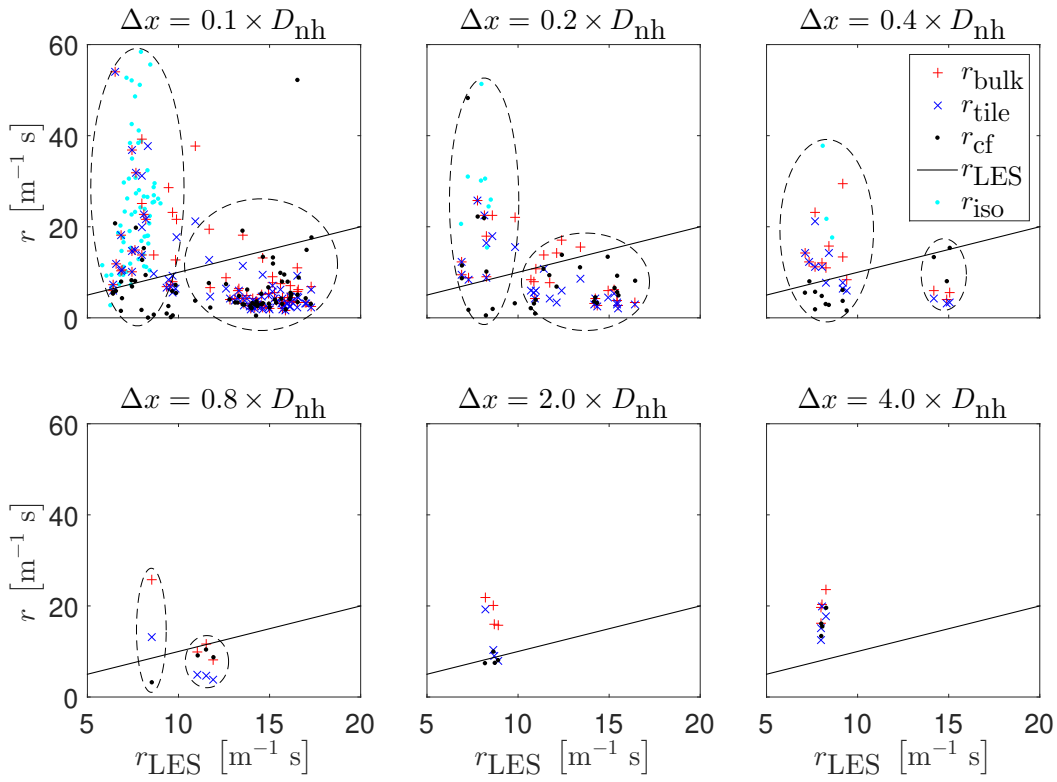

FIG. 10. Scatter plots of r_{bulk} (red crosses), r_{tile} (blue crosses), and r_{cf} (black dots) against the LES reference r_{LES} (black solid line) for the test case 3 and varying test-MSM grid cell dimensions (different subplots). The isolated cells, defined by $r_{\mathrm{iso}} = r_{\mathrm{bulk}} = r_{\mathrm{tile}} = r_{\mathrm{cf}}$, are displayed by cyan dots. The dashed ellipses separate inner cells (right ellipses) from outer cells (left ellipses) for the three finer test-MSM grids.

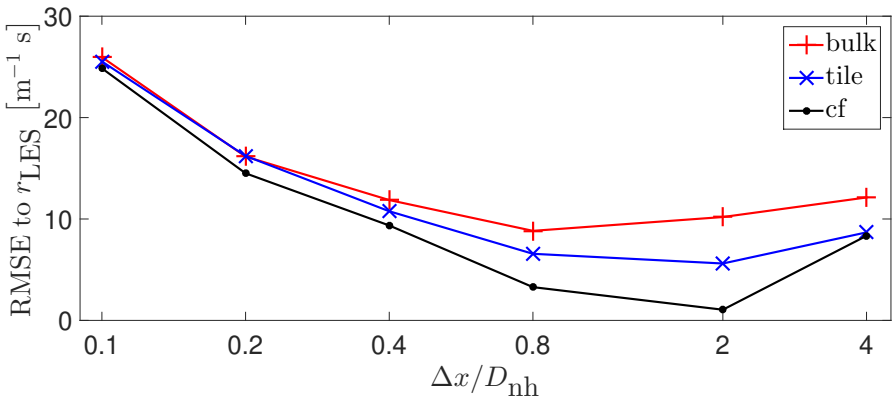

FIG. 11. Root-mean-square error (RMSE) of the bulk (red line), tile (blue line), and covariance function approaches (black line) with respect to the LES reference r_{LES} as a function of the test-MSM grid dimensions for the LES test case 3.

tion to inertial scales in the spectra of Katul et al. (2014) . From this analytical investigation, heterogeneity corrections for the MOST stability correction functions are derived, where three different terms contributed to these corrections: The first term represents the dimension of the test-MSM grid cells, the second term consists of the spectral functions of Katul et al. (2014) for homogeneous terrain, and the third term is the Fourier transform of a map representing the surface heterogeneity. Because advective effects are ignored, wind direction is not a factor in this analysis and the surface heterogeneity map is assumed to hold across all wind directions. This simplification means that highly localized features such differences in transitions from rough-to-smooth and smooth-to-rough surfaces are not explicitly resolved.

To test the performance of the proposed covariance function approach for different heterogeneity types, three LES runs of distinct surface heterogeneities are conducted.

These are defined by heterogeneous surface heat flux and aerodynamic roughness. For test case 1, we used a disc-shaped shaped heterogeneity with a diameter $D_{\mathrm{nh}} = 400$ m, featuring a constant surface heat flux and aerodynamic roughness. We again used a disc-shaped heterogeneity of same size for test case 2, however the surface heat fluxes and roughness length within the disc were now chosen randomly, such that the spatial average corresponds to the constant values of test case 1. For test case 3, we used surface heat flux and roughness length maps (Kröniger et al. 2018) determined above a semi-arid forest (Rotenberg and Yakir 2010). Case 3 represents a natural surface heterogeneity over a rough canopy surface. However, we downscaled the extension of the forest to coincide with the discs of the previous test cases and increased the surface heat fluxes to guarantee the same energy input in all three LES. We further constructed six test-MSM grids of different grid resolutions ($\Delta x/D_{\mathrm{nh}} = 0.1, 0.2, 0.4, 0.8, 2.0, 4.0$) for resolving the surface heterogeneity of the three scenarios. Using these test-MSM grids and the LES results as reference, we compared the aerodynamic resistance from the covariance function approach with the aerodynamic resistances from the tile (Stoll and Porté-Agel 2009) and the bulk similarity approach (Mahrt 1996; Brutsaert 1998). This comparison showed that the covariance function method mainly features the smallest deviations from the reference for the three scenarios and different test-MSM grids. While the covariance function approach provides corrections to the bulk method for all considered grid dimensions, the tile approach only corrects the bulk method for the grid resolutions larger than $0.2 \times D_{\mathrm{nh}}$. However, for the largest investigated grid dimension, these corrections decrease again for both methods, which is due to the large size of the grid cell in comparison to the heterogeneity. Besides, the covariance function parametrization emerges as the most robust method when increasing the surface heterogeneity from test case 1 to test case 2 to test case 3. This finding is explained by the different approach of considering all scales of surface heterogeneity in the spectra, while the tile and bulk approach directly apply MOST in more or less sophisticated ways.

Despite the various assumptions made for the derivation of the covariance function approach, the comparison of the three parametrization schemes show that this novel method is able to decrease deviations from LES computed outcomes by up to a factor of five with respect to the tile and even by up to one order of magnitude with respect to the bulk approach. However, including dispersive fluxes, or using more sophisticated models of the spectra have the potential to increase the quality of the covariance function approach even further, which is a topic suitable for future research. The proposed method is not only limited to improving aerodynamic resistance parametrization, but can provide correction factors wherever MOST is applied over heterogeneous surfaces. As these factors only have to be computed once for a given test-MSM grid and surface heterogeneity map, the proposed covariance function approach requires the same computational costs as the bulk method and is therefore cheaper than methods referring to a subgrid scale model, like the "mosaic" approach (Koster and Suarez 1992; Giorgi and Avissar 1997; de Vrese et al. 2016). Concerning the application of the covariance function approach to more realistic cases, the determination of the heterogeneity map will be an important factor. While we derived this map from the specified heterogeneous surface heat flux maps, other sources such as satellite images, now exponentially proliferating, might be used for this construction in the future.

In conclusion, the current work proposes a framework for determining correction factors to MOST, which might even have several applications besides improving subgrid scale parametrizations. Additional numerical studies and comparison to measurements are still needed to judge the performance of the covariance function approach in different scenarios. Hence, the work here is not offering any finality to the aforementioned problem, only blue prints on how to proceed.

Acknowledgments. The authors thank the PALM group at Leibniz University Hannover for their open-source PALM code and their support. Furthermore, the authors gratefully acknowledge the Gauss Centre for Supercomputing e.V. (www.gauss-centre.eu) for funding this project by providing computing time on the GCS Supercomputer SuperMUC at Leibniz Supercomputing Centre (LRZ, www.lrz.de). This research was supported by the German Research Foundation (DFG) as part of the German-Israel collaborative project "Climate feedbacks and benefits of semi-arid forests" (CliFF; YA-274/1-1 and SCHM-2736/2-1), and the project "Capturing all relevant scales of biosphere-atmosphere exchange - the enigmatic energy balance closure problem" (VH-NG-843), which is funded by the Helmholtz-Association through the President's Initiative and Networking Fund, and by KIT. G.K. acknowledges support from the National Science Foundation (NSF-EAR-1344703 and NSF-AGS-1644382) and the Helmholtz Research School MICMoR Visiting Scientist Fellowship through KIT/IMK-IFU (HGF VH-KO-505).

APPENDIX

Deriving u_* from the covariance function approach

To derive $u_{*,\mathrm{ah}}$, the uw-budget equation is considered:

$$\begin{aligned}\partial_t \overline{F}_{uw} = &\left[-S\overline{F}_{ww} - \partial_z \overline{w' F_{uw}} + \overline{\Pi}_u - 2\nu k^2 \overline{F}_{uw}\right] + \\ &+\Big[-\overline{u}_j \partial_j \overline{F}_{uw} - \partial_l \overline{u_l' F_{uw}} - \overline{F}_{uu_j}\,\partial_j \overline{w} - \\ &-\overline{F}_{u_l w}\,\partial_l \overline{u} + \overline{\Pi}_w + \beta \overline{F}_{uT}\Big],\end{aligned} \tag{A1}$$

where $S = d_z\overline{u}$ and we ordered Eq. A1 such that the terms in the first line are relevant for an horizontally-homogeneous scenario and the terms in residual lines are correction terms, in analogy to Eq. 7. While neglecting the first five correction terms of Eq. A1 is in line with the discussion in Section 2b, the term $\beta\overline{F}_{uT}$ did not appear in Eq. 7. However, as this term is related to an horizontal heat flux, we also assume this term to be negligible for the considered derivation. Further, we again assumed stationary flow, a Rotta closure model for the pressure term (Katul et al. 2013), and neglected dissipation and transfer terms to yield:

$$\overline{F}_{uw} = -C_{uw}S\overline{F}_{ww}\tau_{uw}, \tag{A2}$$

where τ_{uw} is the relaxation time of the Rotta model, and C_{uw} is a constant also originating from the Rotta model. Further, note that u_* and the corresponding uw covariance function ($\overline{F}^{\mathrm{nh}}_{uw}$) are linked by

$$(u_*)^2 = -\overline{u'w'} = -\int_{\mathbf{k}} \overline{F}_{uw}\left((\mathbf{r},z),\mathbf{k}\right). \tag{A3}$$

The same rational is used as for the r_{cf} derivation by inserting Eq. A2 into Eq. A3 and applying spatial averages over the test-MSM grid cell to the resulting equation. Expressing the heterogeneous covariance function through the associated homogeneous one (Section 2c), using the Katul et al. (2014) model for expressing those (Section 2e), and employing MOST to express $\varepsilon_{\mathrm{ah}}$ for neutral stratification yields

$$u_{*,\mathrm{ah}} = \tilde{C}_3\, S_{\mathrm{ah}}\, z\, I^{-1}_{ww}, \tag{A4}$$

where we defined $\tilde{C}_3 = \frac{7}{4}(2\pi)^{-10/3} C_{uw}C_0\kappa^{-1/3}$. Solving Eq. A4 for $S_{\mathrm{ah}} = d_z\overline{u}_{\mathrm{ah}}$, performing the z-integration, and subsequently solving for $(u_{*,\mathrm{ah}})^{-1}$ finally yields:

$$(u_{*,\mathrm{ah}})^{-1} = \left(\tilde{C}_3\overline{u}_{\mathrm{ah}}\right)^{-1} \int_{z_{0m}}^{z-d} d\tilde{z}\, \frac{I_{ww}(\tilde{z})}{\tilde{z}}. \tag{A5}$$

This is the sought result.

References

Arakawa, A., and V. R. Lamb, 1977: Computational design of the basic dynamical processes of the UCLA general circulation model. *Methods Comput. Phys.*, **17**, 173–265, doi:10.1016/B978-0-12-460817-7.50009-4.

Avissar, R., and R. A. Pielke, 1989: A parameterization of heterogeneous land surfaces for atmospheric numerical models and its impact on regional meteorology. *Mon. Weather Rev.*, **117 (10)**, 2113–2136, doi:10.1175/1520-0493(1989)117⟨2113:APOHLS⟩2.0.CO;2.

Banerjee, T., F. De Roo, and M. Mauder, 2017: Explaining the convector effect in canopy turbulence by means of large-eddy simulation. *Hydrol. Earth Syst. Sci.*, **21 (6)**, 2987, doi:10.5194/hess-2017-4.

Brutsaert, W., 1998: Land-surface water vapor and sensible heat flux: Spatial variability, homogeneity, and measurement scales. *Water Resour. Res.*, **34 (10)**, 2433–2442, doi:10.1029/98WR01340.

de Vrese, P., and S. Hagemann, 2016: Explicit representation of spatial subgrid-scale heterogeneity in an ESM. *J. Hydrometeorol.*, **17 (5)**, 1357–1371, doi:10.1175/JHM-D-15-0080.1.

de Vrese, P., J.-P. Schulz, and S. Hagemann, 2016: On the representation of heterogeneity in land-surface–atmosphere coupling. *Boundary-Layer Meteorol.*, **160 (1)**, 157–183, doi:10.1007/s10546-016-0133-1.

Deardorff, J. W., 1980: Stratocumulus-capped mixed layers derived from a three-dimensional model. *Boundary-Layer Meteorol.*, **18 (4)**, 495–527, doi:10.1007/BF00119502.

Foken, T., 2006: 50 years of the Monin–Obukhov similarity theory. *Boundary-Layer Meteorol.*, **119 (3)**, 431–447.

Fujita, T., 1986: Mesoscale classifications: their history and their application to forecasting. *Mesoscale Meteorol. Forecast.*, Springer, 18–35, doi:10.1007/978-1-935704-20-1_2.

Giorgi, F., and R. Avissar, 1997: Representation of heterogeneity effects in earth system modeling: Experience from land surface modeling. *Rev. Geophys.*, **35 (4)**, 413–437, doi:10.1029/97RG01754.

Harlow, F. H., and J. E. Welch, 1965: Numerical calculation of time-dependent viscous incompressible flow of fluid with free surface. *Phys. Fluids*, **8 (12)**, 2182–2189, doi:10.1063/1.1761178.

Harman, I. N., M. Böhm, J. J. Finnigan, and D. Hughes, 2016: Spatial variability of the flow and turbulence within a model canopy. *Boundary-Layer Meteorol.*, **160 (3)**, 375–396, doi:10.1007/s10546-016-0150-0.

Heinemann, G., and M. Kerschgens, 2005: Comparison of methods for area-averaging surface energy fluxes over heterogeneous land surfaces using high-resolution non-hydrostatic simulations. *Int. J. Climatol.*, **25 (3)**, 379–403, doi:10.1002/joc.1123.

Katul, G. G., A. G. Konings, and A. Porporato, 2011: Mean velocity profile in a sheared and thermally stratified atmospheric boundary layer. *Phys. Rev. Lett.*, **107 (26)**, 268 502, doi:10.1103/PhysRevLett.107.268502.

Katul, G. G., A. Porporato, C. Manes, and C. Meneveau, 2013: Co-spectrum and mean velocity in turbulent boundary layers. *Phys. Fluids*, **25 (9)**, 091 702, doi:10.1063/1.4821997.

Katul, G. G., A. Porporato, S. Shah, and E. Bou-Zeid, 2014: Two phenomenological constants explain similarity laws in stably stratified turbulence. *Phys. Rev. E*, **89 (2)**, 023 007, doi:10.1103/PhysRevE.89.023007.

King, J. C., A. Jrrar, and W. M. Connolley, 2007: Sensitivity of modelled atmospheric circulation to the representation of stable boundary layer processes. *Geophys. Res. Lett.*, **34 (6)**, doi:10.1029/2006GL028563.

Kolmogorov, A. N., 1941: The local structure of turbulence in incompressible viscous fluid for very large Reynolds numbers. *Dokl. Akad. Nauk SSSR*, Vol. 30, 299–303.

Koster, R. D., and M. J. Suarez, 1992: A comparative analysis of two land surface heterogeneity representations. *J. Clim.*, **5 (12)**, 1379–1390, doi:10.1175/1520-0442(1992)005⟨1379:ACAOTL⟩2.0.CO;2.

Kröniger, K., and Coauthors, 2018: Effect of secondary circulations on surface-atmosphere exchange of energy at an isolated semi-arid forest. *Boundary-Layer Meteorol.*, **(in press)**.

Liu, S., L. Lu, D. Mao, and L. Jia, 2007: Evaluating parameterizations of aerodynamic resistance to heat transfer using field measurements. *Hydrol. Earth Syst. Sci.*, **11 (2)**, 769–783, doi:10.5194/hess-11-769-2007.

Mahrt, L., 1996: The bulk aerodynamic formulation over heterogeneous surfaces. *Boundary-Layer Meteorol.*, **78**, 87–119, doi:10.1007/BF00122488.

Mahrt, L., and N. Gamage, 1987: Observations of turbulence in stratified flow. *J. Atmos. Sci.*, **44 (7)**, 1106–1121, doi:10.1175/1520-0469(1987)044⟨1106:OOTISF⟩2.0.CO;2.

Maronga, B., and Coauthors, 2015: The Parallelized Large-Eddy Simulation Model (PALM) version 4.0 for atmospheric and oceanic flows: model formulation, recent developments, and future perspectives. *Geosci. Model Dev.*, **8 (8)**, 2515, doi:10.5194/gmd-8-2515-2015.

Raasch, S., and M. Schröter, 2001: PALM–a large-eddy simulation model performing on massively parallel computers. *Meteorol. Z.*, **10 (5)**, 363–372, doi:10.1127/0941-2948/2001/0010-0363.

Rotenberg, E., and D. Yakir, 2010: Contribution of semi-arid forests to the climate system. *Science*, **327 (5964)**, 451–454, doi:10.1126/science.1179998.

Stoll, R., and F. Porté-Agel, 2009: Surface heterogeneity effects on regional-scale fluxes in stable boundary layers: surface temperature transitions. *J. Atmos. Sci.*, **66 (2)**, 412–431, doi:10.1175/2008JAS2668.1.

Townsend, A. A., 1976: *The structure of turbulent shear flow*. 2nd ed., Cambridge university press, Cambridge, UK.

Yang, K., N. Tamai, and T. Koike, 2001: Analytical solution of surface layer similarity equations. *J. Appl. Meteorol.*, **40 (9)**, 1647–1653, doi:10.1175/1520-0450(2001)040⟨1647:ASOSLS⟩2.0.CO;2.